A CONCURRENT MULTISCALE MODEL FOR THE THERMOMECHANICAL RESPONSE OF POLYCRYSTALLINE MATERIALS

A Thesis
Presented to
The Academic Faculty

by

Jean-Baptiste P. M. Bouquet

In Partial Fulfillment
of the Requirements for the Degree
Doctor of Philosophy in the
School of Aerospace Engineering

Georgia Institute of Technology
May 2017

A CONCURRENT MULTISCALE MODEL FOR THE THERMOMECHANICAL RESPONSE OF POLYCRYSTALLINE MATERIALS

Approved by:

Professor Julian J. Rimoli, Advisor
School of Aerospace Engineering
Georgia Institute of Technology

Professor Massimo Ruzzene
School of Aerospace Engineering
Georgia Institute of Technology

Professor Min-Feng Yu
School of Aerospace Engineering
Georgia Institute of Technology

Professor Graeme Kennedy
School of Aerospace Engineering
Georgia Institute of Technology

Professor Min Zhou
School of Mechanical Engineering
Georgia Institute of Technology

Date Approved: December 2, 2016

I dedicate my dissertation to my family

ACKNOWLEDGEMENTS

First and foremost, I would like to express my sincere appreciation to my advisor Dr. Julian Rimoli. I want to thank you for giving me the opportunity to join your group. Your mentorship, encouragement, and guidance have been priceless. Your advice on research and your wealth of ideas have greatly contributed to my professional development. You have been a tremendous mentor.

I would also like to thank my committee members Dr. Graeme Kennedy, Dr. Massimo Ruzzene, Dr. Minfeng Yu and Dr. Min Zhou. Thank you for your interest in my research and for the time you dedicated to me. Your useful insights inspired me to explore new research directions. In addition, I also would like to thank Dr. Claudio Di Leo. I truly value your enthusiasm and your positive energy.

A special thank goes to my fellow labmates and friends at Georgia Tech, especially: Frédéric Burgaud, Matteo Carrara, German Capuano, Luca Guidoni, Juan Rojas, Amir Hossein Salahshoor Pirsoltan, Aaron Schinder, and Giuseppe Trainiti. You made the office a fun place to work and to relax. I really enjoyed your company and I wish you the best of luck for your upcoming adventures. I hope our paths will cross again.

Last but not least, I want to thank my family. To my parents, the life philosophy and the quality of education you provided me with led me to accomplish my Ph.D. at Georgia Tech. I appreciate your understanding and your constant and unfailing support in the journey I pursued so far from home. This entire experience would not have been possible without your genuine faith in me. To my brother, the year we spent together in Atlanta was tremendous and made this experience significantly more enjoyable and meaningful. I dedicate y'all this thesis.

TABLE OF CONTENTS

DEDICATION . . . . . **iii**

ACKNOWLEDGEMENTS . . . . . **iv**

LIST OF TABLES . . . . . **ix**

LIST OF FIGURES . . . . . **x**

NOMENCLATURE . . . . . **xiii**

SUMMARY . . . . . **xvi**

I INTRODUCTION **1**

1.1 Overview 1

1.2 Motivations 2

1.3 State-of-the-Art 3

1.3.1 Length Scale Effect 4

1.3.2 Length Scale Effect in Thermomechanical Analysis 6

1.3.3 Multiscale Modeling in Polycrystals 9

1.4 Scope of this Work and Outline of Study 10

1.5 Contributions 11

II THERMOMECHANICAL MODEL **13**

2.1 Solid State Physics 13

2.1.1 Crystal Lattice, Reciprocal Lattice and Brillouin Zone 14

2.1.2 Lattice Vibration and Phonons 16

2.1.3 Density of States 24

2.2 Heat Conduction in Bulk Material 26

2.2.1 Mean Free Path and Phonon Scattering Processes 26

2.2.2 Matthiessen's Rule 31

2.2.3 Phonon Boltzmann Transport Equation 32

2.2.4 Bulk Thermal Conductivity 34

2.2.5 Fourier's Law and Heat Equation 37

2.3 Size Effects in Heat Transfer 38

2.3.1 Classical Size Effect 39

2.3.2 Quantum Size Effect . . . 46
2.4 Thermomechanical Model . . . 47
2.4.1 Mechanical Model . . . 47
2.4.2 Thermomechanical Coupling . . . 51
2.4.3 Thermomechanical Fracture . . . 53
III MULTISCALE NUMERICAL ANALYSIS . . . 55
3.1 Polycrystal Generation and Meshing Techniques . . . 55
3.1.1 Generation of the Polycrystal . . . 55
3.1.2 Mesh Refinement Requirement . . . 57
3.2 Microscale-level: Thermal Conductivity Calculation . . . 59
3.2.1 Distance Phonon to Grain Boundary . . . 59
3.2.2 Numerical Integration of the Thermal Conductivity . . . 63
3.2.3 Multiscale Framework . . . 64
3.3 Continuum-level: Finite Element Implementation . . . 66
3.3.1 Continuum-level Thermal Model . . . 66
3.3.2 Continuum-level Mechanical Model . . . 67
3.3.3 Thermomechanical Coupling . . . 69
3.3.4 Time Scheme . . . 70
3.4 Continuum-level: Interface Element . . . 76
3.4.1 Thermal Fracture . . . 77
3.4.2 Mechanical Fracture . . . 79
3.4.3 Thermomechanical Coupling . . . 81
3.5 High Performance Implementation . . . 81
3.5.1 Mesh Generation and Subdivision . . . 82
3.5.2 Partitioning . . . 85
3.5.3 Communication Scheme . . . 86
3.5.4 Parallel Solvers . . . 87
3.5.5 Implementation Validation and Scalability Analysis . . . 89
IV VALIDATION AND RESULTS . . . 94
4.1 Size-dependent Heat Transfer . . . 94

4.1.1 Thin Films: In-plane and Out-of-Plane Thermal Conductivity . . . 94
4.1.2 Nanowires: Axial Thermal Conductivity . . . 97
4.1.3 Micro-grain Thermal Conductivity . . . 98
4.1.4 Heat Transfer in Graded Polycrystals . . . 100
4.1.5 Other Materials . . . 105
4.1.6 Conclusion . . . 106
4.2 Physical Insight - MFP . . . 107
4.2.1 Motivation and Goals . . . 107
4.2.2 Single MFP . . . 108
4.2.3 Polarization-dependent MFP . . . 110
4.2.4 MFP within the Brillouin Zone . . . 111
4.2.5 Conclusion . . . 113
4.3 Heat Transfer Optimization in Micro-electronic Devices . . . 113
4.3.1 Genetic Algorithm . . . 115
4.3.2 Optimization Methodology . . . 116
4.3.3 Verification of Separation of Scales Assumption . . . 122
4.3.4 Numerical Results . . . 124
4.3.5 Conclusion . . . 132
4.4 MFP Kapitza Resistance . . . 132
4.4.1 Kapitza Resistance Models . . . 134
4.4.2 MFP Calibrated Kaptiza Models . . . 139
4.4.3 Numerical Results . . . 143
4.4.4 Conclusion . . . 151
4.5 Thermal Residual Stresses . . . 151
4.5.1 Stress Generation in the absence of interface elements . . . 152
4.5.2 Stress Generation in the presence of interface elements . . . 155
4.5.3 Conclusion . . . 160
V CONCLUSION AND FUTURE WORK . . . 161
5.1 Summary . . . 161
5.2 Contributions . . . 163
5.3 Future Work . . . 165

APPENDIX A — GENERATED CODE 167

Bibliography 171

LIST OF TABLES

1 Material constants for bulk silicon. 31

2 Characteristic times for different sizes of silicon grain. 72

3 Parallel Implementation Analysis - Solver Time (in seconds). 90

4 Extreme values of the interface stress fields. 160

LIST OF FIGURES

1 Multiscale Approach in Engineering. 4
2 Heat Conduction Regime 8
3 Face-centered cubic unit cell and its associated primitives vectors. 15
4 Brillouin zone of the face-centered cubic unit cell. 17
5 1D oscillator chain: monoatomic and diatomic 18
6 Dispersion curve of monoatomic 1D oscillator. 19
7 Dispersion curve of diatomic 1D oscillator. 21
8 Dispersion curves of silicon 22
9 Computed phonon dispersion and group velocity for acoustic branches. . . . 23
10 Surface of constant energy in the reciprocal space 25
11 Phonon mean free path in bulk material. 27
12 Two different phonon-phonon processes. 29
13 Bulk thermal conductivity of silicon 37
14 Reduced phonon mean free path. 39
15 Thin film schematics 41
16 Reflection at the boundary: specular and diffuse 42
17 Reduced thermal conductivity in cylindrical nanowires. 45
18 Schematics for computing the reduced phonon mean free path 45
19 Reference and deformed configuration of a body $\mathcal{B}$. 48
20 Solid body $\mathcal{B}$ partially separated by a crack. 53
21 Numerical generation of the polycrystalline structure. 57
22 Mesh refinement analysis - Square polycrystal of size $25\mu m$. 58
23 Configuration of the intersection in 2D between the line and the line 60
24 Configuration of the intersection in 3D between the plan and the line. . . . 61
25 Distance from the quadrature point to the bottom grain boundary. 62
26 Convergence on the integration over θ. 64
27 Concurrent multiscale scheme. 65
28 Mesh refinement interpolation technique. 69
29 Flowchart of the static analysis 73

30 Flowchart of the quasi-static and dynamic analyses 75
31 Opening of a two-dimensional interface element 77
32 Influence of the Kapitza conductivity on the thermal field between two elements. 78
33 PPR Traction separation-law in 2D 80
34 Full Thermomechanical coupling - Influence of cracks on the thermal field. . 81
35 Framework of the High Performance Computing process. 83
36 Barycentric vs '8-subtetrahedron' subdivisions in 3D. 84
37 Comparison of mesh quality between barycentric and regular subdivision techniques 85
38 Non-contiguous vs contiguous partitions in 2D. 86
39 Interface elements - Ghost node concept. 86
40 Scalability Analysis of the HCP parallel implementation. 91
41 Schematic of thin film considered for length-dependent thermal conductivity 95
42 In-plane and cross-plane thermal conductivity of silicon thin films 96
43 Thermal conductivity of nanowires for different diameters 97
44 Direction-dependent thermal conductivity for a silicon micro-grain 98
45 Full-domain calculations of length-dependent thermal conductivity 99
46 Size-dependent thermal conductivity for silicon. 100
47 Schematics and computational domains for the 3 cases under study 101
48 Convergence analysis 102
49 Evolution of temperature distribution for the 3 cases 103
50 Bulk thermal conductivity as a function of the temperature. 105
51 Fitting parameters. 106
52 Model comparison: full MFP vs Single MFP vs 2 Polarization MFP 109
53 Contribution of the MFP to the cumulative thermal conductivity 111
54 Equivalent size-dependent MFP 112
55 Ashby graph of thermal conductivity vs. thermal expansion coefficient . . . 115
56 Schematics for optimization problem with and without mesh adaption . . . 118
57 Optimization results with and without mesh adaption 119
58 Comparison between discrete versus continuous optimization approaches. . 121
59 Schematics of procedure for verification of the separation of scales assumption. 123

60 Thermal conductivity as a function of temperature and grain size. 125
61 Geometry and boundary conditions of the sample problem #1. 126
62 Influence of the thermal conductivity gradient on the optimal average temperature. 127
63 Influence of thermal gradient constraint on temperature distribution. 128
64 Geometry and boundary conditions for sample problem #2. 130
65 Distribution of thermal conductivity and temperature field for three different configurations. 131
66 Surface of average D as a function of grain size and temperature 133
67 Comparison 'full MFP' and 'homogenized MFP' models. 135
68 Variation of the thermal conductivity D within a grain 137
69 Grain size dependence of the effective thermal conductivity D_{eff} for SiC. . . 139
70 Schematic illustrating the calculation of the thermal conductivities at grain boundaries 141
71 Grain size dependence of the Kapitza resistance R_K and the intragranular conductivity D_{intra} 143
72 Heat conduction simulations for the Kapitza models 145
73 Temperature profiles across the simulation domain 146
74 Analytical normalized grain boundary temperature jump as a function of grain size. 147
75 Effective thermal conductivity across a uniform polycrystal with varying average grain size 148
76 Geometry of the graded polycrystalline structure. 149
77 Thermal conductivity and temperature field of graded polycrystalline structures 150
78 Mechanical boundary conditions and grain orientation for case 1 153
79 Evolution of the thermal stress over time 154
80 Stress field at steady-state 155
81 Thermomechanical simulations of a uniform polycrystal 157
82 Transcient thermomechanical simulations of a uniform polycrystal. 158
83 Normal and Tangential stresses in the cohesive elements. 159
84 Framework applied to matematerial 165

NOMENCLATURE

Abbreviations

2D	Two-dimensional
3D	Three-dimensional
BTE	Boltzmann transport equation
BZ	Brillouin zone
DoS	Density of states
GA	Genetic algorithm
GB	Grain boundary
MFP	Mean free path
RTA	Relaxation time approximation

Constants

$\hbar$	Reduced Plank constant	$1.05e^{34}\ J.s$
k_b	Boltzmann constant	$1.38e^{-23}\ J.K^{-1}$

Variables - Greek symbol

α	Thermal diffusivity	$m^2.s^{-1}$
Δt	Time increment	s
ϵ	Phonon energy	J
ξ	Phonon deviation from equilibrium distribution	
Λ	Mean free path	m
Λ_0	Bulk mean free path	m
Ω	Density of states	
$\bar{\omega}$	Velocity space	
ω	Angular frequency	$rad.s^{-1}$
ω_m	Dispersion maximum frequency	$rad.s^{-1}$
ρ	Mass density	$kg.m^{-3}$
τ	Effective relaxation time	s
τ_0	Bulk effective relaxation time	s
Θ_D	Debye Temperature	K

Variables - Upper case

C_p	Specific heat capacity	$J.kg^{-1}.K^{-1}$
$\mathbf{D}$	Thermal conductivity tensor	$W.K^{-1}.m^{-1}$
D	Thermal conductivity	$W.K^{-1}.m^{-1}$
D_0	Bulk thermal conductivity	$W.K^{-1}.m^{-1}$
D_{intra}	Intragranular thermal conductivity	$W.K^{-1}.m^{-1}$
D_K	Kapitza conductance	$W.K^{-1}.m^{-2}$
$\mathbf{F}$	Force vector	$kg.m.s^{-2}$
$\mathbf{G}$	Reciprocal unit vector	
L_c	Characteristic length	m
N_i	Interpolation/Shape function	
$\mathbf{R}$	Lattice translation vector	m
R_K	Kapitza resistance	$K.m^2.W^{-1}$
T	Temperature	K
U	Total lattice energy	J
W	Scattering probability	
$\mathbf{X}$	Equilibrium position vector	

Variables - Lower case

$\mathbf{a}$	Acceleration vector	$m.s^{-2}$
a	Lattice constant	m
f	Phonon distribution function	
f_0	Equilibrium phonon distribution	
$\mathbf{k}$	Wavevector	m^{-1}
p	Specularity parameter	
$\mathbf{q}$	Heat flux vector	$W.m^{-2}$
$\mathbf{r}$	Location vector	
t_c	Characteristic time	s
$\mathbf{v}$	Velocity vector	$m.s^{-1}$
$\mathbf{v_g}$	Group velocity	$m.s^{-1}$
$\mathbf{v_p}$	Phase velocity	$m.s^{-1}$

SUMMARY

The work presented in this thesis establishes and implements a novel concurrent multiscale framework to predict the size-dependent thermomechanical response of engineering materials. As such, this work focuses on determining the interactions among length scales. More precisely, it aims at capturing the local variations on thermal conductivity at the subgrain level, the resulting repercussion on the mesoscopic temperature field, and the consequent impact on thermal stresses. Therefore, the ultimate goal is to better understand the role of the grain size and the grain shape on heat transfer of polycrystalline materials and the influence on the underlying thermal stresses concentration, driving to the localized failure of the material.

A review of current modeling approaches reveals a lack of numerical tools in the determination of the size effect on geometries presenting complex features. Current numerical methods are only capable of modeling thermomechanical processes at the macroscale. In contrast, analytical thermal models have been developed to quantify the size effect in subgrain structures, but the applications are limited to relatively simple geometries such as thin films, nanowires or single cubic grains. Further, size-dependent thermomechanical approaches are completely non-existent. To bridge that gap, a novel concurrent multiscale framework is developed herein to account for any arbitrary microstructural configuration. The proposed technique is achieved by capturing the microscale size effect on the thermal conductivity and incorporating it into the macroscale analysis.

The numerical framework along with several numerical demonstrations are unique contributions of this thesis. In particular, the multiscale scheme accounts for: (a) a submicron scale model for the thermal conductivity based on the Boltzmann transport equation under the relaxation time approximation, (b) a classic Fourier heat transport model at the mesoscale, and (c) a continuum model of thermomechanical deformation that explicitly resolves the microscopic geometric features of the material. The capabilities of the model are

demonstrated through a series of examples, which highlight the potential of the procedure for designing materials with enhanced thermomechanical responses.

Among other applications, this research uses the developed concurrent multiscale framework to analyze the influence of the microscopic features on the thermal and thermomechanical properties. In particular, the analysis of functionally graded polycrystals is performed, highlighting the influence of the grain size distribution on the temperature field and on the thermal stress distribution. From those results, further novel optimization approaches are conducted using length-dependent modeling of polycrystalline materials. More specifically, an innovative multiscale optimization technique is formulated. The size-dependent thermal properties obtained from the model are coupled with an adaptive topology optimization algorithm to improve the spatial grain size distribution on single-material polycrystalline systems. This technique creates a unique tool for the manufacturing of single-material systems with enhanced thermal properties. Finally, this framework provides a physically based and accurate computational tool for defining a 'mean free path (MFP) calibrated' Kapitza resistance at the grain boundary, where both the Kapitza resistance R_K and the intragranular thermal conductivity D_{intra} are size-dependent. This particular study highlights the benefits of the innovative concurrent multiscale framework for the study of thermomechanical phenomena. It notably allows to recover the accurate effective thermal conductivity of polycrystals. Additionally, it reduces spurious temperature jumps and related thermal stresses at the grain boundary, that appears to be artifacts of the current numerical approaches.

CHAPTER I

INTRODUCTION

1.1 Overview

The work presented in this thesis investigates a concurrent multiscale framework for the size-dependent thermomechanical response of polycrystalline materials with arbitrary microstructures. The methodology is based on a length-dependent model accounting for the size effect on the subgrain thermal conductivity tensor due to the interaction of phonons with microstructural features such as grain boundaries. Throughout this work, the capabilities of the model are demonstrated by a series of examples, which highlights the potential of the approach for designing materials with improved thermal and thermomechanical responses. In addition, an innovative multiscale optimization technique is created. It extends the multiscale model to the creation of enhanced microstructures by coupling it with a topology optimization algorithm. The concurrent multiscale framework is also employed to define a new thermomechanical interface model at the grain boundary, accounting for the size-dependent effects.

This introductory chapter starts with a thorough description of the motivations and goals of the performed work. Then, a review of the state-of-the-art in size-dependent thermomechanical modeling of polycrystals is presented. It aims at identifying the current modeling approaches designed for the prediction of thermomechanical processes across scales. More importantly, this overview examines the gap present in the literature and the reasons behind those limitations. It also highlights the related challenges. The intent of this thesis lies in filling the identified gaps by providing an innovative concurrent multiscale framework accounting for the size effect. Finally, this chapter highlights the scope of the work along with the contributions to the state-of-the-art.

1.2 Motivations

Over the last decade, a strong research focus has been placed in the design of modern and innovative materials for applications where extreme environment conditions exist. For instance, engine turbine blades [1], rocket propulsion systems [2] or MEMS packaging technology [3] require reliable enhanced materials, operating over a large temperature range. In order to improve the related properties such as heat propagation or thermomechanical failure, it is necessary to use new design approaches to accelerate the development of materials with enhanced performances.

One area of strong interest is the development of ceramics presenting advanced microstructures [2, 4]. Novel manufacturing and material synthesis techniques allow for the manipulation of characteristic material length scales. For instance, it is now possible to tailor the microstructural features by controlling the grain size [5, 6] and the grain size distribution [7, 8]. Still, the key challenge resides in defining the most efficient microstructure towards the desired macroscopic behavior. Numerical simulations become prominent to define such behavior.

Predictive modeling of material behavior is a critical challenge as it spans several scales. To numerically determine the behavior of those new materials, it is necessary to couple together microscale and macroscale properties. Consequently, mesoscale models are becoming essential to bridge that gap. However, as highlighted in the next section, several issues arise with current mesoscale models. Among others, length scale independent thermal transport properties and equivalent equilibrium state assumption considering uniform temperature fields [9, 10], are oversimplifying assumptions that poorly reflect the response of complex polycrystals. In reality, thermal transport process modeling must overcome those limitations and combines the atomistic level with the continuum models needed by designers and engineers.

Under those circumstances, the core objective of this thesis is to provide, for arbitrary configurations, a concurrent multiscale framework able to carry critical information about the microstructure of the system. More explicitly, the analysis motivating this work aims at

capturing local variations on the thermal conductivity at the subgrain level, the resulting repercussions on the mesoscopic temperature fields, and the consequent impact on thermal stresses. In essence, the multiscale aspect of this work focuses on determining the interactions among length scales on the thermomechanical response of engineering materials. It intends to better understand the role of the grain size and the grain shape on heat transfer of polycrystalline materials and the influence on the underlying thermal stresses concentration, driving to the localized failure of the material. The concurrent aspect of that work focuses on the strong coupling across the scales. For instance, the microscale thermal conductivity distribution influences the macroscale temperature field while in return the macroscale temperature field impacts the microscale thermal conductivity. This phenomenon leads to simultaneous computation at multiple levels.

As a result, the numerous numerical studies included in this thesis provide a better understanding of the underlying phenomena, as many insights are gained from the computational model. Consequently, it allows for the development of cutting-edge applications. The methodology results in the ability to accurately predict and tune the material properties at microscale in order to optimize macroscale thermal and thermomechanical performances. Among others, an innovative multiscale optimization technique is created to enhance microstructures by coupling the concurrent multiscale framework with a topology optimization algorithm. To some extent, this work is at the intersection of solid mechanics and material sciences.

1.3 State-of-the-Art

In this subsection, the state-of-the-art in size-dependent thermomechanical modeling of polycrystalline structures is reviewed. The focus is placed on: (a) the length scale effect among various physics phenomena, (b) the length scale effect in the particular case of thermomechanical problems, and (c) the multiscale modeling of polycrystals.

1.3.1 Length Scale Effect

Physical properties of materials at nanoscale and microscale differ from the ones of the corresponding bulk material. Nevertheless, observable properties are macroscopic results of complex phenomena arising at lower scales. That is, in order to accurately describe the physics involved, information obtained at those small length scales needs to be incorporated into the larger system. This transfer of information from one scale to another makes the understanding of the microscale of prime importance for the development of new materials and structures.

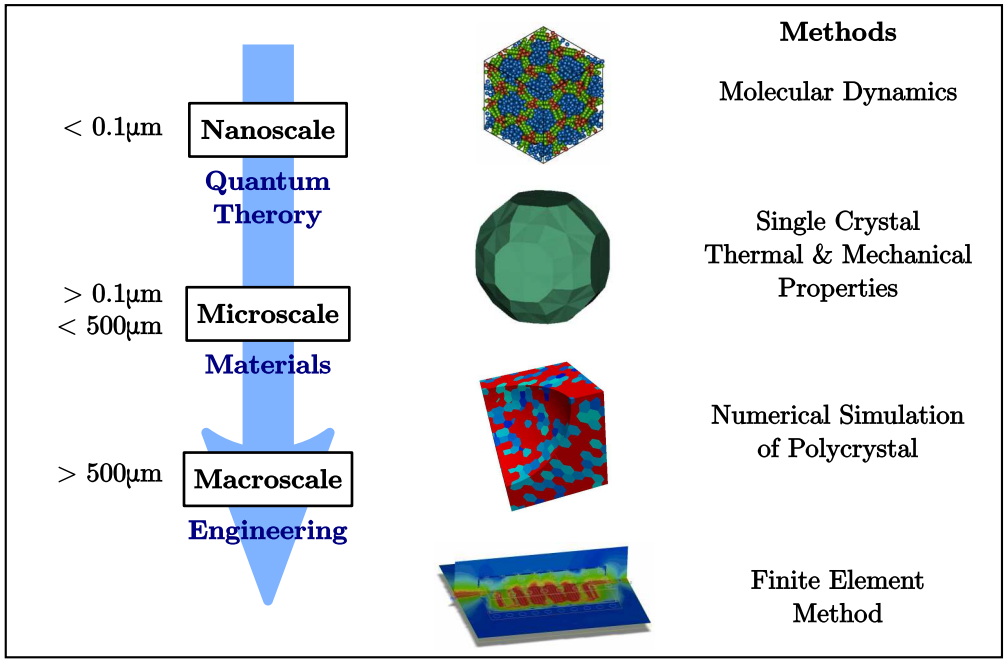

Figure 1: Multiscale Approach in Engineering.

This work focuses on one of the groups of material most commonly used in engineering applications: polycrystalline solids. For those materials, properties at the microscale and at the macroscale are both significantly important. For each phenomenon, in order to differentiate the microscale from the macroscale, there exists a characteristic length under which the macroscale continuum assumptions break down, and a significant deviation from classical physics can be expected [11]. Commonly, the macroscopic level considers systems

whose size is around a millimeter and above. At that scale, the material is assumed to be continuous. The lower length scale is the microscale level and ranges from 100nm to 500μm. At that level, the microstructural arrangement of the material becomes essential. The properties of each individual grain are determined as they impact the overall behavior of the material. Finally, the lowest characteristic length is the atomic scale and ranges from a few Angstroms to a few hundreds of nanometers. This scale is beyond the scope of this thesis. A representation of the different scales along with the numerical methods to model them is given in Figure 1.

Over the past two decades, in order to gain greater insight into the material behavior, a strong focus has been placed on the material properties at microscale. For instance, mechanical properties such as Young's modulus [12], mechanical strength [13], or nonlinear damping [14], among others, have been extensively studied. From those analyses, it is concluded that the properties are characterized by the length of the material and show a different behavior when the size of the system decreases. For a complete discussion of the topics addressed, the readers should refer to [15, 16], among others. More recently, in an attempt to extend this understanding to the impact of the microstructure on the macroscopic behavior, attention has been redirected at bridging the scales between the microscale and the macroscale [11]. This new focus results in the definition of an in-between scale level, known as the mesoscale. That is, this overall approach allows for the description of material behavior phenomena that occur over a larger range of length scales.

The field of mechanics of materials has been taking advantage of the ongoing numerical progress to address problems having more than one characteristic dimension. Applications focus on microstructures and mechanical properties over a variety of challenges such as elastic moduli of elastic composites [17], toughness and fracture resistance of polycrystalline metals [18], hardening and softening behavior in heterogeneous materials [19], and dislocation and crack propagation in brittle solids [20]. On the contrary, multiscale modeling of thermomechanical phenomena is a new and relatively untouched topic. However, providing such a predicting capability is essential in the design of innovative materials for applications under extreme environments. Consequently, the work provided in this thesis aims at

overcoming this limitation by linking microscale and macroscale properties, from a thermal and thermomechanical perspective.

In the next subsection, the state-of-the-art about thermomechanical properties, for each length scale, is reviewed.

1.3.2 Length Scale Effect in Thermomechanical Analysis

The previously introduced concept of separation of scale is critical to understand thermal and thermomechanical problems. In the context of this thesis, the work focuses on ceramics and semiconductors. Accordingly, the thermal process is governed by the phonons, i.e. the atomic vibrations of the crystal lattice that carry the heat. Their behavior is highly impacted by the characteristic length of the system. More specifically, for thermal diffusion processes, the frontier between the microscale and the macroscale is defined by the phonon mean free path. This latter property corresponds to the average distance a phonon travels before colliding with another phonon. In the case of silicon, the phonon mean free path in bulk material is reported to be around 300nm. The different thermal regimes and their respective domain of application are depicted in Figure 2. It is worth noting that fundamental phonon interactions are quantum processes in nature, thus being governed by the Schrodinger equation. However, in this work, the focus is put on a classical description of atomic interactions. Hence, only the microscale and macroscale levels are relevant.

At the macroscopic level, the characteristic length of the system is in the order or higher than a couple of bulk phonon mean free paths. This length scale corresponds to the domain where Fourier's law and the heat diffusion equation can be applied in order to describe the propagation of the thermal energy within the system. Commonly, for such dimensions, homogenized material properties are adopted to predict the effective macroscopic thermal response of a given material [21]. Yet, those techniques do not account for non-uniform properties such as the thermal conductivity field whose variation results from internally varying characteristic length scales. Thus, it is necessary to investigate smaller scales, starting by the microscale.

At the microscale level, the characteristic size of the system is around the length of the bulk phonon mean free path. This length domain is characterized by the classical size effect [13]. Particularly, due to the presence of microstructural interfaces, the characteristic length scale of the material is reduced. Thus, in materials where heat conduction is mediated mainly by phonons, this reduction translates into a shortening of the bulk phonon mean free path [22, 23] as a result of phonon scatterings at the microstructural interfaces [24, 25]. For this reason, its effective thermal conductivity decreases drastically [26, 27]. This length scale and its interaction with the macroscale are of prime interest in this thesis.

At smaller characteristic lengths, the size of the system is in the order of the wavelength of the lattice vibration. Consequently, a wave behavior approach of the thermal process needs to be considered. At that length level, the system is mostly described by the Schrodinger equation and quantum size effect becomes significant. Phenomena such as quantum tunneling [28] or wave interferences [29] reduces the thermal conductivity even further. As a result, this domain is mostly studied using molecular dynamics. And, while it presents a significant interest from an academic standpoint, the related applications are rather limited. For this reason, this length scale is not treated in this thesis.

Understanding thermal and thermomechanical properties from an experimental perspective raises many challenges. Experiments to determine the thermal properties can be inaccurate, difficult to interpret and might require some phenomenological models. For instance, the phonon mean free path can not be directly measured and is actually derived from other measurements, leading to an accumulation of assumptions and errors [30]. On the contrary, computational approaches offer the opportunity to better understand and evaluate thermal properties. At the lower scale, atomistic approaches such as molecular dynamics simulations [31] or lattice vibration simulations [32] are very powerful techniques providing an accurate description of the interatomic interactions such as dispersion relationships or specific heat. However, due to the significant computational cost, they are limited to problems of relatively small size and short simulation time. For instance, molecular dynamics models are computationally prohibitive for problems of practical size [33]. On the other

end of the spectrum, continuum numerical models allow for the study of large problematic geometries but they are unable to capture the size-dependent features of the microstructure of the system.

At the microscale, a keen interest has been devoted to the development of analytical solutions. Recently, several studies have focused on a multiscale approach to model the thermal transport process at the device level, while accounting for size-dependent phenomena [34]. Nevertheless, those approaches are restricted to simple geometries, and the case of more complex systems such as polycrystals has not been addressed yet. For example, kinetic theory approaches are limited to problems with straightforward geometries, such as thin films [27, 35], wires [36, 37], or monosized polycrystals [38].

The core goal of this thesis is to overcome all these limitations by establishing a concurrent multiscale computational framework able to capture the microscale properties and transfer them to the macroscopic system, for any geometry with complex microstructures. By reaching such an objective, this framework aims at bridging the scale between the microscale and the macroscale, as schematized on Figure 2.

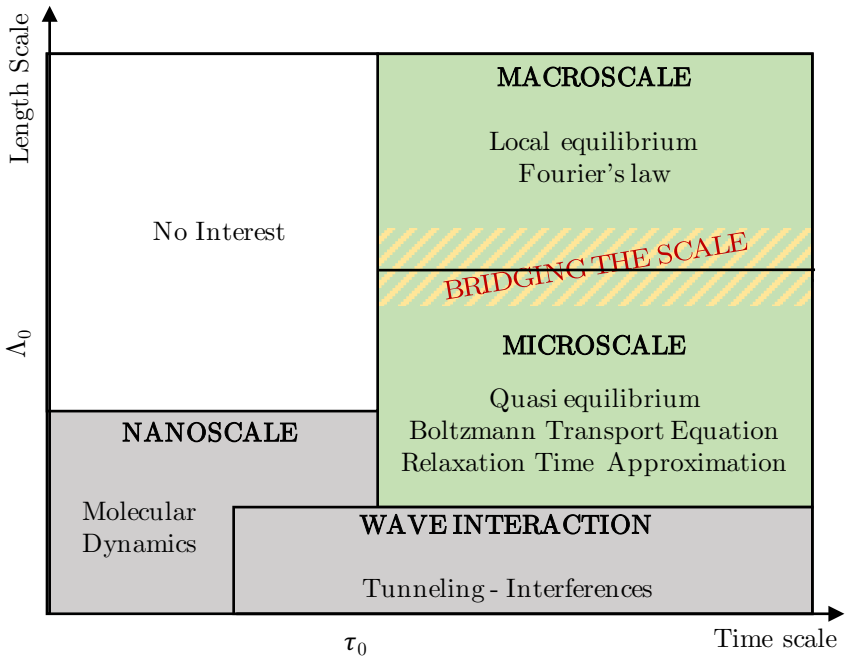

Figure 2: Heat Conduction Regime - after [39].

1.3.3 Multiscale Modeling in Polycrystals

In order to account for the wide range of length scales inherent to a number of phenomena and processes in materials science, multiscale analyses have been developed. A historical review on multiscale materials modeling for different disciplines of solid materials can be found in [40]. It is worth noting that the concept of multiscale approach has been extensively addressed in mechanical problems. A review of those precise works can be found in [16]. Conversely, the state-of-the-art in modeling thermal processes at the mesoscale still lags behind its mechanical counterpart. As previously explained, the literature contains very little or no work in the area of multiscale modeling of thermal and thermomechanical problems. In fact, the current approaches for modeling the thermomechanical response of materials do not allow to predict their behavior at the near-micron and sub-micron scales. Particularly, while analytical research has been conducted on the impact of length scale on thermal [27, 41] and mechanical [42, 43, 44] properties of materials, little is known about the impact that length scale could have on their combined thermomechanical response.

The finite element method appears to be the most appropriate tool to couple multiphysics and multiscale phenomena. However, traditional finite element method is based on continuum models. As a result, modeling the influence of the microstructure is a challenging task. In fact, models able to predict such complex interactions are not readily available in the literature. That is, the development of predictive mesoscale models for the combined thermomechanical response of materials has remained an elusive goal. This gap in the literature reveals a need for the development of a practical approach towards a multiscale framework incorporating the microscale, the mesoscale and the macroscale, thus allowing for thermal analyses of more complex structures. The development of such multiscale and multiphysics models is required to successfully analyze mechanisms relevant to heat conduction transfer.

A major challenge of this thesis lies in the implementation of the developed concurrent multiscale framework. The flexibility needed to perform such analyses prevents from using any existing FEM software. Therefore, every step of this work needs to be implemented

into an 'in-house' FEM code. However, modeling both microscale and macroscale within a single model generates a large number of degrees of freedoms - over tens of millions. Under those circumstances, the initial sequential FEM code is implemented in parallel to speed up the simulations. The use of distributed memory is also an inherent bottleneck in the implementation of the parallel code. For this reason, a large amount of time is spent implementing and validating the FEM code.

1.4 Scope of this Work and Outline of Study

The work produced in this thesis follows two majors research drivers. The physical portion corresponds to the leading motivation and is highlighted in all the following chapters. The other key component focuses on the numerical implementation. The large dimension of the concurrent multiscale multiphysics problem leads to specific computational requirements that are also addressed in this work. Combining those two elements allows to obtain new physical insights on the thermal process at microscale as well as the opportunity to develop new computational tools stimulating the generation of cutting-edge materials. More specifically, this thesis is structured as follows.

Chapter 2 presents the key concepts and analytical formulations of the multiscale thermomechanical model. It starts by recalling the notion of phonons, and by the derivation of the bulk thermal conductivity using the Boltzmann Transport Equation [45]. The contribution of the different types of phonon scatterings is highly emphasized. The prime focus is on the methodology developed to obtain the size-dependent thermal conductivity for arbitrary grain geometries. This section also describes in more details the current numerical methodologies found in the literature as well as the improvement achieved in order to overcome current limitations and to model more complicated geometries. Finally, the coupling between the thermal and mechanical components is provided.

Chapter 3 focuses on the technicality to implement and run the concurrent multiscale simulations. While this chapter and the related implementation does not directly translate

into published work, it is the backbone of the entire results obtained in this thesis and represents the most time-consuming task of this Ph.D. This section explains the models implemented for the bulk and grain boundary elements from a thermal and mechanical perspective. A strong focus is placed on the techniques used to calculate the size-dependent thermal properties. Finally, some details are given about the High Performance Computation framework and the related parallel implementation. While more computationally oriented, this chapter aims at keeping the implementation details to a higher level.

Chapter 4 combines the multiscale methodology developed with the implemented numerical framework to obtain advanced and reliable results. This section corresponds to most of the work published during that Ph.D. as well as some unpublished results. In particular, the validation of the developed framework is presented - as in [46] - as well as its application, especially in the domain of thermal optimization - as in [47]. Next, this chapter compares the different modeling techniques of the thermal resistance at the grain boundary - as in [48]. Finally, the influence of all the previous thermal analysis on the stress distribution is presented.

Chapter 5 concludes that work by restating and highlighting the major contributions accomplished during that Ph.D., and it opens possible new research directions to be followed in the future.

1.5 Contributions

Achievement of the objectives outlined in Section 1.2 leads to the following contributions to the state-of-the-art

1. Formulation of a concurrent multiscale framework to capture and couple in a single simulation both microscale and macroscale thermal phenomena.

2. Development and implementation of a multiscale optimization technique to determine polycrystalline microstructures handling predefined objective functions.

3. Formulation and implementation of a size-dependent thermomechanical interface model

preventing factitious temperature jumps and stress concentrations.

Those achievements are developed throughout the thesis and summarized in more detail in the conclusion, presented in Chapter 5.

CHAPTER II

THERMOMECHANICAL MODEL

Chapter 2 presents the theoretical foundations of heat transfer across different scales. It aims at providing an analytical formulation of the multiscale thermomechanical model. As mentioned in the introduction, the concept of multiscale approach in mechanical problems has been extensively addressed. Conversely, multiscale approach for thermal processes still lags behind. Therefore, this chapter puts a large emphasis on the thermal aspect.

First, this chapter recalls the concept of phonons and derives the bulk thermal conductivity using the Boltzmann Transport Equation under the relaxation time approximation. The contribution of the different types of phonon scatterings is highly emphasized. Next, the developed methodology associated with the size-dependent thermal conductivity is detailed. This part represents the main focus of the chapter. Finally, the coupling between the thermal and mechanical components is provided.

2.1 Solid State Physics

To clearly understand the phenomena related to lattice thermal transport, this work starts with a presentation of the theory of atomic vibrations in lattice. The features associated with the crystal lattices are first introduced. Next, the vibrations of the lattice and the related properties are explained. This ultimately leads to the definition of the concepts of phonon and more generally to the temperature. Nevertheless, for more in-depth information on these topics, the readers should refer to Ziman [24], among others.

2.1.1 Crystal Lattice, Reciprocal Lattice and Brillouin Zone

A crystalline structure is generated by the continuous repetition in space of an identical highly ordered arrangement of atoms. That is, a crystal can be perceived as a periodic network of repeating ideal lattices that extends along the principal directions - allowing to recover the full bulk arrangement of atoms within the crystal. As a consequence, all lattice points are identical to one another.

For this reason, a crystal structure is usually described by its unit cell. The unit cell is the smallest group of particles in the material that is used as a repeating pattern. It completely describes the symmetry and the structure of the entire crystal lattice. The unit cell is represented in terms of its lattice constants, also referred to as lattice parameters. Those parameters characterized the lengths of the cell edges as well as the angles between the edges. Consequently, the position of the atoms inside the unit cell is obtained through a set of atomic positions measured from a lattice point. Commonly, the position of the atoms within the unit cell is expressed relatively to the unit cell lengths, which results in fractional coordinates.

The repeating patterns are said to be located at the points of the Bravais lattice. This set of discrete points is generated by a translation

$$\mathbf{R} = l_1\mathbf{a}_1 + l_2\mathbf{a}_2 + l_3\mathbf{a}_3 \tag{2.1.1}$$

where l_i are integers and the three vectors $\mathbf{a}_i$ are known as the primitive vectors. For any location of the position vector $\mathbf{R}$, the lattice looks exactly the same due to the translational invariance of the crystal lattice.

In three dimensions, there exists fourteen distinct types of crystal lattices. Bravais lattices are then categorized into seven crystal systems: cubic, hexagonal, monoclinic, orthorhombic, rhombohedral, tetragonal and triclinic. A full description of those systems can be found in [49]. To illustrate this notion, the face-centered cubic (FCC) Bravais lattice is detailled below. This choice is motivated by the fact that most of the materials studied in this work - including silicon, germanium and silicon carbide - have a diamond cubic crystal structure, which follows the FCC Bravais lattice. Figure 3 represents the crystal of silicon

and the associated primitive vectors are given by

$$\begin{aligned} \mathbf{a}_1 &= \frac{a}{2}(\mathbf{y}+\mathbf{z}) \\ \mathbf{a}_2 &= \frac{a}{2}(\mathbf{x}+\mathbf{z}) \\ \mathbf{a}_3 &= \frac{a}{2}(\mathbf{x}+\mathbf{y}) \end{aligned} \tag{2.1.2}$$

where a is the lattice constant that refers to the physical dimension of unit cells. Commonly, the lattice constant of ceramics and semiconductors is around a few Angstroms. In the case of silicon, $a = 5.431\mathring{A}$. It is worth noting that the set of primitive vectors $\mathbf{a}_i$ is not uniquely defined and several sets can describe the same crystal. While this description is arbitrary, it is desirable to consider the simplest unit cell possible.

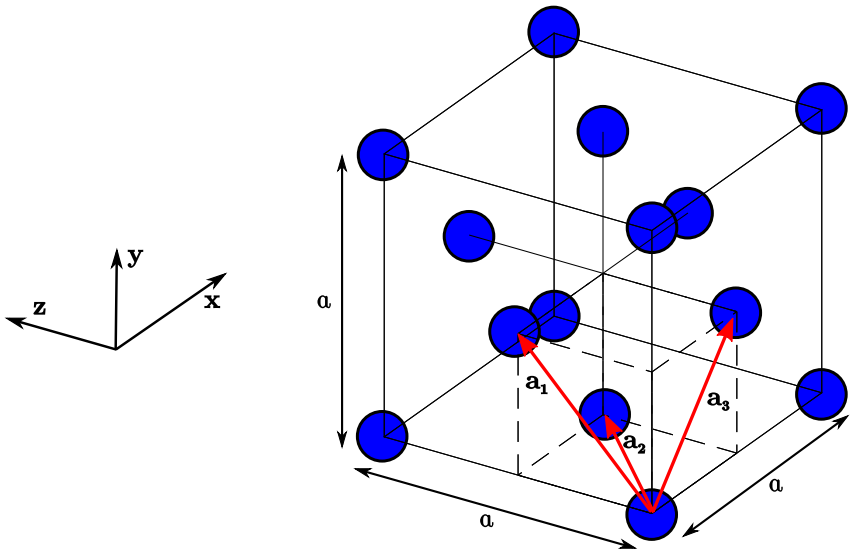

Figure 3: Face-centered cubic unit cell and its associated primitives vectors.

In order to better interpret wave propagation phenomena within the periodic crystalline structure, the concept of reciprocal lattice has been introduced [24]. Its goal is to reproduce the periodicity of the Bravais lattice in the so-called reciprocal space. Considering the fact that a crystal is a periodic array of lattices in real space, the reciprocal lattice is obtained by performing a spatial Fourier transform of the crystal. Consequently, the reciprocal lattice is the Fourier transform of the Bravais lattice and it exists in the reciprocal space, also known as the momentum space or K-space. This concept is explained in-depth in [49]. Similarly

to the Bravais vectors, the full reciprocal lattice can be recovered through translation by the vector

$$\mathbf{G} = m_1\mathbf{b}_1 + m_2\mathbf{b}_2 + m_3\mathbf{b}_3 \tag{2.1.3}$$

where m_i are integers and the three vectors $\mathbf{b}_i$ are known as the reciprocal lattice vectors defined as

$$\begin{aligned}
\mathbf{b_1} &= 2\pi\frac{\mathbf{a_2}\times\mathbf{a_3}}{\mathbf{a_1}\cdot(\mathbf{a_2}\times\mathbf{a_3})} \\
\mathbf{b_2} &= 2\pi\frac{\mathbf{a_3}\times\mathbf{a_1}}{\mathbf{a_2}\cdot(\mathbf{a_3}\times\mathbf{a_1})} \\
\mathbf{b_3} &= 2\pi\frac{\mathbf{a_1}\times\mathbf{a_2}}{\mathbf{a_3}\cdot(\mathbf{a_1}\times\mathbf{a_2})}
\end{aligned} \tag{2.1.4}$$

The reciprocal lattice to an FCC lattice is the body-centered cubic (BCC) lattice. The unit cell within the reciprocal space is known as the Brillouin zone, such that the reciprocal lattice is broken up into several Brillouin zones. The concept of Brillouin zone was developed by Léon Brillouin (1889–1969), a French physicist. Given the reciprocal lattice, the Brillouin zone is defined as the set of points that are closer to the origin of the reciprocal lattice than they are to any other reciprocal lattice points. From the Bloch wave approach of waves in a periodic medium, it is proven that the Brillouin zone completely characterized the crystal behavior [49]. Finally, it is worth pointing out that the Brillouin zone is the Voronoi cell around the origin of the reciprocal lattice. Figure 4 represents the Brillouin zone of silicon with its associated reciprocal vectors. Γ denotes the center of the Brillouin zone. Λ, Δ and Σ are the primary directions. L, U, X, W and K are the points of high symmetry. Those directions and points are of particular importance when representing the dispersion curves, as described in Subsection 2.1.2.

2.1.2 Lattice Vibration and Phonons

2.1.2.1 Concept of Phonons

As described above, atoms take a specific position in the crystal lattice. However, the crystal lattice is never rigid and the atoms constantly vibrate about their position of equilibrium.

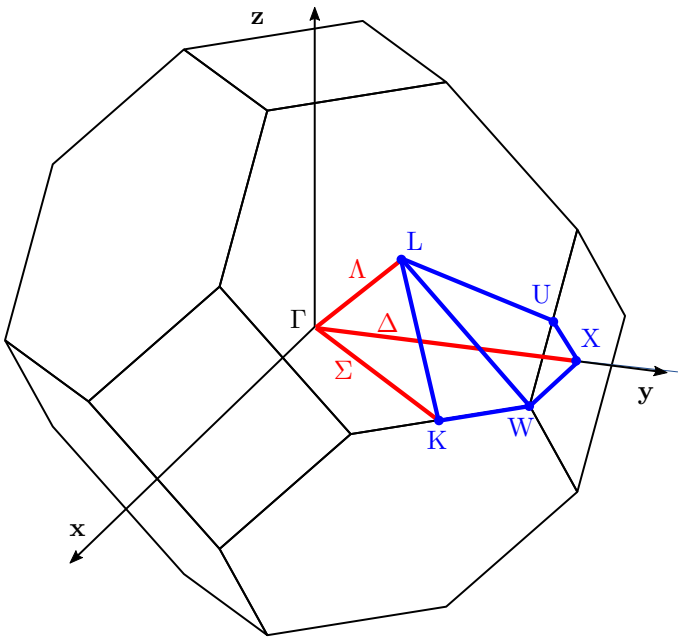

Figure 4: Brillouin zone of the face-centered cubic unit cell.

Those vibrations are responsible for the energy propagation and storage within the lattice, as they generate lattice waves that travel within the crystal. As proven below, the vibrational modes can accept energy only in discrete amounts, and phonons correspond to the energy quanta of lattice wave.

2.1.2.2 Oscillator and Dispersion Relationship

For the purpose of understanding the essential features of the lattice motions and vibrations - especially the dispersion relationship - Einstein proposed in 1907 a simple harmonic oscillator model. With such an approach, he obtained the specific heat as a function of temperature by characterizing the quantized energy levels. This subsection gives a brief presentation of the simple one-dimensional monatomic linear chain, as well as the case of the diatomic linear chain. It is worth noting that the dynamic motions of the linear lattice can also be obtained through the determination of the total potential energy, using an Hamiltonian approach. For sake of simplicity, this latter approach is disregarded in this thesis.

An infinite linear chain composed of identical atoms is first considered. Those atoms

have a mass m and are spaced by a distance a, as displayed in Figure 5a. They are linked together through linear springs of stiffness γ. From a lattice perspective, the spring represents the attractive and repulsive forces that atoms exert on each other. The atom displacement is supposed to be sufficiently small such that the linear assumption is valid.

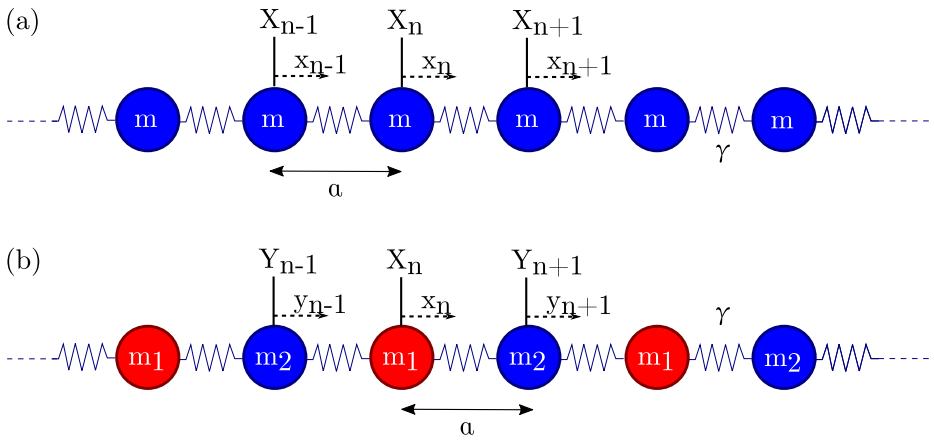

Figure 5: 1D oscillator chain: (a) monoatomic - (b) diatomic.

The equilibrium position of the n^{th} atom is denoted X_n and its displacement with respect to the equilibrium position is denoted x_n. The nearest-neighbor model is chosen to describe the motion of the chain. It implies that the forces applied on an atom come only from the nearest neighbors. Applying Newton's second law to this system, the equation of motion is obtained as

$$m\frac{\partial^2 x_n}{\partial t^2} = -\gamma\ (2x_n - x_{n+1} - x_{n-1}) \tag{2.1.5}$$

The time-dependent solution to Equation (2.1.5) is a standing wave whose expression is given by

$$x_n(t) = x_0 e^{i(kan-\omega t)} \tag{2.1.6}$$

where x_0 is the amplitude of oscillation, k is the 1D wavevector, a is the spacing between two consecutive atoms, ω is the frequency and t is time. Expression (2.1.6) is substituted into Equation (2.1.5) to obtain after simplification

$$-m\omega^2 = -2\gamma\ (1 - \cos ka) \tag{2.1.7}$$

This leads to the following relation

$$\omega(k) = 2\sqrt{\frac{\gamma}{m}}\left|\sin\frac{ka}{2}\right| \tag{2.1.8}$$

Equation (2.1.8) is called the dispersion relationship and it describes the relation between the vibration frequency ω and the phonon wavevector k. The expression of k is contingent on the boundary conditions applied to the system as explicated below. The representation of Equation (2.1.8), known as the dispersion curve, is given on Figure 6. The frequency range $[-\Pi/a, \Pi/a]$ - that represents the Brillouin zone - describes the full system due to symmetry.

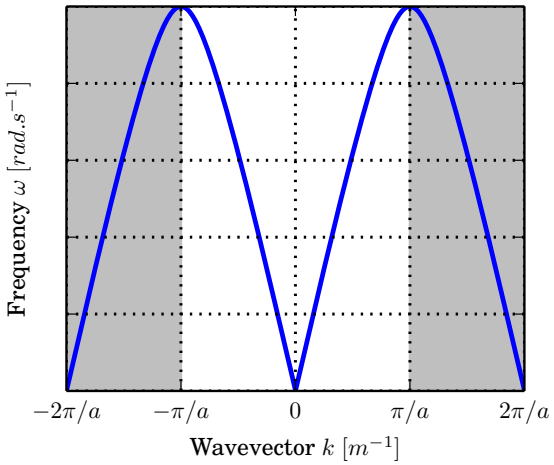

Figure 6: Dispersion curve of monoatomic 1D oscillator.

In unit cells composed of several distinct atoms, the monoatomic linear chain is unable to capture the physics involved. Thus, in a similar fashion, the crystal lattice is now considered to be a diatomic linear chain. It is formed of two atoms of mass m_1 and m_2 respectively, and of displacement x and y with respect to their position of equilibrium X and Y. This system is represented on Figure 5b. Following the methodology set out for the monoatomic chain, the two equations of motion are given by

$$\begin{cases} m_1\dfrac{\partial^2 x_n}{\partial t^2} = -\gamma\,(2x_n - y_{n+1} - y_{n-1}) \\ m_2\dfrac{\partial^2 y_n}{\partial t^2} = -\gamma\,(2y_n - x_{n+1} - x_{n-1}) \end{cases} \tag{2.1.9}$$

The solution of the system of Equations (2.1.9) is given by

$$\begin{cases} x_n(t) = x_0 e^{i(kan-\omega t)} \\ \\ y_n(t) = y_0 e^{i(kan-\omega t)} \end{cases} \tag{2.1.10}$$

This leads, after simplification, to the following system of equations

$$\begin{cases} -m_1\omega^2 x = \gamma\ (1 - e^{-ika}) - 2\gamma x_0 \\ \\ -m_2\omega^2 y = \gamma\ (1 - e^{ika}) - 2\gamma y_0 \end{cases} \tag{2.1.11}$$

It can be written in a matrix form as

$$\begin{bmatrix} 2\gamma - \omega^2 m_1 & -\gamma(1 + e^{ika}) \\ -\gamma(1 + e^{-ika}) & 2\gamma - \omega^2 m_2 \end{bmatrix} \begin{bmatrix} x_0 \\ y_0 \end{bmatrix} = 0 \tag{2.1.12}$$

A non-trivial solution of the matrix equation (2.1.12) is found only if the determinant of the matrix is zero. Solving for this system of equations provides the following solution

$$\omega^2 = \gamma \left(\frac{1}{m_1} + \frac{1}{m_2} \right) \pm \gamma \left[\left(\frac{1}{m_1} + \frac{1}{m_2} \right)^2 - \frac{4}{m_1 m_2} \sin^2 \frac{ka}{2} \right]^{1/2} \tag{2.1.13}$$

From Expression (2.1.13), two branches are formed, as depicted on Figure 7. The lower branch, known as the acoustic branch, corresponds to the 'minus' sign. The upper branch is called the optical branch and corresponds to the 'plus' sign. Once again, the dispersion curves are periodic of period $\omega = 2\Pi/a$, meaning that any results outside the Brillouin zone can be obtained by translation. Thus, the Brillouin zone allows to fully describe the dispersion relation.

The monoatomic and diatomic linear chains previously considered, are assumed to be infinite, leading to continuous dispersion curves. As explained earlier, the full crystal is recovered by translation of the unit cell, leading to the existence of periodic boundary conditions. This periodicity is known as the Born–von–Karman boundary conditions [50] and it restricts the wave function to be periodic on a certain Bravais lattice. It is stated as

$$x_n = x_{n+N} \tag{2.1.14}$$

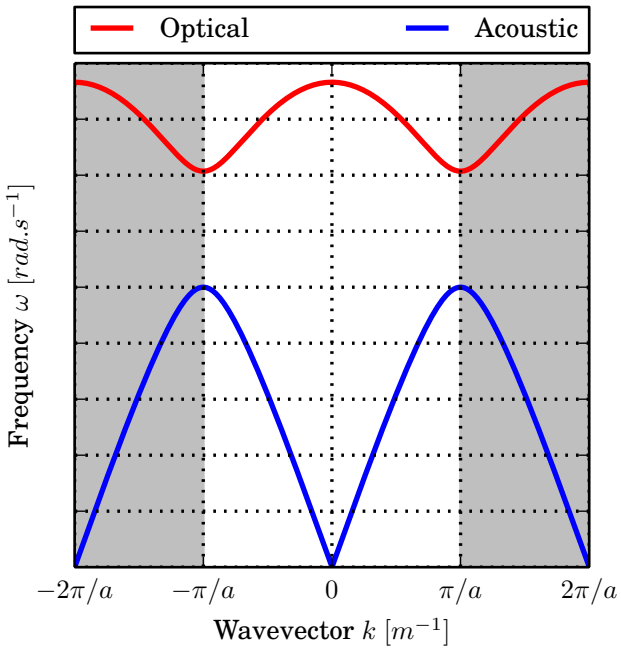

Figure 7: Dispersion curve of diatomic 1D oscillator.

where N represents the number of atoms between atoms in phase. In the case of N=1, the previous equation becomes

$$x_0 e^{i(kan-\omega t)} = x_0 e^{i(k(n+1)a-\omega t)} \tag{2.1.15}$$

which can be simplified into

$$1 = e^{ika} \tag{2.1.16}$$

Thus, the wavevectors are quantized to

$$k_p = p\frac{2\Pi}{a} \tag{2.1.17}$$

where p is a positive integer. Consequently, the dispersion relation is not represented by a continuous curve anymore but by a series of closely spaced points characterizing the possible modes of vibrations, also called states.

While this thesis focuses on a classical description of phonons, the same conclusion can be obtained from quantum mechanics. Indeed, the latter description has identically demonstrated that the energy levels of the harmonic oscillator are quantized. As such, the energy level of the lattice vibrations are quantized. The detailed proof of this argument can be

found in [51].

As introduced by Holland [52] and explained in more details in the following sections of this chapter, the calculation of the thermal conductivity must take into consideration the dispersion relationship of the crystal lattice under consideration. For more complex structures than the monoatomic and diatomic linear oscillators, the dispersion relationship can be obtained from indirect measurement such as phonon spectroscopy [53] or through theoretical computation such as molecular dynamics [54]. This work does not attempt to obtain the dispersion relationship numerically. For this reason, dispersion curves $\omega(\mathbf{k})$ from the literature are considered and the obtained data are fitted to low order polynomials.

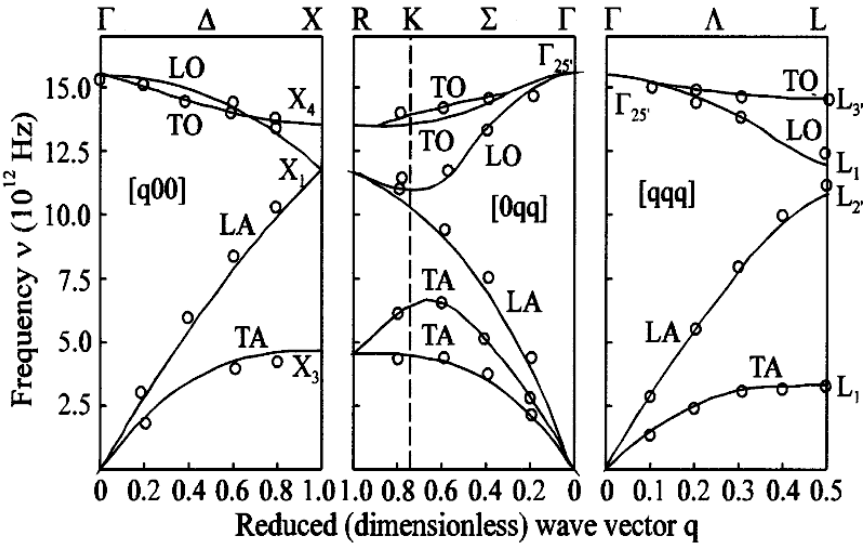

Figure 8: Dispersion curves of silicon - from [52].

For illustration purposes, the dispersion curves of silicon, obtained from experimental data [52] are displayed in Figure 8. Due to the three dimensional nature of the silicon crystal, the dispersion relationship exhibits three acoustic and three optical dispersion curves, categorized as one longitudinal and two transversals, for both acoustic and optical branches. As represented on Figure 8, four different polarizations exists: TO=Transverse Optical,

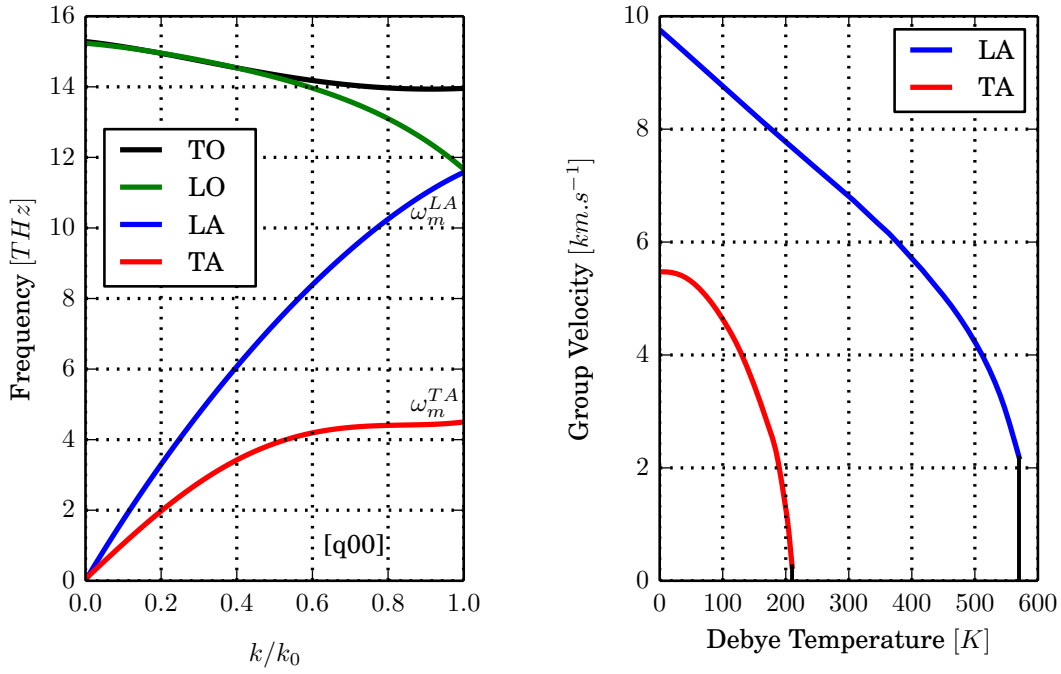

Figure 9: Computed phonon dispersion and group velocity for acoustic branches.

TA=Transverse Acoustic, LO= Longitudinal Optical, LA=Longitudinal Acoustic. This multiplicity is responsible for the presence of the summation term in the expression of the thermal conductivity. That is, the result takes into account each polarization separately. The fitting of the experimental data to the polynomials along the [100]-direction is displayed in Figure 9a.

The different polarizations exhibit a significant difference in the maximum frequencies ω_m reached. This feature impacts their respective contribution to the thermal conductivity, as explained in the following sections. This maximum frequency ω_m is commonly expressed in terms of Debye temperature which is defined as

$$\Theta_D = \frac{h\omega_m}{k_b} \tag{2.1.18}$$

where k_b is Boltzmann's constant, h is Planck's constant, and ω_m is the maximum frequency of the atom vibrations. The Debye temperature is different for each solid, as it reflects the rigidity of the lattice. The value of the Debye temperature of the materials considered in this work are given in Table 51.

A common assumption [49, 55, 56], adopted in this work, is to neglect the optical phonon contributions in the calculation of the overall thermal conductivity. Indeed, due to their low group velocity $\mathbf{v_g}$ defined as

$$v_g(\mathbf{k}) = \frac{\partial \omega(\mathbf{k})}{\partial \mathbf{k}} \tag{2.1.19}$$

it is observed that the optical phonons do not contribute to the energy transport, and they will not be included in the calculation of the thermal conductivity. It is worth noting that the group velocity is not necessarily parallel to the wavevector and that it tends to zero as it reaches the boundary of the Brillouin zone.

2.1.3 Density of States

As explained in the previous subsection, phonons are quantized lattice vibrations. They occupy states with wavelengths and propagation directions dictated by the crystal structure. At a given energy level, only specific quantized states are allowed. This particular distribution of states is called the density of states, which can be expressed as a function of either energy or wavevector $\mathbf{k}$. It describes the number of states per interval of energy that phonons can occupy.

In this thesis, the dispersion relationship is assumed to be isotropic. The Brillouin zone of FCC Bravais lattice is a truncated octahedron, as depicted in Figure 4, and it can be approximated by a surrounding sphere. The adopted simplification is thus legitimate.

Consequently, when considering the reciprocal space, the isotropic dispersion relation is represented by the condition: $\omega(\mathbf{k}) = constant$. For sake of representation, Figure 10 depicts the dispersion of the two dimensional isotropic density of states. The shaded domain corresponds to the differential quantity $|k|dkd\theta$ and it uses for the calculation of the thermal conductivity.

In a three dimensional isotropic crystal, as examined in this work, the density of states in the reciprocal space can be expressed as

$$\Omega(\omega) = \frac{V}{8\Pi^3} \tag{2.1.20}$$

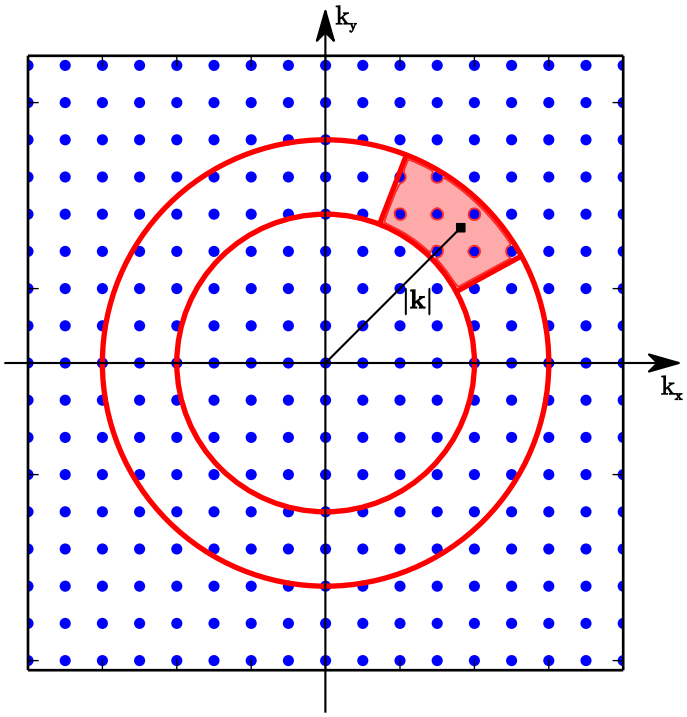

Figure 10: Surface of constant energy in the reciprocal space - after [57].

where V is the volume of the crystal [57]. Similarly to the two dimensional circle in Figure 10, the number of states to be calculated is now enclosed in a sphere of radius $k = |\mathbf{k}|$. Due to the assumed isotropy, any angular integral can be 'neglected', such that the total number of states within the Brillouin zone, and denoted N_T, can be simplified to

$$N_T = 4\Pi \int_0^k \Omega k^2 dk = \frac{V}{2\Pi^2} \int_0^k k^2 dk = \frac{V k^3}{6\Pi^2} \tag{2.1.21}$$

The density of space can be formulated in the frequency domain ω as

$$\Omega(\omega) = \frac{1}{V}\frac{dN_T}{d\omega} = \frac{1}{V}\frac{dk}{d\omega}\frac{dN_T}{dk} = \frac{1}{v_g}\frac{k^2}{2\Pi^2} \quad \text{so} \quad \Omega(\omega) = \frac{1}{2\Pi^2}\frac{\omega^2}{v_p^2 v_g} \tag{2.1.22}$$

Expression (2.1.22) is used in the rest of this work. As shown in the following chapters, the isotropic density of states assumption is valid and is able to recover the appropriate thermal conductivity.

2.2 Heat Conduction in Bulk Material

The application of a temperature gradient within the material is responsible for an energy unbalance. In order to recover a state of equilibrium, the heat is transferred from the hot region towards the cold one. The velocity at which the temperature propagates is symbolized by the thermal conductivity. The thermal conductivity within the macroscopic material has been extensively studied using the phonon Boltzmann transport equation or BTE. It has been proven to accurately describe the thermal conductivity of crystals [45].

2.2.1 Mean Free Path and Phonon Scattering Processes

Phonon scattering corresponds to the collision of phonons against impurities, other phonons, material microstrustural features or material boundaries. It governs the thermal transport properties in semiconductor materials as it drives the average distance that phonons can travel before encountering a scattering. Various phonon scattering mechanisms provide thermal resistance over different temperature regimes [24], as explained later in this subsection.

2.2.1.1 Bulk Mean Free Path

The bulk phonon mean free path $\Lambda_0(\mathbf{k})$ corresponds to the average distance traveled by a phonon within the bulk material between two successive scattering events, that can potentially modify its direction or energy or momentum. The phonon mean free path is mainly determined by two phenomena

1. the rate of scattering with other phonons.
2. the scattering with impurities or boundaries of the crystal.

The concept of bulk phonon mean free path is illustrated in Figure 11.

The effective relaxation time $\tau_0(\mathbf{k})$ is defined as the average time between two consecutive

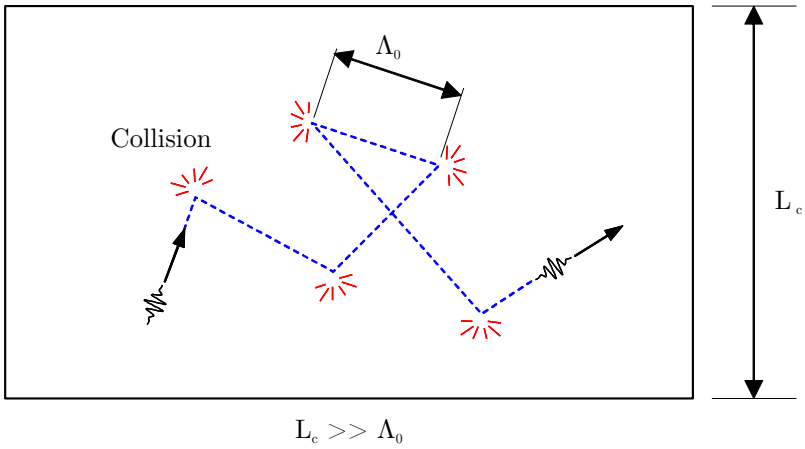

Figure 11: Phonon mean free path in bulk material.

scatterings. It is related to the bulk phonon mean free path through the formula

$$\Lambda_0(\mathbf{k}) = v_g(\mathbf{k})\tau_0(\mathbf{k}) \tag{2.2.1}$$

It takes into consideration all the scattering processes. More details about the distinct scattering processes are provided in the following Subsections.

2.2.1.2 Phonon-phonon scattering

The phonon-phonon scattering represents the collisions among phonons. It results from the anharmonic vibration of the lattice. This is an inelastic process because the phonons have different frequencies before and after the scattering. Thus, in order to conserve the energy, at least three phonons need to be part of the mechanism: either two phonons collide to create a third one or one phonon breaks into two others. Interactions with more than three phonons are less likely to happen and are not included in this work.

The quantum of energy corresponding to a frequency ω is defined as $\epsilon = \hbar\omega$ [49]. Therefore, for any phonon-phonon scattering, the conservation of the phonon energy is given by

$$\hbar\omega_1 + \hbar\omega_2 = \hbar\omega_3 \quad or \quad \hbar\omega_1 = \hbar\omega_2 + \hbar\omega_3 \tag{2.2.2}$$

In Equation (2.2.2), the left hand side corresponds to the phonon(s) before the scattering occurs, while the right hand-side represents the phonon(s) after the scattering occurs.

Two different phonon-phonon scattering processes, whose representation is given in Figure 12, exist

1. Normal: for this process, the phonon wavevectors stay inside the Brillouin zone. This process conserve the crystal momentum such that

$$\hbar\mathbf{k}_1 + \hbar\mathbf{k}_2 = \hbar\mathbf{k}_3 \quad or \quad \hbar\mathbf{k}_1 = \hbar\mathbf{k}_2 + \hbar\mathbf{k}_3 \tag{2.2.3}$$

   As a consequence, the direction of the energy flow is not impacted by the Normal process. It does not contribute to the thermal resistance and has no effect on the thermal conductivity. That is, normal processes are not considered in the effective relaxation time.

2. Umklapp: for this process, at least one of the formed phonon is outside the Brillouin zone. Thus, while the conservation of the energy holds, the wavevector is modified from $\mathbf{k}$ to $\mathbf{k}'$ such that

$$\mathbf{k}' = \mathbf{k} + \mathbf{G} \tag{2.2.4}$$

   where $\mathbf{G}$ is the reciprocal lattice vector, introduced in Subsection 2.1.1. The momentum relation for Umklapp process is

$$\hbar\mathbf{k}_1 + \hbar\mathbf{k}_2 = \hbar\mathbf{k}_3 + \hbar\mathbf{G} \quad or \quad \hbar\mathbf{k}_1 + \hbar\mathbf{G} = \hbar\mathbf{k}_2 + \hbar\mathbf{k}_3 \tag{2.2.5}$$

   The net momentum of the phonons is not conserved. This generates thermal resistance and leads to the reduction of the thermal conductivity.

Following the description of the two different phonon-phonon scatterings, the Umklapp scattering is the sole process impacting the thermal conductivity of the material. Several expressions of its relaxation time have been developed in the literature, especially among [24, 58]. The relaxation time obtained is proven to be inversely proportional to ω^2 such that

$$\tau_U^{-1} = A_{U,p}\ \omega^2\ T\ \exp(-b/T) \tag{2.2.6}$$

where $A_{U,p}$ and b are fitting parameters, described below in this subsection.

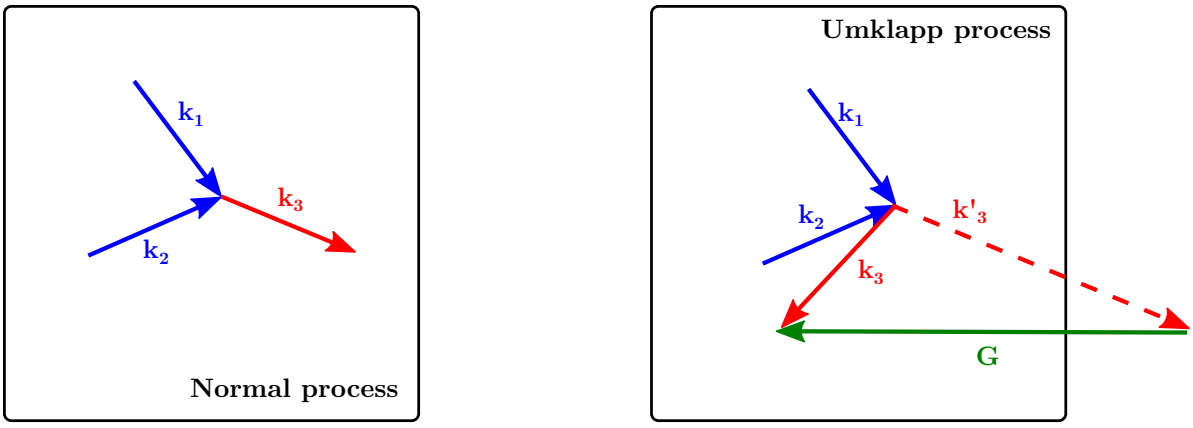

Figure 12: Two different phonon-phonon processes.

2.2.1.3 Phonon-isotope scattering

The phonon-isotope scattering represents the collisions between phonons and impurities inside the crystal. For most semiconductors, the thermal conductivity **D** peaks within the range $[20 - 100]\,K$. For those low temperatures, phonon-phonon scatterings are weak and phonon scatterings from isotopic mass defects are the main limiting factor of the thermal conductivity. Hence, this process is of limited interest for the temperature range considered in this work and the readers can refer to the literature such as [59], for more details.

The phonon-isotope relaxation time is inversely proportional to ω^4 [24, 52] such that

$$\tau_I^{-1} = A_I \omega^4 \tag{2.2.7}$$

where A_I is a fitting parameter, described below in this subsection.

2.2.1.4 Casimir limit

As the temperature decreases towards 0 Kelvin, Umklapp and phonon-isotope scatterings vanish. This potentially leads to an infinite effective relaxation time, and thus to an unbounded thermal conductivity. In reality, for most materials, the bulk thermal conductivity reaches a maximum value at a given temperature and then decreases as the temperature diminishes. This low temperature range corresponds to the Casimir regime [24, 60], symbolized by the relaxation time τ_C. It represents the prominent enlargement of the bulk phonon mean free path, which is only limited by the surface of the bulk sample. This relaxation

time is generally defined as $\tau_C^{-1} = v_g/B$, where B is a constant [61, 62]. The group velocity v_g is nearly constant for most materials within the temperature ranges considered in this work, allowing to define the Casimir relaxation time as

$$\tau_C^{-1} = A_C \tag{2.2.8}$$

where the constant A_C has no influence on the prediction of the bulk thermal conductivity as the temperature increases.

2.2.1.5 Fitting parameters

The previously introduced constants $A_{U,p=\{L,T\}}$, A_I, A_C and b are intrinsic material properties and are determined to fit the bulk thermal conductivity of the material through a large temperature range. However, the three scattering processes introduced above governs the thermal transfer for different temperature ranges. As a reminder, around a few degrees Kelvin, sample edges give the largest resistance, while around and above room temperature anharmonic phonon-phonon scattering is strongest. In between, the phonon-isotope process is the main driver. As a result, the influence of each fitting parameter is limited to the temperature range of its corresponding scattering process.

In order to fit the bulk thermal conductivity, the methodology proposed in this work relies on the data available in the literature. Among others, the attention is mostly focused on silicon, as all necessary material properties are broadly available. This data provides both inputs for the models (through the dispersion relationship) as well as means of validation of our results (through the reported experimental measurements).

While in general the bulk thermal conductivity can be recovered for different sets of constants, the proportion of heat transport respectively achieved by longitudinal and transverse phonons can largely affect results at the microscale and mesoscale. Based on the studies from Hamilton and Parrott [63], these constants should be fitted in such a way that 80% of the heat transport occurs through transverse phonons, within the bulk material.

Besides phonon-phonon scattering and phonon-isotope scattering, phonons can also be impacted by the microstructure of the material, such as grain and system boundaries. This

Table 1: Material constants for bulk silicon.

Constant	Value
$A_{U,L}$	$3.28 \times 10^{-19}\ s.K^{-2}$
$A_{U,T}$	$6.94 \times 10^{-20}\ s.K^{-2}$
A_I	$2.50 \times 10^{-45}\ s^3$
A_C	$6.18 \times 10^{5}\ s^{-1}$
b	$140\ K$

so-called 'phonon-boundary' scattering is significant in polycrystalline structures and will be explained in details in Subsection 2.3.1.

2.2.2 Matthiessen's Rule

In the previous subsection, the different phonon scatterings responsible for the thermal resistance are separately investigated and a different expression is obtained for each specific relaxation time. However, when considering the material, the phonons encounter those scattering mechanism simultaneously. Consequently, the previously defined bulk effective relaxation time $\tau_0(\mathbf{k})$ needs to accounts for all the different scattering processes encountered in the model. This value can be considered as an average relaxation time among all the process.

The Matthiessen's rule [64, 65], developed by British physicist Augustus Matthiessen (1831–1870), states that the total thermal resistance of the material is the sum of the individual resistance due to each individual scattering. Thus, the bulk effective relaxation time is obtained as

$$\tau_0^{-1} = \tau_U^{-1} + \tau_I^{-1} + \tau_C^{-1} \tag{2.2.9}$$

where τ_U, τ_I and τ_B are the relaxation times respectively associated with Umklapp, phonon-isotope and Casimir limit scatterings, as introduced in the previous subsection.

The Matthiessen's rule is an empirical approximation that aims at simplifying the problem. However, it is not universally true. Indeed, the individual scattering resistance cannot be summed unless they are independent of each other [66]. Consequently, if the drivers responsible for the various phonon scatterings depend on each other, the Matthiessen's rule fails. Even when considering scattering processes to be independent of each other, it has

been proven from variational principal [24] that the Matthiessen's rule tends to slightly overestimate the exact effective relaxation time and the resultant thermal conductivity.

In order to overcome those limitations, more sophisticated formulations attempt to take these effects into account. Not only those formulations are behind the scope of this work, but the following chapters validate the use of the Matthiessen's rule.

2.2.3 Phonon Boltzmann Transport Equation

As previously introduced, the thermal conductivity, denoted $\mathbf{D}$, is the property of a material to conduct heat. In the framework of classical transport theory, the underlying physics is modeled by the Boltzmann transport equation or BTE. It is worth noting that it can be applied behind the scope of this work, for systems with small length scales and small timescales. A thorough description of the Boltzmann transport equation can be found in the literature. For instance, the history, formulation, and solution techniques of the BTE can be found from Chapman and Cowling [67], Tien and Lienhard [68] and Cercignani [69]. A detailed summary of the formulation is provided in this subsection in order to facilitate the understanding of the following chapters.

As described in Section 2.1, the energy of lattice vibration is quantized and the corresponding quantum of energy defines the concept of phonon. By conceiving phonons as particles, the theory of distribution function for phonons may now be introduced. The key driver is to determine the probability of finding a phonon in the reciprocal space. For such a purpose, suppose at time t, a particle of mass m at the spatial location $\mathbf{r}$ moving with a velocity $\mathbf{v}$. At $t + dt$, without collision, the particle will move to $\mathbf{r} + d\mathbf{r} = \mathbf{r} + \mathbf{v}dt$ and its velocity becomes $\mathbf{v}+d\mathbf{v} = \mathbf{v}+\mathbf{a}dt$, where $\mathbf{a} = \mathbf{F}/m$ is the acceleration, due to the body force $\mathbf{F}$. Thus, in the absence of collision, the probability of finding a particle does not change with time. It can be expressed by a nonlinear partial differential equation, known as the Liouville equation, named after the French mathematician Joseph Liouville (1809–1882)

$$\frac{f(\mathbf{r} + \mathbf{v}dt, \mathbf{v} + \mathbf{a}dt, t + dt) - f(\mathbf{r}, \mathbf{v}, t)}{dt} = \frac{\partial f}{\partial t} + \mathbf{v}.\frac{\partial f}{\partial \mathbf{r}} + \mathbf{a}.\frac{\partial f}{\partial \mathbf{v}} = 0 \tag{2.2.10}$$

where

$$\frac{\partial f}{\partial \mathbf{r}} = \nabla f = \frac{\partial f}{\partial x}\mathbf{x} + \frac{\partial f}{\partial y}\mathbf{y} + \frac{\partial f}{\partial z}\mathbf{z} \tag{2.2.11}$$

is the gradient and

$$\frac{\partial f}{\partial \mathbf{v}} = \nabla_v f = \frac{\partial f}{\partial v_x}\mathbf{x} + \frac{\partial f}{\partial v_y}\mathbf{y} + \frac{\partial f}{\partial v_z}\mathbf{z} \tag{2.2.12}$$

While the Liouville equation supposes the absence of collision, phonons actually collide with each other at high frequency, due to the scattering processes introduced in Subsection 2.2.1. Adding this term to the previously defined Liouville Equation (2.2.10) allows to obtain the total rate of change in the phonon distribution function f. This leads to the Boltzmann transport equation (BTE) which is most commonly written as

$$\frac{\partial f}{\partial t} + \mathbf{v}.\frac{\partial f}{\partial \mathbf{r}} + \mathbf{a}.\frac{\partial f}{\partial \mathbf{v}} = \left[\frac{\partial f}{\partial t}\right]_{collision} \tag{2.2.13}$$

In order to investigate the Boltzmann transport equation, the collision term needs to be expressed explicitly. As described in the literature on heat transfer [39], the collision term can be viewed as the difference in terms of scattering and written as

$$\left[\frac{\partial f}{\partial t}\right]_{collision} = \sum_{\mathbf{v}'}(W(\mathbf{v},\mathbf{v}')f(\mathbf{r},\mathbf{v}',t) - W(\mathbf{v}',\mathbf{v})f(\mathbf{r},\mathbf{v},t)) \tag{2.2.14}$$

where $W(\mathbf{v},\mathbf{v}')$ is the scattering probability, defined as the fraction of particles with a velocity $\mathbf{v}'$ that will change their velocity to $\mathbf{v}$ per unit time due to collision. The function W depends on the nature of the scatterings and is usually a complicated non-linear function of the velocities.

Following the previous remark, the BTE appears to be a nonlinear integro-differential equation of the distribution function in terms of space, velocity, and time. Consequently, a explicit solution can not be easily found. In order to solve it, the simplification known as the relaxation time approximation (RTA) provides an accurate solution under conditions not too far away from the equilibrium [70]. The collision term is replaced by a linear expression such that

$$\left[\frac{\partial f}{\partial t}\right]_{collision} = \frac{f_0 - f}{\tau_0} \tag{2.2.15}$$

where f_0 is the equilibrium phonon distribution and τ_0 is the bulk effective relaxation time. The solution of the first order differential Equation (2.2.15) suggests that the equilibrium will be recovered in a time $\Delta t = t - t_0$ that is on the order of τ_0 and where t_0 is the initial time when the system deviates from the equilibrium. The return to the equilibrium state is due the collisions. Two main limitations are associated with the relaxation time approximation

1. the characteristic time must be greater than the relaxation time.

2. the length scale must be greater than the mean free path.

Under those two conditions and in the absence of body force, the BTE can be expressed in its well-known form

$$\frac{\partial f}{\partial t} + \mathbf{v}.\frac{\partial f}{\partial \mathbf{r}} = \frac{f_0 - f}{\tau} \tag{2.2.16}$$

2.2.4 Bulk Thermal Conductivity

In the present subsection, the bulk thermal conductivity expression is derived by coupling together the phonon Boltzmann transport equation with the Fourier's law.

Considering Equation (2.2.16) obtained in the previous subsection and assuming that the variation from the equilibrium is due to a temperature gradient, the BTE can be rewritten using the chain rule, leading at steady state to the expression

$$(\mathbf{v}.\nabla T).\frac{\partial f}{\partial T} = \frac{f_0 - f}{\tau_0} \tag{2.2.17}$$

Furthermore, by considering the condition of local equilibrium, f is assumed to not deviate too far from its equilibrium distribution f_0, such that

$$\frac{\partial f}{\partial T} \simeq \frac{\partial f_0}{\partial T} \tag{2.2.18}$$

Thus, the distribution function can be considered to be

$$f \simeq f_0 - \tau(\mathbf{v}.\nabla T)\frac{\partial f_0}{\partial T} \tag{2.2.19}$$

The phonon distribution function can also be related to the the phonon energy density, as introduced in [71]. Indeed, the total lattice energy U corresponding to all phonons of all polarizations may be obtained by integrating over all phonon modes such that

$$U = \int_{\bar{\omega}} f \epsilon d\bar{\omega} = \int_{\bar{\omega}} f h\omega d\bar{\omega} \tag{2.2.20}$$

where $\bar{\omega}$ is the velocity space. Finally, the heat flux can be derived from the more general energy flux, such that

$$\mathbf{q} = U\mathbf{v} = \int_{\bar{\omega}} f h\omega \mathbf{v} d\bar{\omega} \tag{2.2.21}$$

Substituting the distribution function f by its expression derived in Equation (2.2.19), the heat flux expression becomes

$$\mathbf{q} = \int_{\bar{\omega}} \left(f_0 - \tau_0 \left(\mathbf{v}.\nabla \mathbf{T} \right) \frac{\partial f_0}{\partial T} \right) \hbar\omega \mathbf{v} d\bar{\omega} \tag{2.2.22}$$

Since f_0 is the equilibrium distribution, the corresponding integral over the reciprocal domain vanishes such that

$$\int_{\bar{\omega}} f_0 \hbar\omega \mathbf{v} d\bar{\omega} = 0 \tag{2.2.23}$$

It ultimately leads to

$$\mathbf{q} = -\int_{\bar{\omega}} \tau_0 \mathbf{v}.\nabla T \frac{\partial f_0}{\partial T} \hbar\omega \mathbf{v} d\bar{\omega} = -\left(\int_{\bar{\omega}} \tau_0 \mathbf{v}. \frac{\partial f_0}{\partial T} \hbar\omega \mathbf{v} d\bar{\omega} \right) \nabla T \tag{2.2.24}$$

As described in more details in Subsection 2.2.5, the thermal conductivity $\mathbf{D}$ is related to the thermal flux through Fourier's empirical law of thermal conduction, such that

$$\mathbf{q} = -\mathbf{D}.\nabla T \tag{2.2.25}$$

By comparing Equation (2.2.24) and Equation (2.2.25), the thermal conductivity can be expressed as

$$\mathbf{D} = \int_{\bar{\omega}} \tau_0 \mathbf{v} \frac{\partial f_0}{\partial T} \hbar\omega \mathbf{v} d\bar{\omega} \tag{2.2.26}$$

Due to the fact that the energy levels are closely spaced, the equilibrium phonon distribution f_0 used for the calculation of the thermal conductivity is the Bose-Einstein probability distribution [39]. This distribution is defined as

$$f_0(\omega) = \frac{1}{exp(\frac{\hbar\omega}{k_B T}) - 1} \tag{2.2.27}$$

Deriving with respect to the temperature and substituting Equation (2.2.27) into Equation (2.2.26), the expression of the thermal conductivity becomes

$$\mathbf{D} = \int_{\bar{\omega}} \tau_0 \mathbf{v} \frac{\hbar\omega}{k_B T^2} \frac{exp(\frac{\hbar\omega}{k_B T})}{(exp(\frac{\hbar\omega}{k_B T}) - 1)^2} \hbar\omega \mathbf{v} d\bar{\omega} \tag{2.2.28}$$

In general, it is convenient to integrate over the frequency ω by accounting for each polarization P, in the direction $\mathbf{n}$ along which the thermal conductivity is to be evaluated

$$D(\mathbf{n}) = k_b \sum_{P=L,T} \int_0^{\infty} \tau_0(\omega) v_{g,n}^2(\omega) \left(\frac{\hbar\omega}{k_b T}\right)^2 \frac{\exp(\hbar\omega/k_b T)}{[1 - \exp(\hbar\omega/k_b T)]^2} \Omega(\omega) d\omega \tag{2.2.29}$$

where Ω is the density of states of phonons, introduced in Subsection 2.1.3. As presented earlier, the density of states is used to convert the integration over the reciprocal space $\bar{\omega}$ into an integration over the frequency ω. Considering its definition from Equation (2.1.22), the bulk thermal conductivity is finally obtained as

$$D(\mathbf{n}) = \frac{k_b}{(2\Pi)^3} \sum_{P=L,T} \int_{BZ} \tau_0(\mathbf{k}) v_{g,n}^2(\mathbf{k}) \left(\frac{\hbar\omega}{k_b T}\right)^2 \frac{\exp(\hbar\omega/k_b T)}{[1 - \exp(\hbar\omega/k_b T)]^2} d\mathbf{k} \tag{2.2.30}$$

where $v_{g,n}$ corresponds to the component of the group velocity in the direction $\mathbf{n}$.

As a reminder, k_b and $\hbar$ are respectively the Boltzmann and the reduced Planck constants, P is the phonon polarization, τ_0 is the effective bulk relaxation time, ω is the phonon frequency, T is the temperature, v_g is the phonon group velocity. The variable of integration $d\mathbf{k}$ is the elementary volume in the reciprocal space and the integration is performed over the first Brillouin zone (BZ) of the lattice. This prediction of the thermal conductivity incorporates the contribution of both longitudinal and transverse acoustic phonons. As presented in Subsection 2.1.2, optical phonons are not incorporated into the calculation of the thermal conductivity, due to their slow group velocity.

It is worth noting that the direction $\mathbf{n}$ is not explicitly expressed. As a result, the thermal conductivity can be carried out for $2D$ and $3D$ geometries by accordingly defining $v_{g,n}$ and the integration limit of the Brillouin zone.

In order to validate Equation (2.2.30), Figure 13a shows the calculated thermal conductivity for bulk silicon for a wide temperature range. The agreement between the theoretical model and measured data is remarkable. In addition, Figure 13b shows that indeed our set of fitting constants gives the right contribution for each polarization. The numerical implementation providing those results will be explained in Chapter 3.

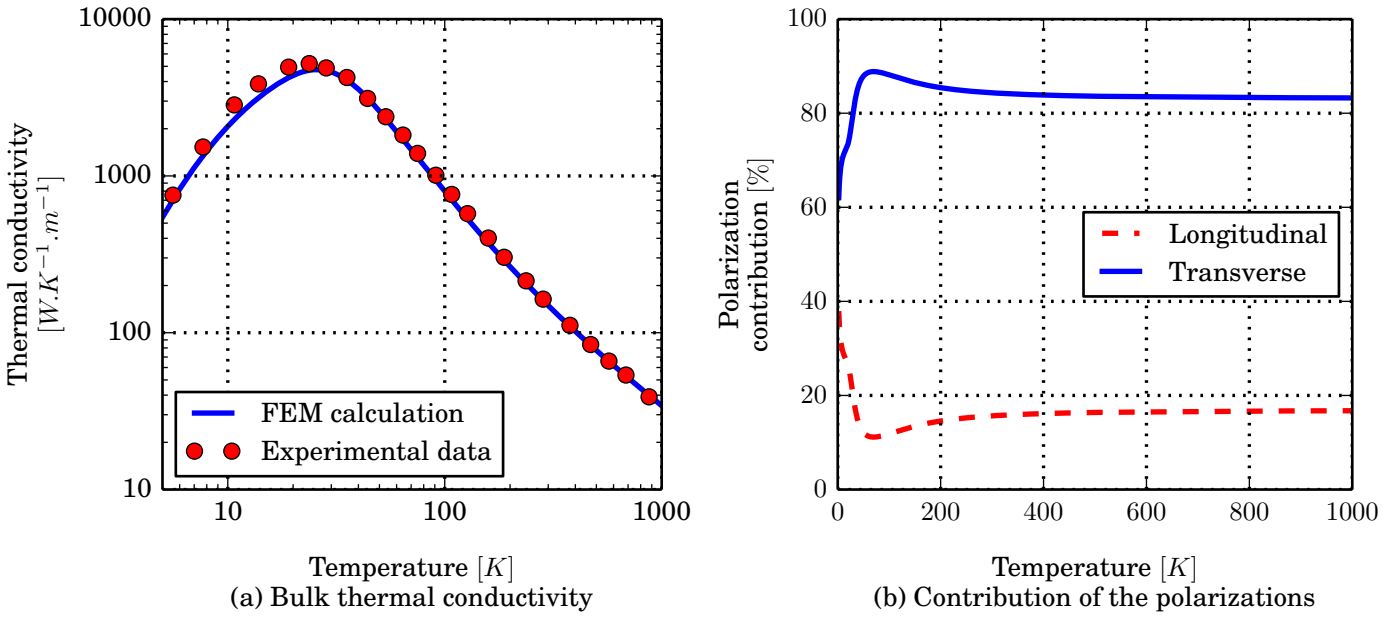

(a) Bulk thermal conductivity

(b) Contribution of the polarizations

Figure 13: Thermal conductivity of silicon.

2.2.5 Fourier's Law and Heat Equation

The differential equation governing the heat transfer process is obtained in a straightforward fashion by applying a control volume analysis using energy balance. Over a defined domain, it leads to the following governing equation

$$\nabla.(D\nabla T) + q = \rho C_p \frac{\partial T}{\partial t} \tag{2.2.31}$$

where ∇ is the divergence operator, T is the temperature, q is the volumetric thermal energy generation rate, ρ is the mass density and C_p is as the specific heat capacity. This equation is called the heat diffusion equation or more commonly the heat equation. The thermal

energy generation term q corresponds to the conversion of other types of energy to thermal energy, such that the total energy of the system is conserved.

By prescribing the appropriate initial temperature distribution and the boundary conditions (such as constant temperature, constant heat flux, convection or radiation) of the system to the heat equation, a boundary value problem is created. It can be solved analytically for simple cases. For more complicated geometrical features, numerical simulations are necessary, as performed in the present work.

If the material is not at thermal equilibrium, a heat transfer process occurs and the heat flows from the hot region towards the cold region. This flows is represented by the heat transfer rate per unit area, more commonly called heat flux. Fourier's law states that

$$\mathbf{q} = -\mathbf{D}.\nabla T \tag{2.2.32}$$

where $\mathbf{D}$ is the thermal conductivity tensor and T is the local temperature. It is worth noting the heat flux $\mathbf{q}$ is always perpendicular to the isotherms and opposite to the temperature gradient.

2.3 Size Effects in Heat Transfer

The concept of thermal conductivity $\mathbf{D}$ is mostly used for modeling the heat flow at continuum level, through either Fourier's law or the heat equation. Thus, at macroscale, it is commonly considered as a constant property of the material. However, it has been shown from experiments [23] and analytical formulations [27, 39] that as the characteristic length of the material under study decreases, the thermal conductivity follows the same trend and becomes size-dependent. This size dependence, also referred to as size effect, is extensively defined and derived in the current section.

Subsection 2.3.1 presents the classical size effect that occurs when the size of the device is in the order of a few bulk phonon mean free paths. Subsection 2.3.2 introduces the quantum size effect that occurs when the size of the device is even smaller, in the order of magnitude of the wavelength. The latter effect is discussed for the sake of completeness.

Indeed, it is of interest for characteristic lengths shorter than the ones presented in this work and thus falls behind the scope of this work.

It is important noting that the size effect phenomenon is the core concept of this work. The overall goal is to capture the effect of the microstructural arrangement within the material by means of a size-dependent thermal conductivity and then transfer this information to the continuum model. This methodology enables the formalism of a concurrent thermal model whose numerical implementation will be described in details in Chapter 3. The validation of those models and the applications to various examples will be carry out in Chapter 4.

2.3.1 Classical Size Effect

When the characteristic length of the material under study (such as the thickness of a film, the diameter of a wire or the grain sizes of a polycrystaline structure) is comparable or shorter than the bulk phonon mean free path, the thermal conductivity departs away from its bulk value. Boundary or interface scattering are significantly responsible for this deviation. This reduction of the mean free path is illustrated in Figure 14. Subsequently, the thermal conductivity decreases and becomes size dependent.

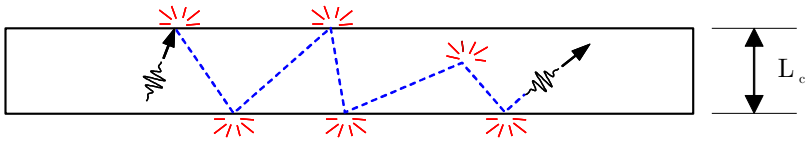

Figure 14: Reduced phonon mean free path.

As a reminder, the Boltzmann transport equation in the absence of body force can be expressed as

$$\frac{\partial f}{\partial t} + \mathbf{v}.\frac{\partial f}{\partial \mathbf{r}} = \frac{f_0 - f}{\tau_0} \tag{2.3.1}$$

In Subsection 2.2.3, the phonon distribution function f is assumed to not deviate too far from its equilibrium distribution, under the condition of local equilibrium. Thus, by expressing f_d as the deviation from the equilibrium distribution f_0, the distribution function

f can be written as

$$f = f_0 + f_d \tag{2.3.2}$$

In the case of Subsection 2.2.4, the deviation from equilibrium f_d was solely due to the applied temperature gradient such that

$$f_d = -\tau_0(\mathbf{v}.\nabla T)\frac{\partial f_0}{\partial T} \tag{2.3.3}$$

In the current subsection, the deviation is due to the geometry of the specimen. The expression of f_d is derived in Subsection 2.3.1.1 for the case of the thin film. Then, Subsections 2.3.1.2 and 2.3.1.3 respectively consider the cases of nanowire and single crystal grain.

2.3.1.1 Thin film

In order to look at the influence of the film thickness, a thin film is considered, having a temperature gradient in the x-direction and boundaries perpendicular to the z-direction, as represented in Figure 15. The thin film configuration mathematically translates into the following simplifications

1. The temperature gradient is along the x-direction, implying that the temperature does not change in the y- and z-directions: $\partial f_0/\partial y = \partial f_0/\partial z = 0$.

2. There is no boundary along the y-direction: $\partial f_d/\partial y = 0$.

3. $\partial f_d/\partial x$ is supposed to be small in comparison to the other terms, so it can be neglected, meaning that $\partial f_d/\partial x \ll \partial f/\partial x$. This approximation directly refers to the local equilibrium approximation such that $\partial f/\partial x = \partial f_0/\partial x$. It supposes a thermodynamic equilibrium and it is correct only if the temperature gradient is not too large in regard of the mean free path.

4. The steady-state condition is such that : $\partial f/\partial t = 0$.

By considering the Equation (2.3.1), the Boltzmann transport equation can be expanded

as follows

$$\cancel{\frac{\partial f}{\partial t}} + v_x\left(\frac{\partial f_0}{\partial x} + \cancel{\frac{\partial f_d}{\partial x}}\right) + v_y\left(\cancel{\frac{\partial f_0}{\partial y}} + \cancel{\frac{\partial f_d}{\partial y}}\right) + v_z\left(\cancel{\frac{\partial f_0}{\partial z}} + \frac{\partial f_d}{\partial z}\right) = \frac{f_0 - f}{\tau_0} = \frac{f_d}{\tau_0} \tag{2.3.4}$$

where the previously stated assumptions lead to the crossed-out terms. Thus, the simplified expression reduces to

$$v_x\frac{\partial f_0}{\partial x} + v_z\frac{\partial f_d}{\partial z} = \frac{f_d}{\tau_0} \quad or \quad \frac{\partial f_d}{\partial z} - \frac{f_d}{v_z\tau_0} = -\frac{v_x}{v_z}\frac{\partial f_0}{\partial x} \tag{2.3.5}$$

The solution of the differential equation (2.3.5) is derived as

$$f_d(z) = -\tau_0 v_x\frac{\partial f_0}{\partial x}\left[1 - C_d exp\left(\frac{-z}{v_z\tau_0}\right)\right] \tag{2.3.6}$$

where the value of the constant C_d is found using the boundary conditions of the system.

In order to define the boundary conditions at the top and bottom layers of the film, the underlying physics need to be clearly understood. The study by Fuchs [72] and Sondheimer [73] is of primary importance in this task. Indeed, an analogy can be drawn with the so-called '*F.S.*' model that analyzes the electron size effect phenomenon in thin film, which is due to the reduction of the film thickness. The presence of the surfaces limiting the travel of the phonons is driving the reduction of the thermal conductivity.

A simple common assumption is to assume that all phonons return to equilibrium at the boundary, meaning that the scattering is fully diffuse. This is a purely artificial model and this thesis prefers to focus on a more general theory. Indeed, it adopts the concept that part of the phonons are reflected back in the material. For such a purpose, the specularity

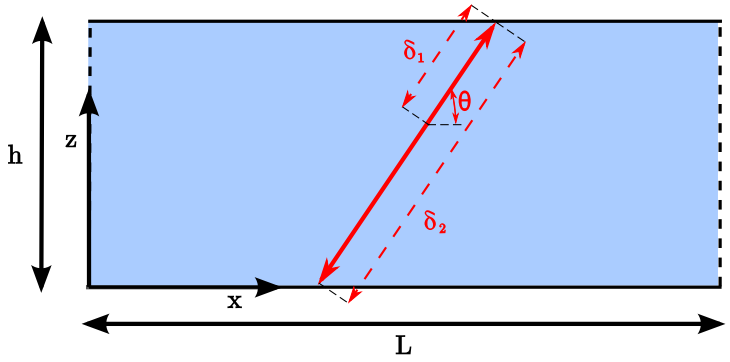

Figure 15: Thin film schematics.
Finite in the z-direction and infinite in the x-direction.

parameter p allows for the reflection to be fully specular, fully diffuse or in between, such that phonons traveling through a boundary are either specularly reflected with a probability p or scattered into the equilibrium distribution with a probability $1-p$. Therefore, a diffuse reflection ($p = 0$ for fully diffusive boundaries) reduces the conductivity of the material, contrary to a specular reflection ($p = 1$ for fully specular boundaries). It is worth noting that this specularity depends on the properties of the involved surface, especially the surface roughness [74]. This phenomenon can be visualized by Figure 16.

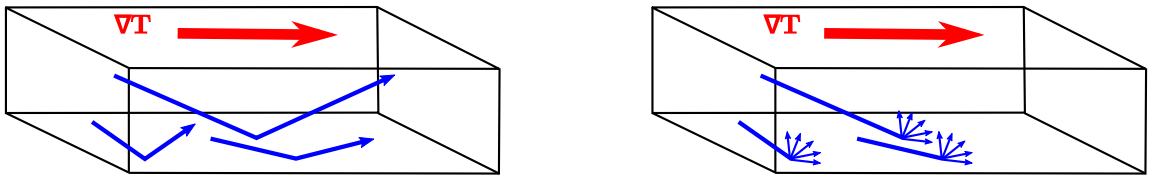

(a) Specular reflection (b) Diffuse reflection

Figure 16: Fully specular (p =1) and fully diffuse (p =0) reflection at the boundary.

Based on the previous description of the *F.S.* model, the two boundary conditions of the thin film layer can be written as a system of two equations

$$\begin{cases} f_0 + f_d^+(0) = p\ \left[f_0 + f_d^-(0)\right] & + (1-p) f_0 \\ f_0 + f_d^-(h) = p\ \left[f_0 + f_d^+(h)\right] & + (1-p) f_0 \end{cases} \tag{2.3.7}$$

where f_d^+ and f_d^- represent the phonon traveling respectively towards the top and bottom surface, as depicted in Figure 16.

After simplification, two easier expressions are obtained

$$\begin{cases} f_d^+(0) = p\ f_d^-(0) \\ f_d^-(h) = p\ f_d^+(h) \end{cases} \tag{2.3.8}$$

By plugging the expression from Equation (2.3.6) into the system of equations (2.3.8), the two specularity boundary condition equations lead to the following expressions of the deviation in both directions

$$f_d^+(z) = -\tau_0 v_x \frac{\partial f_0}{\partial x} \left[1 - \frac{(1-p)}{1 - p\ exp(-\frac{h}{V_z \tau})} exp\left(-\frac{z}{V_z \tau}\right)\right] \tag{2.3.9}$$

$$f_d^-(z) = -\tau_0 v_x \frac{\partial f_0}{\partial x}\left[1 - \frac{(1-p)}{1-p\ exp(-\frac{h}{V_z\tau})} exp\left(\frac{h-z}{V_z\tau}\right)\right] \tag{2.3.10}$$

The expression of the phonon distribution function accounting for the previously expressed deviation from the equilibrium can be substitute into Equation (2.2.21). This defines the heat flux across the thickness of the thin film. In order to obtain the size effect thermal conductivity, the average thermal flux across the film is calculated by integrating over the thickness and correctly accounting for the expression of the deviation, as expressed in Equations (2.3.9) and (2.3.10). Thorough details about the derivation methodology can be found in [73], where a similar expression is obtained for the reduced electrical conductivity for metallic thin films.

Hence, the reduced thermal conductivity is obtained as

$$D(\mathbf{n}) = \frac{k_b}{(2\Pi)^3} \sum_{P=L,T} \int_{BZ} \tau_0(\mathbf{k}) g(\mathbf{k}) v_{g,n}^2(\mathbf{k}) \left(\frac{\hbar\omega}{k_b T}\right)^2 \frac{\exp(\hbar\omega/k_b T)}{[1-\exp(\hbar\omega/k_b T)]^2} d\mathbf{k} \tag{2.3.11}$$

where the function g is called the 'size effect reduction function'. Its expression unfold from the integration of the deviation component of the phonon distribution function and thus its expression is

$$g = 1 - \frac{(1-p)\ exp\left(-\delta_1/\Lambda_0\right)}{1-p\ exp\left(-\delta_2/\Lambda_0\right)} \tag{2.3.12}$$

where p is the specularity parameter, $\Lambda_0 = v_z\tau_0$ is the bulk phonon mean free path. Finally, δ_1 and δ_2 are the distances from the phonon emission at the point 'z' to the surface of the thin film, as depicted in Figure 15. During the mathematical integration, the contribution of the two Equations (2.3.9) and (2.3.10) as been written into a single expression.

Equation (2.3.12) represents the impact of the boundaries of the system on the thermal conductivity, due to the reduction of the phonon mean free path. Hence, the phonon mean free path is reduced from its bulk value and it is proportional to the size effect reduction function such that

$$\Lambda(\mathbf{k}) = g(\mathbf{k})\Lambda_0(\mathbf{k}) \tag{2.3.13}$$

The reduction of phonon mean free path is equivalent to a reduction of the effective relaxation time, which leads to a similar expression

$$\tau(\mathbf{k}) = g(\mathbf{k})\tau_0(\mathbf{k}) \tag{2.3.14}$$

The derived thermal conductivity expression is obtained for the case of the thin film. However, as highlighted below, it can be adapted for any geometry. The only requirement is to be able to calculate the distance from the phonon emission point to the boundary of the system in the direction of interested. As an illustration, in the following subsections, the case of the nanowire and the case of a polycrystal are explained in more details.

Finally, Equation (2.3.11) is generally derived using the thermal gradient along the thin film. However, the expression of the size effect reduction function can be modified to account for different directions of the thermal gradient within the film. This is highlighted in Chapter 4 where the out-of-plane thermal conductivity in thin films is calculated. This constitutes a key contribution that has not been found in the literature.

2.3.1.2 Nanowire

The geometry of the nanowire is analogous to the thin film, but only allows for the propagation of the phonon along the axis direction. Consequently, the size effect is expected to be more pronounced as the boundaries play a more important role. The geometry under consideration is presented on Figure 17. The size effect reduction function follows the same expression as for the thin film, such as

$$g = 1 - \frac{(1-p)\ exp\left(-\delta_1/\Lambda_0\right)}{1 - p\ exp\left(-\delta_2/\Lambda_0\right)} \tag{2.3.15}$$

This expression is expected as the $2D$ analogy of the infinite nanowire and of the thin film are the same. In 3D, the calculations are performed in a similar fashion, but the distance δ_1 and δ_2 are more restricted in the case of the nanowire, as depicted in Figure 17. The differences obtained from the numerical calculation will be highlighted in Chapter 4.

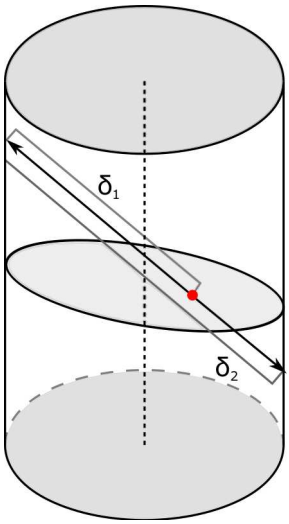

Figure 17: Reduced thermal conductivity in cylindrical nanowires.

2.3.1.3 Single Grain

A strong emphasis is placed on the reduced thermal conductivity of a single grain. Indeed, this work deals mainly with polycrystalline structures and each grain boundary limits the propagation of the phonon. Contrary to the cases of the thin film or nanowire, the single grain does not offer any infinite traveling direction for the phonons as the grain boundaries are present everywhere.

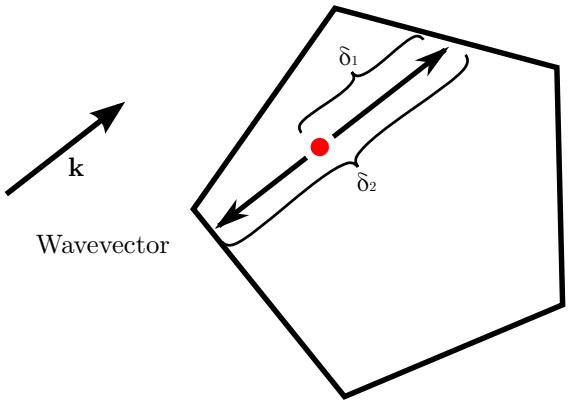

Figure 18: Schematics for computing the reduced phonon mean free path at the point denoted with a dot, for a given wavevector **k**.

Furthermore, the single grain calculation presents a greater challenge as the geometry is arbitrary. In the cases of the thin film and the nanowire, the simpler geometry allows for

the derivation of analytical expressions, with little simplications. On the other hand, the polycrystalline structure can be composed of grains of significantly different sizes, shapes and orientations. Thus, Equation (2.3.16) needs to accounts for the particular characteristics of each grain. While the full methodology is presented in Subsection 3.3.3, the initial focus is placed on single grains.

The assumption is made that phonons can travel following a straight line, from any point in any direction until they reach a grain boundary. Then, by performing the same calculations as for the thin film and for the nanowire, the following expression of the size reduction function is obtained

$$g = 1 - \frac{(1-p)exp\left(-\delta_1/\Lambda_0\right)}{1 - pexp\left(-\delta_2/\Lambda_0\right)} \tag{2.3.16}$$

The length δ_1 and δ_2 are presented on Figure 18. The values depend on the shape and size of the grain. As such, the calculation of the thermal conductivity in this case is complicated but present a greater interest. In this work, those values are numerically obtained through a ray-casting method, explained in Subsection 3.2.1.

2.3.2 Quantum Size Effect

The analysis provided in this work assumes that the physical characteristic dimensions of the system under study are in the order or higher than the bulk phonon mean free path Λ_0. However, for even smaller dimensions, when the characteristic dimension is in the other of the wavelength of the lattice vibration, the classical size effect is not appropriate anymore to describe the phenomena observed in the material. For dimension in the other of the nanometer range, the thermal properties are impacted by the so-called 'quantum size effect' that requires a wavelike treatment of the vibrational modes. Some phenomena occurring are for instance the presence of quantum wells or of hot spots. The quantum size effect is beyond the scope of this work as the devices considered here are in the order of a few micrometers. Nonetheless, the readers should refer to the literature for more details on those topics. Some recommended readings include [25, 75], among others.

2.4 Thermomechanical Model

2.4.1 Mechanical Model

The present subsection introduces the balance equations that govern both the mechanical behavior of the grains in the polycrystal as well as the cohesive response between them. After a brief description of the kinematic considerations and the corresponding notation, the equations of conservation of mass, linear momentum and angular momentum are developed. For a complete discussion of the topics addressed here, see references [76], among others.

2.4.1.1 Kinematic Considerations

The initial step of the mechanical description consists in defining a one-to-one deformation mapping , called φ. It is such that the motion of a body $\mathcal{B}$ in a certain reference configuration is completely defines by φ (ruling out interpenetration of matter and tearing). That is, the coordinates $\mathbf{x}$ of a given material point after deformation are expressed as

$$\mathbf{x}(t) = \varphi(\mathbf{X}, t) \tag{2.4.1}$$

A clear understanding of the deformation mapping, along with the notations used for the reference and deformed configurations is reached by referring to Figure 19. Consequently, the material velocity field is given by

$$\mathbf{v}(t) = \frac{\partial \varphi}{\partial t} \tag{2.4.2}$$

Analogously, the material acceleration field is given by

$$\mathbf{a}(t) = \frac{\partial^2 \varphi}{\partial t^2} \tag{2.4.3}$$

The mapping φ represents the deformation of infinitesimal material vector d$\mathbf{X}$ initially located in $\mathbf{X}$. Hence, its action is completely determined by the deformation gradient, denoted $\mathbf{F}$, whose components are expressed as

$$F^i_J = \frac{\partial \varphi^i}{\partial X^J} \tag{2.4.4}$$

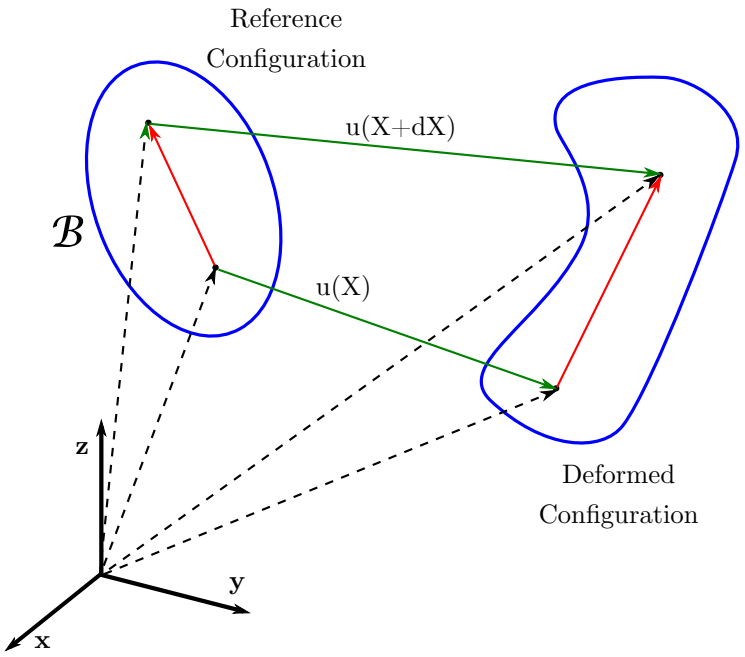

Figure 19: Reference and deformed configuration of a body $\mathcal{B}$.

This deformation gradient allows to determine the change in area and volume of the body from its reference configuration to its deformed configuration. In fact, the deformed oriented area da is related to the initial undeformed oriented area dA by the Piola transformation such that

$$n_i da = JF_i^{I^{-T}} N_I dA \tag{2.4.5}$$

where $J = det(\mathbf{F})$ is the Jacobian of the deformation, n_i are the components of the unit normal to the area in the deformed configuration and N_I are the components of the corresponding vector in the reference configuration. Similarly, the deformed and undeformed volumes are related by J, which is a direct measure of the volumetric deformation. That is, the following relation yields

$$dv = JdV \tag{2.4.6}$$

2.4.1.2 Conservation of Mass

The total mass $m(\mathcal{S})$ of any sub-body $\mathcal{S}$ within a deformable solid must be conserved. This conservation leads to a relation between the mass density of the reference body and of the

deformed body. The mass density of the reference volume dv is denoted ρ_0 and the mass density of the deformed volume dV is denoted ρ. Thus, the total mass of the sub-body $\mathcal{S}$ is defined as

$$m(\mathcal{S}) = \int_{\mathcal{S}} \rho_0(\mathbf{X}) dV = \int_{\varphi(\mathcal{S})} \rho(\mathbf{x}) dv \tag{2.4.7}$$

Using Equation (2.4.6), the two integrals can be expressed over the reference configuration. As a result, the total mass of the sub-body $\mathcal{S}$ becomes

$$m(\mathcal{S}) = \int_{\mathcal{S}} \rho_0(\mathbf{X}) dV = \int_{\mathcal{S}} J\rho(\varphi(\mathbf{X})) dV \tag{2.4.8}$$

Since $\mathcal{S}$ is defined as any arbitrary subregion, the previous equation holds only if

$$\rho_0(\mathbf{X}) = J\rho(\varphi(\mathbf{X})) \tag{2.4.9}$$

2.4.1.3 Conservation of Linear Momentum

As in the previous section, an arbitrary sub-body $\mathcal{S} \in \mathcal{B}$ is considered. In the deformed configuration, the conservation of linear momentum is defined as

$$\int_{\partial\varphi(\mathcal{S})} \mathbf{t} da + \int_{\varphi(\mathcal{S})} \rho \mathbf{b} dv = \frac{d}{dt} \int_{\varphi(\mathcal{S})} \rho \mathbf{v} dv \tag{2.4.10}$$

where $\mathbf{t}$ is the traction vector, $\mathbf{b}$ is the volumetric force vector per unit mass and $\mathbf{v}$ is the material velocity as defined in Equation (2.4.2).

From the Cauchy's tetrahedron theorem, the traction $\mathbf{t}$ on a plane with normal $\mathbf{n}$ is related to the Cauchys stress tensor $\boldsymbol{\sigma}$ by the relation

$$\mathbf{t} = \boldsymbol{\sigma}.\mathbf{n} \tag{2.4.11}$$

Equation (2.4.10) can be rewritten by insertion of Equation (2.4.11). Using the Leibniz–Reynolds transport theorem, the time derivative can be moved into the integral. Finally, the integral over the surface can be transformed into an integral over the volume by means

of the divergence theorem. As a result, the equation of the conservation of linear momentum becomes

$$\int_{\varphi(\mathcal{S})} div(\sigma)dv + \int_{\varphi(\mathcal{S})} \rho\mathbf{b}dv = \int_{\varphi(\mathcal{S})} \rho\mathbf{a}dv \tag{2.4.12}$$

where $\mathbf{a}$ is the material acceleration, as defined in Equation (2.4.3). Collecting terms within a single integral, the previous equation becomes

$$\int_{\varphi(\mathcal{S})} \left[div(\sigma) + \rho\mathbf{b} - \rho\mathbf{a}\right] dv = 0 \tag{2.4.13}$$

Since the previous identity is defined for any arbitrary subregion $\mathcal{S}$, it holds only if

$$div(\sigma) + \rho\mathbf{b} = \rho\mathbf{a} \tag{2.4.14}$$

Equation (2.4.14) is the strong form of the conservation of linear momentum and will be used to derive the weak form implemented in the finite element algorithm.

2.4.1.4 Conservation of Angular Momentum

The conservation of angular momentum for a subregion $\mathcal{S} \in \mathcal{B}$ is expressed in its integral form as

$$\int_{\partial\varphi(\mathcal{S})} \mathbf{x} \times \mathbf{t}da + \int_{\varphi(\mathcal{S})} \mathbf{x} \times \rho\mathbf{b}dv = \frac{d}{dt}\int_{\varphi(\mathcal{S})} \mathbf{x} \times \rho\mathbf{v}dv \tag{2.4.15}$$

This expression can be simplified into a single integral by using, as in the previous section: the Cauchy's tetrahedron theorem, the Leibniz–Reynolds transport theorem and the divergence theorem. It yields to the following equation

$$\int_{\varphi(\mathcal{S})} \left[\rho a_i - \rho b_i - \sigma_{ij,j}\right] + e_{ijk}\sigma_{jk}\right] dv = 0 \tag{2.4.16}$$

Due to the previously introduced conservation of linear momentum, Equation (2.4.16) is reduced to

$$\int_{\varphi(\mathcal{S})} e_{ijk}\sigma_{jk}dv = 0 \tag{2.4.17}$$

Since the previous identity must hold for any subregion $\mathcal{S} \in \mathcal{B}$, it is necessary that

$$e_{ijk}\sigma_{jk} = 0 \tag{2.4.18}$$

The permutation symbol is an anti-symmetric operator, thus the stress tensor σ is required to be symmetric in order to make the previous equation hold. This is expressed as

$$\sigma = \sigma^T \tag{2.4.19}$$

2.4.2 Thermomechanical Coupling

2.4.2.1 Thermal Effect on Mechanical Problems

When a material temperature changes, its dimension is affected as the material expands. For an increase in temperature, the volume of most materials increases, whereas a decrease in temperature causes the volume of most materials to decrease. The strain generated from this deformation is called thermal strain and the component of the thermal strain tensor, denoted $\epsilon^{\mathbf{t}}$ are defined as

$$\epsilon_{ij}^t = \alpha_{ij}\Delta T \tag{2.4.20}$$

where α_{ij} is the component (i, j) of the coefficient of thermal expansion and ΔT is the temperature change. This linear relationship is proven to be appropriate for small and moderate temperature changes.

The thermal strains have inherently a dilatational nature which means that a change in temperatures does not induce shear strains. This translates into a diagonal thermal expansion matrix such as

$$\boldsymbol{\alpha} = \begin{bmatrix} \alpha_{11} & 0 & 0 \\ 0 & \alpha_{22} & 0 \\ 0 & 0 & \alpha_{33} \end{bmatrix} \tag{2.4.21}$$

In particular, the total strain is the sum of the thermal strains ϵ^T (due to the temperature change) and mechanical strain ϵ^m (due to the application of forces). As such, the total strain component can be written as

$$\epsilon_{ij} = \epsilon_{ij}^m + \epsilon_{ij}^t = \epsilon_{ij}^m + \alpha_{ij}\Delta T \tag{2.4.22}$$

As seen previously, the elasticity problem is driven by three groups of equations

1. the equilibrium equations: those are not affected by the thermal strains as they involve only forces and not deformations.

2. the strain-displacement relationships: those remain unchanged, even though the strains now incorporate the thermal component.

3. the constitutive laws: those are directly impacted by the presence of the thermal strains, as explained below.

Forthwith, the coupling between the mechanical and thermal response of the material is attained through the constitutive laws. It can account for fully nonlinear stress-strain relations including: visco-elasticity, thermal strains, and heat generation due to dissipative processes [77, 78]. However, these complex constitutive models could be significantly simpler in many cases of interest.

For example, polycrystalline ceramics can be modeled through a relatively straightforward thermoelastic relation. Once a detailed geometric description of the polycrystal is generated, material properties are assigned to each grain of the system. Properties include the components of the elasticity tensor $\mathbf{C}$, thermal expansion tensor $\boldsymbol{\alpha}$, crystal orientation matrix $\mathbf{R}$, and bulk thermal conductivity tensor $\mathbf{D}$. Then, stresses are computed in the rotated frame from strains and temperature fields by the relation

$$\sigma_{ij} = C_{ijkl}\epsilon^m_{kl} = C_{ijkl}(\epsilon_{kl} - \alpha_{kl}\Delta T) \tag{2.4.23}$$

where ϵ_{kl} are the components of the infinitesimal strain tensor, and ΔT is a local temperature change.

2.4.2.2 Mechanical Effect on Thermal Problems

When a fully-coupled model is considered, the stress field can also affect the heat flux in the material. For instance, plastic deformation will generate heat in the elastoplastic region of the material. In this work, the stress-strain relationship is supposed to be elastic. As a result, the only mechanical effect on the thermal crack will be generated through

the nucleation and growth of cracks. Indeed, those cracks behave like thermal barriers as the thermal conduction is prevented. Then, the thermal transfer can be achieved through convection and radiation or by modifying the thermal conduction expression, as explained in the next subsection.

2.4.3 Thermomechanical Fracture

In the presence of cracks, the body $\mathcal{B}$ is not continuous anymore. The crack, here denoted S, split the body in 2 regions S_i^+ and S_i^-. A representation of the configuration is given in Figure 20. Both the conservation of linear momentum (given in Equation (2.4.14)) and the heat equation (given in Equation (2.2.31)) need to be modified in order to take into consideration the impact of the crack. In those two cases, this procedure is achieved by using the Galerkin procedure [79].

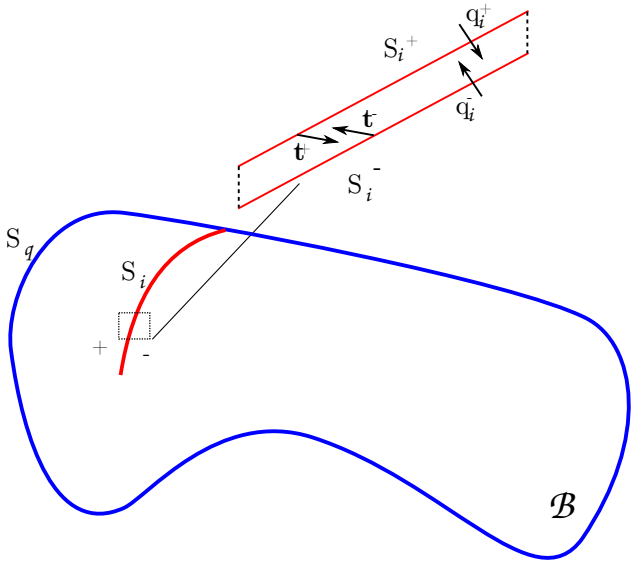

Figure 20: Solid body $\mathcal{B}$ partially separated by a crack.

2.4.3.1 Thermal Fracture

Using the Galerkin procedure, the weak form of the heat diffusion equation is written as

$$\int_V \rho C_p \dot{T} \delta T dV + \int_V \mathbf{q} \boldsymbol{\nabla} \delta T dV = \int_{S_q} \bar{q} \delta T dS + \overbrace{\int_{S_i^+} q_i^+ \delta T^+ dS + \int_{S_i^-} q_i^- \delta T^+ dS}^{\text{fracture terms}} \quad (2.4.24)$$

The continuity condition on the thermal flux leads to

$$\int_V \rho C_p \dot{T} \delta T dV + \int_V \mathbf{q} \boldsymbol{\nabla} \delta T dV = \int_{S_q} \bar{q} \delta T dS + \overbrace{\int_{S_i^+} q_i^+ (\delta T^+ - \delta T^-) dS}^{\text{fracture terms}} \tag{2.4.25}$$

Equation (2.4.25) is solved by means of finite element method, which allows to consider complex geometries. This discretization is explained in more details in the next Chapter.

2.4.3.2 Mechanical Fracture

Again, using the Galerkin procedure, the weak form of the conservation of linear momentum is written as

$$\int_V \boldsymbol{\sigma} \boldsymbol{\nabla} \delta \mathbf{x} dV + \int_V \delta \mathbf{x} dV = \int_{S_q} \mathbf{t} \delta \mathbf{x} dS + \overbrace{\int_{S_i^+} \mathbf{t}^+ \delta \mathbf{x}^+ dS + \int_{S_i^-} \mathbf{t}^- \delta \mathbf{x}^- dS}^{\text{fracture terms}} \tag{2.4.26}$$

The continuity condition on the traction leads to

$$\int_V \boldsymbol{\sigma} \boldsymbol{\nabla} \delta \mathbf{x} dV + \int_V \delta \mathbf{x} dV = \int_{S_q} \mathbf{t} \delta \mathbf{x} dS + \overbrace{\int_{S_i^+} \mathbf{t}^+ (\delta \mathbf{x}^+ - \delta \mathbf{x}^-) dS}^{\text{fracture terms}} \tag{2.4.27}$$

Similarly, Equation (2.4.27) is solved by means of finite element method. The procedure is explained in the next Chapter.

CHAPTER III

MULTISCALE NUMERICAL ANALYSIS

In this chapter, the numerical implementation related to the concurrent thermomechanical model is reported to ease the understanding and to facilitate the repeatability of the implementation. As stated in the introduction, the work presented in this section is the backbone of all obtained results and represents the most time-consuming task of this thesis. This chapter highlights most of the implementation concepts. In particular, the microscale level implementation, the continuum implementation as well as the coupling between both scales are deeply emphasized in this part of the thesis. The heavy detailed technicalities are way beyond the interest of this text. Nevertheless, the final subsection presents the needs for a parallel implementation as well as the challenges associated with it.

3.1 Polycrystal Generation and Meshing Techniques

Many major phenomena occurring in polycrystalline materials are strongly dependent on the attributes of the microstructural features. Some well-known components include the Young's modulus, the thermal conductivity or the thermal expansion coefficient. In this thesis, the mesh accounts for that aspect by explicitly examining the geometry of each grain. This approach is commonly known as the direct numerical simulation of polycrystals.

3.1.1 Generation of the Polycrystal

In this work, the generation of the polycrystal is a three step process that is depicted in Figure 21. It includes

1. the generation of the initial mesh: the primal mesh.

2. the definition of the grains: the dual mesh.

3. the refinement of the mesh.

An initial mesh, called the primal mesh, is first generated. It provides the geometry of the system under consideration, as represented in Figure 21a. While it is not a representation of the polycrystalline structure, it is worth noting that each node of the primal mesh will later correspond to the location of the centers of each grain. As such, the number of nodes in the primal mesh equals the number of grains in the final polycrystalline structure. This primal mesh can be structured or unstructured. This distinction is important as it influences the granular arrangement. Indeed, the former one leads to a distribution of uniform grains within the polycrystal. The latter allows for a more realistic representation by generating grains of arbitrary shapes, as displayed in Fugre 21b. Consequently, the numerical model takes into consideration the non-uniformity of the grain size and the grain shape. Moreover, to represent a specific microstructure, the grain location can be spaced according to the required grain size distribution. This aspect is of prime importance during grain distribution optimization as presented in Subsection 4.3.

The primal mesh is based on the notion of simplicial complex that is explained in-depth in [80], among others. This property offers the convenient possibility of defining the region corresponding to each grain in the model. That is, the primal mesh presented in Figure 21a can easily generate the polycrystalline structure, obtained in Figure 21b. To achieve this goal, the concept of dual mesh has to be introduced. The central idea underlying the notion of dual mesh is to associate to each primal k-simplex (where k represents the dimension of the simplex) of the n-dimensional cell complex S a dual $(n-k)$-cell of the dual complex. For example, for each 0-cell (node) in a 2-dimensional cell complex a dual 2-cell (triangle) can be defined. An in-depth discussion of the concept of duality can be found in [81].

The grains resulting from the dual mesh (Figure 21b) can be classified as the Voronoi tessellations corresponding to a given initial distribution of 0-cells within the primal mesh (Figure 21a). Many papers deal with the generation of those meshes, such as [82, 83]. Depending on the location of the nucleation points, some grains of the Voronoi tessellation can be non-convex, which is not experimentally observed. In this work, to avoid this phenomenon, the dual is generated using the discrete Hodge operator [84]. This methodology

alleviates from performing any addition mesh modification such as the previously used energy relaxation step at the grain boundary, as in [85]. As a result of this procedure, the explicit representation of the microstructure of the material is reached, and it comprises only of convex grains.

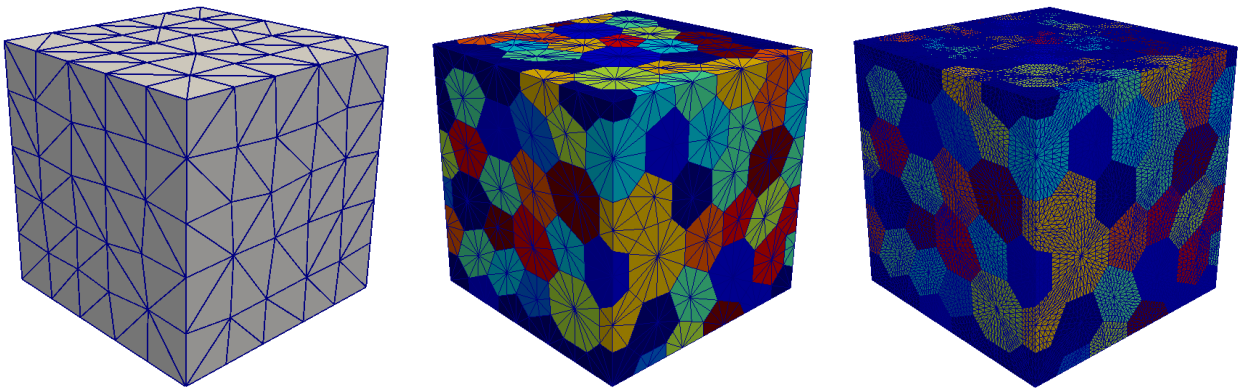

(a)
Primal Mesh
848 elements

(b)
Dual Mesh
11,076 elements

(c)
Refined Mesh
708,864 elements

Figure 21: Numerical generation of the polycrystalline structure.

3.1.2 Mesh Refinement Requirement

To obtain an accurate numerical solution, the finite element spatial discretization needs to be fine enough. Therefore, once the dual mesh (representing the polycrystalline structure, as pictured in Figure 21b) has been generated, the elements within each grain are subdivided, leading to the mesh represented in Figure 21c. Several phenomena present in this work impact the mesh requirements, including but not limited to the following: the presence of a thermal boundary layer, the localization phenomenon that leads to a concentration of the stress, the presence of the cohesive zone elements, the anisotropy of the material. This need for a fine mesh is pointed out with the mesh refinement analysis presented in Figure 22. For a fine enough mesh (i.e. having three or more subdivisions), the multiscale framework recovers the boundary layer effect and the associated converged temperature field. This localization near the grain boundary can be related to the concept of Kapitza resistance

as frequently used in numerical thermal modeling. More discussion on that topic will be addressed in Chapter 4.

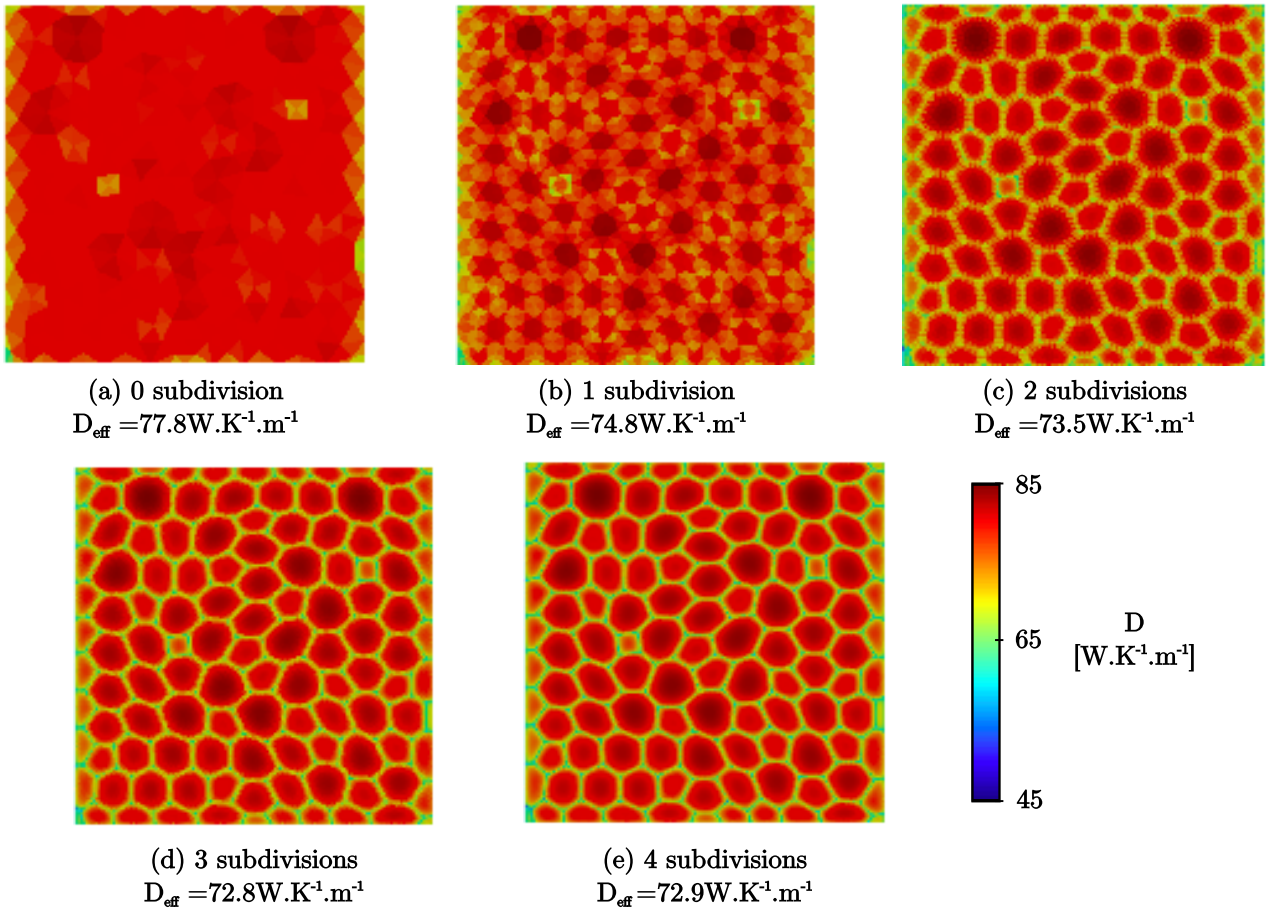

Figure 22: Mesh refinement analysis - Square polycrystal of size $25\mu m$.

Different subdivision techniques exist for two and three-dimensional analyses, such as the commonly used barycentric subdivision [86]. Unfortunately, consecutive iterations of this subdivision lead to elements of poor quality, i.e having a high aspect ratio. To overcome this limitation, the aforementioned work considers another type of subdivision, called (in three dimensions) the '8-subtetrahedron' subdivision, as presented in [87]. This implementation provides the benefit of maintaining the quality of the element. More details, as well as a comparison between those two subdivision techniques, are given in Subsection 3.5.1.

3.2 Microscale-level: Thermal Conductivity Calculation

As explained in Section 2.3.1, the thermal conductivity is a size-dependent property of the material, whose formula is given by

$$D(\mathbf{n}) = \frac{k_b}{(2\Pi)^3} \sum_{P=L,T} \int_{BZ} \tau_0(\mathbf{k}) g(\mathbf{k}) v_{g,n}^2(\mathbf{k}) \left(\frac{\hbar\omega}{k_b T}\right)^2 \frac{\exp(\hbar\omega/k_b T)}{[1-\exp(\hbar\omega/k_b T)]^2} d\mathbf{k} \tag{3.2.1}$$

where the function g is given by

$$g = 1 - \frac{(1-p)\ exp\,(-\delta_1/\Lambda_0)}{1-p\ exp\,(-\delta_2/\Lambda_0)} \tag{3.2.2}$$

The calculation of the thermal conductivity is accomplished by integrating over all spatial directions. However, the integral can not be analytically computed. Consequently, it is replaced by a discrete sum. This summation over the Brillouin zone includes a finite number of values or directions in which the wavevector is considered. To perform this calculation, the following steps are required

1. retrieve the nodes and their position for each edge (in two dimensions) and each surface (in three dimensions), on the outer boundary. This information allows to reconstruct the grain boundary during the calculation of δ_1 and δ_2.

2. calculate the distances fromt the phonon to the grain boundary.

A more in-depth description of those two steps is provided in the rest of this subsection.

3.2.1 Distance Phonon to Grain Boundary

3.2.1.1 Implementation in 2D

The configuration under study is given in Figure 23, which considers the previous case from Figure 18. The grain boundary segment is determined by the extremity points P_1 and P_2. The line passes through the quadrature point P_q and the point P_d in the specific direction θ such that

$$\begin{aligned} x_d &= x_q + L_{qd}\cos\theta \\ y_d &= y_q + L_{qd}\sin\theta \end{aligned} \tag{3.2.3}$$

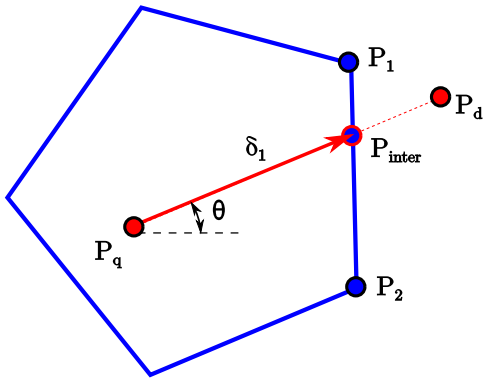

Figure 23: Configuration of the 2D intersection between the grain boundary $[P_1, P_2]$ and the line (P_q, P_d).

where L_{qd} is a strictly positive scalar arbitrarily selected that represents the distance between the points P_q and P_d. It should be at least several times the largest grain size in order to ensure that the line crosses the grain boundary. The location of the intersection point P_{inter} is given by its two coordinate components

$$x_{inter} = \frac{\begin{vmatrix} \begin{vmatrix} x_1 & y_1 \\ x_2 & y_2 \end{vmatrix} & x_1 - x_2 \\ \begin{vmatrix} x_q & y_q \\ x_d & y_d \end{vmatrix} & x_q - x_d \end{vmatrix}}{\begin{vmatrix} x_1 - x_2 & y_1 - y_2 \\ x_q - x_d & y_q - y_d \end{vmatrix}} \qquad y_{inter} = \frac{\begin{vmatrix} \begin{vmatrix} x_1 & y_1 \\ x_2 & y_2 \end{vmatrix} & y_1 - y_2 \\ \begin{vmatrix} x_q & y_q \\ x_d & y_d \end{vmatrix} & y_q - y_d \end{vmatrix}}{\begin{vmatrix} x_1 - x_2 & y_1 - y_2 \\ x_q - x_d & y_q - y_d \end{vmatrix}} \tag{3.2.4}$$

3.2.1.2 Implementation in 3D

As for the two-dimensional case, the distance from the emission of the phonon (represented by the quadrature point) to the grain boundary (represented by a plane) is calculated in three dimensions. In order to do so, the distance from the quadrature point to all the planes of the grain is determined. The boundary surface is determined by the points P_1, P_2, and P_3. Indeed, only three arbitrary points belonging to the plane are necessary to define the whole plane.

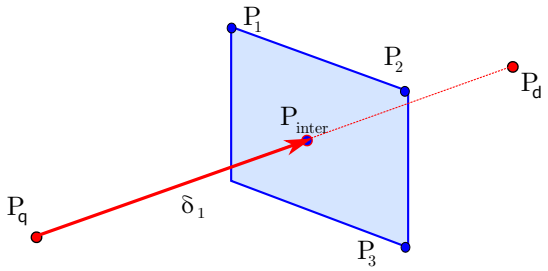

Figure 24: Configuration of the intersection in 3D between the plan and the line.

The line passes through the quadrature point P_q and the point P_d in the specific direction ϕ and θ such that

$$\begin{aligned} x_d &= x_q + L_{qd} \cos\theta \sin\phi \\ y_d &= y_q + L_{qd} \sin\theta \sin\phi \\ z_d &= z_q + L_{qd} \cos\phi \end{aligned} \tag{3.2.5}$$

where L_{qd} is a strictly positive scalar. The plane formed by the three points P_1, P_2, and P_3 can be expressed in the determinant form as

$$\begin{vmatrix} x & y & z & 1 \\ x_1 & y_1 & z_1 & 1 \\ x_2 & y_2 & z_2 & 1 \\ x_3 & y_3 & z_3 & 1 \end{vmatrix} = 0 \tag{3.2.6}$$

while the location of the intersection point P_{inter} is given by its 3 coordinate components

$$\begin{aligned} x_{inter} &= x_q + (x_d - x_q)\ t_{inter} \\ y_{inter} &= y_q + (y_d - y_q)\ t_{inter} \\ z_{inter} &= z_q + (z_d - z_q)\ t_{inter} \end{aligned} \tag{3.2.7}$$

where the parameter t_{inter} is given by

$$t_{inter} = -\frac{\begin{vmatrix} 1 & 1 & 1 & 1 \\ x_1 & x_2 & x_3 & x_q \\ y_1 & y_2 & y_3 & y_q \\ z_1 & z_2 & z_3 & z_q \end{vmatrix}}{\begin{vmatrix} 1 & 1 & 1 & 0 \\ x_1 & x_2 & x_3 & x_{inter} - x_q \\ y_1 & y_2 & y_3 & y_{inter} - y_q \\ z_1 & z_2 & z_3 & z_{inter} - z_q \end{vmatrix}} \tag{3.2.8}$$

The configuration of the situation is represented in Figure 24.

For illustration purposes, Figure 25 represents the distance δ_1 at every quadrature points for a phonon traveling along the z-direction ($\theta = 0$ and $\phi = 0$) towards the bottom grain boundary. This grain has a size of $1\mu m$. From a numerical perspective, the calculation of the determinant is an expensive operation. As a consequence, those distances are stored during the early steps of the computation. As presented later in this thesis, when the temperature evolves the thermal conductivity needs to be updated. However, the distances stay the same, and the values are retrieved from the previously saved data rather than recalculated.

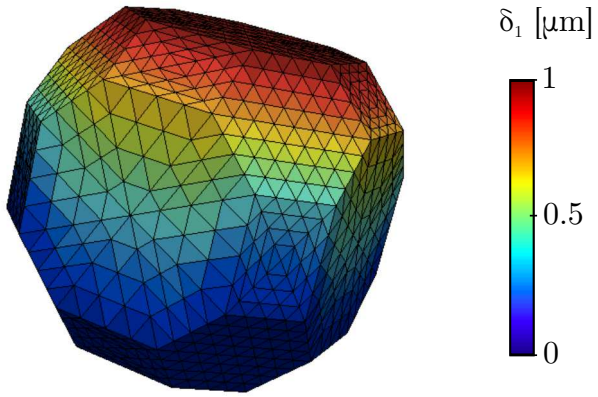

Figure 25: Distance from the quadrature point to the bottom grain boundary.

3.2.2 Numerical Integration of the Thermal Conductivity

The procedure explained in Subsection 3.2.1 presents the calculation of δ_1 and δ_2 for a single direction of the wavevector. In order to calculate the thermal conductivity, all directions must be taken into consideration. From a numerical standpoint, only a discrete number of directions is considered in the computational calculations. Due to the large number of grains, coupled with the large number of quadrature points per grain, the number of directions needed for the integration of the thermal conductivity is crucial. To some extent, a large number of directions might lead to no enhancement in the thermal conductivity value while requiring long computational time. To determine the appropriate number, a convergence analysis is run.

As a matter of fact, the integration is performed following the trapezoidal numerical integration [88]. The domain of integration is discretized in N equally spaced panels. Considering a function f continuous on the interval $[a, b]$, the trapezoidal rule is given by

$$\begin{aligned} \int_a^b f(x)\,dx &\approx \frac{b-a}{2N}\sum_{k=1}^{N}\left(f(x_{k+1})+f(x_k)\right) \\ &= \frac{b-a}{2N}\left(f(x_1)+2f(x_2)+\cdots+2f(x_N)+f(x_{N+1})\right) \end{aligned} \tag{3.2.9}$$

where a and b are the limits of integration, such that $a = x_1 < x_2 < ... < x_{N+1} = b$ and N is the number of subdivisions of the interval $[a, b]$. The number of subdivisions and the underlying length impacts the accuracy of the integration. The more intervals, the more accurate is the calculation. However, the computational time is linearly proportional to the number of intervals. In order to optimize this trade-off situation, a convergence analysis is run, where the optimal number of subdivisions is determined. Two different grain shapes are analyzed: (a) a regular hexagon and (b) an elongated grain. The thermal conductivity is expected to convergence faster in the regular hexagon case, due to the symmetry. The error $\epsilon^{(i)}$ is defined as

$$\epsilon^{(i)} = \left|\bar{D}^{(i)} - \bar{D}^{(N)}\right| \tag{3.2.10}$$

where $\bar{D}$ is the average thermal conductivity over the grain, N is the maximum number of directions examined, and i is the number of directions considered, such that $i \in [0, N]$.

As depicted in Figure 26, the number of subdivisions in the trapezoidal integration is of prime importance. To reach a converged solution with a difference of less than 0.1%, the integration in two dimensions should consider at least 200 directions. In three dimensions, the same angle increment is kept over the two angular directions of integration.

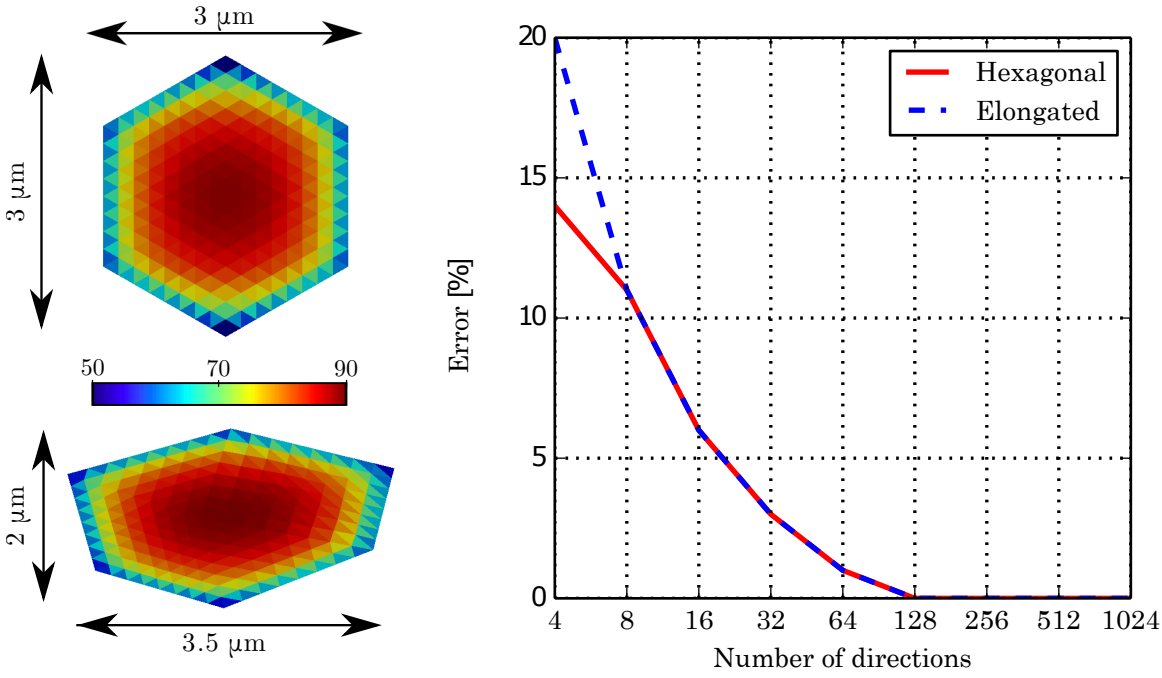

(a) Grains used for the analysis

(b) Convergence Analysis

Figure 26: Convergence on the integration over θ.

3.2.3 Multiscale Framework

The microscale calculation of the thermal conductivity is fully explained in the previous subsections. It accounts for the size effect through the calculation of δ_1 and δ_2, representing the distance from the phonon emission point to the grain boundary. Once the integration is performed using the numerical trapezoidal rule, the thermal conductivity for each grain is obtained. The literature provides simplified calculations for uncomplicated geometries, such as square grains or nanowires, that lead to the same results.

The key novelty of this thesis lies in the development of a concurrent multiscale framework. It allows to incorporate the information calculated at the sub-grain level into the macroscale thermal transport model. As such, this numerical model requires two levels of integration: (a) the microstructure of the polycrystal and (b) the macroscopic behavior.

Coupling with the sub-grain scale is completed at the integration points of the mesh: the full thermal conductivity tensor is computed at each quadrature point considering the actual geometric features. That is, each quadrature point in the model knows to which grain it belongs, its position within the grain, as well as the exact geometry of the grain. In this sense, computations at the quadrature point level are not local as in traditional FEM approaches, being this key to capture the size-dependent effect. Then, the sub-grain thermal conductivity tensor is adopted as material property for the continuum model described in the next subsection. Figure 27 shows a schematic representation of this approach.

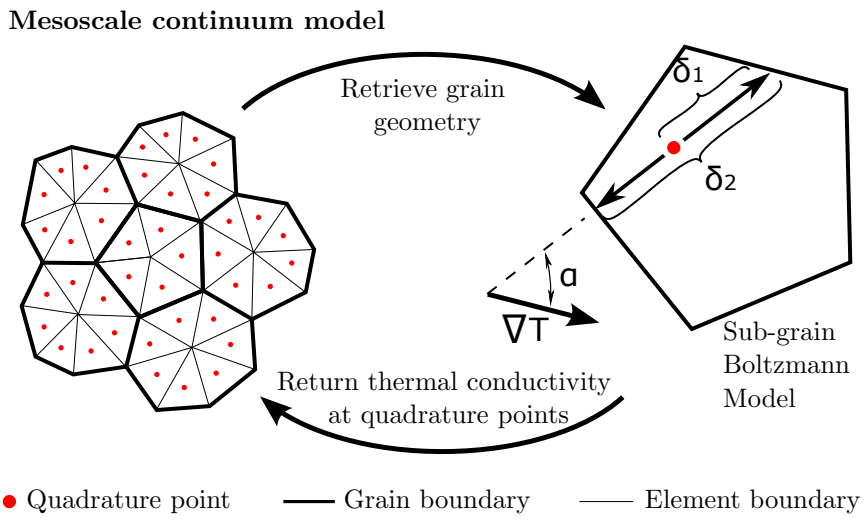

Figure 27: Concurrent multiscale scheme.

The proposed model constitutes a concurrent multiscale scheme, as computations at both scales take place simultaneously. Ideally, this procedure should be performed after every integration step during computations as the thermal conductivity depends on temperature, which evolves with time. In practice, computational cost can be reduced by performing this operation only after a predetermined temperature threshold is attained at

the quadrature point. The precise value of the temperature change threshold can be determined through a simple convergence analysis. This point will be developed in Chapter 4.

3.3 Continuum-level: Finite Element Implementation

3.3.1 Continuum-level Thermal Model

3.3.1.1 Boundary Value Problem

A key component of the proposed approach is to assume the separation of scales. That is, at the continuum level, the thermal conductivity of the material is assumed to be a locally (point-wise) defined quantity that depends on the temperature at that point and the characteristic grain size of the microstructure at the same location. This approach allows to model a continuum as a material obeying Fourier's heat equation, with the consideration that the thermal conductivity is no longer a constant quantity. This is the key concept of the concurrent multiscale analysis, presented in this thesis. As a reminder, the heat transport problem is modeled by the heat equation (2.2.31). Its expression can be written in an orthonormal basis with coordinates x^i as

$$\frac{\partial}{\partial x^i}\left(D(T)\frac{\partial T}{\partial x^i}\right) = \rho C_p \frac{\partial T}{\partial t} \tag{3.3.1}$$

where T is the temperature, $D(T)$ is the temperature-dependent thermal conductivity, ρ is the mass density, and C_p is the specific heat capacity. The corresponding boundary conditions are given by

$$T = \bar{T} \quad on\ \partial\mathcal{S}_1, \qquad q^i = \bar{q}^i \quad on\ \partial\mathcal{S}_2 \tag{3.3.2}$$

where q^i represents the components of the heat flux vector expressed in an orthonormal basis with coordinates x^i, and $\partial\mathcal{S}_1$. The boundary of the model $\partial\mathcal{S}$ is subdivided into regions $\partial\mathcal{S}_1$ or $\partial\mathcal{S}_2$ of respectively Dirichlet and Neumann boundary conditions such that

$$\partial\mathcal{S}_1 \cup \partial\mathcal{S}_2 = \partial\mathcal{S}, \quad \partial\mathcal{S}_1 \cap \partial\mathcal{S}_2 = \emptyset \tag{3.3.3}$$

3.3.1.2 Spatial Discretization

To compute the heat transfer problem on arbitrary domains - which is the goal of this framework- , the diffusion problem can be expressed in weak form and subsequently discretized by means of a finite element scheme, resulting in

$$M_{ab}\frac{\partial \hat{T}_b}{\partial t} + K_{ab}\hat{T}_b = Q_a \tag{3.3.4}$$

with

$$M_{ab} = \int_{\mathcal{S}} \rho C_p N_a N_b d\mathcal{S} \qquad K_{ab} = \int_{\mathcal{S}} \frac{\partial N_a}{\partial x^i} D_{\text{eff}} \frac{\partial N_b}{\partial x^j} d\mathcal{S} \qquad Q_a = -\int_{\partial \mathcal{S}_2} N_a N_b \hat{\bar{q}}_b^i \, n_i \, dS \tag{3.3.5}$$

where $\hat{T}_b$ is the temperature at node b, $\hat{\bar{q}}_b^i$ are the components of the heat flux vector at node b, n_i are the components of the unit normal to the surface $\partial\mathcal{S}_2$, and N_i are the interpolation or shape functions. The terms M_{ab} and K_{ab} are called the mass and stiffness matrices respectively by analogy with solid mechanics problems, and Q_a is referred to as the forcing term. The integrals in Equation (3.3.5) are evaluated through a quadrature scheme, and the resulting differential Equation (3.3.4) is usually integrated in time using a forward Euler procedure. When the study focuses on steady-state problems, the temporal derivative vanishes and Equation (3.3.4) then reduces to

$$K_{ab}\hat{T}_b = Q_a \tag{3.3.6}$$

which can be solved by inverting the matrix K_{ab}.

3.3.2 Continuum-level Mechanical Model

3.3.2.1 Boundary Value Problem

For the same domain as considered in the previous section, the equation of conservation of linear momentum is given by

$$\frac{\partial \sigma_{ij}}{\partial x^j} + \rho b_i = \rho \tag{3.3.7}$$

where σ_{ij} are the components of the Cauchy's stress tensor expressed in an orthonormal basis with coordinates x^j, b_i and a_i the components of the body forces and acceleration

respectively, and ρ the material density. The corresponding boundary conditions are given by

$$\sigma_{ij} n_j = \bar{t}_i \quad on\ \partial\mathcal{S}_3, \qquad u_i = \bar{u}_i \quad on\ \partial\mathcal{S}_4 \tag{3.3.8}$$

where n_j and t_j are the normal and traction vectors defined on the external surface $\partial\mathcal{S}_3$ respectively and u^i are the components of the displacement field. The boundary of the model $\partial\mathcal{S}$ is subdivided into regions $\partial\mathcal{S}_3$ or $\partial\mathcal{S}_4$ of respectively Neumann and Dirichlet boundary conditions such that

$$\partial\mathcal{S}_3 \cup \partial\mathcal{S}_4 = \partial\mathcal{S}, \quad \partial\mathcal{S}_3 \cap \partial\mathcal{S}_4 = \emptyset \tag{3.3.9}$$

and

3.3.2.2 Spatial Discretization

To compute the stress problem on arbitrary domains, the mechanical problem can be expressed in weak form. Starting from the strong form of the conservation of linear momentum given in Equation (2.4.14), it leads to

$$div(\boldsymbol{\sigma}) + \rho\mathbf{b} = \rho\mathbf{a} \tag{3.3.10}$$

where the stress tensor is such that

$$\sigma_{ij} = C_{ijkl}\epsilon_{kl} \tag{3.3.11}$$

where $\boldsymbol{C}$ is the stiffness tensor, written in the indicial notation and $\boldsymbol{\epsilon}$ is the strain tensor. This relation is the anisotropic form of the Hooke's law. The strain component is defined as

$$\epsilon_{kl} = \frac{\partial \mathrm{x}^{\mathrm{k}}}{\partial x^l} \tag{3.3.12}$$

Thus, the relation 3.3.10 is discretized by means of a finite element scheme, resulting in

$$M_{ab}\frac{\partial^2 \hat{\mathrm{x}}_b^i}{\partial t^2} + K_{ab}\hat{\mathrm{x}}_b^i = Q_a \tag{3.3.13}$$

with

$$M_{ab} = \int_{\mathcal{S}} \rho N_a N_b d\mathcal{S} \qquad K_{ab} = \int_{\mathcal{S}} \frac{\partial N_a}{\partial x^i} C_{ijkl} \frac{\partial N_b}{\partial x^j} d\mathcal{S} \qquad Q_a = -\int_{\partial\mathcal{S}_2} N_a N_b \hat{\bar{Q}}_a^i \, n_i \, dS \tag{3.3.14}$$

Again, the integrals in Equation (3.3.14) are evaluated through a quadrature scheme, and the resulting differential Equation (3.3.13) is usually integrated in time by means of a forward Euler procedure. When the study focuses on steady-state problems, the temporal derivative vanishes and Equation (3.3.13) then reduces to

$$K_{ab}\hat{\mathrm{x}}_b^i = Q_a \tag{3.3.15}$$

which can be solved by inverting the matrix K_{ab}.

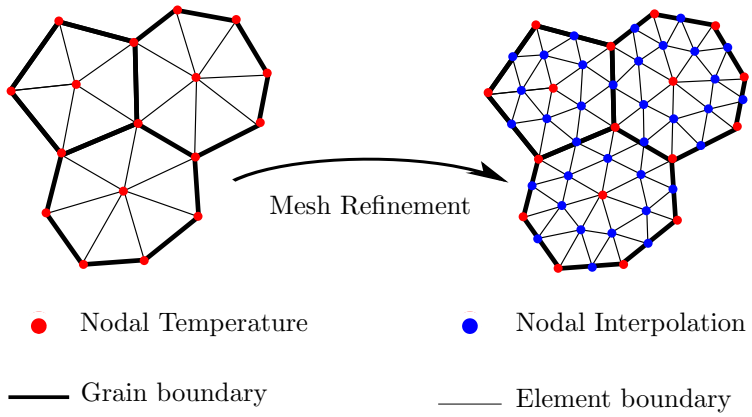

Figure 28: Mesh refinement interpolation technique.

3.3.3 Thermomechanical Coupling

Variation of stresses within the mechanical model is much more pronounced than that of the temperature field. This phenomenon is mainly driven by the anisotropy of the elastic properties and the fact that grains have a random orientation. Thus, in order to capture the stress localization at the grain boundaries, the mesh utilized for the thermal problem is refined in such a way that each initial triangle results in four smaller triangular elements, see Figure 28. The figure is made for illustration purposes as the actual meshes for each grain possess a higher level of refinement. Once the temperature information is carried from the thermal model to the mechanical model, the resulting thermal stresses can be calculated.

3.3.4 Time Scheme

Starting with the same time discretization expression, different temporal analyses can be performed: static, quasi-static and dynamic. In the case of the developed concurrent multiscale framework, the choice of the analysis type to be performed depends on two main criteria

1. the coupling between the thermal and mechanical models.

   In this work, most of the analyses is made with Hookean elastic material in the absence of cracks. Thus, the stress field has no influence on the thermal one. However, in the case of plasticity, the plastic regime can lead to the generation of heat. While in the case of fracture, the cracks can prevent the heat flux to flow through the material. In those two situations, the stress field impacts the thermal properties, and the two models need to be fully coupled.

2. the speed at which the system evolves.

   In general, the mechanical model is significantly faster than the diffusion model. It means that the stress waves propagate at a higher speed than the heat. In that case, the two models can be weakly coupled. However, those two velocities vary differently as the grain size decreases. To some extent, the two models can reach equilibrium around the same time. Hence, the influence of the grain size on the characteristic times is studied later in this subsection.

In the rest of the subsection, the advantages and disadvantages of the different temporal analyses, as well as the selection process, are discussed. A strong emphasis is placed on the thermal diffusion problem. As observed in Chapter 2, the thermal conductivity is a function of the temperature field. This strong coupling requires specific integration techniques that are explained below.

3.3.4.1 Time Discretization

Equation (3.3.4) represents the spatial discretization of the diffusion problem. Consequently, solving this equation provides the temperature field within the domain at a given time t. To obtain the evolution of the temperature field over time and solve the transient problem, the boundary value problem needs to be temporally discretized. The time discretization of the thermal diffusion problem (2.2.31) is expressed in matrix notation as

$$\mathbf{M}\dot{\mathbf{T}} + \mathbf{K}\mathbf{T} = \mathbf{Q} \tag{3.3.16}$$

The family of generalized trapezoidal methods assumes the following time-discretization

$$\mathbf{M}\dot{\mathbf{T}}_{n+1} + \mathbf{K}\mathbf{T}_{n+1} = \mathbf{Q}_{n+1} \tag{3.3.17}$$

with

$$\mathbf{T}_{n+1} = \mathbf{T}_n + \Delta t \dot{\mathbf{T}}_n \tag{3.3.18}$$

where Δt is the time-step. Equation (3.3.18) is referred as an explicit integration since the temperature field $\mathbf{T}_{n+1}$ can be expressed explicitly from the existing solution values $\mathbf{T}_n$. The same time discretization technique can be used for the mechanical equation.

3.3.4.2 Characteristic Times

The characteristic time is an estimate of the order of magnitude of the time needed by the unbalanced system to return to equilibrium. From a quantitative standpoint, the characteristic time is easily derived from the governing equation such that

1. the thermal characteristic time is given by

$$t_T = \frac{L_c^2}{\alpha} \tag{3.3.19}$$

   where L_c is the characteristic size of the system and α is the thermal diffusivity, defined as

$$\alpha = \frac{D}{\rho C_p} \tag{3.3.20}$$

2. the mechanical characteristic time is given by

$$t_M = \frac{L_c}{c} \tag{3.3.21}$$

where c is the wave speed.

Both characteristic times depend on the characteristic size of the system and on the material properties. In the case of the polycrystalline structure, the characteristic size corresponds to the length of the grain. Table 2 compares those times for small and large grains of silicon.

Table 2: Characteristic times for different sizes of silicon grain.

	Small grain	Large grain
$\rho\ [kg.m^{-3}]$	2329	
$C_p\ [J.kg^{-1}.K^{-1}]$	712	
$c\ [m.s^{-1}]$	8433	
$L_c\ [\mu m]$	0.1	10
$D\ [W.K^{-1}.m^{-1}]$	12	116
$t_T\ [s]$	1.38×10^{-9}	1.42×10^{-6}
$t_M\ [s]$	1.19×10^{-11}	1.18×10^{-9}
$\frac{t_T}{t_M}$	116	1205

The characteristic times of mechanical and thermal problems are apart by several orders of magnitude. Therefore, the transient problem can be solved using a staggered approach, which allows to uncouple the thermal and mechanical models. However, it is worth noting that the ratio t_T/t_M decreases as the grain size is reduced. Hence, for smaller grains than the ones considered in this work, it might be necessary to couple both models.

As a result, for grains having a size of $0.1\mu m$ or higher, the coupling between the models is limited to the impact of the stress field on the thermal problem; mainly through the nucleation and propagation of cracks.

The next subsection focuses on the description of the three different types of analyses: static, quasi-static and dynamic. As previously mentioned, the focus is put on the thermal diffusion problem as the thermal conductivity is a function of the time-dependent temperature field. The mechanical problems are governed by similar equations. However, in this work, the elastic properties are constant, leading to a simpler temporal approach.

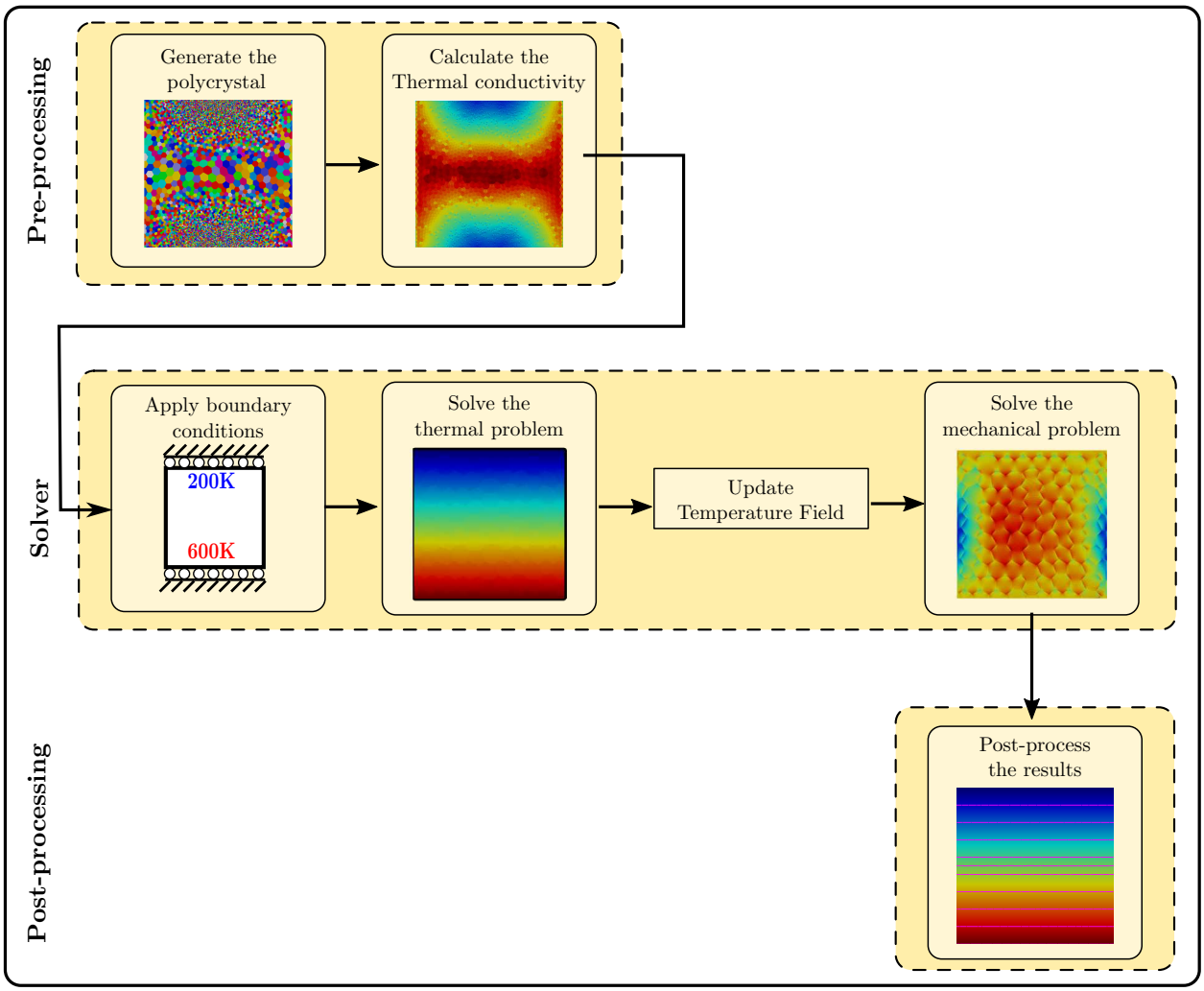

Figure 29: Flowchart of the static analysis for thermomechanical problems.

3.3.4.3 Static Analyses

For statics analyses, the time-dependent derivative vanishes and Equation (3.3.16) is simplified to

$$\mathbf{KT} = \mathbf{Q} \tag{3.3.22}$$

Thus, for the thermal model, the temperature vector $\mathbf{T}$ is obtained by inverting the thermal conductivity matrix $\mathbf{K}$. As the matrix $\mathbf{K}$ is temperature-dependent, the obtained solution is valid if and only if the temperature change between the initial and final configurations has a limited influence on the thermal conductivity. Otherwise, a quasi-static analysis must be carried out.

Static analyses can be solved numerically by inverting the matrix $\mathbf{K}$. However, this task becomes cumbersome for large matrices. For this reason, approximation techniques can be used such as gradient or conjugate gradient methods, among others. In this thesis, most of the static analyses are performed using a specific nonlinear conjugate gradient method, known as the Polak–Ribière solver.

Once the temperature field is obtained, the mechanical problem is solved using the same approach. It is worth noting that static analyses are not able to handle crack simulations. The flowchart of the solution procedure is given in Figure 29.

3.3.4.4 Quasi-Static Analyses

As previously presented, the temperature dependence of the thermal conductivity limits static analyses to problems in which the initial conditions are not far from the final equilibrium. Then again, those problems can be of limited interest.

To solve more complex problems, while staying away from dynamic analyses, a quasi-static analysis is adopted for which the boundary conditions are incrementally changed, in order to move from a state of equilibrium to the next one. That is, the quasi-static load is applied so slowly that the influence on the material is also very slow. Therefore, the inertia term from the equilibrium equation is small and can be ignored. Under those circumstances, the initial and final states can be far from each other as long as the duration of the change is significantly larger than the problem characteristic time.

This type of analysis is decisive when the material properties change over time. For instance, in the thermal problem before each update of the thermal boundary conditions, the thermal conductivity matrix must be recalculated by considering the last temperature state. The flowchart of the solution procedure is given in Figure 30. It is such that the thermal conductivity $D(T)$ is updated if the temperature change ΔT is higher than a predefined critical change ΔT_c. The quasi-static analysis also allows to update the geometry resulting from the stress field. That is, resulting cracks impacts the temperature field.

3.3.4.5 Dynamic Analyses

It is worth noting that the dynamic analyses can be performed using either an implicit or an explicit solver. In implicit analyses, the solution at each step is obtained through several

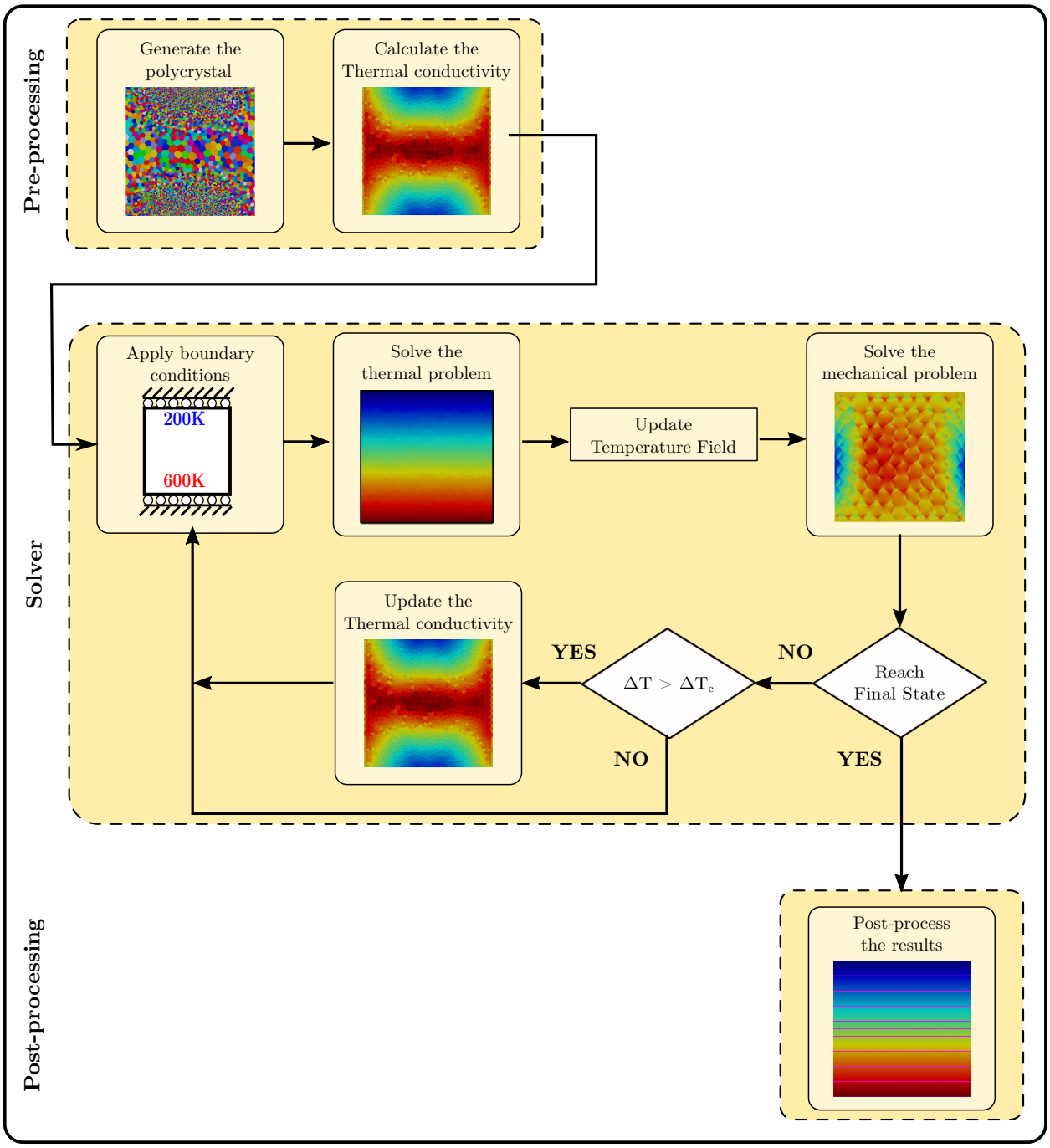

Figure 30: Flowchart for quasi-static and dynamic analyses.
Quasi-static solver: Polak–Ribière - Dynamic solver: Forward Euler.

iterations in order to establish the equilibrium within a specified tolerance. On the other hand, explicit analyses directly solve for the nodal accelerations. While each explicit step is relatively fast compared to the implicit solver, the time step in explicit analyses must be less than the Courant time step, i.e. the time it takes for the wave to travel across an element [89]. This constraint is a bottleneck for large problems, which is partially handled by the parallel implementation of the FEM code. A thorough comparison between those two different approaches can be found in [90].

The various analyses performed in this work use an explicit solver. Following the Courant condition, the value of the time step Δt is selected in order to avoid any stability issue. As a rule of thumb, the value of the time increment is deduced from the characteristic time of the considered problem such that

$$\Delta t \leq 0.1 \; t_c \tag{3.3.23}$$

In this thesis, two solvers are used to perform dynamic analyses. The thermal problems are solved using a forward Euler (FE) solver while the mechanical problems are solved through an explicit dynamic (ED) solver. As such, the flowchart for dynamic analyses is the same as the quasi-static one, presented in Figure 30, with the exception that the solvers used are different.

3.4 Continuum-level: Interface Element

In order to have a fully coupled thermomechanical model, both the thermal and mechanical analyses need to account for the influence of the grain boundary. Hence, interface elements can be inserted between bulk elements whose edges represent a grain boundary. Those elements are called Kapitza and Cohesive Zone elements, respectively for the thermal and mechanical models. It is worth noting that the selection of those elements is a challenging task, which is handled through some topological operators; including the concept of boundary and coboundary. While those operators have been implemented within the FEM code, technical details are not reported in this thesis. The readers should refer to [81], among

others.

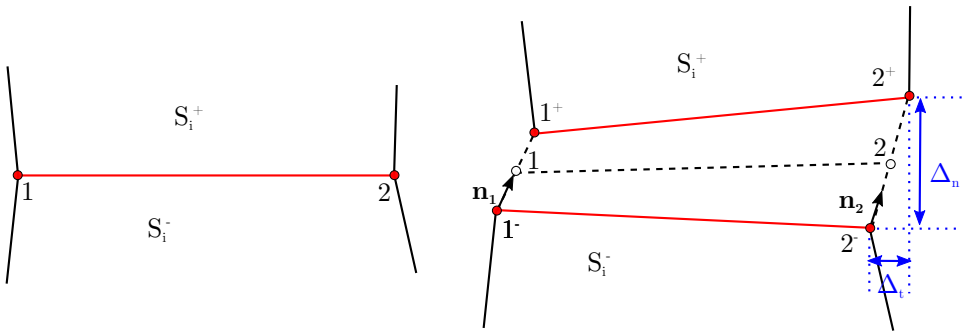

(a) Undeformed configuration (b) Deformed configuration

Figure 31: Opening of a two-dimensional interface element.

From a thermal perspective, the grain boundary induces a thermal resistance. Even for an undamaged material, Chapter 2 explained in details the existence of a boundary layer. As presented in the results of Chapter 4, the effect of the boundary layer can be lumped at the grain boundary, reinforcing the need for the Kapitza elements. Moreover, in the presence of damage, the Kapitza elements also account for the existence of cracks that reduce the thermal flux.

From a mechanical perspective, the grain boundary is the locus of intergranular cracks. This phenomenon is addressed using cohesive zone elements, which relate the stress in the grain boundary to the opening of the interface.

In order to better formulate the numerical implementation of both thermal and mechanical interface elements, the configuration and notation of a two-node elements for a two-dimensional problem is taken into consideration, as depicted in Figure 31.

3.4.1 Thermal Fracture

The interface term from Equation (2.4.25) can be discretized as

$$\int_{S_i^+} q_i^+(\delta T^+ - \delta T^-)d\mathrm{T} = \sum_{k=1}^{n_{el}} \int_{S_e^k} q_i^+ \delta[\![T]\!] dS \tag{3.4.1}$$

where S_e^k is the surface of element 'k' and $[\![T]\!]$ represents the temperature jump defined by

$$[\![\underline{T}]\!] = N_1(T_1^+ - T_1^-)\mathbf{n_1} + N_2(T_2^+ - T_2^-)\mathbf{n_2} \tag{3.4.2}$$

where N_1 and N_2 are the shape functions and $\mathbf{n_1}$ and $\mathbf{n_2}$ are the normal vectors to the element edges.

With this approximation, at any particular integration point, the normal and tangential components of the interface heat flux vector can be evaluated as

$$\mathbf{q} = (1 - d)\ \mathbf{D}\ [\![\underline{\mathbf{T}}]\!] \tag{3.4.3}$$

where d is the opening ratio, also known as the damage parameter and it is defined as

$$d = 0\ for\ \delta < \delta_c \tag{3.4.4}$$

$$d = \frac{\delta}{\delta_{max}}\ for\ \delta_c \leq \delta \leq \delta_{max} \tag{3.4.5}$$

$$d = 1\ for\ \delta_{max} \leq \delta \tag{3.4.6}$$

where δ is the opening of the corresponding cohesive element, δ_c is the critical opening and δ_{max} is the maximum opening, commonly defined as $\delta_{max} = 6\delta_c$. As a result, this methodology allows to model the change in thermal conductivity resulting from the nucleation of propagation of cracks. The heat flux through the crack is a linear function of the crack

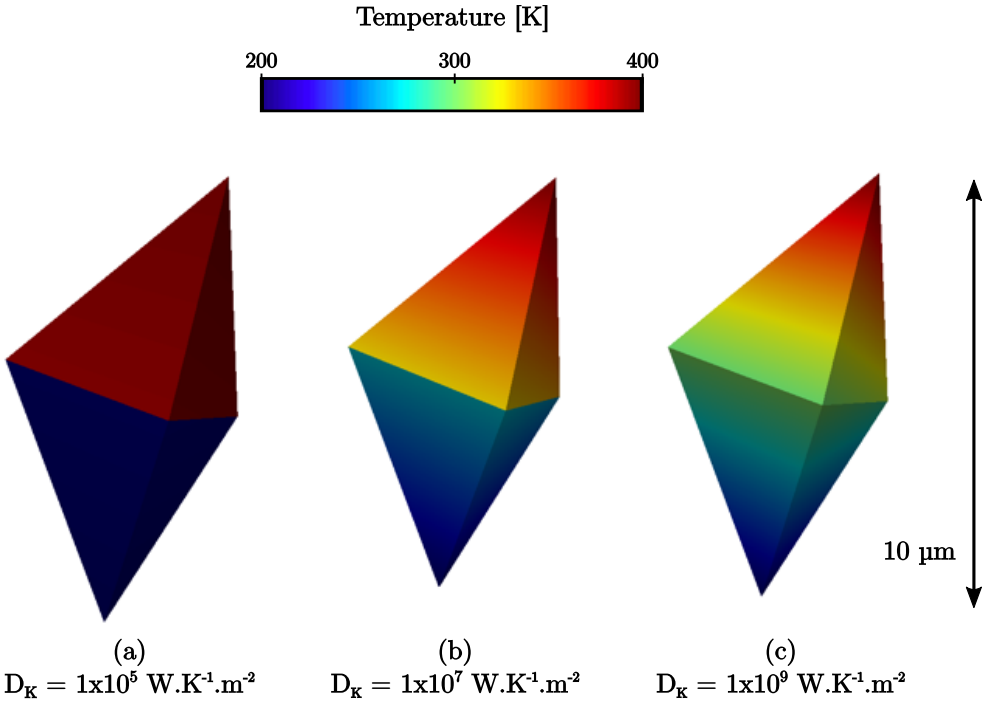

Figure 32: Influence of the Kapitza conductivity on the thermal field between two elements.

opening. When the crack is entirely opened, the heat is unable to propagate anymore.

The Kapitza resistances are also useful in the absence of cracks. Indeed, they allow to constrain the thermal conductivity at the microstructural features. For instance, imposing a different thermal conductivity at the interface elements than in the surrounding bulk elements will affect the temperature distribution.

Within the Kapitza element, the thermal flux is governed by the relation

$$\mathbf{q} = D_K \, [\![\underline{\mathbf{T}}]\!] = \frac{1}{R_K} \, [\![\underline{\mathbf{T}}]\!] \tag{3.4.7}$$

where D_K is the Kapitza conductance and R_K is the Kapitza resistance. An illustrative example of the influence of the value of D_K is given in Figure 32. As observed in Chapter 2, the size effect is significant at the grain boundary with the appearance of a boundary layer. This phenomenon can be captured through a Kapitza element. A thorough analysis of the usage of the Kapitza element is provided in Section 4.4.

3.4.2 Mechanical Fracture

In a similar manner, the interface term from Equation (2.4.27) can be discretized as

$$\int_{S_i^+} \mathbf{t}^+ (\delta \mathbf{x}^+ - \delta \mathbf{x}^-) dS = \sum_{k=1}^{n_{el}} \int_{S_e^k} \mathbf{t} \delta [\![\mathbf{x}]\!] dS \tag{3.4.8}$$

where $[\![\mathbf{x}]\!]$ represents the displacement opening and is composed of a normal and a tangential component expressed in the local coordinate system, such that $[\![\mathbf{x}]\!] = [\Delta_n, \ \Delta_t]$, as represented in Figure 31. The expression of $\mathbf{t} = [t_n, \ t_t]$ depends on the traction separation law.

Many laws have been developed over the years. Some most commonly used are the Xu-Needleman [92], the Smith-Ferrante [93], among others. An exhaustive comparison of the different traction-separation law can be found in [94]. In this work, a potential-based cohesive model of mixed-mode fracture, developed by Park, Paulino, and Roesler and known as the PPR traction-separation law, is used. The traction-separation constitutive relations of the PPR cohesive zone element are

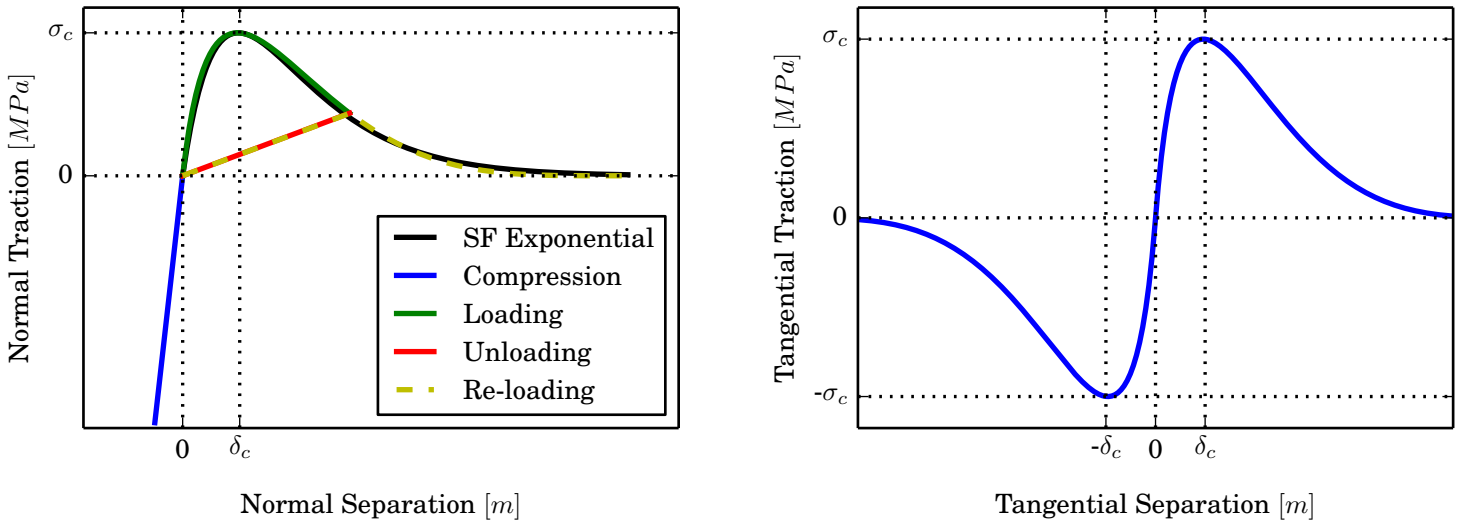

Figure 33: PPR Traction separation-law in 2D - after [91].

$$t_n(\Delta_n,\Delta_t)=\frac{G_n}{\delta_n}\left[m\left(1-\frac{\Delta_n}{\delta_n}\right)^{\alpha}\left(\frac{m}{\alpha}+\frac{\Delta_n}{\delta_n}\right)^{m-1}-\alpha\left(1-\frac{\Delta_n}{\delta_n}\right)^{\alpha-1}\left(\frac{m}{\alpha}+\frac{\Delta_n}{\delta_n}\right)^{m}\right]\left[G_n\left(1-\frac{\Delta_n}{\delta_n}\right)^{\alpha}\left(\frac{m}{\alpha}+\frac{\Delta_n}{\delta_n}\right)^{m}+\langle\Phi_n-\Phi_t\rangle\right]\frac{\Delta_n}{|\Delta_n|} \tag{3.4.9}$$

$$t_t(\Delta_n,\Delta_t)=\frac{G_t}{\delta_t}\left[n\left(1-\frac{|\Delta_t|}{\delta_t}\right)^{\beta}\left(\frac{n}{\beta}+\frac{|\Delta_t|}{\delta_t}\right)^{n-1}-\beta\left(1-\frac{|\Delta_t|}{\delta_t}\right)^{\beta-1}\left(\frac{n}{\beta}+\frac{|\Delta_t|}{\delta_t}\right)^{n}\right]\left[G_t\left(1-\frac{|\Delta_t|}{\delta_t}\right)^{\beta}\left(\frac{n}{\beta}+\frac{|\Delta_t|}{\delta_t}\right)^{n}+\langle\Phi_t-\Phi_n\rangle\right] \tag{3.4.10}$$

where G_n and G_t are the normal and tangential fracture toughness, δ_n and δ_t are the characteristic normal and tangential critical openings, m and n are non-dimensional exponents of the model, α and β are shape parameters characterizing the material softening responses, Φ_n and Φ_t are mode I and II fracture energies and the operator $\langle.\rangle$ is the Macaulay bracket. More details on the derivation as well as the relationships between the different parameters are provided in [91].

The representation of the traction separation in two dimensions is displayed in Figure 33.

3.4.3 Thermomechanical Coupling

Similarly to the bulk elements, the thermal and cohesive elements need to exchange some information. It is actually a one-way flow. Only the mechanical opening needs to be transferred to the Kapitza element in order to update the damage parameter d. This influences the thermal flux and thus the thermal field, as illustrated in Figure 34.

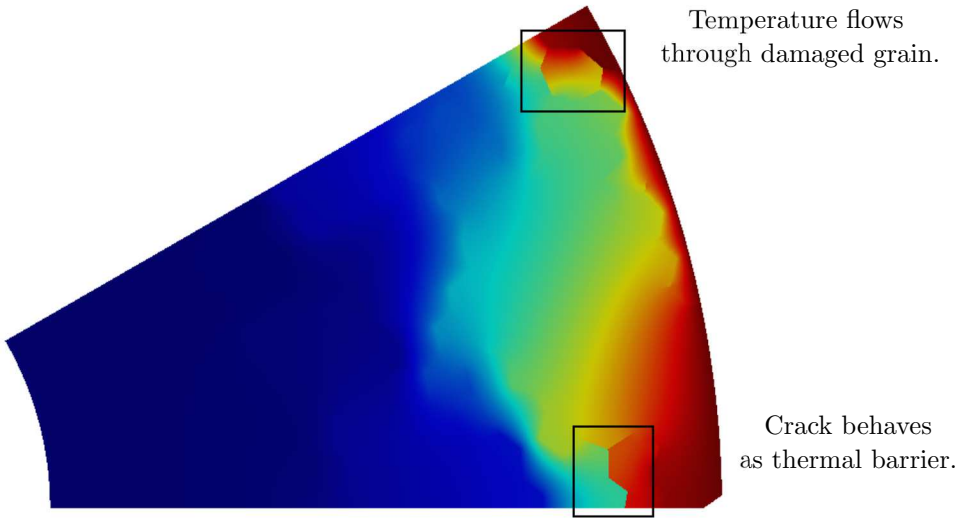

Figure 34: Full Thermomechanical coupling - Influence of cracks on the thermal field.

3.5 High Performance Implementation

The need for a High Performance Computing (HPC) framework comes from the heavy computational requirements of the simulations. As explained in the previous sections, in order to be consistent, a RVE requires several hundreds of grains. Furthermore, due to the localization phenomena near the grain boundary, each grain is composed of at least one hundred elements. Thus, most simulations considered in this work are made of several millions of degrees of freedom and simulations take weeks or months to converge, when running on a single processor.

To alleviate this restriction, the FEM code has been implemented in parallel using the

Message Passing Interface (MPI) framework. This implementation is qualified as distributed parallel computing, meaning that each processor owns its private memory. Thus, nodes on the edges of a partition are duplicated, and a significant amount of data is exchanged between the processors by passing messages. The integration of this framework into the modeling flow is succinctly summarized in this section. A description of the added classes can be found in Annex A. The sequence of the successive steps is described in the flowchart provided in Figure 35. The different processes within the HCP framework are outlined in the next subsections.

3.5.1 Mesh Generation and Subdivision

The primal mesh is generated as a random mesh, with elements having the appropriate aspect ratio. Different methodologies can be used to achieve the desired result. For instance, the primal mesh can be generate using a probability function distribution and then optimize to obtain a mesh of higher quality, as explained in [95]. Once this primal mesh is obtained, the polycrystalline structure is generated by following a procedure similar to the one proposed in [85] with the only difference that a dual based on the discrete Hodge operator [96] is adopted instead of a barycentric one. In this way, the grain boundary energy relaxation step is removed. This grain generation technique requires, as initial data, the location of the centers of each grain that are given by the primal mesh. As a result, an explicit representation of the microstructure of the optimized material is obtained.

Once the polycrystal is defined, the mesh needs to be refined. A new subdivision technique has been implemented in the 'in-house' FEM code. Indeed, the initially exciting barycentric subdivision produces elements of poor quality which impact the FE solutions for highly refined meshes. Instead, the so-called '8-subtetrahedron' subdivision [87] is adopted, for which the successive subdivisions produce a maximum of three different tetrahedra. The difficulty of this implementation lies in updating the connectivity matrix by using only the topological information. A comparison of those two subdivision techniques, in three dimensions, is provided in Figure 36.

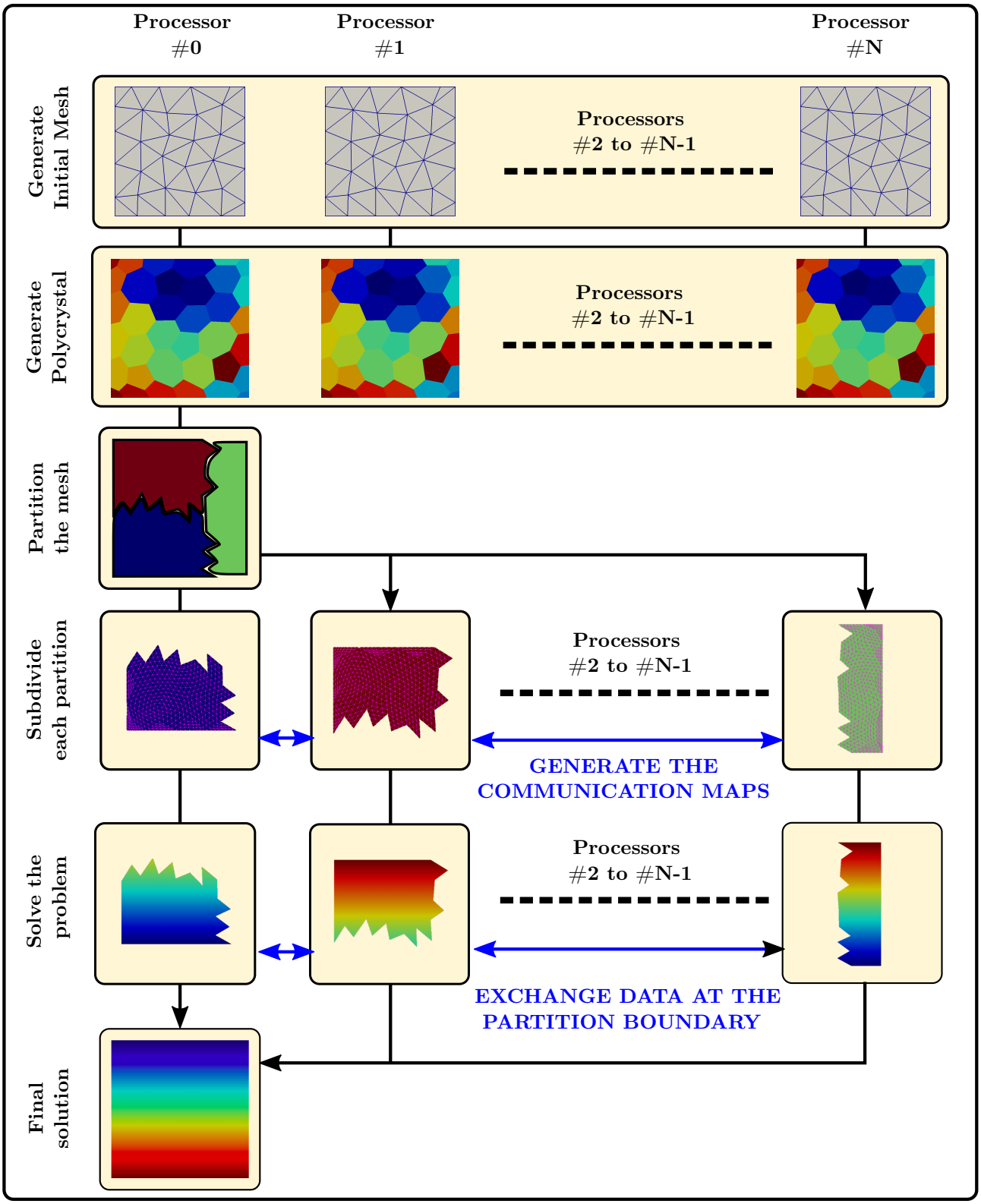

Figure 35: Framework of the High Performance Computing process.

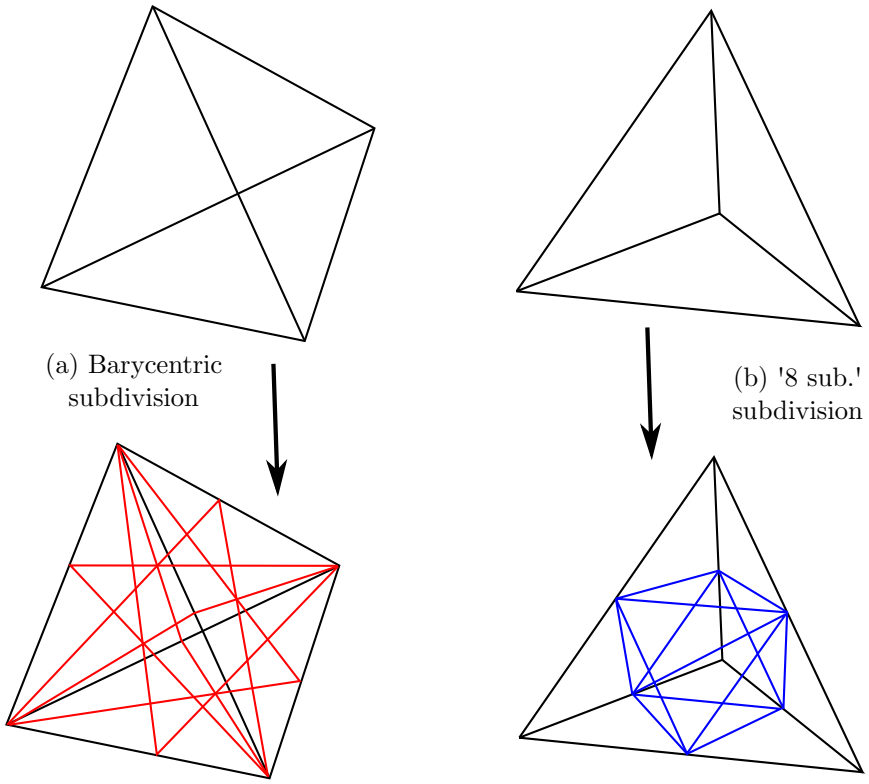

Figure 36: Barycentric vs '8-subtetrahedron' subdivisions in 3D.

Under those circumstances, the mesh quality is preserved, as highlighted in Figure 37. The top row represents the barycentric subdivision, and the bottom row represents the '8-subtetrahedron' subdivision. While the initial mesh (with one subdivision) presents a better aspect ratio with the barycentric technique, the increasing number of subdivision deteriorates the quality of the elements. As such, the average aspect ratio after four barycentric subdivisions is over 3. On the other hand, the quality of the mesh is unaffected by the subdivisions in the case of the '8. sub.' technique. Therefore, it allows to obtain a converged solution, using a fine mesh of high quality. This subdivision technique is utilized in every case studied in this thesis.

In the FE implementation, during the subdivision process, each smaller elements need to keep the information about the grain to which it belongs and thus the subsequent maps need to be updated.

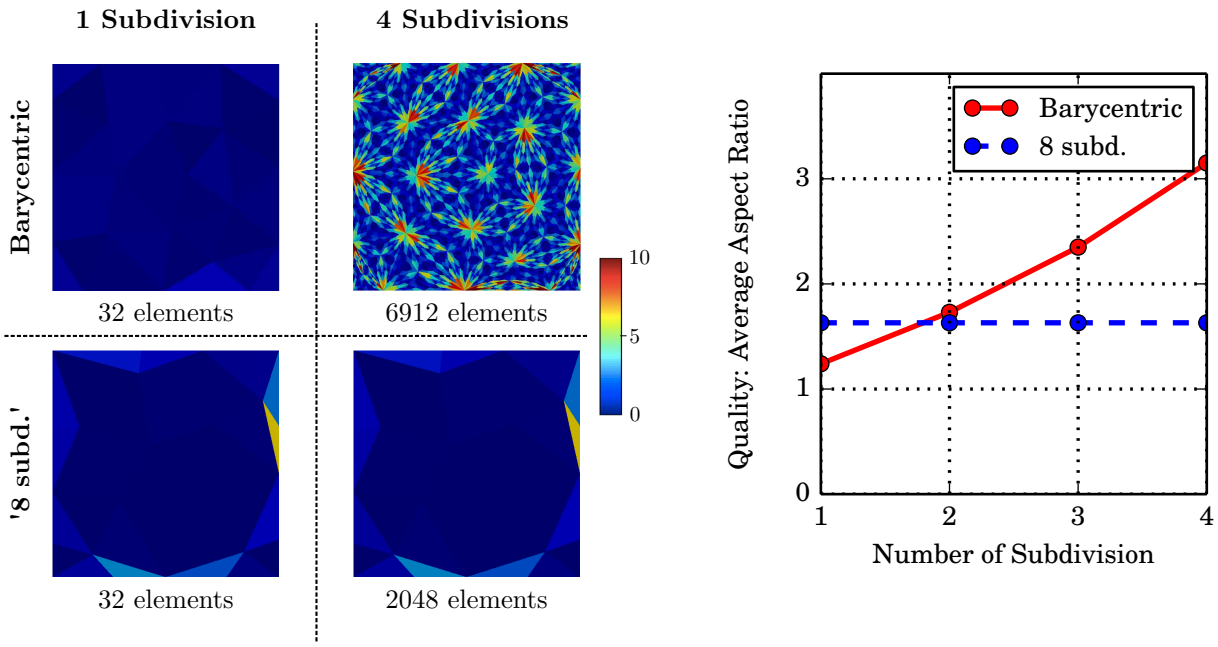

Figure 37: Comparison of mesh quality (as aspect ratio)
between barycentric and regular subdivision techniques - in 2D.

3.5.2 Partitioning

The partitioning of the mesh is done using Metis: a C library for graph partitioning that implements various multilevel algorithms. Several options are present in the library to obtain the desired optimal partitioning. For the HPC framework, the objective is to minimize the overall computational time. This goal leads to a trade-off between the communication and calculation times. Too small partitions have a communication time that is not negligible with regards to the computational time. One way of optimizing the communication time is to generate contiguous partitions, as depicted in Figure 38. Indeed, contiguous partitions tend to minimize the number of communications between partitions.

The insertion of interface elements is also a key partitioning challenge; as some of those elements are in–between partitions. It requires different schemes depending on the type of cracks considered. In any case, interface elements on the border of a partition require the introduction of a ghost layer. This ghost layer corresponds to the storage of nodes that are owned by neighboring partitions. In the case of interface elements on the edge of two partitions, the partition owning the element needs to know all the nodal data belonging to

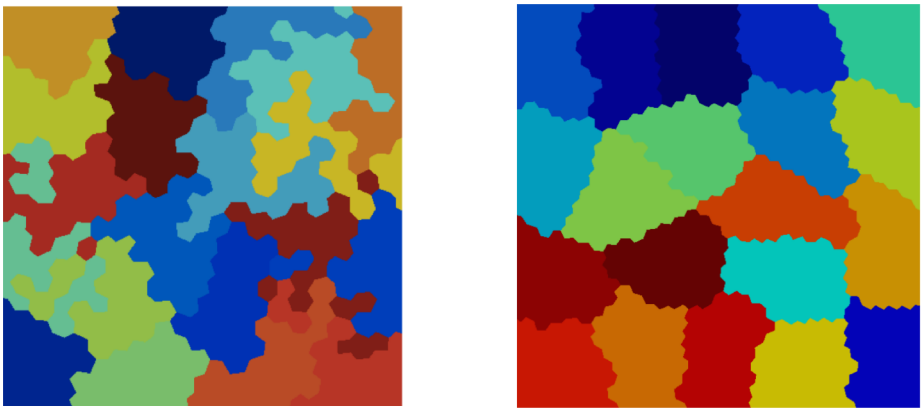

(a) Non-contiguous partitioning (b) Contiguous partitioning

Figure 38: Non-contiguous vs contiguous partitions in 2D.

the element on the other partition. Thus, those nodes are duplicated again. A representation of the ghost layer is provided in Figure 39. It is worth mentioning that partitioning schemes of models containing only intergranular interface elements are better suited for a partitioning on the primal mesh, as it prevents grains to be cut between different partitions.

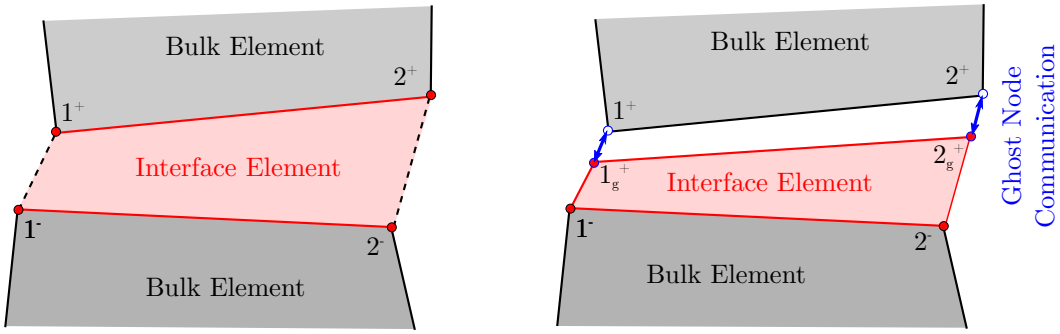

(a) Interface element within a single partition.

(b) Interface element between two partitions.

Figure 39: Interface elements - Ghost node concept.

3.5.3 Communication Scheme

The HPC implementation is realized through the Message Passing Interface (MPI) protocol. This standardized and portable message-passing system defines the syntax and semantics of a core of library routines useful to develop portable and scalable large scale parallel applications. Details on the MPI protocol can be found in [97], among others.

The initial architecture of the 'in-house' FE code is an inherent obstacle to the parallel implementation of the code. Indeed, all the properties are stored using maps whose keys are physical memory addresses. This feature becomes a serious handicap during the parallel implementation process on distributed memory. Indeed, it leads to more complex communications between duplicated nodes as those nodes have different memory addresses and each cluster gets only access its own memory.

To overcome this limitation, new maps linking the memory addresses to some unique identification numbers have been implemented. Different schemes have been designed in order to account for the different types of duplication. The detail of those schemes is not presented in this thesis.

3.5.4 Parallel Solvers

Throughout this work, the need for an HPC framework requires parallelizing the different solvers used. For each partition, the solver is run following the same flow as for a serial implementation. However, before the end of each iteration, the 'forcing terms' on duplicated nodes have to be summed up in order for the duplicated nodes to have the same states. In this subsection, the operation flow performed by the different solvers is explained and presented in the algorithms detailed at the end of this chapter. It is worth noting that the operations behind the communications between partitions depend on the considered problem. For instance, in the presence of cracks, the communication and reduction steps need to be performed in a particular order starting from the ghost layer.

3.5.4.1 Polak–Ribière Solver

The Polak–Ribière solver is a nonlinear conjugate gradient method. That is, it generalizes the conjugate gradient method to nonlinear optimization. The conjugate gradient method is often implemented as an iterative algorithm. It is especially useful in the case of sparse systems that are too large to be handled by a direct implementation.

In this work, the Polak–Ribière solver is the sole solver used to solve static or quasi-static problems. While direct solvers inverting the matrix K are available, matrix inversion appears to be a computationally expensive operation, compared to matrix multiplication. Hence, iterative methods (such as the Polak–Ribière solver) are a better-suited approach. This choice is also based on the implementation convenience of the parallel implementation and on its efficiency. The solver implementation is presented in Algorithm 1.

The Polak–Ribière solver necessitates the calculation of several mathematical operators such as dot products or forcing term products, among others. To prevent the obtained solution to be dependent on the number of procedure, the methodology ensures that the duplicated and ghost nodes are correctly accounted for. Thus, the communications between partitions are more complex than simply summing up the forcing terms.

3.5.4.2 Forward Euler Solver

The Euler method is a first-order numerical procedure for solving ordinary differential equations with a given initial value. It uses the formula

$$y_{n+1} = y_n + hf(x_n, y_n) \tag{3.5.1}$$

Thus, the solution y advances from x_n to $x_{n+1} = x_n + h$. This method increments a solution through an interval h using derivative information calculated only at the beginning of the interval. This method is the simplest RungeKutta method and it often serves as the basis to construct more complex algorithms. Nevertheless, the accuracy and the stability of this method is reasonable as long as the Courant stability condition is fulfilled. Its error is in the order of $O(h^2)$. The solver implementation is presented in Algorithm 2.

3.5.4.3 Explicit Dynamic Solver

The dynamic solver is used to obtain numerical approximations to the solutions of time-dependent differential equations, like the ones considered in this thesis. The solver implementation is presented in Algorithm 3.

3.5.5 Implementation Validation and Scalability Analysis

3.5.5.1 Implementation Validation

The validation of the HPC framework has been performed with a variety of intermediary steps throughout the development of the different classes. Among others: simple cases of few elements coupled with comparisons to analytical solutions or results from Abaqus have been used during the implementation of the code and for testing purposes. The final validation has been obtained on larger models by running them both in a serial and in a parallel manner. The success of the parallel implementation is achieved as the solution, and the iterative errors are the same (up to computer accuracy) for every iterative step of the analysis.

3.5.5.2 Scalability Analysis

Simulations considered in this work have been shown to incorporate a very large number of degrees of freedom; up to tens of millions. Hence, the computational power needed to solve those simulations is significant. The HCP parallel implementation is the key to overcoming the limitation of sequential programming. Ideally, the additional processors scale up linearly. That is, doubling the number of processors should half the run time of the program. However, this objective can be difficult to achieve. For instance, communications between partitions require extra operations that impact the overall computational time.

In parallel computing, two measures of the performance are generally encountered in the literature: the speed–up S and the efficiency E. The underlying goal is to compare the performance of the parallel implementation to the serial one. The speed–up measures the overall performance gained by running the code with a parallel implementation. For n processors, it is given by

$$S_n = \frac{t_1}{t_n} \tag{3.5.2}$$

where t_i represents the time to run a specific problem using i processors. Efficiency measures how well each processor is utilized. It is defined as

$$E_n = \frac{t_1}{n\ t_n} = \frac{S_n}{n} \tag{3.5.3}$$

The estimation of the performance of the implementation is provided through a simple thermal example with constant thermal conductivity to which boundary conditions are imposed at the top and bottom. Figure 40 presents the speed–up and the efficiency of this problem. Three different meshes are analyzed: (a) coarse with 865 dof, (b) medium with 101,440 dof, and (c) fine with 489,616 dof. As expected the computation does not scale linearly for a large number of processors. It is worth noting that the efficiency is better for larger problems. Indeed, each partition still carries a significant amount of calculations, which dominates over the communication time. On the other hand, the performance of the parallel implementation for the small case degrades quickly as the communication between processors is actually taking more time than the calculations. The solver-time of the different configurations is recorded and displayed in Table 3.

During the implementation, the performances have been optimized by using the profiler Allinea Map, that identifies the MPI bottlenecks. The choice of the C++ and MPI standards also alters the performance of the FE code. For the cluster used to solve the simulations, the best combination is to select the intel compiler (over gcc) and the mvapich implementation of MPI.

Table 3: Parallel Implementation Analysis - Solver Time (in seconds).

		Number of processors								
Model	**dof**	1	2	4	8	16	32	64	128	256
Small	865	2.26	1.15	0.59	0.33	0.17	1.8	6.5	10.5	11.5
Medium	101,440	6,613	3,517	1,672	836	469	229	143	220	153
Large	489,616	59,269	32,987	15,802	7,448	4,156	2,394	1,472	685	463

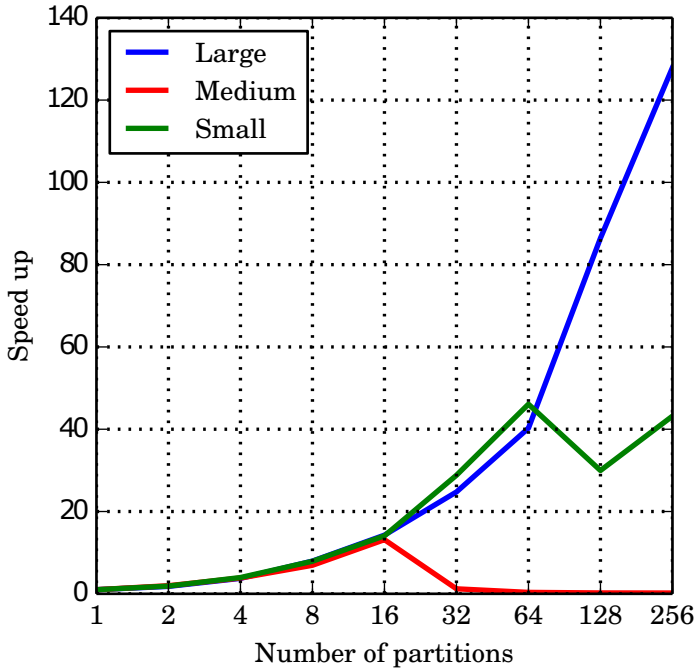

(a) HPC speed-up measurement

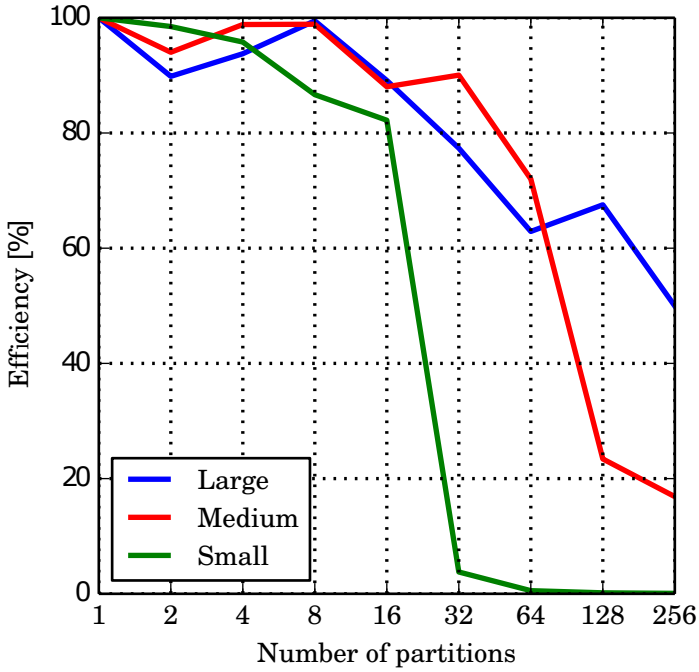

(b) HPC efficiency measurement

Figure 40: Scalability Analysis of the HCP parallel implementation.

Algorithm 1 Parallel non-linear conjugate gradient solver.

1: **procedure** PR(x, force function DE(), max iter N, tol T, small number ϵ)
2: $\alpha \leftarrow \beta \leftarrow dr \leftarrow 0$
3: $f \leftarrow DE(x)$
4: Update communication matrix with f on the partition boundaries
5: Send force vectors to other partitions ▷ MPI_Isend
6: Receive force vectors from other partitions ▷ MPI_Irecv
7: Wait for communications to complete ▷ MPI_Waitall
8: Assemble forces at the partition boundaries
9: $f_n \leftarrow f$
10: $d \leftarrow f$
11: **for** k ∈ [0,N] **do**
12: $x \leftarrow x + \epsilon d$
13: $df \leftarrow \frac{(DE(x)-f).d}{\epsilon}$
14: Update communication matrix with df on the partition boundaries
15: Send force vectors to other partitions ▷ MPI_Isend
16: Receive force vectors from other partitions ▷ MPI_Irecv
17: Wait for communications to complete ▷ MPI_Waitall
18: Assemble forces at the partition boundaries
19: $\alpha \leftarrow \frac{fd}{df} - \epsilon$
20: $x \leftarrow x + \alpha.d$
21: $f_n \leftarrow DE(x)$
22: Update communication matrix with f_n on the partition boundaries
23: Send force vectors to other partitions ▷ MPI_Isend
24: Receive force vectors from other partitions ▷ MPI_Irecv
25: Wait for communications to complete ▷ MPI_Waitall
26: Assemble forces at the partition boundaries
27: $Error \leftarrow \|f_n\|$
28: **if** (Error ≤ T) **then**
29: Update Local State
30: break
31: **end if**
32: $\beta \leftarrow \frac{f_n(f_n-f)}{r^2}$
33: **if** ($\beta \leq$ T) **then**
34: $\beta = 0$
35: **end if**
36: $d \leftarrow f_n + \beta d$
37: $f \leftarrow f_n$
38: **end for**
39: **end procedure**

Algorithm 2 Parallel Forward Euler solver.

```
1: procedure FE(x, force function DE(), dt, m, t_f)
2:     for t ∈ [0,t_f] do
3:         f ← DE(x)
4:         Update Communication Matrix with values of f on the partition boundaries
5:         Send force vectors to other partitions                    ▷ MPI_Isend
6:         Receive force vectors from other partitions               ▷ MPI_Irecv
7:         Wait for communications to complete                       ▷ MPI_Waitall
8:         Assemble forces at the partition boundaries
9:         x ← x − dt.f/m
10:        Update Local State
11:    end for
12: end procedure
```

Algorithm 3 Parallel Explicit Dynamic solver.

```
1: procedure ED(x, v, force function DE(), dt, m, t_f)
2:     for t ∈ [0,t_f] do
3:         f ← DE(x)
4:         Update Communication Matrix with values of f on the partition boundaries
5:         Send force vectors to other partitions                    ▷ MPI_Isend
6:         Receive force vectors from other partitions               ▷ MPI_Irecv
7:         Wait for communications to complete                       ▷ MPI_Waitall
8:         Assemble forces at the partition boundaries
9:         a ← −f/m
10:        v ← v + dt.a
11:        x ← x + dt.v + 1/2.dt^2.a
12:        Update Local State
13:    end for
14: end procedure
```

CHAPTER IV

VALIDATION AND RESULTS

The novel numerical framework presented in Chapter 3 permits to express the thermal properties of polycrystalline materials derived in Chapter 2. In this chapter, different specific features obtained from this multiscale approach are highlighted. Among others, the presented results include: (a) the evaluation of both in-plane and cross-plane thermal conductivities in thin films, (b) the recovery of the full anisotropic thermal conductivity tensor for crystal, (c) the optimization of the polycrystalline microstruture to tailor the thermal properties, and (d) a comparison of the different thermal grain boundary resistance.

4.1 Size-dependent Heat Transfer

4.1.1 Thin Films: In-plane and Out-of-Plane Thermal Conductivity

In this subsection, both the in-plane and cross-plane thermal conductivities of a silicon thin film are calculated. Several studies have addressed the differences between those two orthogonal directions of the thermal conductivity [55, 98, 99, 100]. However, the prediction methods vary. While accurate analytical models exist for the in-plane thermal conductivity, the cross-plane thermal conductivity is usually numerically evaluated by using stochastic methods such as Discrete Ordinate or Monte Carlo methods [55, 56, 101]. The few existing analytical models are based on multiple simplifications and produce limited results [100]. This difference in methodology lies in the nature of the heat transfer. Albeit the in-plane thermal conductivity is diffuse, the cross-plane thermal conductivity is considered to some extent ballistic.

The film depicted in Figure 41 is under consideration. The length l of the film is along the x-direction while the height h of the film is along the z-direction. The film is supposed infinite in the y-direction as well as infinite in the x-direction by assuming the condition

$l \gg h$.

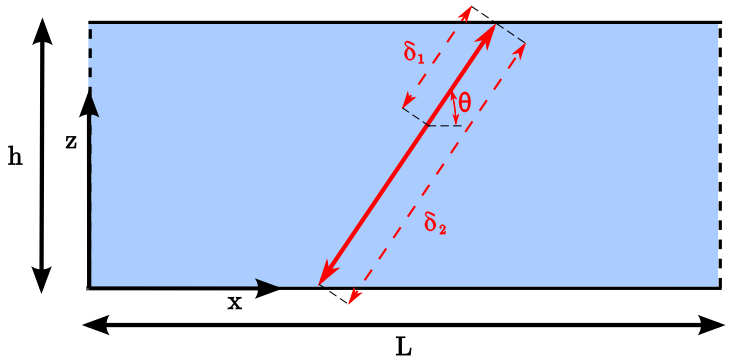

Figure 41: Schematic of thin film considered for length-dependent thermal conductivity.

The length-dependent model leads to the correct prediction of the in-plane and cross-plane thermal conductivity. The validity of this approach is highlighted by modeling two different film thicknesses: $h = 20nm$ and $h = 100nm$. Both values are above the acoustic thin limit. As in previous calculations, the silicon film is assumed to be isotropic in the reciprocal space. The physical properties are those of bulk silicon along the [100]-direction. Those properties are computed from available measurements [102, 103].

The specularity p in the expression (2.3.12) is obtained from the choice of the RMS deviation of the surface η. This free variable is determined by fitting the calculation to the in-plane thermal conductivity from experimental data and it is kept constant for the related cross-plane thermal conductivity. Thus, the local equilibrium approximation is required to apply to both cases. This formulation assumes the characteristic dimensions of the system to be large enough such that most phonons collide with each other or with defects inside the medium before reaching the boundary.

Finally, to obtain an effective thermal conductivity, the symmetry implied by the thin film geometry is taken advantage of and the thermal conductivity value is averaged from several calculations across the thickness of the film. Results are plotted in Figure 42 where both numerical models as well as experimental measurements and computational estimations are shown. The calculated thermal conductivities are in good agreement with the experimental and numerical data available in the literature [55, 107]. It is worth noting that most experimental estimations of the thermal conductivity at microscale are obtained

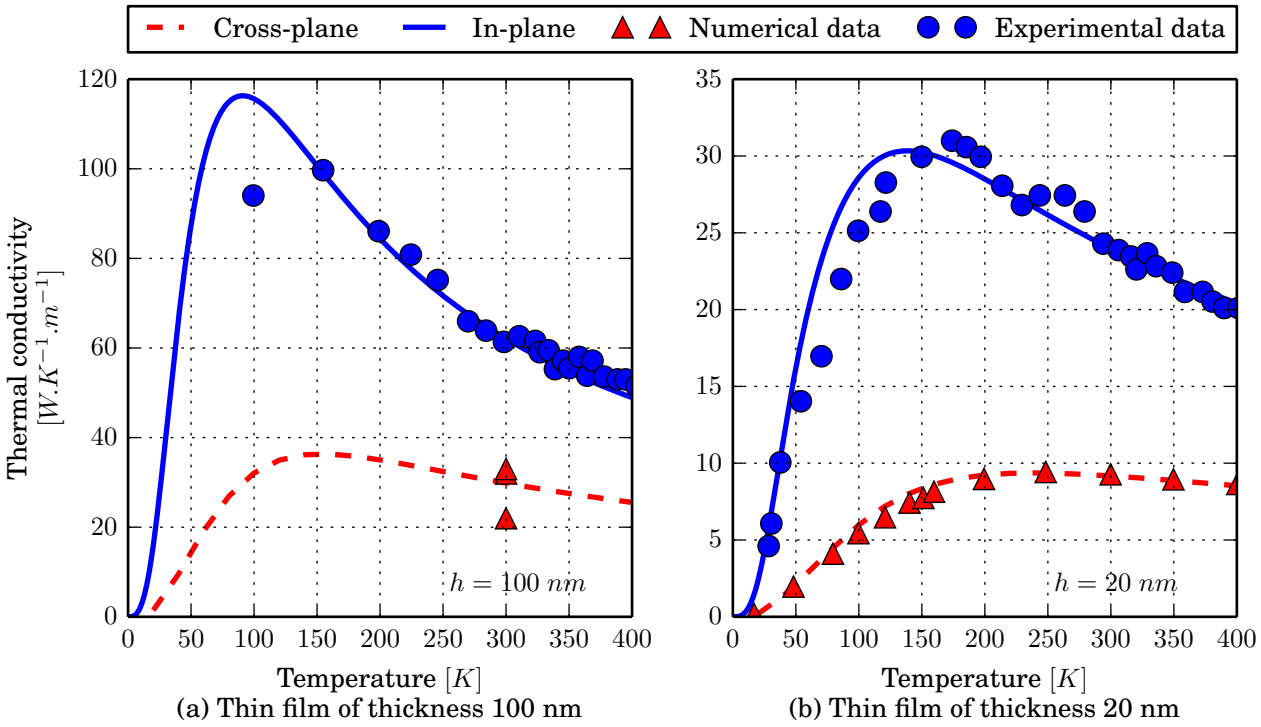

Figure 42: In-plane and cross-plane thermal conductivity of silicon thin films. Reference data: $\triangle$: (a)[55, 101, 98], (b)[55, 101, 104] - o : (a)[105, 106], (b) [105, 106].

using electrical-resistance thermometry, also known as resistance temperature detectors [105]. Those sensors evaluate the temperature fields and provide an accurate measure of the thermal resistance and, by extension, of the thermal conductivity. Through this analysis, the size dependence is fully established. For instance, at room temperature, the in-plane thermal conductivity varies from $D = 63\ W.K^{-1}.m^{-1}$ for $h = 100nm$ down to $D = 24\ W.K^{-1}.m^{-1}$ for $h = 20nm$, for a 61.9 % reduction. Same noticeable variations are obtained for the cross-plane thermal conductivity.

Thus, the model is able to predict both values of the thermal conductivity over a wide range of temperatures and for multiple film thicknesses, while adopting a unique set of material parameters. There are no such calculations reported in the literature predicting simultaneously both the in-plane and cross-plane thermal conductivities in thin films. Finally, the comparison between both directions shows that the cross-plane thermal conductivity is noticeably smaller than the in-plane one. This highlights the existence of a significant

anisotropy within the film and it provides evidence that a similar effect should be observed on silicon grains.

4.1.2 Nanowires: Axial Thermal Conductivity

The thin film previously considered limits the phonon propagation in only two directions. The nanowire case offers more constraints by allowing for the free displacement of phonons along the axial direction only. This added limitation allows to test the validity of the model within a more restricted environment. The geometry presented earlier in Figure 17 is under study in the present subsection. With the same framework allowing to calculate the distance δ_1 and δ_2, the value of the axial thermal conductivity is calculated for different diameter values of a nanowire made of silicon. The results as a function of the temperature are presented in Figure 43. The obtained values are compared against experimental results [108]. The match between both sets of results is evident. This analysis validates the implemented model in the case of a single free direction of phonon propagation. The next step is to consider the case of a grain, for which all directions of propagation are limited.

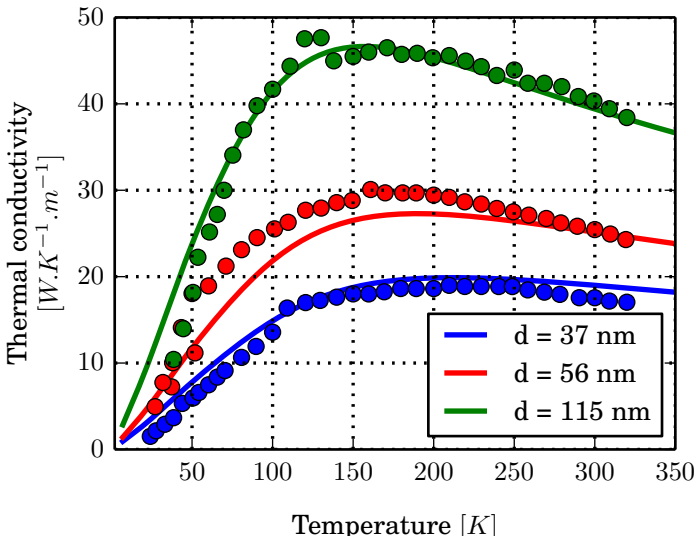

Figure 43: Thermal conductivity of nanowires for different diameters d.
Line: Numerical Estimations - Dot: Experimental data.

4.1.3 Micro-grain Thermal Conductivity

In this subsection, the prediction of the local thermal conductivity inside a silicon micro-grain of arbitrary shape, as the one depicted in Figure 44, is achieved. To highlight the length-dependent effect, the grain size is chosen on the order of a few mean free paths. Calculations are performed around room temperature, for T=300K. The study of micro-grains is of particular interest as the model does not require any fitting to the experimental data due to the fact that the specularity parameter p is null [109].

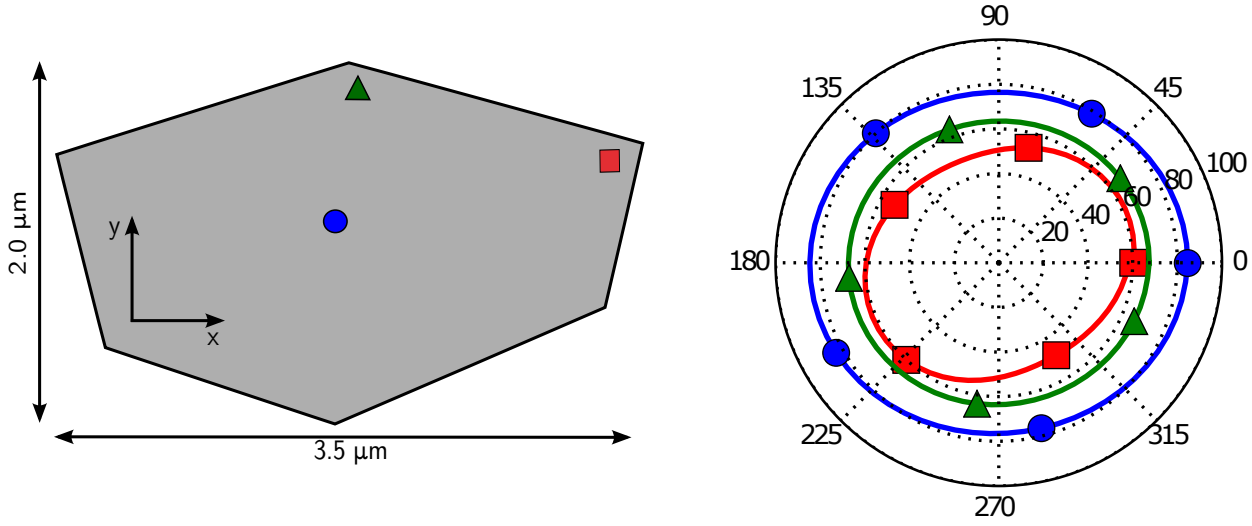

(a) Grain schematics

(b) Polar plot of the thermal conductivity

Figure 44: Direction-dependent thermal conductivity for a silicon micro-grain.

Instead of computing the thermal conductivity for only one or two directions as for, respectively, the nanowire and the thin film cases, the procedure is repeated for several different directions of the thermal gradient. The obtained values **D** are plotted on a polar plot. Figure 44b depicts the values obtained for three different points highlighted on the grain schematics, see Figure 44a. The three points present drastically different thermal conductivity representations. At the center point, the thermal conductivity is the largest and almost isotropic, with a slight increase (7.8%) in the value corresponding to the x-direction in which the grain is more elongated. At points 2 and 3, the value of the thermal conductivity decreases significantly due to the reduction of the phonon mean free paths

(the distance between the emitted phonon and the grain boundary becomes very short). Another interesting observation is that the thermal conductivity is highly anisotropic at points where the reduction of the phonon mean free path is much more important in one direction than in the others. The difference in pattern for each point inside the crystal highlights the existence of strong variations not only on the mean value of the thermal conductivity but also on its anisotropy.

By fitting the obtained values of the thermal conductivity $\mathbf{D}$ to an ellipse, the principal values and directions of the thermal conductivity tensor $\mathbf{D} = D^{ij}\mathbf{e_i}\mathbf{e_j}$ can be determined. For example, Figure 45 shows the values of: (a) D_{xx} and (b) D_{yy} for the entire domain of the grain. The values of these components are larger at the center of the grain and decrease as the emission point approaches the grain boundaries. Also, due to the elongation of the grain in the x-direction, the values of D_{xx} are overall larger than the values of D_{yy}, showcasing the previously mentioned anisotropy. In addition, these plots reveal the existence of a homogenized length-dependent effect due to the presence of a boundary layer that develops close to the grain boundaries. The larger the grain boundary becomes the smaller is the relative size of such boundary layer, rendering at some point the homogenized length-dependent effect negligible.

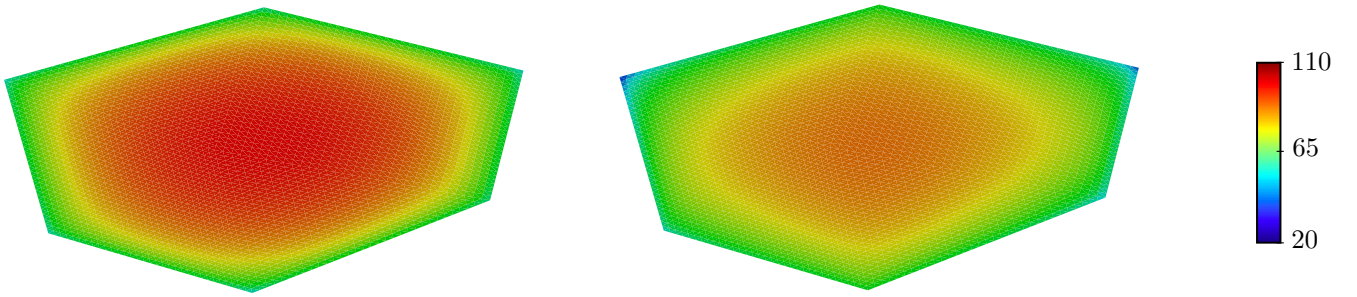

(a) Component D_{xx} (b) Component D_{yy}

Figure 45: Full-domain calculations of length-dependent thermal conductivity.

The previous results highlight a key component of the concurrent multiscale approach: by repeating this procedure at each quadrature point within the domain, an accurate length-dependent value of the full thermal conductivity tensor is provided, which is then utilized as material data by the continuum-level thermomechanical model.

In order to better understand the influence of the grain size on the thermal conductivity, a grain size represented by a regular hexagon, as presented in Figure 26 is considered. In this particular case, the thermal conductivity tensor is considered as a scalar. This approximation is legitimate as all the direction have a similar length. The thermal conductivity scalar D as a function of the grain size is calculated and results are presented in Figure 46.

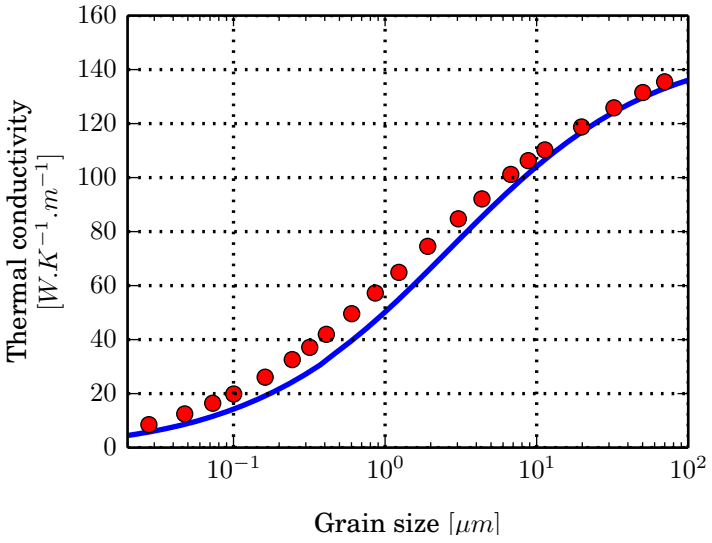

Figure 46: Size-dependent thermal conductivity for silicon.

Based on those results, the grain size highly influences the thermal conductivity value. Thus, when considering a polycrystal made of thousand of grains, the distribution of the grain can be of prime importance. This aspect is studied in the next subsection.

4.1.4 Heat Transfer in Graded Polycrystals

In this section, the problem of heat transfer in functionally graded silicon polycrystals is studied. For the sub-grain model, the same material properties as in the previous example of the silicon grain are adopted. The density and specific heat capacity are considered constant at: $\rho = 2329kg.m^{-3}$ and $Cp = 712J.kg^{-1}.K^{-1}$. The domain of analysis consists of a 30μm by 90μm rectangle with grains varying in size from $0.\mu$m to 10μm, see Figure 47. The model is composed of $2,314$ grains, having 24 elements each for a total of $52,552$

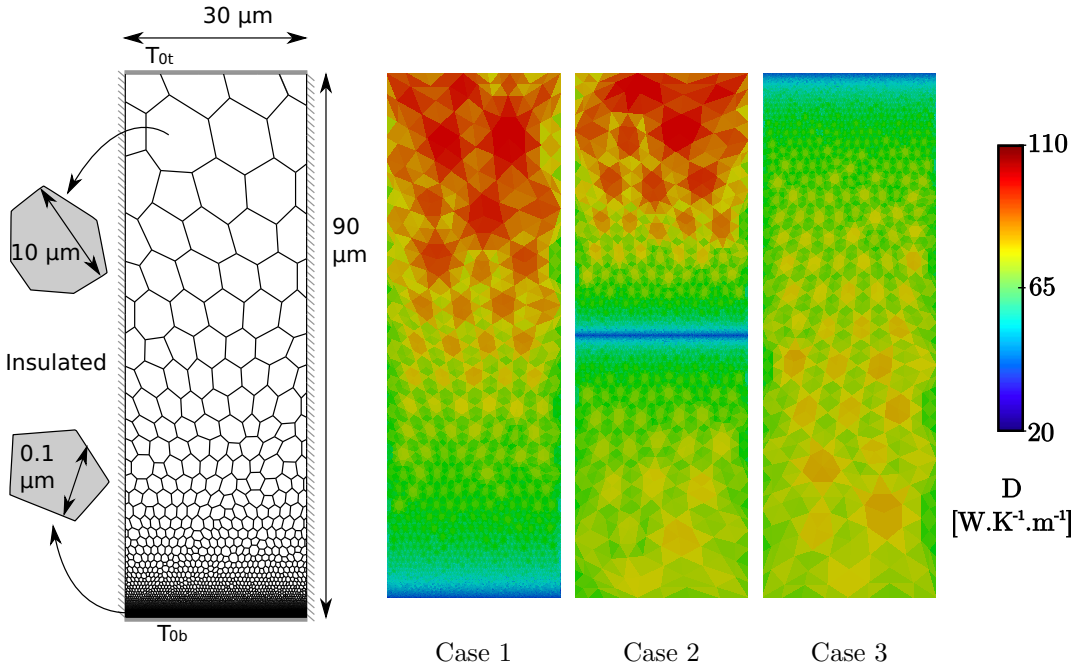

Figure 47: Schematics and computational domains for the 3 cases under study. Mesh coloring represents value of thermal conductivity at steady state.

3-node linear triangles. The specimen is insulated on the longest edges, and a constant temperature is applied at both end boundaries: $T_b = 420K$ is at the bottom boundary and $T_t = 320K$ is at the top boundary. The grain size varies linearly along the longest direction of the rectangle, and 3 cases are considered

1. smaller grains at the bottom boundary.

2. smaller grains at the center of the domain.

3. smaller grains at the top boundary.

For the grain sizes considered in the model ($0.1\mu m < d < 10\mu m$), the boundary Kapitza contribution in the polycrystal effective thermal conductivity is negligible [27], thus Kapitza resistance is not being accounted for.

The macroscopic thermal gradient is constrained by the temperature boundary condition along the vertical direction of the rectangle, which gives a particular importance to this specific component of the thermal conductivity tensor $\mathbf{D}$. As such, the macroscopic

thermal conductivities are fitted to that single value and an isotropic thermal conductivity tensor is assumed. The regular non-elongated shape of the grains in the graded polycrystal does not show any pronounced anisotropy, reinforcing the choice for an isotropic thermal conductivity. As a reminder, the thermal conductivity is function of temperature. Consequently, as the heat transfer evolves from its initial condition to the steady state, the thermal conductivity needs to be adjusted to account for the temperature evolution. Thus, the steady-state analysis becomes non-linear and an iteration scheme must be implemented to obtain the convergence of both thermal conductivity and temperature distribution. In that situation, the used quasi-static framework is the one presented in Figure 30.

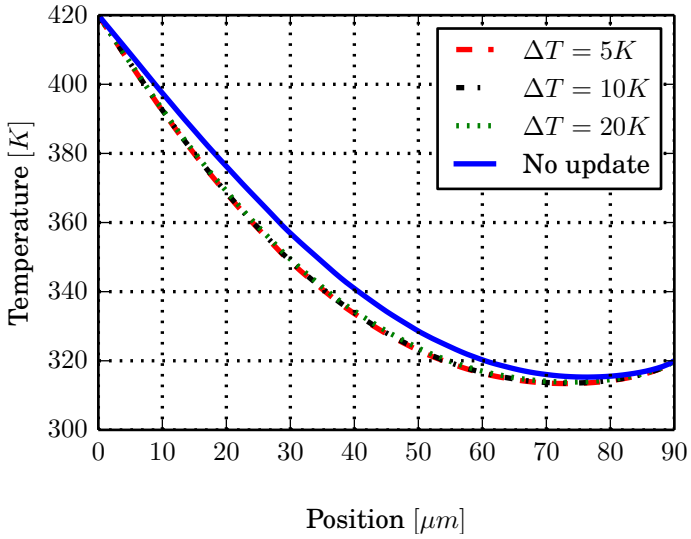

Figure 48: Convergence analysis.

For dynamic analyses, time integration is performed based on a forward Euler time marching scheme, as explained in Algorithm 2. The dynamic analysis requires to recalculate the thermal conductivity during the simulation. However, computing the thermal conductivity at each time step is computationally expensive and unnecessary. This framework updates the thermal conductivity at a quadrature point if the locally attained temperature change is higher than a predefined threshold ΔT. The choice of the threshold value ΔT is obtained through a convergence analysis, as depicted in Figure 48. Convergence is studied based on the temperature distribution achieved up to a chosen time step. For the

chosen time-step, the maximum temperature difference between simulations is obtained at a distance $y = 26.1\mu m$ from the bottom edge. The temperatures for the 4 cases are : (a) $\Delta T = 5K$: $T = 356.00K$, (b) $\Delta T = 10K$: $T = 356.23K$, (c) $\Delta T = 20K$: $T = 358.40K$, (d) No update: $T = 364.32K$. The difference between $\Delta T = 5K$ and no update is 8.32% while it is only 0.23% between $\Delta T = 5K$ and $\Delta T = 10K$. Thus, the rest of the calculations are

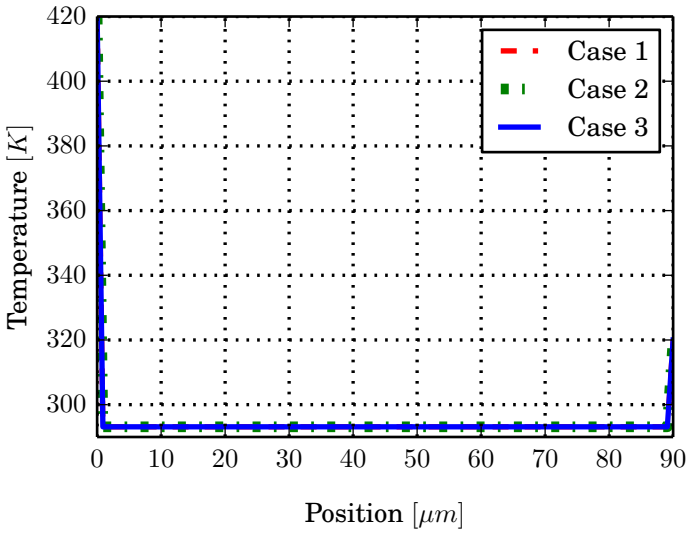

(a) Initial Condition

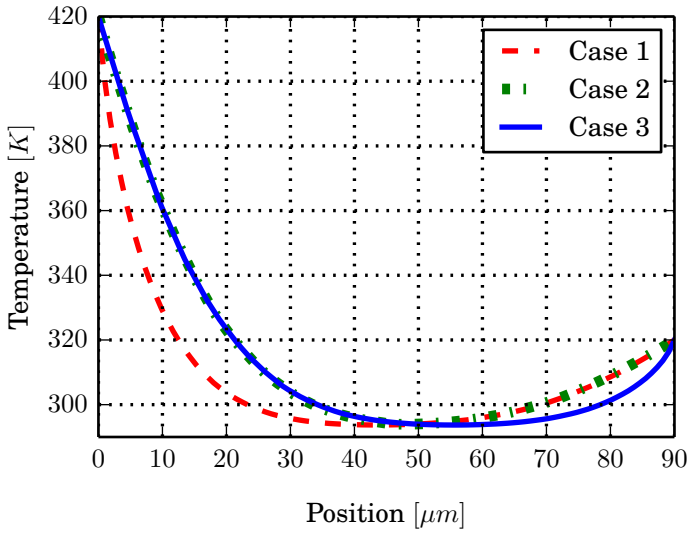

(b) Time t_1

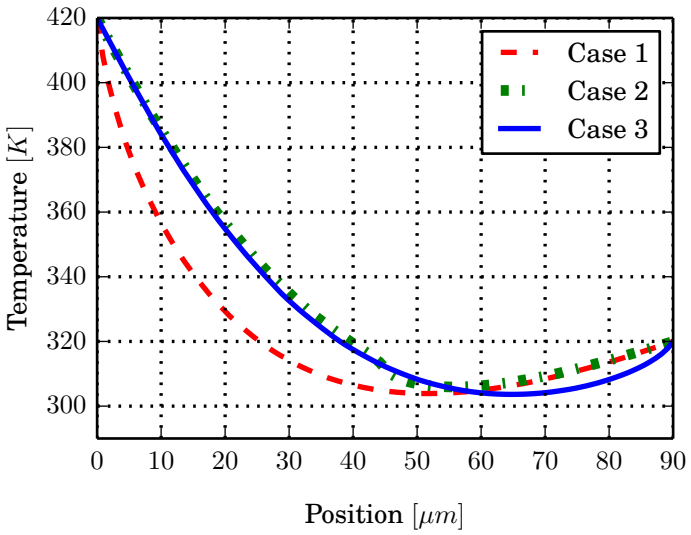

(c) Time t_2

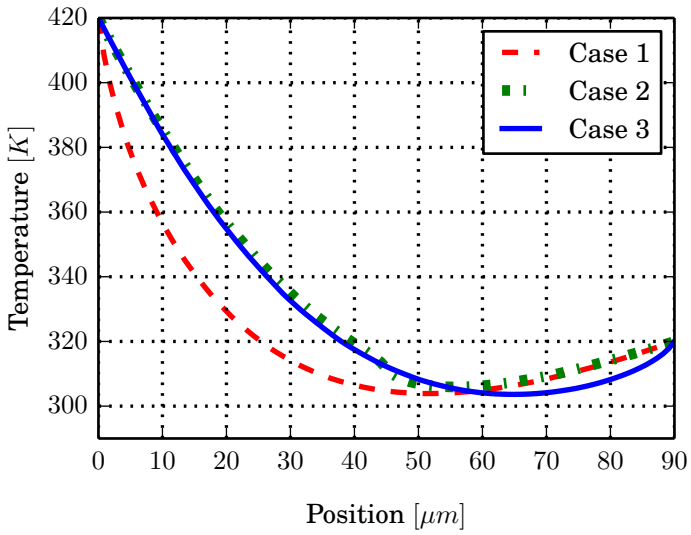

(d) Steady State

Figure 49: Evolution of temperature distribution for the 3 cases.
(a) initial state, (b) time $t_1 = 1.5 \times 10^{-7}s$, (c) time $t_2 = 7.5 \times 10^{-7}s$, and (d) steady state.

carried out with $\Delta T = 5K$. It is worth noting that this threshold value is problem-specific. Performing such as analysis allows to determine the values of ΔT_c in the dynamic framework presented in Figure 30.

Figure 47 shows the values for the steady-state thermal conductivity for the domains under consideration. The case 2, with small grains located in the middle of the rectangle presents different thermal conductivity at both of its ends while the grain sizes are identical, highlighting the temperature dependence of the thermal conductivity.

The evolution of temperature profiles, for each case, are depicted in Figure 49. The impact of the thermal conductivity on the temperature distribution is significant and evolves over time. Starting from the same initial condition, the heat takes advantage of the larger grains and propagates more quickly at the bottom edge for cases 2 and 3, and at the top edge for cases 1 and 2. At time $t_1 = 1.5 \times 10^{-7} s$, case 2 highlights this outcome by providing the temperature profile of case 1 at the bottom end and of case 3 at the top end. At time $t_2 = 7.5 \times 10^{-7} s$, the small grains at the middle of case 2 present an interesting feature by acting as a thermal capacitor, leading to the accumulation of heat on the bottom part, where the temperature is even higher than the one observed for case 1, despite having higher thermal conductivity in that region. Finally, at steady state, the mean temperatures for the three cases are: (a) $T_{m1} = 359.85K$, (b) $T_{m2} = 367.85K$, (c) $T_{m3} = 375.41K$. Thus, the maximum variation is observed between case 1 and case 3 at 15.56% as normalized by the $100K$ boundary condition difference. This difference could be even larger with a different grain distribution, as these three cases were selected for illustration purposes without any previous optimization.

This example highlights the possibility of using this model as a predictive tool to be coupled with optimization algorithms for the design of optimal thermal microstructures. For example, grain distribution could be selected to achieve a specific objective function such as averaged mean temperature or temperature diffusivity. This type of optimization could be of great relevance for a wide range of applications, including the design of micro-electromechanical systems (MEMS), chip packaging, and temperature sensors.

4.1.5 Other Materials

The main focus of this work is on the study of silicon for two reasons

1. the large amount of data available in the literature allows for comparison.

2. the heavy usage of silicon in almost every industries.

However, in order to demonstrate the larger validity of the multiscale framework developed in this work, a comparison against experimental data of other materials is needed. The considered materials are: Germanium (Ge) and Silicon Carbide (SiC)
The different bulk thermal conductivities as a function of the temperature are presented in Figure 50.

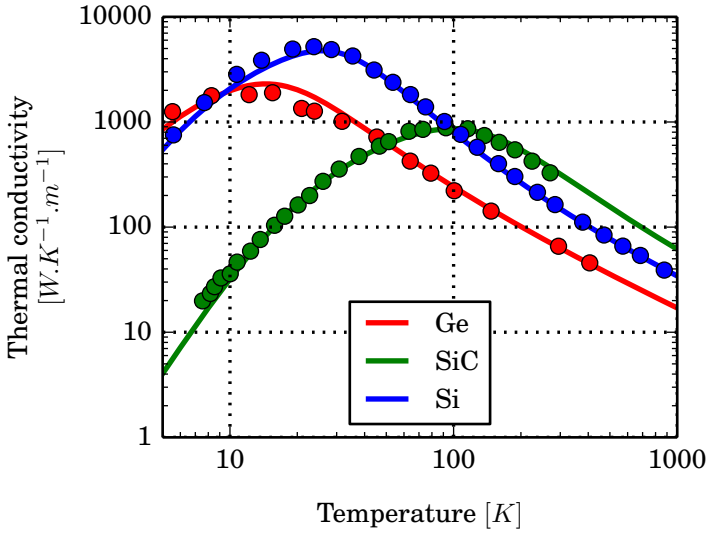

Figure 50: Bulk thermal conductivity as a function of the temperature.

Each of those materials is separately explained in the following subsections. A summary of the fitting parameters is provided in Table 51.

Germanium and silicon carbide present exactly the same calculation steps as for silicon grains. This is due to the fact that their crystal structure is face-centered diamond-cubic. Thus, the motion of the atoms follows the same pattern. Nevertheless, the value of the thermal conducticity is different. Indeed, germanium and silicon carbide have their specific

	Silicon	**Germanium**	**Silicon Carbide**	Units
a_0	5.43	5.66	4.36	A
Θ_L	570	332	952	K
Θ_T	210	111	536	K
$A_{U,L}$	3.28×10^{-19}	5.08×10^{-19}	4.34×10^{-19}	$s.K^{-2}$
$A_{U,T}$	0.69×10^{-19}	1.07×10^{-19}	8.41×10^{-20}	$s.K^{-2}$
A_I	2.5×10^{-45}	2.9×10^{-45}	4.05×10^{-45}	s^3
A_C	6.18×10^5	6.18×10^5	1.21×10^8	s^{-1}
b	140	62	425	K
$D_0(300K)$	148	58	320	$W.K^{-1}.m^{-1}$

Figure 51: Fitting parameters.

lattice parameter, dispersion relationship as well as group and phase velocity. Once, those parameters (the inputs of the proposed models in Chapter 2) are defined, the very same calculation are achieved. Using experimental data, the values of the fitting parameters related to the scattering phenomena are obtained through a least square method on the bulk thermal conductivity. The obtained values of the fitting parameters are given in Table 51.

Using the aforementioned size effect reduction function g as described in the case of silicon, the size-dependent thermal conductivity is derived for both germanium and silicon carbide. The calculated values are compared with experimental data. The case of silicon carbide is highlighted in Figure 69. In that figure, the values obtained from the methodology derived in this work are a significantly better approximation to the experimental data than previous models found in the literature.

The validation for different materials provide a overall validity of the size-dependent thermal conductivity expression.

4.1.6 Conclusion

This section validates the developed concurrent multiscale framework allowing to analyze the complex mechanisms of heat transfer at the mesoscale and microscale. It presents the benefits of a unified methodology able to capture local variations on thermal conductivity and the resulting variations on the temperature field. In this section, the capabilities of the

model are demonstrated through a series of examples. Among others, the in-plane and cross-plane thermal conductivity of thin films are recovered, using a single set of fitting parameters and the full anisotropic thermal conductivity tensor is determined, for grains of any arbitrary geometries. By presenting the physical significance of the size effect near the grain boundary, this technique highlights the heterogeneous distribution of the thermal conductivity within a single grain. Finally, the comparison of the three different microstructures highlights the potential for designing materials and metamaterials with improved thermomechanical performance.

4.2 Physical Insight - MFP

4.2.1 Motivation and Goals

One of the main limitation of the proposed methodology; called the 'full MFP' model for comparison purpose, is the computational time required to obtain the thermal conductivity for each grain, along with the fact that this step must be performed several times as the temperature evolves. Moreover, the considered models having a large number of grains, this issue becomes even more prominent. As argued in the previous chapter, the high performance parallel framework alleviates some of these limitations. Despite this performance improvement, each processor still needs to perform the integration of the thermal conductivity over the full Brillouin zone. This step becomes the critical bottleneck of the implemented framework.

This section presents the idea of considering an average mean free path instead of integrating over the full range of wavevector. Indeed, most of the models available in the literature considered a constant average value of the mean free path [110]. However, those models lead to thermal conductivity values that are significantly different than the experimental data. Hence, this section aims at simplifying the thermal conductivity expression (2.3.11), by determining a constant mean free path.

The simplest models possible are considered on purpose. By adding complexity, an

accurate approximation can most likely be obtained. However, the goal is to simplify the full MFP model and more complicated models seems irrelevant.

4.2.2 Single MFP

Instead of using the size-dependent thermal conductivity derived in Equation (2.3.11), the reduced thermal conductivity D is obtained by considering the following expression

$$D(L_c, T) = \bar{g}(L_c) D_0(T) \tag{4.2.1}$$

where D_0 is the bulk thermal conductivity as a function of the temperature T, L_c is the characteristic size of the system (thin film thickness, nanowire diameter or grain size) and $\bar{g}$ is a size effect reduction function.

From Equation 2.3.12, the size effect reduction function g has been defined as

$$g = 1 - \frac{(1-p)\ exp\left(-\delta_1/\Lambda_0\right)}{1 - p\ exp\left(-\delta_2/\Lambda_0\right)} \tag{4.2.2}$$

As previously mentioned, in the case of crystalline grains, the specularity parameter p is equal to zero [109]. Hence, Equation (4.2.2) can be simplified as

$$g = 1 - exp\left(-\delta_1/\Lambda_0\right) \tag{4.2.3}$$

where δ_1 is the distance between the phonon emission point and the grain boundary, Λ_0 is the wavevector dependent mean free path, defined as $\Lambda_0(\mathbf{k}) = v_g(\mathbf{k})\ \tau_0(\mathbf{k})$.

It is worth noting that in Equation (2.3.11), the function g is inside the integral over the Brillouin zone. In the current simplification, the Brillouin zone is neglected as the mean free path is considered unique. Thus, the expression of the size effect reduction function $\bar{g}$ is given as

$$\bar{g}(L_c) = \frac{1}{N_b} \sum_{n=1}^{N_b} 1 - exp\left(\frac{n\ L_c}{N_b} \frac{1}{\mathrm{MFP}_s}\right) \tag{4.2.4}$$

The summation is used to account for the contribution of phonon emission points located at different distance from the grain boundary. The MFP_s is the equivalent mean free path, where the subscript 's' stands for single MFP. It is independent of the wavevector. Its value

needs to be determined in order to recover the best thermal conductivity for different grain sizes.

In the literature, the value of the average mean free path is obtained from experimental data [110]. However, there is no direct measurement procedure of the mean free path. This limitation leads to inconsistency in the reported values of the mean free path. Here, the focus is on silicon and the reported values in the literature range from 300 nm to 3 μm.

The derived expression is compared to the proposed model. The results are displayed in Figure 52a. The change in term MFP_s is responsible for a shift along the grain size axis, however the shape of the thermal conductivity curve stays unchanged. The shorter the equivalent MFP, the higher the thermal conductivity D. This effect is due to the fact that the MFP is not impacted as much by the characteristic size of the system. It is undoubtedly possible to optimize the value of MFP_s in order to maximize the recovery of the experimental values, as shown in Figure 52b. However, this is in contradiction with the purpose of the full MFP model where the sole fitting parameters are obtained at the bulk level. Additionally, the shape of the curve is not affected by the value of the MFP_s. As a consequence, the single MFP model is too restrictive and does not predict a correct thermal conductivity.

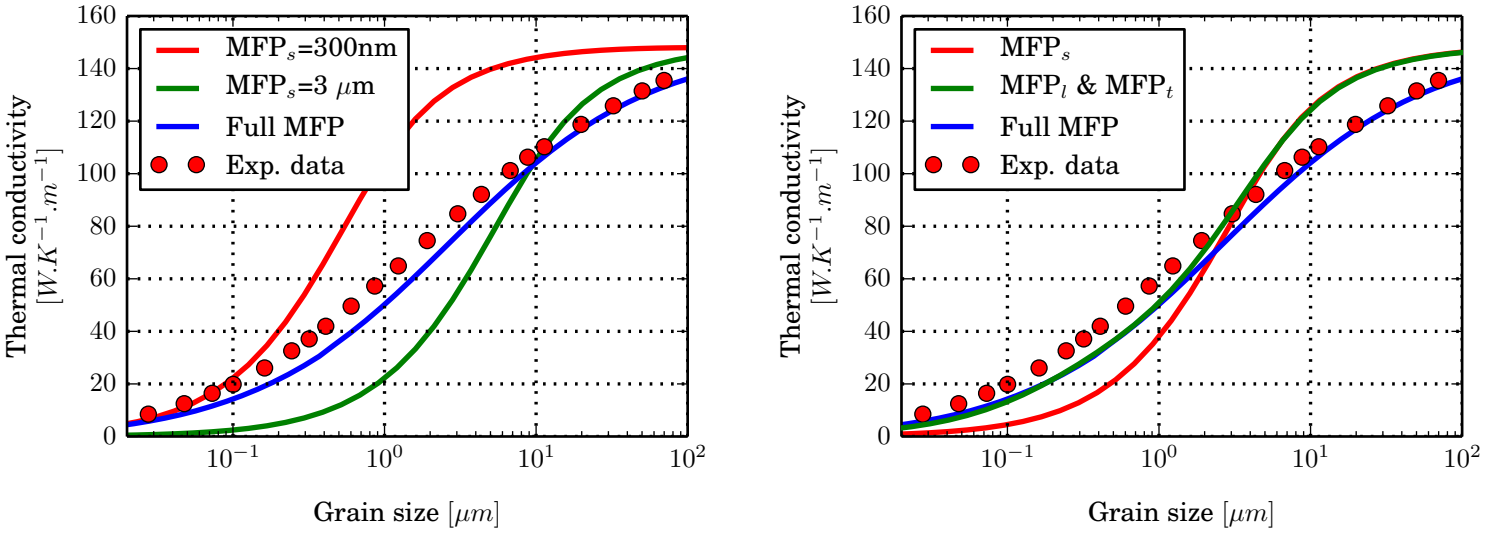

Figure 52: Model comparison: full MFP vs Single MFP vs 2 Polarization MFP.

It is also worth noting that the size-dependent accuracy of the full MFP model resides in the fact that the 80 : 20 ratio between the longitudinal and transverse components is preserved. Thus, the next attempt considers both polarization within a simplified model.

4.2.3 Polarization-dependent MFP

In order to account for both polarization of the phonon dispersion in silicon, the simplified expression of the reduced thermal conductivity is written as

$$D(L_c, T) = \bar{g}_T(L_c) D_T(T) + \bar{g}_L(L_c) D_L(T) \tag{4.2.5}$$

where D_T and D_L are respectively the transverse and longitudinal bulk thermal conductivity components as a function of the temperature T, L_c is the characteristic size of the system and $\bar{g}_T$ and $\bar{g}_L$ are respectively the transverse and longitudinal size effect reduction functions.

Similarly to the derivation done in the previous subsection, the expression of the size effect reduction functions $\bar{g}_T$ and $\bar{g}_L$ are given as

$$\begin{aligned} \bar{g}_T(L_c) &= \frac{1}{N_b} \sum_{n=1}^{N_b} 1 - exp\left(\frac{n\ L_c}{N_b} \frac{1}{\mathrm{MFP}_T} \right) \\ \bar{g}_L(L_c) &= \frac{1}{N_b} \sum_{n=1}^{N_b} 1 - exp\left(\frac{n\ L_c}{N_b} \frac{1}{\mathrm{MFP}_L} \right) \end{aligned} \tag{4.2.6}$$

where MFP_T and MFP_L are respectively the transverse and longitudinal averaged mean free paths. Those two values can only be best determined through fitting to the experimental data. While this is not the goal of this work, it is interesting to fit both the single MFP model and the one considering the two polarizations to better compare them. The optimal fitting for the single MFP model is obtained for $\mathrm{MFP}_T = 1.6\mu m$ and the optimal fitting for the polarization MFP model is obtained for $\mathrm{MFP}_T = 2.0\mu m$ and $\mathrm{MFP}_L = 0.1\mu m$. The respective curves are displayed on Figure 52b. Undoubtedly, the model considering the two polarizations gives a better fit to the experimental data, especially for grains with size lower than $3\mu m$.

The main take away from this current and previous subsections is that in order to recover the shape of the thermal conductivity curve, the full MFP range should be considered.

Thus, in the next subsection, the importance of the different MFP during the integration throughout the Brillouin zone is highlighted.

4.2.4 MFP within the Brillouin Zone

Recent studies [111, 112, 113] have demonstrated that the phonon bulk MFP of silicon spans over six orders of magnitude from $0.1nm$ to $100\mu m$, with 80% of the thermal conductivity being dominated by phonons having MFP below $4\mu m$. Thus, defining an a priori average bulk MFP seems fairly unrealistic. Recovering the size-dependent thermal conductvity is even more problematic.

This subsection aims at defining the contribution of the different phonon MFP for different grain sizes. While this study has been encountered in the literature through the study of the accumulated thermal conductivity [111], the size-dependent approach is still unexplored. The results presented in Figure 53 are obtained by varying the upper boundary in the integration over the Brillouin zone of the thermal conductivity expression.

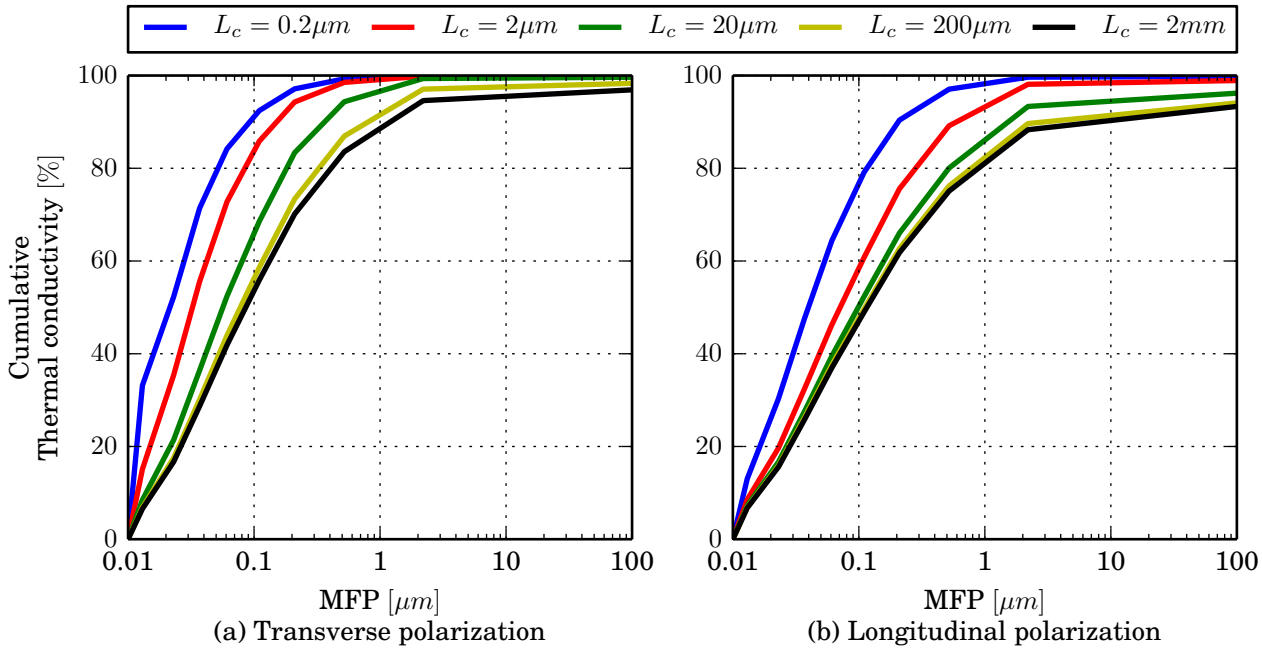

Figure 53: Contribution of the MFP to the cumulative thermal conductivity for transverse and longitudinal components.

The first finding is in the difference between the transverse and longitudinal MFP. For

a grain size of $2\mu m$ (which is representative of the average grain size considered in this thesis) 80% of the traverse component of the thermal conductivity is obtained for MFP below $80nm$, while the same portion of the longitudinal component is obtained for MFP below $300nm$, which corresponds to the value of the bulk MFP of silicon encountered in the literature.

The key take-away is that the MFP is dependent of the grain size. This reinforces the fact that the reduction of the thermal conductivity due to the size effect is driven by a reduction of the mean free path. Thus, defining an equivalent MFP valid for all the grain sizes is highly inaccurate. In order to recover the appropriate thermal conductivity using Equation (4.2.1) or Equation (4.2.5), the expression of the MFP as a function of the grain size is defined by solving the following equation

$$\frac{L_c + \mathrm{MFP}_P \ (-1 + exp(-L_c/\mathrm{MFP}_P))}{L_c} = \frac{D^p(L_c)}{D_0} \tag{4.2.7}$$

where L_c is the characteristic length of the system, P is a free index representing either S, L or T. From that expression, the MFP as a function of the grain size can be determined, as represented in Figure 54.

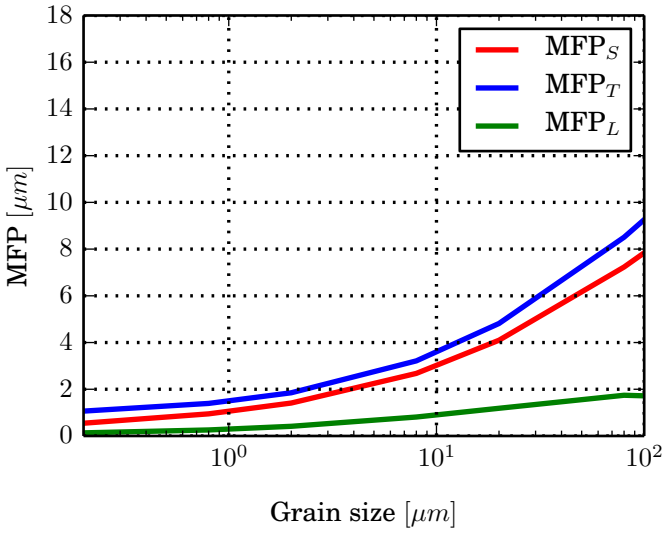

Figure 54: Equivalent size-dependent MFP to be used in Equations (4.2.1) and (4.2.5) to recover the appropriate thermal conductivity.

Expression (4.2.7) presents a limited interest in the prediction of the thermal conductivity. Indeed, in order to solve it, the reduced thermal conductivity needs to be already known. The main advantage of this developed methodology is to obtain the value of the MFP for both polarizations as a function of the grain size. Such results have not been yet published in the literature and represent a key improvement compared to the current determination methods of the phonon MFP.

4.2.5 Conclusion

This section demonstrates the difficulty of deriving more straightforward expressions than the one proposed in Chapter 2. Considering a unique average mean free path leads to wrong estimations of the thermal conductivity as a function of the grain size. While decoupling the contribution of each polarization improves the results, it still does not provide a correct estimation for grain larger than $2\mu m$. Thus, in this section, a quantitative description of the MFP for both polarization as a function of the mean free path is presented. This approach leads to unprecedented results, as such analyses currently exist only for bulk properties.

4.3 Heat Transfer Optimization in Micro-electronic Devices

Subsection 4.1.4 highlights that in a polycrystalline material the microstructure can have a large impact on the macroscopic behavior of the system. Thus, by properly tuning the microstructure, specific objectives can be reached or at least optimized. In this subsection, various thermal objective functions are solved by obtaining the optimal grain size arrangement, using topology optimization.

Topology optimization is a mathematical technique aimed at determining material distribution within an engineering component. The goal of this method is that, for certain boundary conditions and under specific constraints, the component performs optimally in the sense of a given metric. Early works on topology optimization focused on mechanical performance of structures and date back to the beginning of the past century. However,

the field did not reach its full potential until the seminal contribution of Bendsoe and Kikuchi [114], which led to the development of practical and efficient numerical schemes.

Due to the direct analogy between mechanical and thermal problems, topology optimization techniques have subsequently been applied to a rather large variety of heat transfer problems. In this area, the objective is generally to distribute a limited amount of conductive materials within the analysis domain in order to optimize the thermal performance of the component. Common design goals include minimizing the mean temperature over the domain [115, 116] and maximizing the temperature diffusivity of a design [117], to name a few.

Over the past two decades, various optimization methods have been developed in order to solve increasingly complex problems, as well as to improve the robustness of the obtained results. Among them, some prominent approaches include: homogenization method [118], penalized topology optimization [119, 120], evolutionary structural optimization [121], level set-based topology optimization [122], and discrete material optimization [123]. A common feature of all of these approaches is that designs are based on multiphase systems, which generally require high contrast material properties between constituents. Even though this might result in topological configurations that are optimal according to some desired thermal metric, resulting configurations might be impractical from a mechanical standpoint.

As Figure 55 shows, a high contrast in the value of thermal conductivity between materials is generally associated with disparate values on the corresponding thermal expansion coefficients. This implies that, as the temperature of a system departs from a stress-free configuration, large thermal stresses develop at the interfaces between constituent materials. This, in turn, could lead to premature thermomechanical failure. Ideally, the goal would be to optimize the thermal properties of components without compromising their mechanical integrity.

In this subsection, the possibility of circumventing the aforementioned limitation is investigated by optimizing the spatial grain size distribution on single-material polycrystalline systems. By taking advantage of the grain size-dependent thermal properties demonstrated

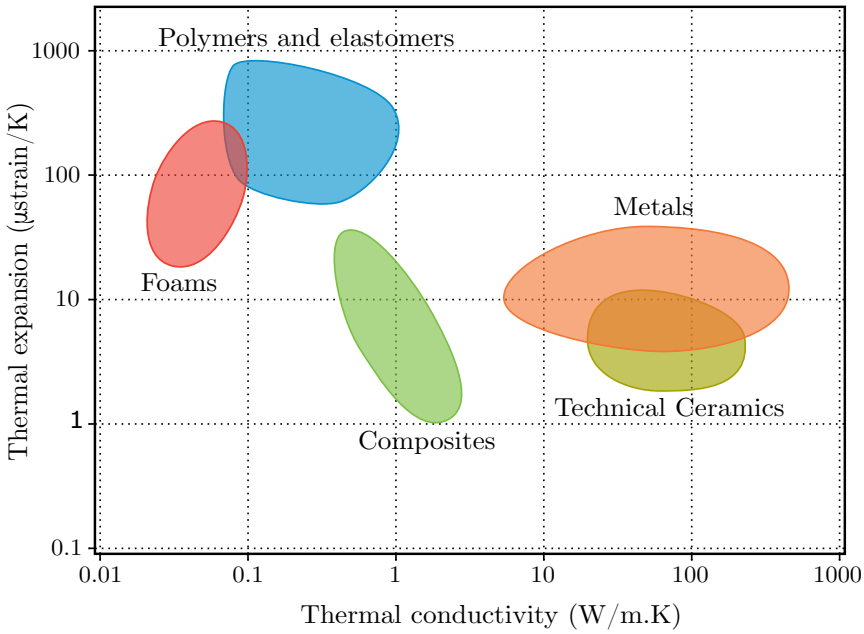

Figure 55: Ashby graph of thermal conductivity vs. thermal expansion coefficient for various material systems.

in Section 4.1, one could tailor the microstructure of a material, e.g. through grading of the grain size, and affect its internal temperature distribution. Combining the concurrent multiscale model with topology optimization techniques allows to develop single-material systems with optimized thermal transport properties.

4.3.1 Genetic Algorithm

In this thesis, optimization is achieved through the use of the genetic algorithm (GA). It is arguably the most commonly used evolutionary algorithm and one of the most conventional non-gradient methods. More precisely, the genetic algorithm is a metaheuristic algorithm inspired by Darwin's theory of natural selection. The algorithm repeatedly modifies a population of individual solutions, through a stochastic selection of the best individuals for reproduction. Mutations and random crossovers prevent local minima. The genetic algorithm allows to handle complex problems such as configurations in which the objective function is discontinuous, non-differentiable, or stochastic. The drawback of this approach is the absence of mathematical convergence theory and thus no assurance of optimality of the

final solution found. Extensive literature can be found about the genetic algorithm in [124, 125], among others. A more specific review of the utilization of the genetic algorithms in heat transfer problems is provided in [126].

While the genetic algorithm is not the latest state-of-the-art optimization technique available, the provided methodology allows for the use of more advanced techniques. By using the genetic algorithm, this section shows the impact of the grain size optimization on the thermal properties. It is believed that the use of more cutting-edge optimization technique might provide slightly better results, reinforcing the need for such a grain size optimization.

4.3.2 Optimization Methodology

Chapter 2 illustrates how it is possible to compute the variation of the thermal conductivity of a given material due to changes in its characteristic length scale. This capability, combined with the separation of scales assumption, allows to perform topology optimization on a thermal system for a continuous distribution of thermal conductivity. This fact, by itself, constitutes a departure from traditional approaches to topology optimization of thermal systems, which generally assume multi-material configurations and the consequent discreteness of the available values of thermal conductivity.

Using the methodology from this work, manufacturing constraints (i.e. range of grain size) and expected operating conditions (i.e. range of temperature) can be translated into an attainable range of thermal conductivity $[D_{\min}, D_{\max}]$. Then, using this range as a constraint, a given objective function can be minimized over the spatial distribution of thermal conductivity for the system under consideration. Commonly adopted objective functions aim at: (a) minimizing the average temperature in the material [127], or (b) maximizing its thermal diffusivity [117]. Other objective functions may be defined as well.

In this approach, the geometry of the system under consideration is discretized using a triangular mesh consisting of N nodes. Design variables, e.g., thermal conductivity, are assigned to each node on the mesh. The value of the effective thermal conductivity at a node

is denoted D_d. Finite element calculations are performed over the same mesh to evaluate the objective function $f(D_d)$, with the values of the thermal conductivity at quadrature points of the finite elements being obtained through interpolation from the design points. The resulting optimization problem is then written as

$$\begin{aligned} \underset{D_d}{\text{minimize}} \quad & f(D_d) \\ \text{subject to} \quad & g(D_d) \leq 0 \\ & D_d \in [D_{\min}, D_{\max}]^N \end{aligned} \tag{4.3.1}$$

where $g(D_d) \leq 0$ represents any other additional constraints, such as the average thermal conductivity over the domain.

By using this procedure, the smoothness and resolution of the optimal solution depend on the geometry of the mesh, as it will be depicted in a sample problem below. Briefly, it can be stated that highly regular meshes constraint the optimal solution to have the same underlying structure. To alleviate this issue, the coordinates of the control points X_d are added to the optimization problem. That is, optimization of the objective function is performed over the distribution of thermal conductivity and location of the control points. This strategy resembles r-adaption schemes adopted for finite element problems in elastostatics [128], resulting in the modified optimization problem

$$\begin{aligned} \underset{X_d, D_d}{\text{minimize}} \quad & f(X_d, D_d) \\ \text{subject to} \quad & g(X_d, D_d) \leq 0 \\ & X_d \in \Omega^N \\ & D_d \in [D_{\min}, D_{\max}]^N \end{aligned} \tag{4.3.2}$$

To illustrate the effects of the mesh adaption technique, or lack thereof, the previously described optimization method is applied to a representative problem first introduced in [117], and represented in Figure 56. The analysis domain is a square of length $L_c = 200\mu m$, composed of two materials, one with thermal conductivity $D_{\max} = 148 W.K^{-1}.m^{-1}$ and the other one with no ability to transfer heat at all. The bottom and top edges include heat sinks at 300 K. The right and left edges are subjected to an incoming heat flux

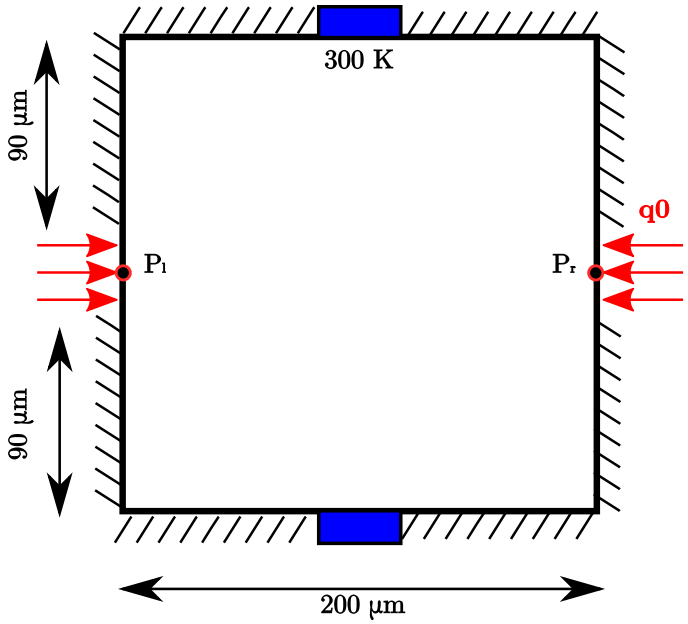

Figure 56: Schematics for optimization problem to be solved with and without mesh adaption.

$q_0 = 353 W.m^{-1}$. Both heat sinks and incoming flux are located at the center of their respective edges over 10% of the edge length. In this problem, the goal is to find the distribution of thermal conductivity that maximizes the thermal diffusivity of the plate. This objective is achieved by minimizing the temperature at points P_l and P_r, located at the middle of the vertical edges. Due to the symmetry of this configuration, the related values T_l and T_r are identical. It is worth noting that an additional constraint on the average thermal conductivity D_mean is added, such that $D_\mathrm{mean} = 45\ WK^{-1}m^{-1}$. Structurally, it means that 32.9% of the material has a thermal conductivity $D_\mathrm{max} = 148\ WK^{-1}m^{-1}$, while the rest has a thermal conductivity $D_\mathrm{min} = 0\ WK^{-1}m^{-1}$.

The problem is solved using two approaches: with and without mesh adaption. The initial mesh for both problems is structured, given by a uniform distribution of design points over a square grid. For the problem without mesh adaption, the design variables are the thermal conductivity values D_d at the design points. For the problem with mesh adaption, the optimization is achieved over the thermal conductivity values D_d and over the design point locations X_d. Notice that the addition of new design variables X_d would result in a

larger optimization problem if the number of design points is to be kept constant. Consequently, the problem with mesh adaption is optimized over fewer design points, maintaining the number of optimization variables for both problems identical, totaling 108 for each of them.

Under these assumptions, the optimization problem with fixed design points is expressed as

$$\begin{aligned} \underset{D_d}{\text{minimize}} \quad & \frac{T_l(D_d) + T_r(X_d, D_d)}{2} \\ \text{subject to} \quad & \frac{1}{L_c^2} \int_{x \in [0, L_c]^2} D(x, D_d) dx \leq D_{mean} \\ & D_d \in \{0, 148\}^N \end{aligned} \tag{4.3.3}$$

whereas for the adaptive problem the optimization problem can be written

$$\begin{aligned} \underset{X_d, D_d}{\text{minimize}} \quad & \frac{T_l(X_d, D_d) + T_r(X_d, D_d)}{2} \\ \text{subject to} \quad & \frac{1}{L_c^2} \int_{x \in [0, L_c]^2} D(x, X_d, D_d) dx \leq D_{mean} \\ & X_d \in [0, L_c]^{2N} \\ & D_d \in \{0, 148\}^N \end{aligned} \tag{4.3.4}$$

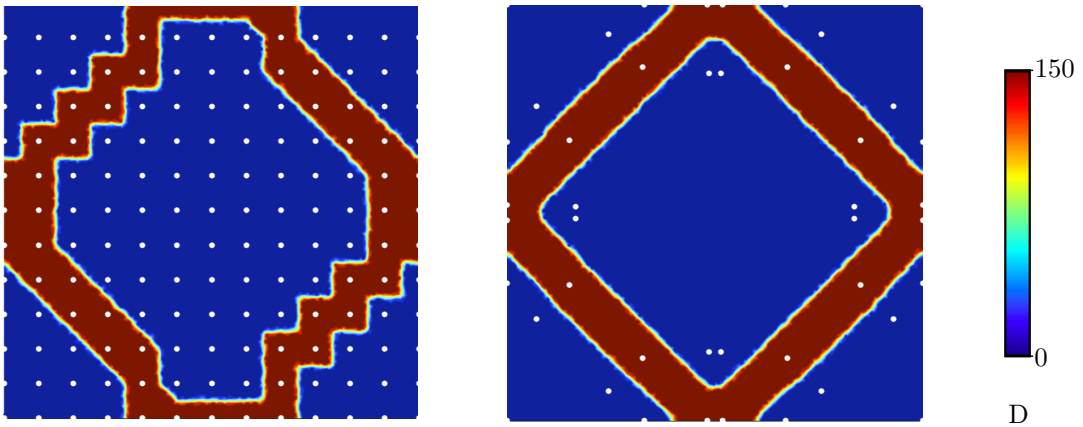

(a) Fixed design points (b) Adaptive mesh

Figure 57: Optimization results with and without mesh adaption.
Red: regions with high the thermal conductivity value.
Blue: regions with no thermal conductivity.

The optimization results for the problem without adaption are shown in Figure 57a. As the thermal conductivity on the control points is interpolated over a regular mesh, the resulting optimal solution is highly structured, and reflects the underlying topology of the mesh.

In contrast, Figure 57b shows the optimal solution for the problem with mesh adaption. Although giving mobility to the control points significantly increases the dimensionality of the problem, it gives more flexibility to the distribution of thermal conductivity, thus enabling more complex and smoother shapes with a lower amount of points. Consequently, the optimal design is less sensitive to the mesh. It can be observed that control points are more densely placed in areas with large variations in thermal conductivity distribution.

It is worth noting that the effect of adaptivity on the optimal value of the objective function is non-negligible. Indeed, with fixed design points the temperature at point P is $T_P = 397.61\ K$, while with the adaptive design mesh it drops to $T_P = 375.30\ K$. Another benefit of allowing the mesh to adapt is that resulting smooth geometries are potentially easier to manufacture than the highly structured ones resulting from regular meshes. With a similar number of variables used in the algorithm, the fixed-point optimization results in a suboptimal configuration due to the lack of freedom over the shape of the thermal conductivity distribution.

In the previous example, optimization was performed over a discrete range of thermal conductivity value for purposes of illustration. In contrast, it seems promising to perform such optimization on single material systems, resulting on a continuous range of attainable thermal conductivity which depends on some characteristic material length scale. The same problem as before is now considered, but the thermal conductivity values are restrained to remain within reported values for nano- and micro-grained silicon: $D \in [40, 110] W.K^{-1}.m^{-1}$. The average thermal conductivity on the domain is constrained

to be $D_{mean} = 61 W.K^{-1}.m^{-1}$. This translates into the following formulation

$$\begin{aligned} \underset{X_d, D_d}{\text{minimize}} \quad & \frac{T_l(X_d, D_d) + T_r(X_d, D_d)}{2} \\ \text{subject to} \quad & \frac{1}{L_c^2} \int_{x \in [0, L_c]^2} D(x, X_d, D_d) dx \leq D_{mean} \\ & X_d \in [0, L_c]^{2N} \\ & D_d \in [40, 110]^N \end{aligned} \tag{4.3.5}$$

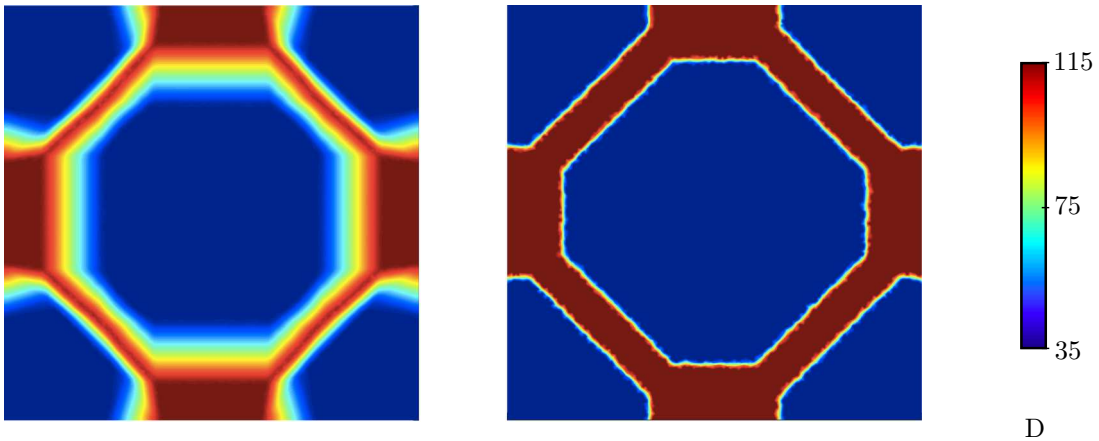

(a) Continuous optimization (b) Discrete optimization

Figure 58: Comparison between discrete versus continuous optimization approaches.

The resulting optimal solution is visualized in Figure 58a. Additionally, Figure 58b shows the optimal configuration for the equivalent discrete problem in which the thermal conductivity is forced to adopt the extreme values of the continuous range, while maintaining the same mean value constraint. The temperature attained at point P is fairly similar for both cases: $T_P = 371.93\ K$ for the discrete configuration, and $T_P = 371.23\ K$ for the continuous one. This highlights the fact that solutions for this kind of optimization problems tend to be very sharp. This could be troublesome from a fabrication perspective, as currently manufacturing techniques only allow for smooth transitions in the grain size distribution.

The previous discussion motivates the introduction of an extra constraint on the model, which relates to the grain size gradient. This restriction is enforced indirectly through a

constraint on the thermal conductivity gradient. The latter gradient is calculated within each element and the maximum value throughout the domain $\nabla D_{\max}$ is bounded by ∇D_{opt}

$$\nabla D_{\max} \leq \nabla D_{\text{opt}} \tag{4.3.6}$$

The calculation of $\nabla D_{\max}$ relies on the derivative of the shape functions $N_i(x, y)$ utilized to interpolate the design variables, such that

$$\nabla D_{\max} = \max_{\text{elts}} \left\{ \sqrt{\left(\sum_{i=1}^{3} \frac{\partial N_i(x,y)}{\partial x} D_i \right)^2 + \left(\sum_{i=1}^{3} \frac{\partial N_i(x,y)}{\partial y} D_i \right)^2} \right\} \tag{4.3.7}$$

where D_i is the effective thermal conductivity at the i^{th} node of the triangle.

The limiting thermal conductivity gradient ∇D_{opt} is defined as

$$\nabla D_{\text{opt}} = \gamma . \frac{D_{\max} - D_{\min}}{L_c} \tag{4.3.8}$$

where $D_{\max}$ and $D_{\min}$ represent the bounds of the thermal conductivity, and L_c is the characteristic length of the analysis domain. Thus, the parameter γ is non-dimensional and can be considered as a parameter of the system.

The methodology introduced thus far allows to obtain, for a given metric and set of constraints, the optimal thermal conductivity distribution within a component. A key assumption throughout this process is that separation of scales holds true, that is, that the model could be optimized at the continuum scale adopting an attainable range of thermal conductivity computed at the mesoscale. The remaining task is then to verify whether or not this assumption holds true. In order to do so, an explicit reconstruction of the microstructure must be generated for the optimized system, and compute the objective function over that domain. This value, in turn, must be compared to its continuum counterpart.

4.3.3 Verification of Separation of Scales Assumption

By following the procedures described in Chapter 3 and in Section 4.3.2, an optimal distribution of thermal conductivity $D(X)$ is obtained over the analysis domain as well as the corresponding temperature field $T(X)$ for the optimal solution. The last step of this

approach consists on the verification of the original separation of scales assumption. This is achieved by explicitly reconstructing the microstructure of the material from the optimization results, and computing the corresponding thermal solution, which is finally compared to the continuous one. The entire procedure, which starts with the results from the optimization problem, is depicted schematically in Figure 59.

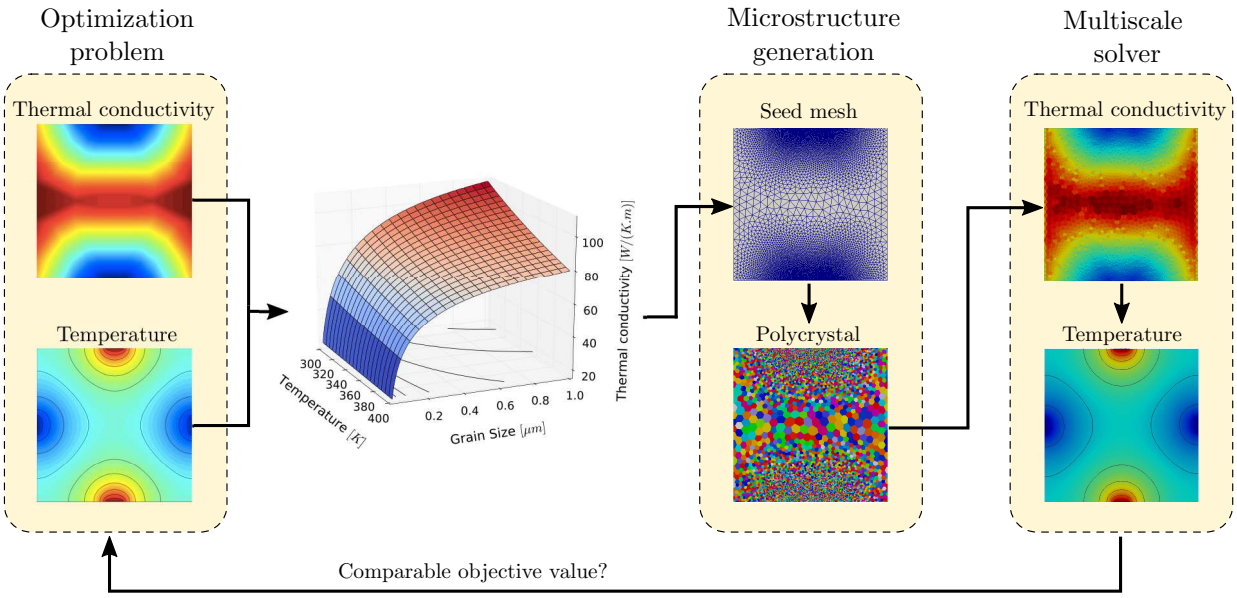

Figure 59: Schematics of procedure for verification of the separation of scales assumption.

The microstructural reconstruction process is performed as follows. Utilizing the original computations of the attainable range of the thermal conductivity, the reverse procedure can be performed: for a given control point with coordinates X_d on the discrete mesh, the corresponding value of the optimal thermal conductivity D_d and temperature T_d are known. Thus, by utilizing the temperature/grain size/thermal conductivity relation, one can infer the characteristic grain size l_d at that point. Then, by adopting the same interpolation scheme as in the finite element calculations, the grain size field $l(X)$ is recovered.

Given the grain size field, a polycrystalline structure is generated by following the procedure explained in details in Section 3.1.1. This grain generation technique requires, as initial data, the location of the centers of each grain, which, in turn, should be spaced according to the required grain size distribution. As a result of this step, an explicit representation of the microstructure of the optimized material is obtained.

Once the polycrystalline structure of the optimized material is generated, the corresponding finite element model is formulated in order to solve for the thermal transport problem. The granular thermal conductivity is calculated at every quadrature point of the model by applying the procedure depicted in Subsection 3.2.3. Then, the Fourier heat conduction problem is solved. This procedure is nonlinear and requires an iterative process as the thermal conductivity depends on temperature. Convergence is generally obtained after a couple of iterations. This fast convergence is expected since the initial grain size distribution takes into consideration both the thermal conductivity and the temperature distribution at a point.

As a final step, the objective function is evaluated utilizing the previously obtained microstructural thermal distribution. The corresponding value of the objective function is calculated and compared to the continuous temperature field resulting from the optimization problem. If results are not within required (problem specific) tolerances, it means that the separation of scales assumption does not hold for the specific problem under consideration. In that case, the optimization problem should utilize the real microstructure at each step, which would obviously incur a significantly higher computational cost.

4.3.4 Numerical Results

In this subsection, the optimization methodology is illustrated through two sample problems. In both problems, the full method, including mesh adaption and manufacturing constraints, is applied to optimize the thermal conductivity distribution within components. Sample problem #1 focuses on the impact of limiting the grain size gradient and its effect on the objective function under consideration. Sample problem #2 highlights the possible implications of grain size optimization by analyzing the relative impact of thermal conductivity optimization on a thermal barrier coating, as compared to the effect of a heat sink. In both of these problems, the focus is on the grain size distribution for polycrystalline silicon, as all necessary material properties are broadly available in the literature.

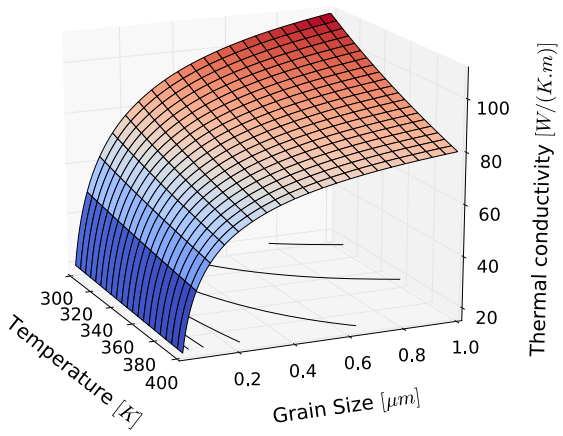

Figure 60: Thermal conductivity as a function of temperature and grain size.

The first step to approach both problems is to determine the attainable range of thermal conductivity, adopting the numerical framework presented in Chapter 3. Although this approach can potentially account for arbitrary grain size and shape (the latter determining thermal conductivity anisotropy), the case of symmetric grains with isotropic thermal conductivity is considered. That is, the focus is solely on the effect of grain size and not on the impact of grain morphology. Thus, non-elongated grains are assumed, shaped as regular hexagons. In order to remain within the scope of classical size effects, grain sizes range within : $l_g \in [0.5, 20]\mu m$. In agreement with boundary conditions for applications presented in rest of the section, this study is limited to the temperature range $T \in [300, 500]\ K$. The corresponding thermal conductivity obtained under these assumptions is depicted in Figure 60. The attainable thermal conductivity range is then $D \in [40, 110]W.K^{-1}.m^{-1}$. It is worth noting that, even though only this range is needed for the optimization problem, the entire surface $F(T, l_g, D) = 0$ must be kept in order to reconstruct the optimized microstructure in the verification step.

4.3.4.1 Example 1

This example evaluates the impact of the thermal conductivity gradient constraint on the optimization outcome. The problem under consideration is depicted by Figure 61. The geometry is a square of length $L_c = 200\mu m$. The bottom and top edges include constant temperature heat sources at $400K$, while the right and left edges include heat sinks at $300K$.

Both heat sinks and sources are located at the center of their respective edges over 10% of the edge length.

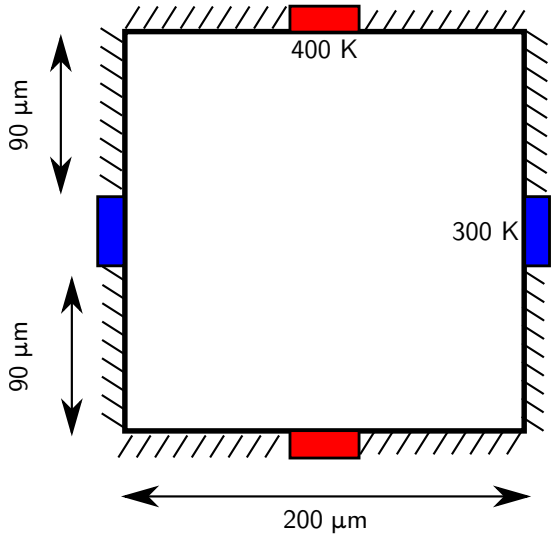

Figure 61: Geometry and boundary conditions of the sample problem #1.

The objective for this problem is to minimize the average temperature within the analysis domain. The corresponding optimization problem is expressed as

$$\begin{aligned} \underset{X_d, D_d}{\text{minimize}} \quad & \frac{1}{L_c^2} \int\limits_{x \in [0, L_c]^2} T(x, X_d, D_d) dx \\ \text{subject to} \quad & \nabla D_{max} < \nabla D_{opt} \\ & X_d \in [0, L_c]^{2N} \\ & D_d \in [40, 110]^N \end{aligned} \tag{4.3.9}$$

The optimal solution is expected to be a trade-off between isolating the heat sources with low thermal conductivity and connecting the heat sink to as much material with high thermal conductivity as possible. This balance is anticipated to be dependent on the thermal conductivity gradient constraint.

Several optimization problems are run with varying values of the non-dimensional parameter $\gamma \in [0, 10]$, as defined by Equation (4.3.8), to assess its effect on the optimal value of the objective function. A value $\gamma = 0$ means no gradient on the thermal conductivity is allowed, or the equivalent assumption of constant thermal conductivity over the entire

domain. It is worth noting that, since optimization is performed over the steady state solution of the thermal transport problem, the solution for the case with constant conductivity ($\gamma = 0$) is independent of the particular value of this material constant. The higher the value of γ, the higher the allowed maximum thermal conductivity gradient. Thus, in the limiting case $\gamma \to \infty$, there is no constraint on the gradient. This flexibility, in turn, allows very sharp contrasts on the thermal conductivity within the domain.

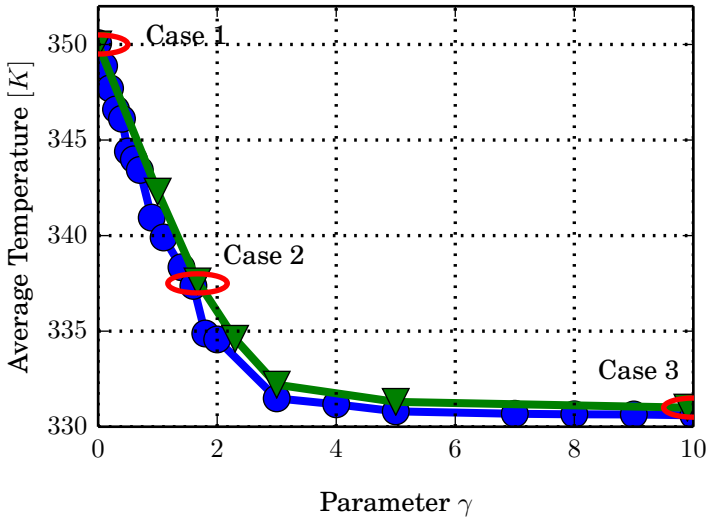

Figure 62: Influence of the thermal conductivity gradient on the optimal average temperature.

Results for varying values of the non-dimensional constant γ are displayed in Figure 62. In the figure, blue circles represent the optimal solution for the continuous optimization problem, whereas green triangles depict the value of the objective function for reconstructed microstructures (verification step). Notice that the verification step is performed on selected cases due to the computational expense associated with microstructural computations. The graph shows that, for the range considered in this example, the separation of scales assumption seems to be adequate.

As expected, a reduction of this constraint (i.e., larger values of γ) produces a better optimal solution. It is worth nothing, however, that while changes in performance are significant in the range $0 \leq \gamma \leq 3$, the effect is only minor for values $\gamma > 3$. This indicates

that, even though sharp solutions are ideal from a thermal performance perspective, a moderate level of manufacturing constraints does not affect much the overall performance of the system.

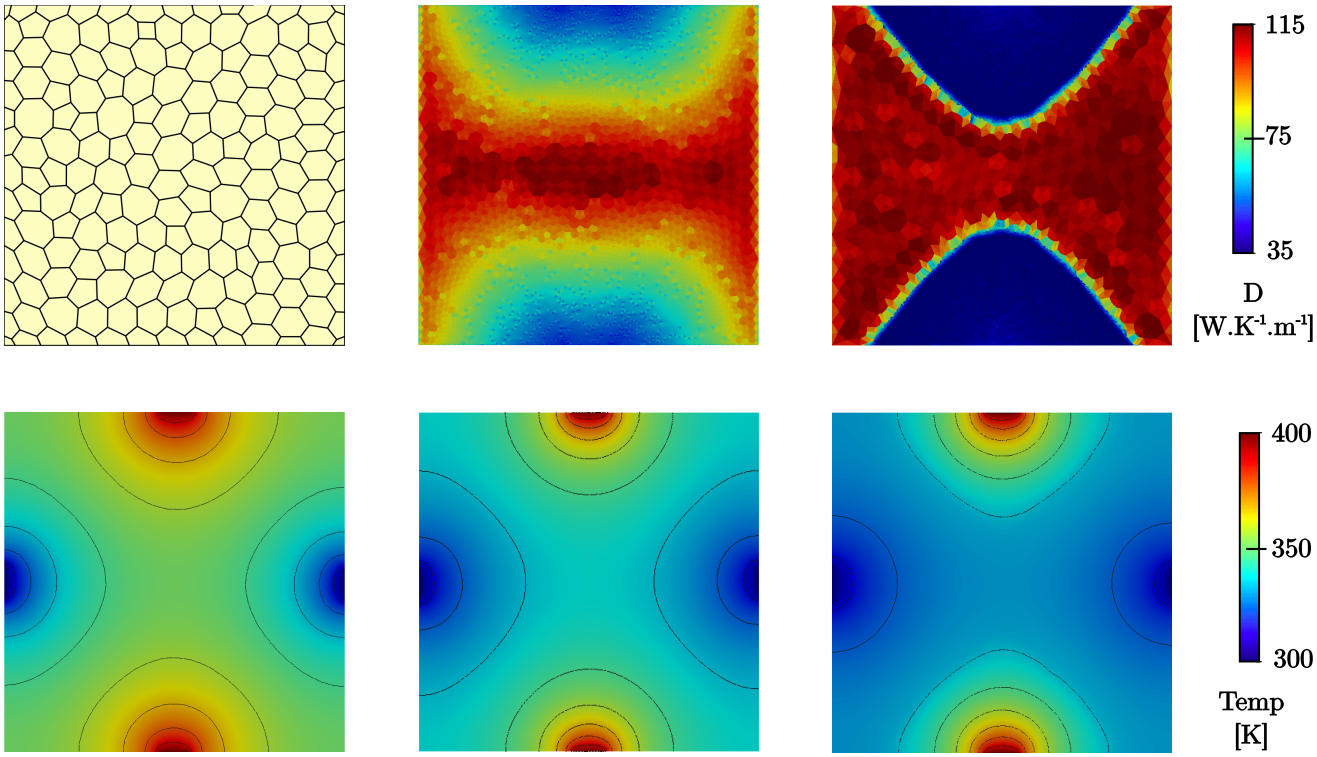

(a) Constant thermal conductivity

(b) Constrained gradient γ=1.67

(c) Unconstrained optimization

Figure 63: Influence of thermal gradient constraint on temperature distribution.

To conclude this sample problem, Figure 63 depicts the reconstructed microstructures for representative cases 1, 2, and 3, as highlighted on Figure 62, along with their corresponding temperature distribution. As previously discussed, case 1 has a constant thermal conductivity in the entire domain. The average temperature for this case is 350 K, as expected when considering the boundary conditions and configuration of the system. Case 2 is characterized by a value of the non-dimensional constant $\gamma = 1.67$. The optimized configuration is defined by large grains around the heat sinks and small ones surrounding the heat source. That is, regions of large thermal conductivity connect heat sinks, while heat sources are isolated by means of areas with low thermal conductivity. The transition from

large to small grain areas is smooth, as dictated by the gradient constrain. For this case, the optimal value of the objective function is 336.8 K and represents an improvement of 13.2% when compared to the constant thermal conductivity configuration. Finally, case 3 is almost free of any constraint, which generates a steep transition from regions with large to small grains. This configuration presents the best performance with an average temperature of 330.4 K, equivalent to a 19.6% improvement with respect to the constant thermal conductivity case.

4.3.4.2 Example 2

In this example of application, the focus is on the optimization of a thermal barrier coating. The geometry and boundary conditions for this problem are depicted in Figure64. The geometry is a rectangle of height $400\mu m$ and width $200\mu m$. The bottom and top surfaces include heat sources at $400K$ and $500K$ respectively. The rectangle is split into two parts of equal height. The bottom part of the model, or substrate, consists of a constant thermal conductivity material, with $D = 148\ WK^{-1}m^{-1}$ that corresponds to the bulk thermal conductivity of silicon. The top part, or coating, represents the design domain where the grain size is optimized. In this region, there is also a cooling pipe (heat sink) at a constant temperature $T = 300K$. The objective for this problem is to minimize the maximum temperature T at the coating/substrate interface.

To better illustrate the effect of grain size optimization, three different configurations are analyzed for this problem. In the first configuration, or case 1, there is no cooling pipe. For this problem, a constant value of thermal conductivity D over the entire coating domain is assigned. For the second configuration, or case 2, the same thermal conductivity D is assigned to the top coating. In addition, the cooling pipe is incorporated into the system. Finally, in case 3, in addition to the presence of a cooling pipe, the thermal conductivity is optimized over the coating domain. To guarantee consistency among the different scenarios, coating thermal conductivity is fixed to $D = 62.6\ WK^{-1}m^{-1}$ for cases 1 and 2, which is the same as the average thermal conductivity over the optimized domain for case 3.

For cases 1 and 2 there is no optimization to be performed, as one just needs to solve

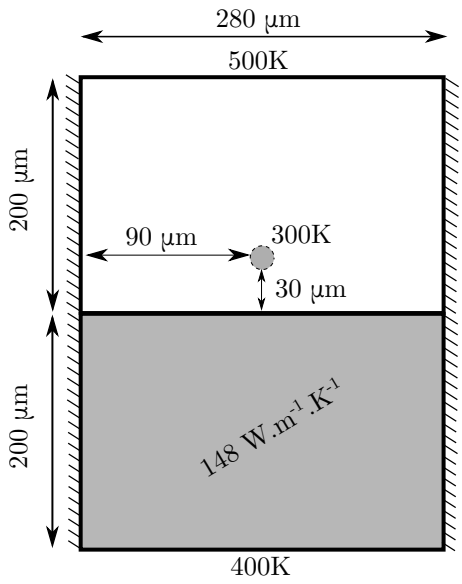

Figure 64: Geometry and boundary conditions for sample problem #2.

for the corresponding temperature fields. For case 3, the optimization problem can be formulated as follows

$$\begin{aligned} \underset{X_d, D_d}{\text{minimize}} \quad & \max_{X_d \in \{X(x,y):\ 0 \le x \le 280,\ y=200\}} T(X_d, D_d) \\ \text{subject to} \quad & \nabla D_{max} \le \nabla D_{opt} = 175 \times 10^3 W.K^{-1}.m^{-1} \\ & X_d \in [0, L_c]^{2N} \\ & D_d \in [40, 110]^N \end{aligned} \tag{4.3.10}$$

The thermal conductivity distribution, as well as the corresponding optimal temperature field for each case is shown in Figure 65. The maximum temperature at the interface for case 1 is 429.9 K. The addition of the pipe on case 2 results in a temperature drop at the interface to a value of 388.2 K. This significant improvement in the objective value (a 41.7 K decrease in maximum temperature at the coating/substrate interface) is expected and adopted as a reference to quantify the impact of the grain size optimization process. Finally, by optimizing the grain size distribution for case 3, the maximum temperature achieved at the interface is 367.7 K. This value represents a further 20.5 K temperature reduction at the interface. Thus, the benefit of the optimized grain size distribution represents 49.2% of the one provided by the pipe. That is, by optimizing the grain size distribution on the coating, it is possible to achieve a temperature reduction comparable to that obtained

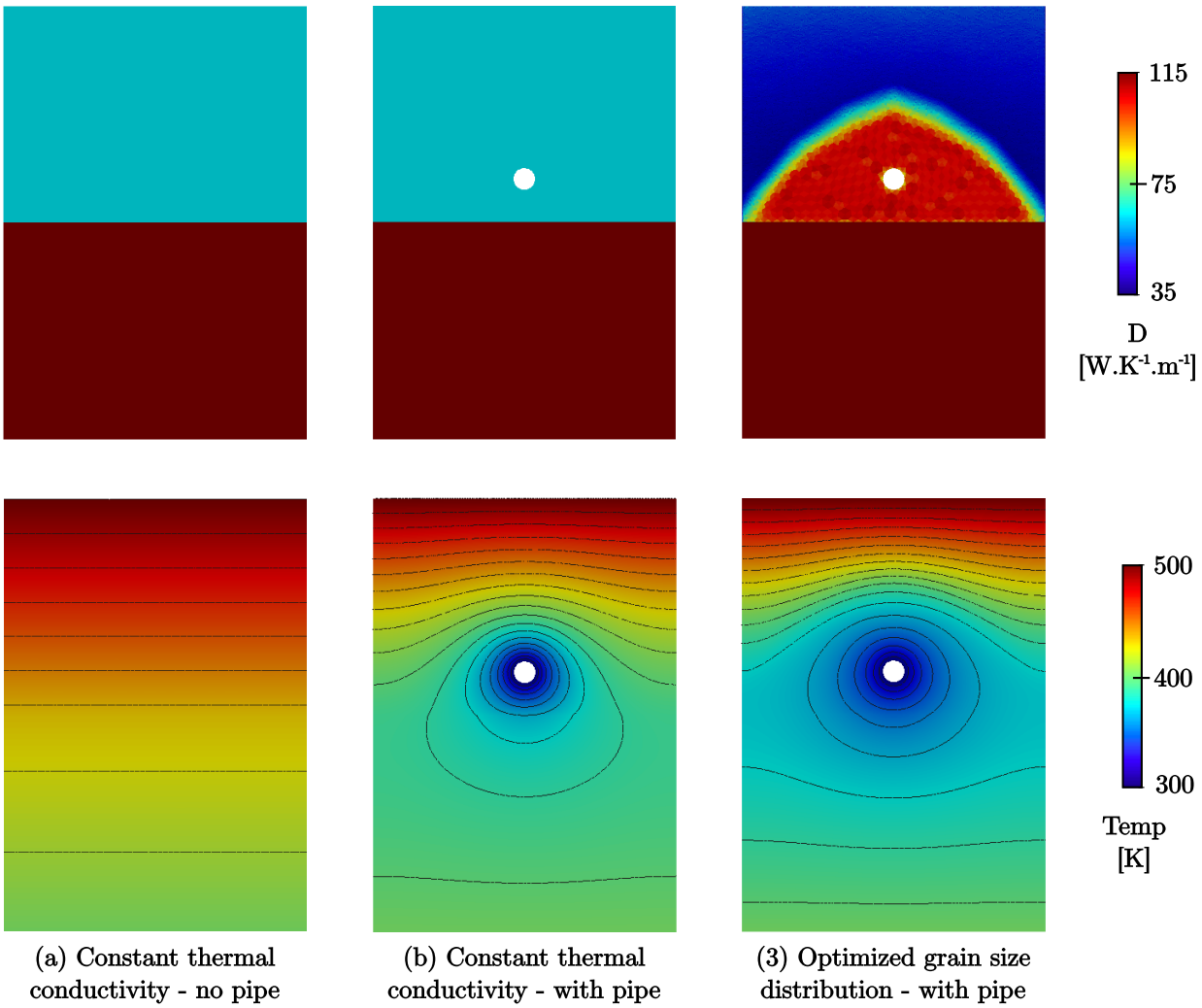

Figure 65: Distribution of thermal conductivity and temperature field for three different configurations.

through the addition of a heat sink. Finally, note that the overall temperature distribution is also remarkably different between the three different cases. It is worth remarking that this effect could be achieved with a single-material system, thus resulting in minimal thermal stresses associated to the variation in thermal conductivity.

Traditional approaches to thermal transport optimization usually rely on the presence of binary material system whose components exhibit a high contrast in the value of thermal conductivity. While such systems might result to be optimal from a thermal transport perspective, in general they would lead to significant thermal stresses at internal interfaces due to the associated high contrast in thermal expansion coefficients. These stresses, in

turn, could lead to premature thermomechanical failure of at internal interfaces. This work demonstrates how to circumvent this limitation by taking advantage of size-dependent effects in the thermal conductivity of materials. In the approach, the combination of the concurrent multiscale modeling with adaptive topology optimization techniques is key to optimize the spatial grain size distribution on single-material polycrystalline systems and their underlying thermal transport properties.

4.3.5 Conclusion

In this section, the traditional approaches to thermal transport optimization relying on the presence of binary material system is circumvented by taking advantage of the size-dependent effects in the thermal conductivity of materials. To obtain such results, the developed concurrent multiscale modeling approach is combined with adaptive topology optimization techniques to optimize the spatial grain size distribution on single material polycrystalline systems. Two specific examples demonstrated that it is possible to develop single-material systems with optimized thermal transport properties. Ultimately, the use of a single material prevents the apparition of significant thermal stresses at internal interfaces between material presenting a high contrast in the value of thermal conductivity.

4.4 MFP Kapitza Resistance

As demonstrated in Section 4.1, the multiscale model developed in this work leads to the creation of a thermal resistance layer near the grain boundary, which are especially noticeable when considering high mesh refinement. This non-uniform thermal conductivity impacts the temperature distribution in the material. Moreover, it can generate a concentration of stress at the grain boundary interface that can lead to crack nucleation.

Numerical finite element modeling of dynamic intergranular fracture in polycrystals is often accomplished through the use of cohesive elements. In such simulations, interface elements are used to discretize the grain boundaries and are prescribed a constitutive relation

which imparts on the boundary a finite stiffness, strength, and/or toughness.

With respect to the thermal problem, the ideal scenario would be to use a constraint to enforce temperature continuity across a grain boundary. However, such constraints invariably lead to prohibitively small stable time increments. Hence, it is crucial from a numerical perspective that a finite thermal resistance, be present at the grain boundary. Such a resistance is referred to as a Kapitza resistance. For instance, it is a common methodology in modeling polycrystalline ceramics, However, as it will be discussed in detail in this section, some drawbacks to current Kapitza resistance models exist, the main one being that they often fail to predict the correct effective thermal behavior.

In this section, the framework developed in the thesis and referred as the 'full MFP' model will be compared to different Kapitza models. The numerical examples consider silicon carbide (SiC). As previously described, the same methodology is used to obtained the surface of the thermal conductivity as a function of the grain size and temperature, as represented in Figure 66.

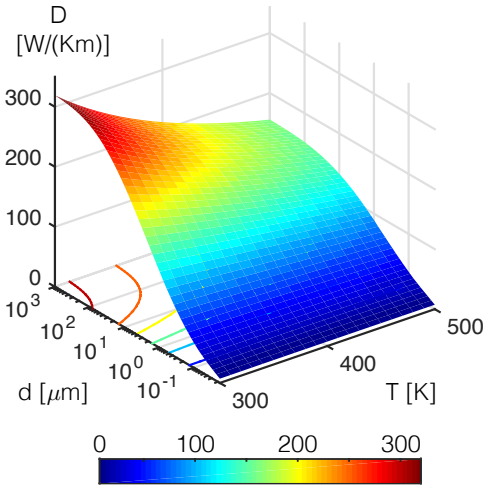

Figure 66: Surface of average D as a function of grain size and temperature computed using the 'full MFP' model.

An alternative approach relies on the use of the full MFP model to develop a homogenized behavior. In this approach, the spatially varying thermal conductivity within each grain is replaced with a constant, yet still grain size-dependent, thermal conductivity equal to

the average value of the spatially varying conductivity. Such a homogenization is shown in Figure 67b, where the granular conductivity is equal to the average over the grain. This model is referred to as the 'homogenized MFP' model. One major benefit of this approach is that it does not require such a fine numerical discretization of the problem, since it is not necessary to resolve the spatially varying conductivity. In addition, it is worth noting that both the full and homogenized MFP models produce the same effective conductivities when applied to modeling the same microstructure. The conductivity for a given grain at a given temperature is efficiently computed by first precomputing the surface, of Figure 66, which returns the thermal conductivity for a given grain size and temperature. The use of this surface will be essential in the Kapitza models developed in this section.

Although both the full and homogenized MFP models can accurately capture various features of the grain size-dependent thermal conductivity, they do so at the additional numerical complexity and cost associated with solving for the thermal conductivity. Moreover, as discussed in detail later, when modeling the thermomechanical behavior of polycrystalline materials including dynamic intergranular fracture, it is desirable, from a numerical perspective, to have a portion of the effective thermal conductivity be determined by a grain boundary conductivity: that is through a Kapitza resistance, as discussed next.

4.4.1 Kapitza Resistance Models

4.4.1.1 Description of Kapitza Resistance

As previously mentioned, an alternative approach to modeling the grain size-dependent thermal conductivity of polycrystaline materials is through the use of a Kapitza resistance. Physically, in such an approach, the deviations of the conductivity near the grain boundary are lumped into a single constant resistance at the grain boundary. Such models have a natural grain size dependence which arises from the increase in surface area to volume ratio at smaller grain sizes. Hence, it increases the effect of the Kapitza resistance at smaller grain sizes.

In general, considering a uniform grain size distribution and the assumption that each

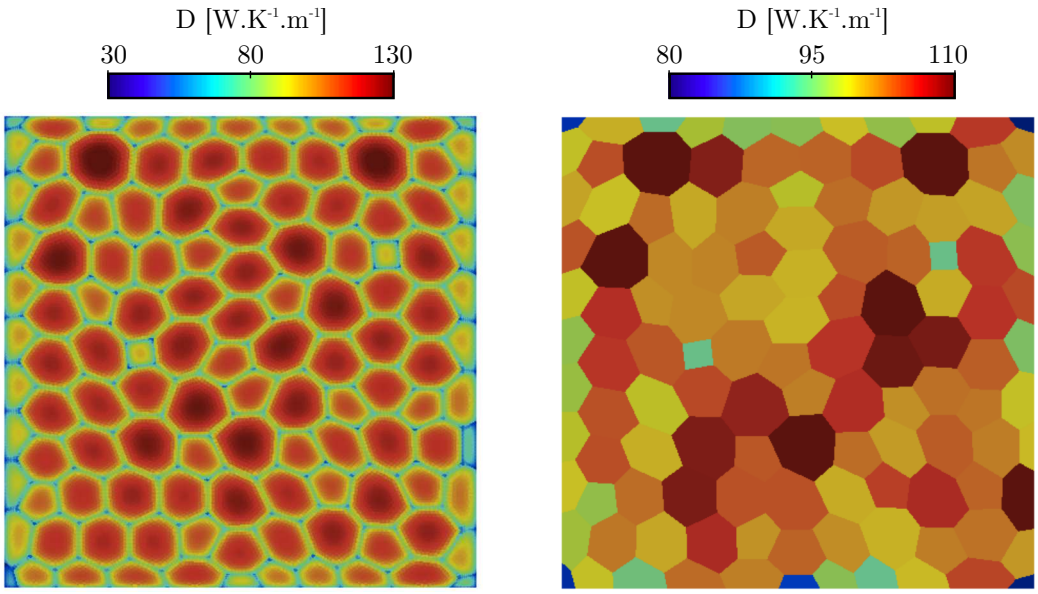

(a) Full MFP (b) Homogenized MFP

Figure 67: Comparison 'full MFP' and 'homogenized MFP' models.

grain boundary is shared by two grains, one may write that the effective conductivity of a polycrystal D_{eff} is expressed as a function of the grain size d through

$$D_{\text{eff}} = \frac{D_{\text{intra}}}{1 + R_K D_{\text{intra}}/d} \tag{4.4.1}$$

where R_K is the Kapitza resistance, and D_{intra} is the intragranular conductivity.

Various models have been developed based on the aforementioned general idea by specifying R_K and D_{intra}. For example, two models recently discussed by Dong et al.[129] are given by

$$D_{\text{eff}}^{(\text{a})} = \frac{D_0}{1 + R_K D_0/d}, \qquad \text{and} \qquad D_{\text{eff}}^{(\text{b})} = \frac{D_0/(1 + \Lambda_0/d^{0.75})}{1 + R_K[D_0/(1 + \Lambda_0/d^{0.75})]/d}. \tag{4.4.2}$$

where R_K is a constant Kapitza resistance, usually determined from molecular dynamics simulations. Model (a) is derived by considering a constant intragranular resistance equal to the bulk thermal conductivity $D_{\text{intra}} = D_0$ [130, 131]. Model (b) is derived assuming a grain size-dependent intragranular conductivity which depends both on the bulk conductivity D_0 and the bulk mean free path Λ_0 [129]. To some extent, model (b) captures the grain size-dependent intragranular conductivity and combines it with an additional Kapitza resistance. Physically, it is unclear how one can justify the use of both a Kapitza resistance as well

as a size-dependent intragranular conductivity to capture the effective conductivity of a polycrystal since both are accounting for one single physical phenomenon. The grain size-dependent intragranular conductivity should suffice in capturing the phenomena of interest, since all of the relevant physics are included. Further, the notion of a Kapitza resistance is based on the presence of a boundary layer near the grain boundary over which the thermal conductivity is decreasing. However, as the grain size decreases the effect of the grain boundary on the thermal conductivity is present throughout the entire grain and no well-defined boundary layer can be identified.

As an illustration, Figure 68 shows the variation of the thermal conductivity D for SiC across the midline of polygonal grains of various sizes, computed using the full MFP model discussed earlier. It is observed that at larger grain sizes of approximately $d > 200\mu$m, there is an explicit boundary layer with a portion of the conductivity within the center of the grain equal to the bulk thermal conductivity. However, as grain sizes approach $d = 200\mu$m and smaller, the boundary layer is no longer well-defined as the entirity of the grain is affected by the presence of the grain boundary.

Models relying on a constant Kapitza and intragranular resistance, such as model (a) in Equation (4.4.2), are thus physically justifiable only for large grain sizes, on the order of $200\mu m$ and above. Below this grain size, there is no longer a well-defined grain boundary. This also has crucial implications for the use of MD simulations in calculating the Kapitza resistance for small grain sizes.

In MD simulations, only a small nanometer region near the boundary is simulated in order to compute the Kapitza resistance [110]. However, as shown in Figure 68, the variation in thermal conductivity is significant throughout the entirety of the grain, and as such the entire grain would need to be modeled. Hence, it can be argued that the use of a Kapitza resistance in modeling the thermal behavior of polycrystals is not physically justifiable. However, as discussed next, there are some unique advantages and benefits, from a numerical modeling perspective, to using a Kapitza resistance model.

The aforementioned Kapitza approaches are beneficial in that they provide a relatively

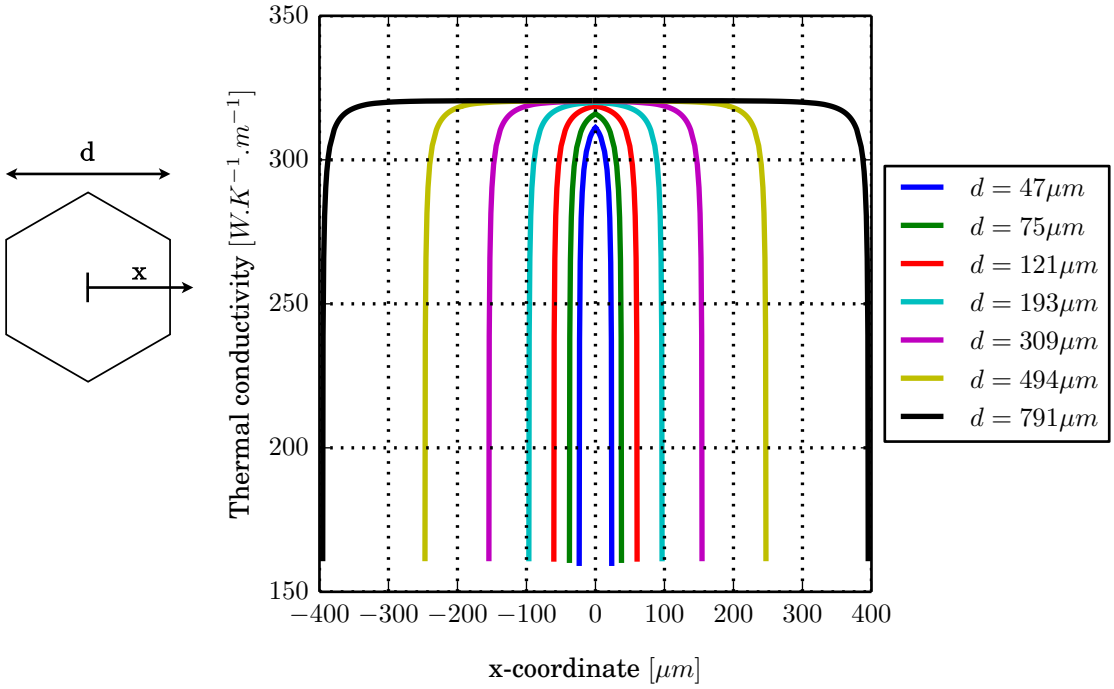

Figure 68: Variation of the thermal conductivity D within a grain as computed using the full MFP model for hexagonal grains of various sizes at $T = 300K$.

simple, and often analytical, approach to modeling grain size-dependent thermal conductivity of polycrystals. Furthermore, from a numerical perspective, the use of a Kapitza resistance is particularly useful in modeling dynamic intergranular fracture of polycrystals, through the use of cohesive elements. In such a system, cohesive elements are used to discretize the grain boundaries of the polycrystal and capture the physics associated with intergranular fracture. That is, to some extent, the use of a Kapitza resistance is justified purely from numerical reasons. However, there are some drawbacks to the current Kapitza models. Namely, they often predict effective conductivities larger than those predicted through experiments and simulations.

4.4.1.2 Comparison of Kapitza Models

Kapitza models predicting the effective conductivity D_{eff} of a uniform polycrystal often predict effective conductivities larger than those obtained through experiments and simulations. At small grain sizes, this effect is in part due to the fact that the intragranular conductivity changes with grain size, a fact that is well captured by the full and homogenized MFP models discussed earlier.

Model (b) in Equation (4.4.2) attempts to rectify this error by using a grain size-dependent intragranular conductivity of the form $D_{\text{intra}} = K_b/(1 + \Lambda_0/d^{\alpha})$, with α a fitting coefficient determined by comparing to MD simulations. It is worth noting that this expression presents some inconsistency in the units when $\alpha \neq 1$. Regardless, their model is included as presented in their work.

To illustrate the different predictions of the two Kapitza models in Equation (4.4.2) as well as the predictions of the full and homogenized MFP models, Figure 69 shows the effective thermal conductivity for the various models as a function of grain size, at $T = 300$K. The results presented are for silicon carbide (SiC), which is chosen due to the availability of material properties in the literature, as well as the fact that Kapitza models are commonly used for this material [110]. For the Kapitza models in Equation (4.4.2), the used values are: $D_0 = 320W.K^{-1}.m^{-1}$, $R_K = 5 \times 10^{-10}K.m^2.W^{-1}$, and $\Lambda_0 = 50$nm, which are reproduced from the literature [110]. The effective conductivity for the full MFP model is computed using the microstructure shown in Figure 67, while varying the grain size. A temperature differential of 10K is applied across the vertical direction in the simulation domain and the steady-state flux is measured. The effective conductivity is then simply obtained as the steady-state flux divided by the temperature differential across the boundary.

As shown in Figure 69, the size-dependent thermal conductivity produced by the Kapitza models is significantly different than the one produced by the MFP model. Further, while all models fail to precisely capture the experimental measurements, the MFP models give the closest approximation of the experimentally measured response. The discrepancy between

the MFP model and the experimental data is attributed to the contribution of imperfections to the experimental measurements, which are not accounted for in the model, as well as potential uncertainty in the actual value of the bulk thermal conductivity. As illustrated through Figure 69, current Kapitza models do not accurately capture the grain size-dependent thermal conductivity of polycrystals.

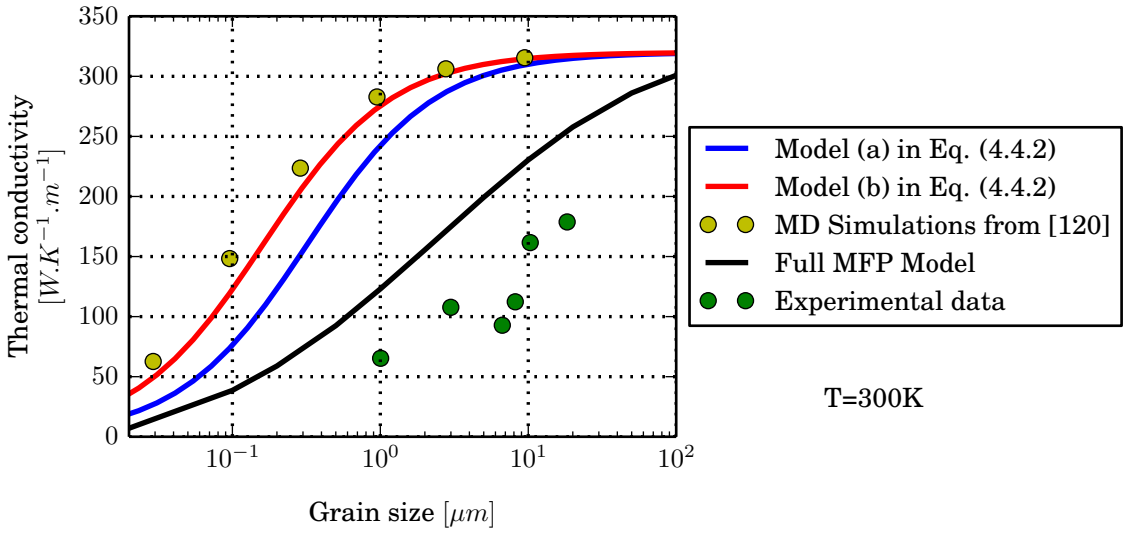

Figure 69: Grain size dependence of the effective thermal conductivity D_{eff} for SiC.

To overcome this issue, various models are next considered in which either the intragranular conductivity D_{intra}, the Kapitza resistance R_K, or both quantities are grain size-dependent. Specifically, it will make use of the homogenized MFP model to develop the correct grain size-dependent D_{intra} and R_K, so as to capture the correct effective conductivity and kinetics.

4.4.2 MFP Calibrated Kaptiza Models

In this subsection, various models are considered in which either the intragranular conductivity D_{intra}, the Kapitza R_K, or both are grain size-dependent. Specifically, the developed models recover the same effective conductivity D_{eff} as the full and homogenzied MFP models. For a given grain, the desired effective D_{eff} and average D_{avg} thermal conductivity are calculated using the full MFP model. This is the same average conductivity as the one used

in the homogenized MFP model, Figure 67b. As a reminder, it is precomputed in the form of the surface shown in Figure 66, and hence can be quickly looked up for a given grain size and temperature.

Consider two grains, A and B, as depicted schematically in Figure 70. At a given integration point i within a given grain, the temperature T_i and grain size d (a constant for a given grain) are inputs to the surfaces generated from our MFP models to compute the average, $D_{\text{avg},i}$, and maximum, $D_{\text{max},i}$, thermal conductivities for that given integration point. The average of these quantities over an entire grain can furter be computed as

$$\bar{D}^A_{\text{avg}} = \frac{1}{n}\sum_{i=1}^{n} D_{\text{avg},i}, \quad \bar{D}^A_{\text{max}} = \frac{1}{n}\sum_{i=1}^{n} D_{\text{max},i}, \tag{4.4.3}$$

where A denotes the particular grain of interest, and n is the total number of integration points for the grain of interest. It is worth noting that an area weighted expression provides the same values, as the FEM elements present the same size and same geometry. For a given grain boundary, one may even define a cross element average of these quantities, following the schematic shown in Figure 70 and computed as

$$\bar{D}^{AB}_{\text{avg}} = \frac{1}{2}\left(\bar{D}^A_{\text{avg}} + \bar{D}^B_{\text{avg}}\right), \quad \text{and} \quad \bar{D}^{AB}_{\text{max}} = \frac{1}{2}\left(\bar{D}^A_{\text{max}} + \bar{D}^B_{\text{max}}\right), \tag{4.4.4}$$

where the superscripts A and B denote the two grains adjacent to the grain boundary of interest.

To guide the design, the simple relation (4.4.1) is used. It relates the effective conductivity of a one-dimensional polycrystal of a given grain size with its intragranular conductivity and Kapitza resistance. For models in which the aim is to compute the Kapitza resistance based on a given intragranular and effective thermal conductivities, Equation (4.4.1) becomes

$$R^{AB}_K = \left(\frac{d^A + d^B}{2}\right)\left(\frac{1}{\bar{D}^{AB}_{\text{eff}}} - \frac{1}{\bar{D}^{AB}_{\text{intra}}}\right) \tag{4.4.5}$$

where the superscript AB denotes the grain boundary defined by two adjacent grains A and B. For models in which the aim is to compute the intragranular thermal conductivity based

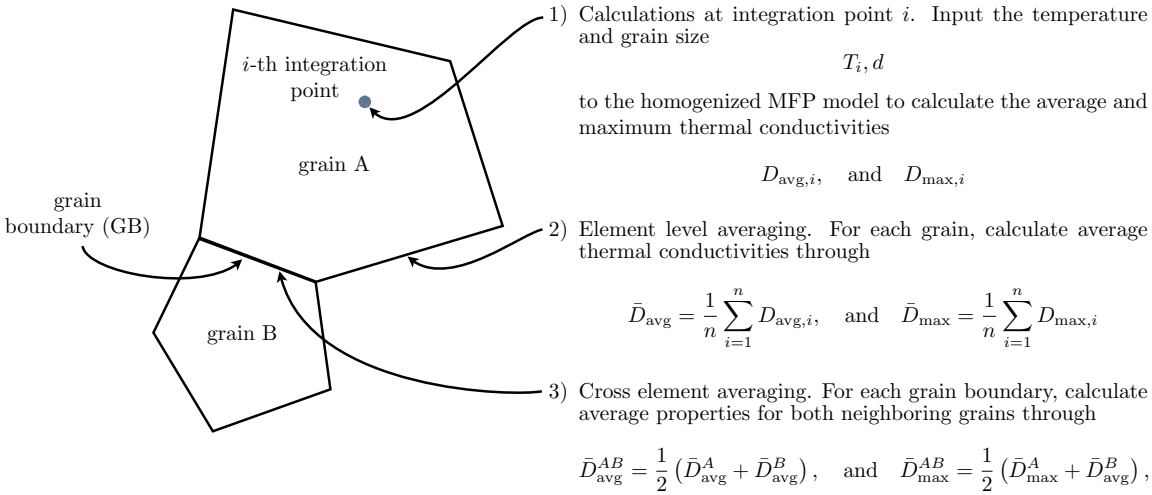

Figure 70: Schematic illustrating the calculation of the average and maximum thermal conductivities at a given grain boundary.

on given effective thermal conductivity and constant Kapitza resistance, (4.4.1) becomes

$$\bar{D}^{A}_{\text{intra}} = \frac{\bar{D}^{A}_{\text{eff}}}{1 - R_K \bar{D}^{A}_{\text{eff}}/d^A} \tag{4.4.6}$$

where A denotes the grain of interest and R_K must be a constant resistance applied to all boundaries surrounding the grain. In order to ensure that all models capture the same effective thermal conductivity, the effective thermal conductivity of a given grain is set equal to the average thermal conductivity computed using the homogenized MFP model. That is, in Equation (4.4.5): $\bar{D}^{AB}_{\text{eff}} = \bar{D}^{AB}_{\text{avg}}$ and in Equation (4.4.6): $\bar{D}^{A}_{\text{eff}} = \bar{D}^{A}_{\text{avg}}$. This ensures that the models developed here will have the same effective thermal properties as those produced by the full and homogenized MFP models.

There are then three options as to how one can taylor D_{intra} and R_K to recover the desired D_{eff}. These three models are illustrated in Figure 71. It shows the Kapitza resistance R_K and the intragranular conductivity D_{intra} as a function of grain size, for three constant temperatures $T = 300$K, $T = 400$K, and $T = 500$K.

The three models are defined as follows

I : D_{intra} is constant and R_K is grain size-dependent.

The intragranular thermal conductivity is chosen as the bulk one, i.e. $D_{\text{intra}} = D_0$, as it is traditionally done in Kapitza models. The Kapitza resistance R_K is then grain

size-dependent and may be computed using Equation (4.4.1) and the desired D_{eff}.

II : R_K is constant and D_{intra} is grain size-dependent.

The Kapitza resistance R_K is arbitrarely chosen equal to a constant. Here, the grain size dependence of D_{intra} is computed using Equation (4.4.1) for a given R_K in order to yield the same D_{eff} as the MFP models. The value of the Kapitza resistance must be smaller than $R_K < d/D_{\text{eff}}$, otherwise an infinite D_{intra} would be required to achieve the desired effective resistance. Beyond this restriction, the Kapitza resistance can be chosen from convenience.

III : Both R_K and D_{intra} are grain size-dependent.

Specifically, at a given grain boundary, the maximum thermal conductivity $D_{\max}$ of the two adjacent grains is computed using the full MFP model and use the average values of these maxima as the intragranular conductivity. Similar to before, the values of $D_{\max}$ for a range of grain sizes and temperature are precomputed using the full MFP model. The Kapitza resistance R_K is then computed using Equation (4.4.1) in order to recover the desired effective behavior.

The three aforementioned models are shown in Figure 71. For model II, two possible values of R_K are considered: the larger $R_K = 2.47 \times 10^{-9} K.m^2.W^{-1}$ is chosen such that the intragranular conductivity does not exceed the bulk conductivity for any grain size. The smaller $R_K = 5.30 \times 10^{-10} K.m^2.W^{-1}$ is chosen as the minimum R_K value for model III. The two values of R_K are chosen in regards of the specific temperature range [300,310]K.

By construction, all three models produce the same effective resistance D_{eff} as the full MFP model and thus provide a good description of the effective grain size-dependent behavior of the polycrystal. However, all three models do not have the same kinetic behavior. For a particular boundary value problems, the various Kapitza models will produce thermal jumps at the grain boundary, the order of which depends on the particular R_K, D_{intra}, and D_{eff} values for a given model. This limitation is illustrated in the next subsection.

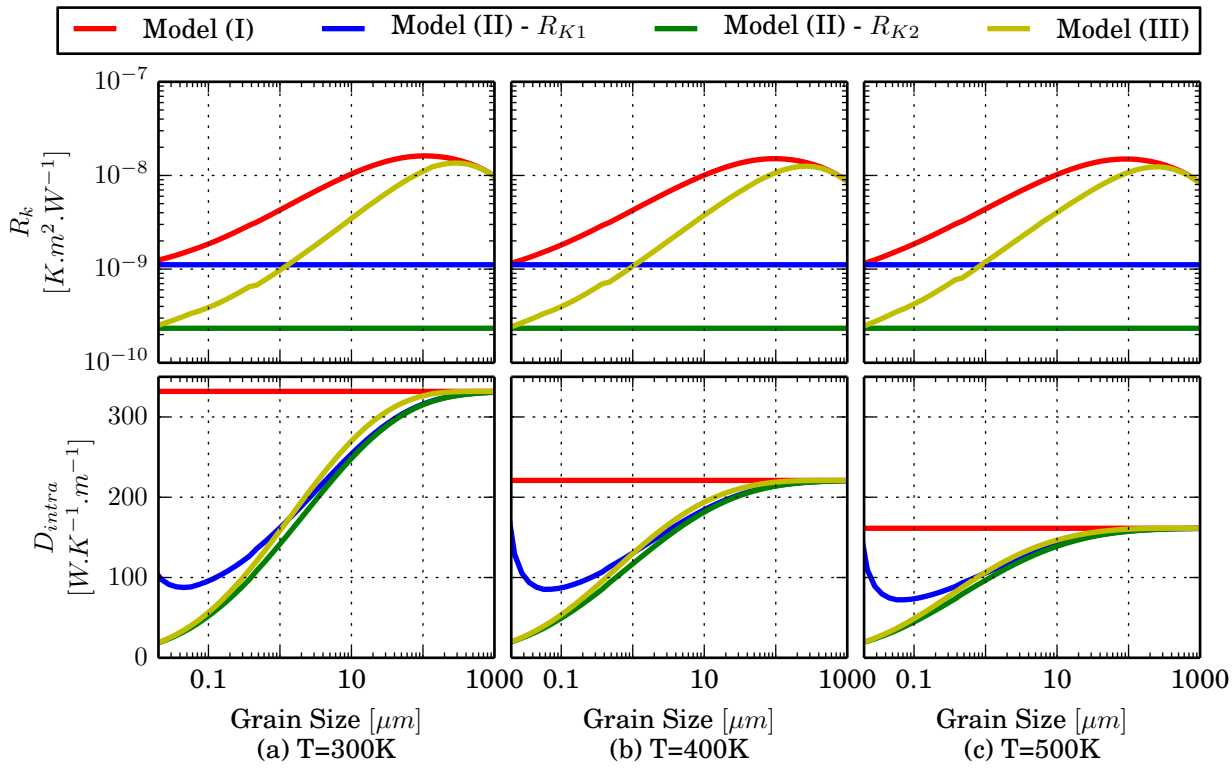

Figure 71: Grain size dependence of
(a) Kapitza resistance R_K and (b) intragranular conductivity D_{intra}.
$R_{K1} = 1.11 \times 10^{-9} K.m^2.W^{-1}$ - $R_{K2} = 2.34 \times 10^{-10} K.m^2.W^{-1}$
Values selected based on the temperature range [200,600]K.

4.4.3 Numerical Results

4.4.3.1 Uniform Polycrystal

To illustrate the concept presented in the previous subsection, heat conduction simulations are performed on a domain containing approximately 100 grains of size $d = 0.5\mu$m. Four simulations were run corresponding to: Model I, Model II with the two values of R_K discussed earlier, and Model III.

The microstructure along with the values of D_{intra} and R_K are displayed in Figure 72. Each hexagonal grain is discretized with 384 triangular fully integrated elements, and each boundary is discretized with 8 cohesive zone elements. Model I, represented in Figure 72a, use a constant intragranular thermal conductivity $D_{\text{intra}} = D_0 = 320 W.K^{-1}.m^{-1}$, and a grain size-dependent R_K. Note that although the grain structure shown is representative of a uniform polycrystal with grain size on the order of $0.5\mu m$, there is naturally a grain

size variation from the construction of the grain structure which leads to the variation in R_K. Model II, represented in Figure 72c and 72e, respectively considers the following values $R_K = 2.47 \times 10^{-9} K.m^2.W^{-1}$ and $R_K = 5.30 \times 10^{-10} K.m^2.W^{-1}$. Both have a grain size-dependent D_{intra} as shown in the figures. Model III, represented in Figure 72g, has a grain size-dependent D_{intra} equal to the maximum conductivity for a given grain size computed using the full MFP model. It also use a grain size dependent R_K. For all three simulations, a constant initial temperature of $T = 300$K is set. At time zero, the bottom boundary is prescribed a temperature equal to $T = 310$K and the top boundary is maintained to the initial temperature. The left and right boundaries are prescribed a zero flux boundary condition. The right column of Figure 72 shows contours of temperature for all models at steady-state.

Form these contours, it is clear that although all of these models produce the same effective conductivity across the microstructure, they do not produce the same temperature distribution with some models producing large temperature jumps at the grain boundaries. Limiting these artificial temperature jumps is of critical importance in modeling the thermomechanical behavior of these materials. Indeed, those jumps could produce unrealistic thermal stresses in the material and hence would affect the ability of the model to predict intergranular failure.

To quantify the thermal jumps, Figure 73 shows profiles of the temperature across the center cross section of the simulation domain at: (a) $t = 2$ns, (b) $t = 10$ns, and (c) $t = 50$ns. For clarity, the temperature profile is plotted only for the first couple of grains. As shown in Figure 73, although all Kapitza resistance models produce a temperature jump at the grain boundary, the magnitude of the jump is significantly worse for Model I and Model II with the larger value of $R_K = 2.47 \times 10^{-6} K.m^2.W^{-1}$. As the simulation time progresses and the gradients in temperature decrease, the magnitude of the temperature jumps at the grain boundaries decrease and become minimum at steady-state, as displayed in Figure 73d.

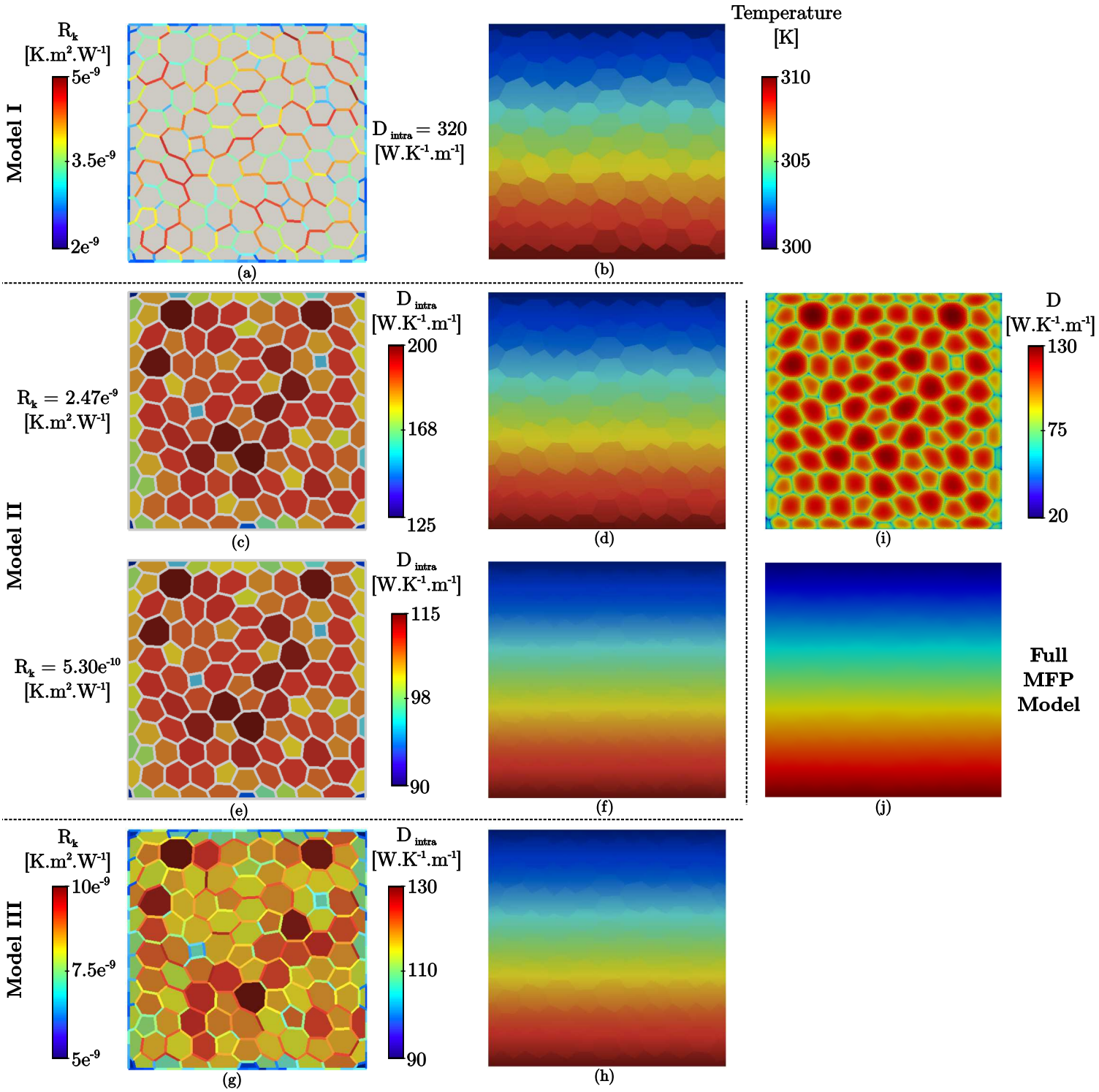

Figure 72: Heat conduction simulations for the Kapitza models.
Model I : constant D_{intra} and grain size-dependent R_K.
Model II : constant R_K and grain size-dependent D_{intra}.
Model III : grain size-dependent R_K and D_{intra}.
Left column = D_{intra} and R_K - Right column = Temperature at steady-state.

The temperature jumps at steady-state can also be analytically predicted. Indeed, the flux at the grain boundary is given by $\Delta T_{\mathrm{GB}}/R_K$ where ΔT_{GB} is the temperature jump across the boundary, and the flux across the entire simulation domain is given by $\Delta T D_{\mathrm{eff}}/(n\,d)$, where ΔT is the prescribed temperature difference across the domain, d is the grain size, and n is the approximate number of grains across the domain which for those simulations is 10. Hence, it yields to the following relation

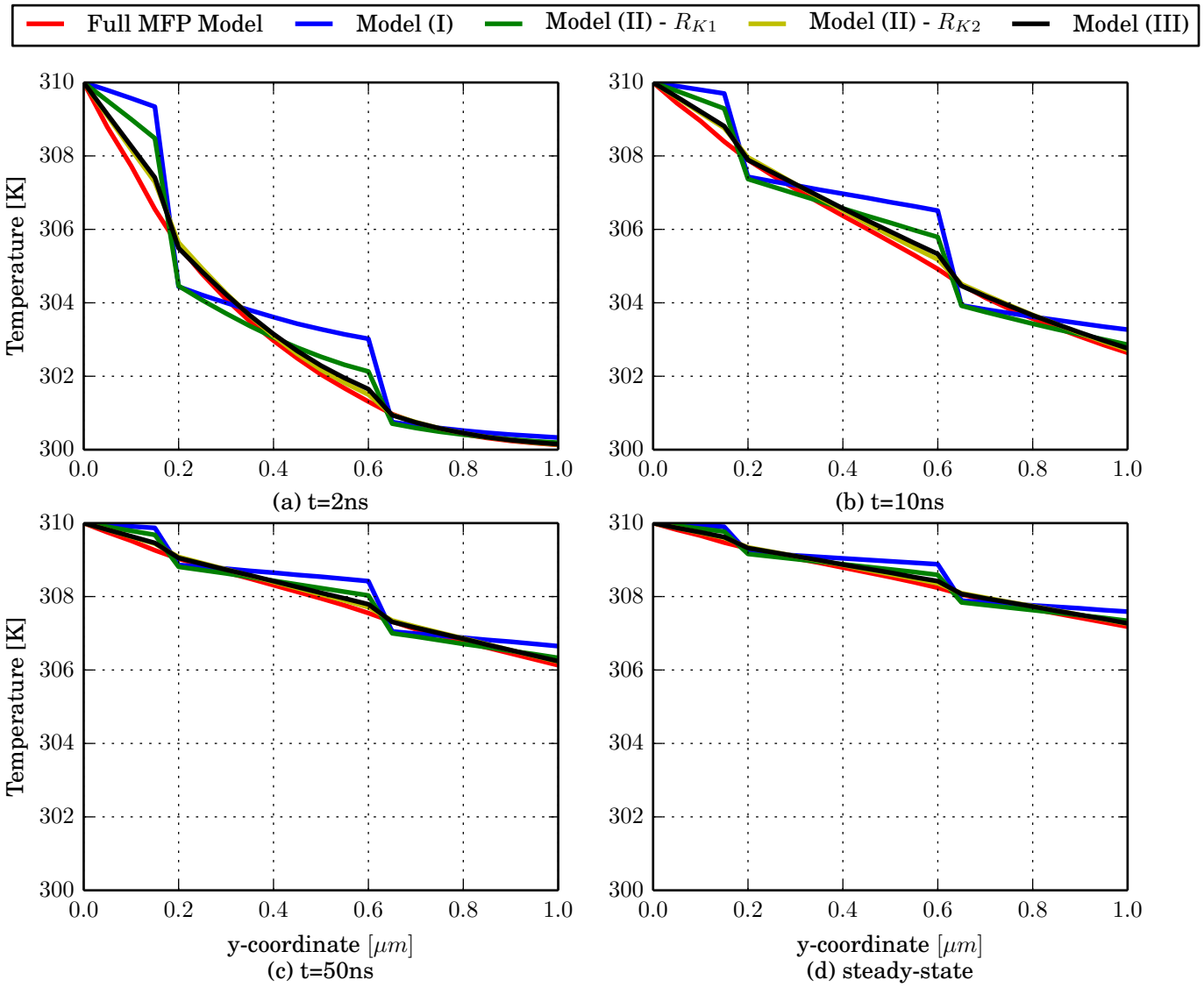

Figure 73: Temperature profiles across the simulation domain at different times. $R_{K1} = 2.47 \times 10^{-9} K.m^2.W^{-1}$ - $R_{K2} = 5.30 \times 10^{-10} K.m^2.W^{-1}$

$$\frac{\Delta T_{\mathrm{GB}}}{\Delta T} = R_K \frac{D_{\mathrm{eff}}}{n\, d}, \tag{4.4.7}$$

where D_{eff} depends on R_K, D_{intra}, and d through Equation (4.4.1). From Equation (4.4.7) it can be notice that larger R_K values invariably lead to larger temperature jumps at the grain boundary interfaces. This effect is also less pronounced at larger grain sizes.

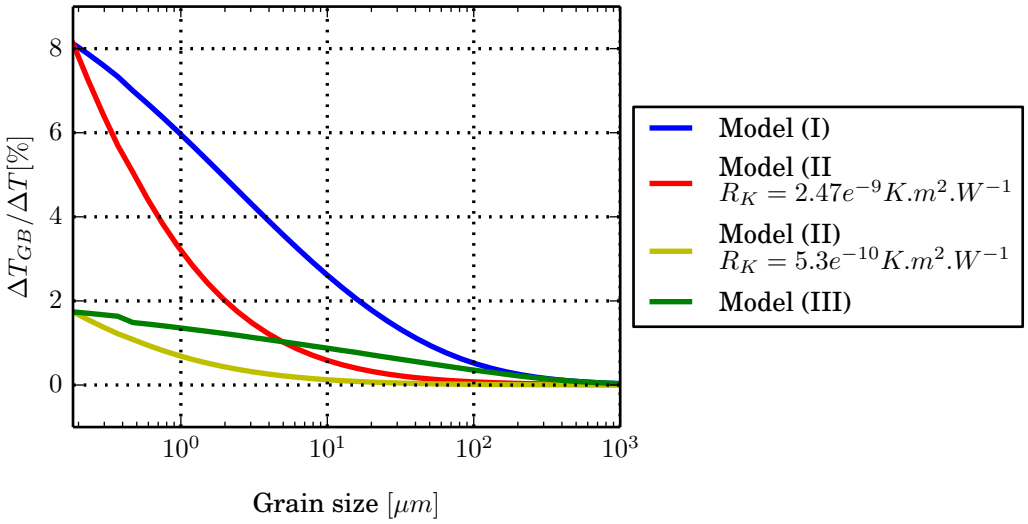

Figure 74: Analytical normalized grain boundary temperature jump as a function of grain size.

Figure 74 shows the normalized temperature jump across the grain boundary $\Delta T_{\mathrm{GB}}/\Delta T$ in percent as a function of grain size for the three different models. It is noticeable that Model II can be tailored to produce virtually any normalized GB temperature jump by choosing an appropriately small value of R_K. For the case where R_K is chosen as the smallest R_K used in Model III, Model II will in fact always outperform all other models in terms of producing the smallest GB temperature jump. However, as discussed earlier, from a computational perspective small values of R_K produce prohibitively small stable time increments for modeling dynamic intergranular fracture. For this reason, Model III provides a good compromise between producing a low GB temperature jump without using a too small value for the Kapitza resistance R_K. Uniquely, unlike the other models, Model III has a clear physical interpretation, where the Kapitza resistance accounts for the variation in the grain size-dependent intragranular resistance from its average value to its maximum

values. Finally, contrary to the MFP models, it accounts for failure of the polycrystalline materials due to intergranular fracture, through the presence of Kapitza resistance at the grain boundary.

Figure 75 presents the effective conductivity that is computed across the simulation domain as $JL/\Delta T$, where J is the steady-state flux on either the top or bottom surface, L is the length of the simulation domain, and ΔT is the applied temperature differential. It is important to reiterate that all previously introduced models produce essentially the same effective conductivity across the uniform polycrystal. In Figure 75, the exactly same polycrystalline microstructure is considered, however the temperature boundary conditions have been changed to 200K at the top edge and 600K at the bottom edge. This analysis allows to verify that the methodologies provide the same D_{eff} over a large range of temperature.

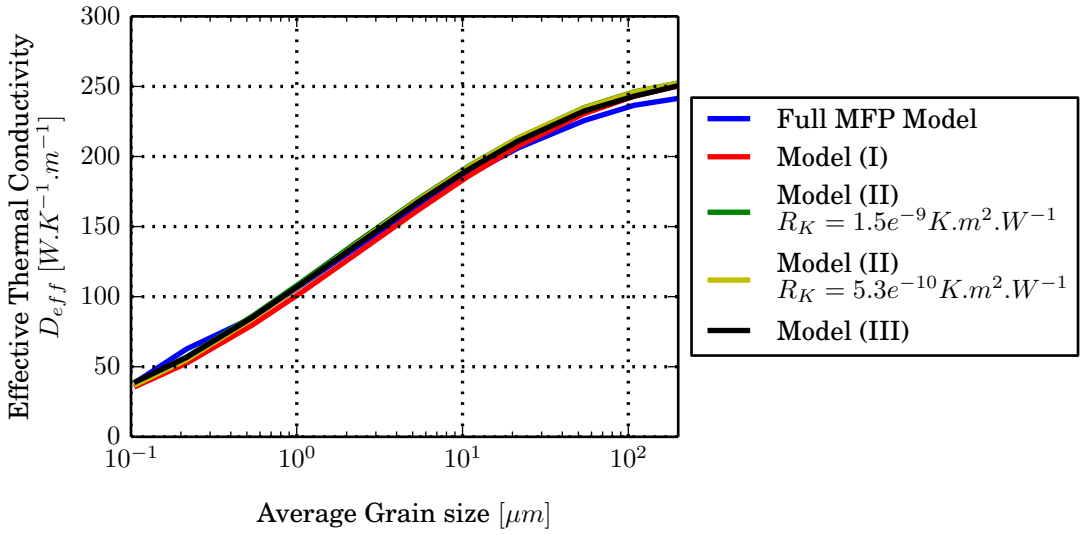

Figure 75: Effective thermal conductivity across a uniform polycrystal with varying average grain size as computed using the MFP calibrated Kapitza models and the full MFP models.

4.4.3.2 Functionally Graded polycrystal

In this subsection, the goal is to verify that the proposed methodology works perfectly when the grain size within the polycrystal is not uniform. Thus, the geometry considered for the graded polycrystal is a slab of length $125\mu m$ and width $25\mu m$. It is composed of grains

whose size vary linearly from $0.5\mu m$ at the bottom to $5\mu m$ at the top. Figure 76 represents the geometry.

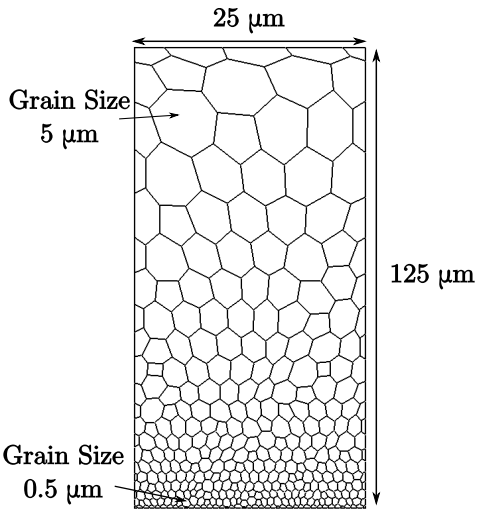

Figure 76: Geometry of the graded polycrystalline structure.

The ratio of 10:1 between the size of the large and small grains generates a significant disparity among the three different Kapitza models presented in Subsection 4.4.2. To obtain such effect, the range of grain size has been purposefully selected. On the one hand, $0.5\mu m$ constitutes a physical limit: grains below that dimension tend to be affected by quantum size effect. On the other hand, $5\mu m$ constitutes a practical limit. For grains over that size, the intragranular thermal conductivity D_{intra} is close to the bulk thermal conductivity D_0, leading to negligible differences between the models. It is worth noting that those ranges depend on the material considered and are given here in the case of silicon carbide.

As presented in the previous section, the different Kapitza models enable to recover the same value of the effective thermal conductivity while having different D_{intra}, as displayed in Figure 77. In this simulation, boundary conditions of $200K$ at the top edge and $600K$ at the bottom edge are prescribed. The full MFP model (see Figure 77c) provides a thermal property of $D_{eff} = 149.5W.K^{-1}.m^{-1}$. As usual, this model constitutes the baseline and an identical value of D_{eff} should be recovered by any other models proposed in this subsection. Resulting from the FEM simulations, the thermal conductivity of models I and III are

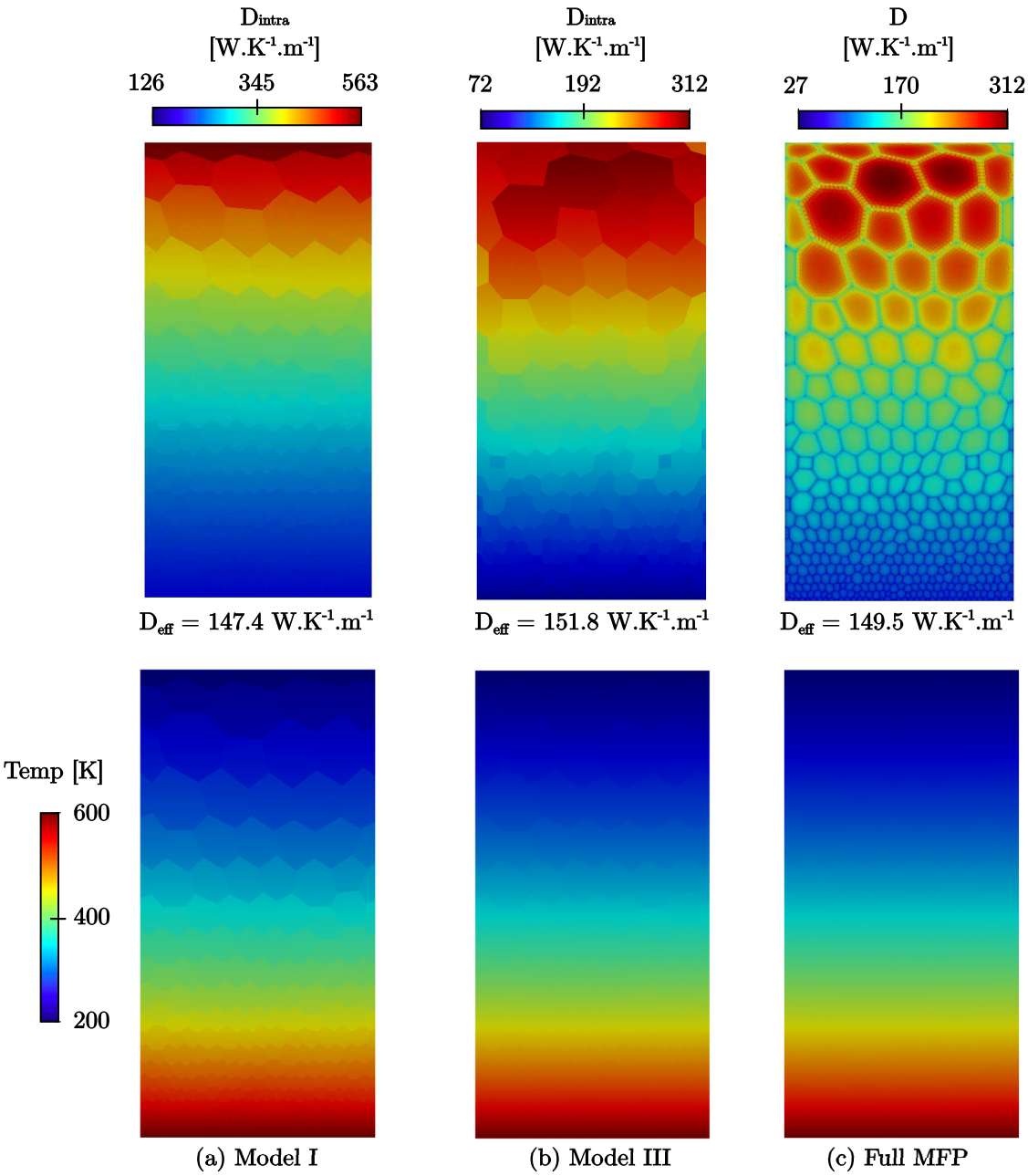

Figure 77: Graded polycrystalline structure.
Thermal conductivity D_{intra} and temperature field.

respectively, $D^I_{eff} = 147.4 W.K^{-1}.m^{-1}$ and $D^{III}_{eff} = 151.8 W.K^{-1}.m^{-1}$. Thus, the disparity between the three models in with a 3% range, which validates the range of application of the Kapitza models. However, while the appropriate balance of the thermal resistance between the grain and the thermal interface recover the effective thermal conductivity, the models produce disparate temperature fields, as depicted in Figure 77. Once again, model

I is responsible for artificial temperature jumps at the grain interfaces.

The key take-away from this example is that the developed Kapitza models recover the effective thermal conductivity over a large range of temperature and over a large range of grain size. To some extent, the proposed geometry in Figure 76 is the most complex case and it correctly handles the macroscopic behavior of the material while accounting for the microstructural features.

4.4.4 Conclusion

In this section, a series of new Kapitza resistance models taking advantage of the concurrent multiscale framework has been developed. In these models, either the Kapitza resistance R_K, the intragranular conductivity D_{intra}, or both of these quantities, are grain size-dependent. In particular, these quantities are chosen to recover the same grain size-dependent effective conductivity. Although all Kapitza resistance models invariably produce a temperature jump at the grain boundary, it is demonstrated through simulations and analytical analyses, that the different models proposed here differ significantly in the degree of temperature jump produced at the grain boundary. It is concluded through several examples that the newly developed model having both a grain size-dependent R_K and D_{intra}, provides the best compromise between having the right kinetics without employing such a small value of R_K that would lead to numerical difficulties. Ths is a critical advancement compared to the methodologies currently used in the literature.

4.5 Thermal Residual Stresses

In this section, the work focuses on the stress generated by the temperature field, known as the residual thermal stress. This concept has been introduced in Chapter 2 and its implementation as been explained in details in Chapter 3, for both the bulk elements as well as the grain boundary elements - both mechanical cohesive and thermal Kapitza. As

discussed, any deviation in temperature from the stress-free state generates thermal residual stresses within the material. Those residual stresses depend on the temperature field and two material properties: the stiffness tensor and the coefficient of thermal expansion.

4.5.1 Stress Generation in the absence of interface elements

First, the analysis focuses on the polycrystalline structure presented in Figure 47 and whose thermal analysis was carried out in Section 4.1.4. In order to obtain the thermal stress resulting from the evolution in temperature field, the mechanical properties need to be added. For instance, silicon grains have a diamond cubic lattice with elastic constants given, in Voight notation, by

$$\begin{pmatrix} 165.7 & 63.9 & 63.9 & 0 & 0 & 0 \\ 63.9 & 165.7 & 63.9 & 0 & 0 & 0 \\ 63.9 & 63.9 & 165.7 & 0 & 0 & 0 \\ 0 & 0 & 0 & 79.6 & 0 & 0 \\ 0 & 0 & 0 & 0 & 79.6 & 0 \\ 0 & 0 & 0 & 0 & 0 & 79.6 \end{pmatrix}$$

The coefficient of thermal expansion is assumed to be isotropic and temperature-independent, with value $\alpha = 2.6 \times 10^{-6}\ K^{-1}$.

Thermal stresses are computed for the three cases presented in the thermal analysis, applying the boundary conditions shown in Figure 78. Nodes on bottom and vertical edges are free to slide along those directions while nodes on the top edge are free. To correctly account for the elastic anisotropy of silicon, each grain is assigned a lattice orientation, as depicted in Figure 78 (right). To comply with the plane strain assumption of the 2D model, the z-direction of the rotation matrix is constrained to point out of the simulation plane while keeping the in-plane rotation random for each grain.

For the problems under consideration, the characteristic times of the thermal (t_T) and mechanical (t_M) problems differ by orders of magnitude. More precisely, considering the

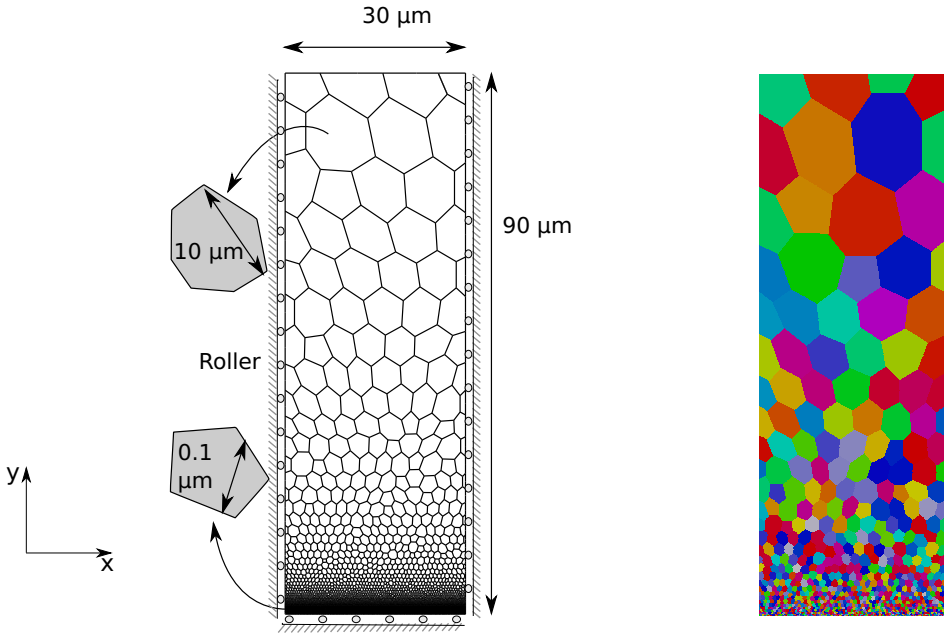

Figure 78: Mechanical boundary conditions and grain orientation for case 1. Colors represent grain orientation.

values of the thermal conductivity attained in the steady state regime, the characteristics times are $t_M = 1 \cdot 10^{-11} s$ and $t_T = 1 \cdot 10^{-9} s$ for the smallest grains in the simulation ($0.1 \mu m$). For the largest grains ($10 \mu m$) the corresponding values are $t_M = 1 \cdot 10^{-9} s$ and $t_T = 1 \cdot 10^{-6} s$. That is, in the worst case scenario (smallest grains) the characteristic times differ by two orders of magnitude. This difference allows to solve the coupled problem using a staggered approach, in which the diffusion problem first evolves with a time marching scheme, and then the thermal stresses are computed in a quasistatic fashion. That is, for the specific problems under consideration, computation of thermal stresses can be performed as a post-processing procedure.

Using the refinement technique explained in Subsection 3.3.3, the mechanical mesh is generated. Hence, the resulting mesh adopted for the mechanical model is composed of $210,208$ 3-node quadratic triangular elements. The temperature field for the mechanical part of the model is obtained by linearly interpolating the temperature distribution obtained in Section 4.1.4 to the nodes the newly created triangulation. The temperature field is then interpolated from those nodes to the quadrature points. Finally, the steady state solution is computed for the residual thermal stresses using a nonlinear conjugate gradient solver for

each time step of interest.

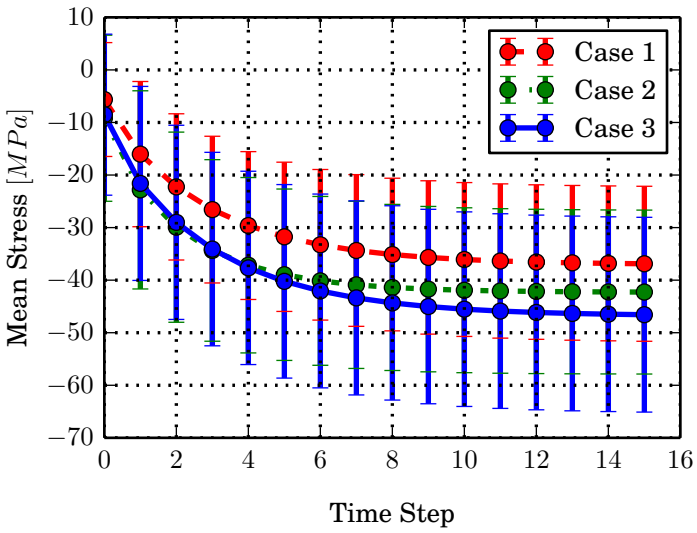

Figure 79: Evolution of the thermal stress over time.

Figure 79 presents the temporal evolution of thermal stresses σ_{xx} for the three cases under consideration, as exhibited by the volume-weighted mean value of the stress field and its standard deviation. For the figure, 15 evenly spaced time steps are selected between the beginning of the simulation and the steady state regime. As the figure shows, initial stress distribution is virtually the same for all three cases at the beginning of the simulation as the temperature field is dictated by the initial value problem. As time progresses, stress distribution diverges very quickly for all three cases and becomes relatively significant in the steady state regime. At steady-state, the absolute mean stress of Case 3 is 27.03% higher than Case 1. The non-uniform temperature distribution is responsible for the large standard deviation, as grains near the colder surface experience much lower stresses than those near the opposite end. Figure 80 depicts the full field for the stress σ_{xx} at the steady state.

Considering that the 3 chosen cases are arbitrary and that the material under consideration is relatively simple (cubic-diamond lattice with high symmetry and isotropic thermal expansion coefficient), the observed difference on temperature and stress distribution among them suggest that engineering the grain size within the material could prove instrumental in

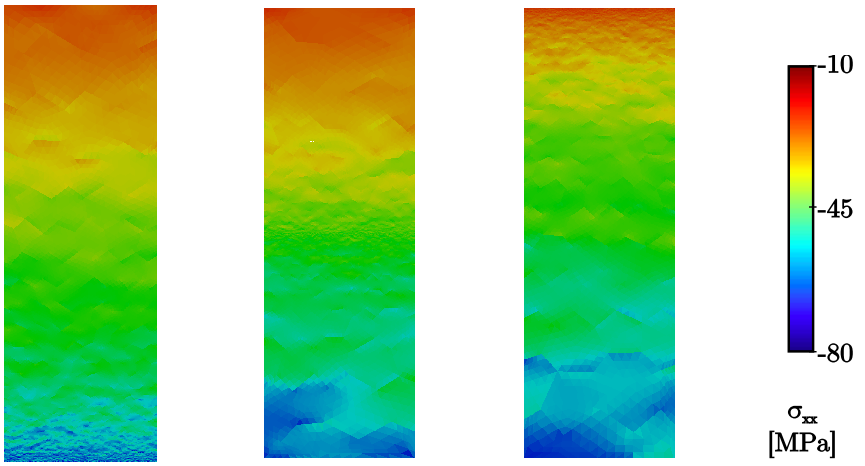

Figure 80: Stress field at steady-state.

developing materials less susceptible to thermomechanical failure, as well as for the design of more efficient thermal insulators.

The observed variations could be much more drastic for materials with anisotropic thermal expansion coefficients and/or lower symmetry in their elastic response. High contrast could be also achieved by manipulating the length-dependent effect through the creation of multiphase metamaterials at the microscale. This could be further exploited when coupling the model with optimization algorithms. For instance, thermal stresses are a major cause of spallation on many coating materials. This could be alleviated through an optimal microscopic design of the material. Finally, the macroscopic geometry of the structure plays an important role not explored in this work. The rectangle under consideration offers a straight forward calculation of the thermal stress, which become only function of the temperature distribution. More complex geometries like hollow cylinders could exhibit even higher thermal stresses, which oftentimes are related not only to the temperature field but also to its gradient.

4.5.2 Stress Generation in the presence of interface elements

In this subsection, the influence of the interface elements on the stress is considered. The goal is to analyze the effect of the various MFP calibrated Kapitza models presented in

Section 4.4 on the thermomechanical response of a polycrystalline structures under thermal loads. Both transient and steady-states thermomechanical heat conduction simulations are provided.

The simulation domain is the same as used in Subsection 4.4.3.1. That is a square domain with 100 hexagonal grains of approximate size $d = 0.5\mu$m. Unlike the purely thermal study, the temperature is here extended to a broader range and it is expected that $D_{\text{avg,i}}$ and $D_{\text{max,i}}$ can vary within a grain. Moreover, it is possible for the grain averaged quantities $\bar{D}^A_{\text{avg}}$ and $\bar{D}^A_{\text{max}}$ (see Figure 70 for reference) to vary across a uniform polycrystal due to variations in temperature.

For all simulations, the initial temperature is given at $T = 600K$. At time $t = 0$, the top boundary is prescribed a temperature of $T = 200K$ while all other surfaces are prescribed a zero flux boundary condition. The mechanical response of the material is governed by a simple small deformation isotropic linear elastic relationship given by $\boldsymbol{\sigma} = E[\boldsymbol{\epsilon} - \boldsymbol{\alpha}(T - T_0)]$, relating the second-order stress tensor $\boldsymbol{\sigma}$ to the second-order strain tensor $\boldsymbol{\epsilon}$, as described in Section 2.4. The material parameters are representative of silicon carbide and given by the Young's modulus $E = 485$GPa, the Poison's ratio $\nu = 0.21$, and the coefficient of thermal expansion $\alpha = 4 \times 10^{-6} K^{-1}$. Finally, the stress free reference temperature is taken as $T_0 = 600K$.

It is worth noting that a thermomechanical analysis of such a microstructure could utilize an anisotropic constitutive law for the behavior of each grain in the microstructure. The use of such a constitutive law will invariably lead to the generation of large stress concentrations between grains due to mismatches in the orientation of neighboring grains. These stress concentrations, although physically relevant, obscure the differences in stress generated by the use of the various MFP calibrated Kapitza models developed in this work. As such, the thermomechanical simulations are performed using an isotropic constitutive law to highlight the effect of the various thermal models on stress generation.

Two simulations were performed with Model I and Model III developed in Subsection 4.4.2. For comparison, the simulation was also performed using the full MFP model.

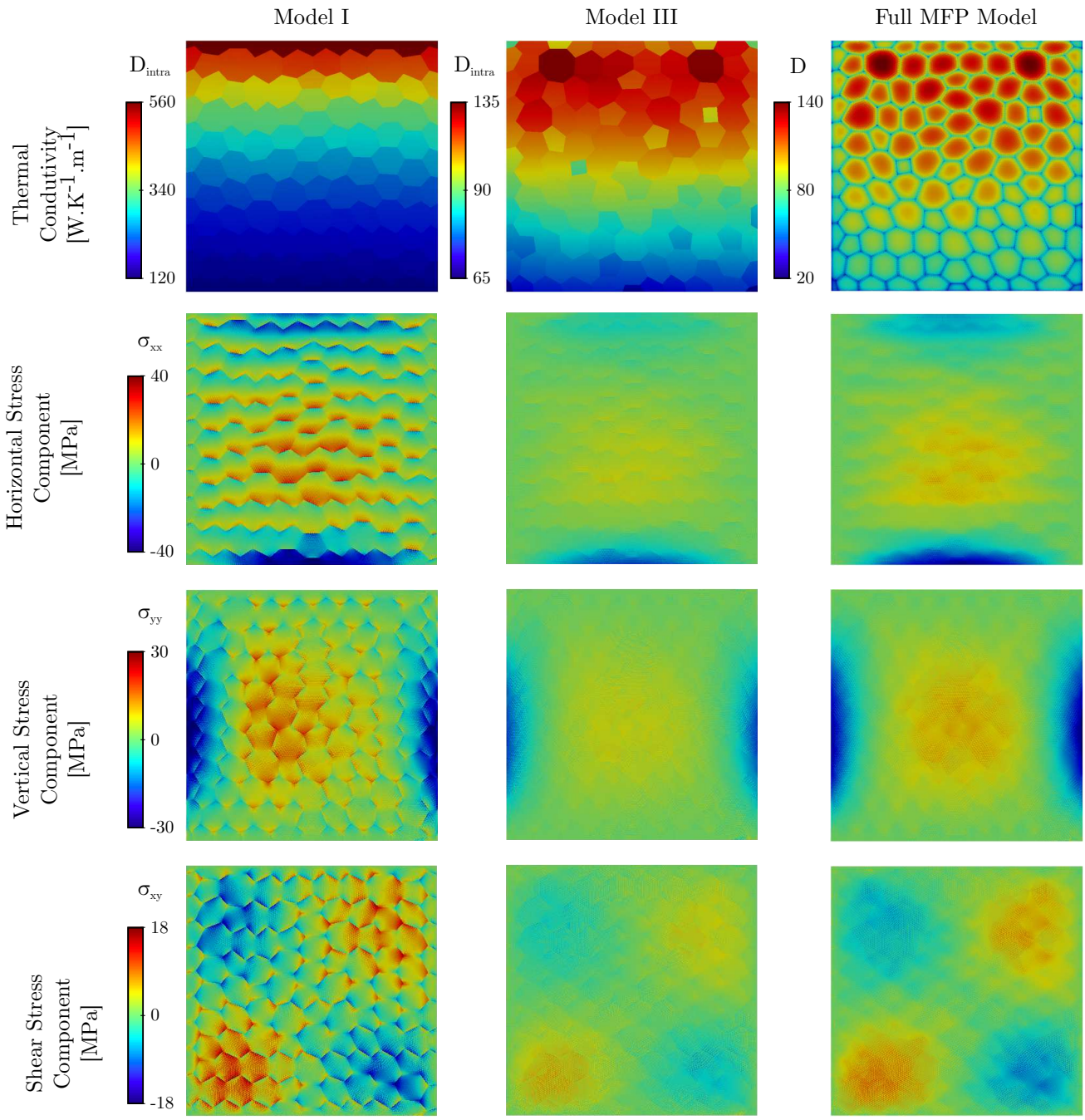

Figure 81: Thermomechanical simulations of a uniform polycrystal. Steady-state results.

Figure 81 shows the steady-state results of the simulations for Model I, Model III, and for the full MFP model. The first row displays the intragranular conductivity D_{intra} for the MFP calibrated Kapitza models, and the thermal conductivity D for the full MFP model. The remaining rows of Figure 81 presents contours of the horizontal σ_{xx}, vertical σ_{yy}, and

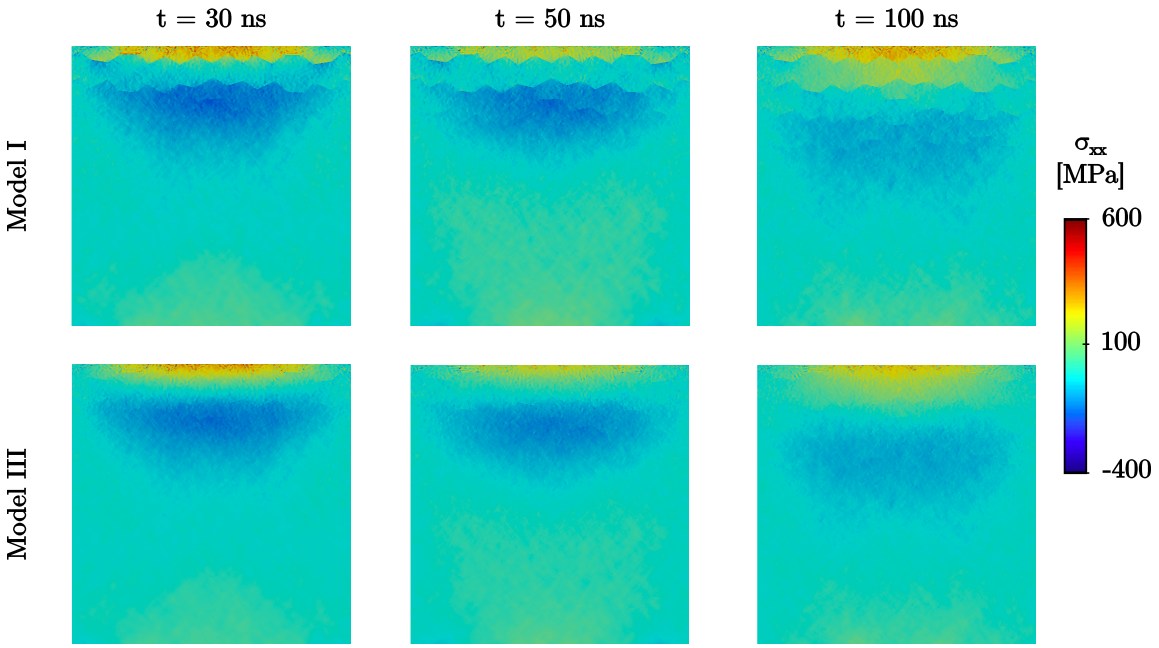

Figure 82: Transcient thermomechanical simulations of a uniform polycrystal. Horizontal stresses are displayed.

shear σ_{xy} components of stress respectively.

For Model I, D_{intra} is a constant for a given grain but varies from grain to grain due to the variation in temperature across the simulation. For Model III, D_{intra} is not necessarily a constant within each grain since. At each integration point, the implementation sets $D_{\text{intra,i}} = D_{\text{max,i}}$ where $D_{\text{max,i}}$ is the maximum thermal conductivity for a given grain size and temperature; precomputed using the full MFP model. When considering the stress field, a significant difference is observed between Models I and III within the grains. Focusing on the horizontal component $\sigma_x x$ (see Figure 81 second row), it is obvious that Model I produces artificially high stress concentrations at grain boundaries, large stress gradients within a grain, as well as larger stress jumps at grain boundaries. In contrast, Model III produces a stress distribution which is in reasonably good qualitative and quantitative agreement with the full MFP model. Similar discrepancies between Model I and III, as well as agreement between Model III and the full MFP model, are observed for the other components of stress. These significant differences will in turn translate to significant differences in the models ability to predict stress driven phenomena such as intra- and intergranular fracture.

The influence of the various MFP calibrated Kapitza models on the stresses can also be

noted during the dynamic behavior of the material. Figure 82 shows the horizontal stress component σ_{xx} as computed using Model I and Model II at three simulation times: (a) $t = 30$ns ,(b) $t = 50$ns, and (c) $t = 100$ns. Again, due to the high intragranular thermal conductivity and Kapitza resistance used in Model I, where the intragranular conductivity is based on the large grain size conductivity, the stresses are significant at the grain boundary. By opposition, the grains are barely noticeable in Model III, due to the smoother temperature variation.

Finally, in order to quantify the tendency of the different models to generate cracks, the stress fields at the interface elements are analysis. Figure 83 displays the normal and tangential stresses at the grain boundary for model I and model III. Qualitatively, from Figure 83, it is obvious that the stresses generated within the model I are higher. When considering the extreme values, model I produce stresses that are more than twice the one generated within model III. The different values are provided in Table 4. This observation reinforces the benefit of full MFP calibrated Kapitza model III that limits the apparition of spurious thermomechanical cracks.

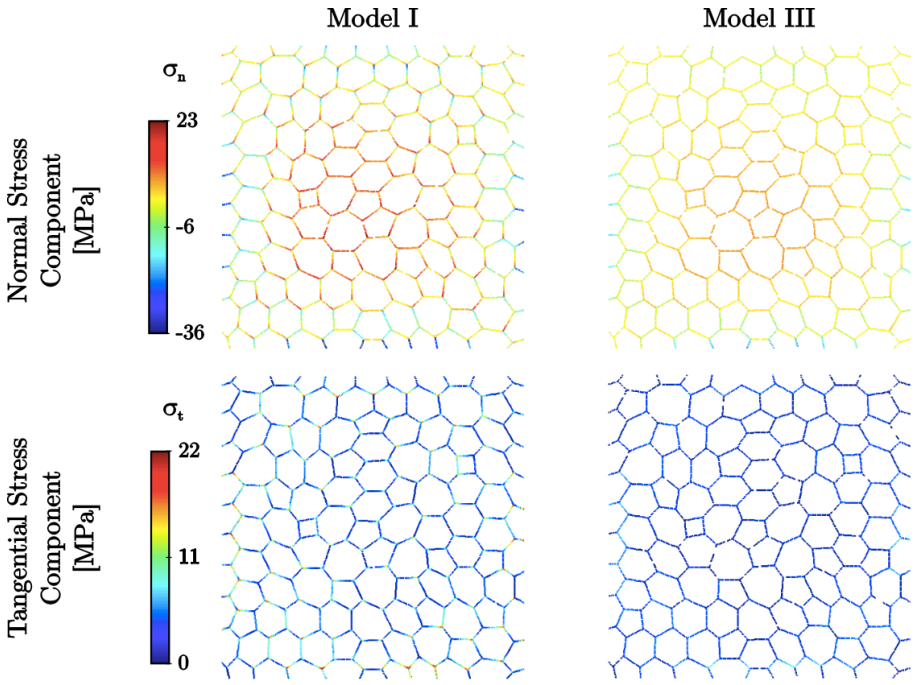

Figure 83: Normal and Tangential stresses in the cohesive elements.

Table 4: Extreme values of the interface stress fields.

	Model I	Model III
Normal [MPa]	$[-36.5,\ 22.5]$	$[-21.1,\ 9.5]$
Tangential [MPa]	$[0\ , 21.6]$	$[0\ , 8.8]$

4.5.3 Conclusion

In this section, the influence of the microstructural features on the thermally induced stresses is clearly demonstrated. First, it is proven that the stress field is highly impacted by the grain size arrangement. It appears that the differences in the thermal fields directly translate in the stress distribution throughout the thermomechanical coupling. More importantly, in the presence of interface elements (allowing for the nucleation and propagation of cracks), the selection of the modeling technique significantly impacts the stress concentration a the grain boundary. An innovative Kapitza resistance model is created from the use of the developed concurrent multiscale framework. This model provides a better determination of the interface parameters (R_K and D_{intra}) considerably reducing the artificial stress in the bulk material as well as halving the spurious interfacial stress at the grain boundary, due to numerical artifacts.

CHAPTER V

CONCLUSION AND FUTURE WORK

5.1 Summary

This thesis establishes a novel concurrent multiscale framework to analyze the complex mechanisms of heat transfer at the mesoscale, microscale, and macroscale. This framework constitutes the cornerstone of this work and many results are derived from its usage. It allows to overcome the current limitation of analytical expressions that are constrained to simple geometries and it permits to determine the interactions among length scales. Several applications are generated from this framework. Among others, an innovative multiscale optimization technique is developed, extending the multiscale model to the creation of enhanced microstructures by coupling it with a topology optimization algorithm. The concurrent multiscale framework is also used to derive a new thermomechanical interface model at the grain boundary, accounting for the size-dependent effects.

In more details, the developed framework considers the thermal properties of the material at different scales. At the microscale, this approach models the thermal conductivity of the material based on the Boltzmann transport equation under the relaxation time approximation. At the mesoscale, a Fourier heat transport model captures the overall heat transfer on the specimens under consideration. Finally, a continuum model of thermomechanical deformation explicitly accounts for the mesoscopic geometric features of the material. The transfer of information from one scale to another provides the unprecedented concurrent multiscale approach.

The key concepts and analytical formulations of the multiscale thermomechanical model are presented in Chapter 2. First, the current work found in the literature is analyzed. Second, the methodology developed to obtain the size-dependent thermal conductivity for arbitrary shapes is detailed. This provides the opportunity to model more complicated geometries. A thorough description of the techniques carried out to overcome the existing

limitations is presented.

The application of the framework relies on a powerful finite element code, whose implementation have been explained in Chapter 3. The backbone of the performed work lies in this implementation. A strong focus is placed on the techniques developed to calculate the size-dependent thermal properties. The ray-casting procedure adopted is key to handling any possible geometries and microstructures. Additionally, some features about the High Performance Computing parallel implementation were explained. That is, this thesis provides enough details about the framework implementation for readers to reproduce it.

Finally, the combination of the multiscale methodology with its numerical implementation provides advanced and novel results. In particular, it is shown that the grain size distribution highly influences the macroscopic thermal behavior of the materials. Indeed, different grain distributions generate different temperature fields, leading to distinct thermal stresses. As a consequence, the capabilities of analyzing the microstructure is essential to correctly model the macroscopic behavior. From this assessment, a novel multiscale optimization approach has been created in order to determine the optimal microstructure for a specific objective function. This methodology constitutes a powerful new approach to obtain devices with high thermal performance while using a single material. Such performances are currently absent from the literature, as thermal optimization is always performed using at least two materials having drastically different properties.

From a numerical approach, the advantage of the concurrent multiscale framework also lies in the definition of a grain boundary layer. A thorough comparison against the existing modeling techniques of the thermal resistance at the grain boundary, known as Kapitza elements, has been performed. Once again, new developed multiscale methodologies are created and provide strong physical insights at the interface. The different models defined and analyzed, having different D_{intra} and R_k, differ significantly in the degree of temperature jump produced at the grain boundary. It is proved that the temperature difference highly impacts the propagation of the stress waves within the materials, potentially leading to artificial cracks.

5.2 Contributions

The research presented in this thesis provides the following unique contributions to the state-of-the-art

1. The formulation of a concurrent multiscale framework to capture and to couple in a single simulation both microscale and macroscale thermal phenomena is an unprecedented advancement in the literature. For the first time, this methodology accounts for

   (a) a sub-micron scale model for the thermal conductivity based on the Boltzmann transport equation under the relaxation time approximation.

   (b) a classic Fourier heat transport model at the mesoscale.

   (c) a continuum model of thermomechanical deformation that explicitly resolves the microscopic geometric features of the material.

   As a result, this numerical model bridges the gap between the microscale, the mesoscale, and the macroscale.

2. Using the developed framework, several thermal properties, currently unsuccessfully predicted, are obtained. Among others, this thesis achieved the following results

   (a) Recovering the in-plane and cross-plane thermal conductivity of thin films, using a single set of fitting parameters.

   (b) Predicting the full anisotropic thermal conductivity tensor, for grains of any arbitrary geometries.

   (c) Presenting the physical significance of the size effect near the grain boundary, through the usage of a numerical ray-casting technique. This technique highlights the heterogenous distribution of the thermal conductivity within a single grain.

3. The development of a novel topology optimization approach for thermal transport problems is presented. It combines multiscale modeling and topology optimization

techniques for the design of polycrystalline single-material systems with enhanced thermal transport properties. The developed multiscale approach allows to compute the attainable range of thermal conductivity due to grain-size effect, given maximum and minimum grain sizes and an operating temperature range. A newly developed adaptive topology optimization technique is used to obtain an optimal grain size distribution while accounting for manufacturing constraints. A series of specific examples demonstrate the extent to which thermal transport properties can be optimized without resorting to the adoption of multi-material systems.

4. A new Kapitza element is created in order to better model dynamic intergranular fracture in polycrystals. Contrary to the usage found in the literature, the values of the intragranular thermal conductivity and of the Kapitza resistance are grain size-dependent and are obtained through the developed multiscale framework. This constitutes a physics based model that provides the right kinetics. Indeed, in this model, the Kapitza resistance has a clear physical interpretation in that it accounts for the variation in the grain size-dependent intragranular resistance from its average value to its maximum value. This model is proven to reduce temperature jumps at the grain boundary, which are an artifact of the numerical simulations. It is shown that the temperature difference highly impacts the propagation of the stress waves within the materials, potentially leading to artificial cracks.

5. During the implementation of the thermomechanical framework, the potential of the 'in-house' FEM software has been extensively improved. Among others, the following capabilities have been added

   (a) Implementation of thermomechanical elements. Those elements were absent from the code but are needed to run multiphysics simulations.

   (b) Implementation of a new subdivision technique. This method preserves the quality of the elements, allowing to generate fine meshes of high quality.

   (c) Implementation of new mechanical interface elements. While cohesive zone elements were present in the code, the added traction separation law prevents the

interpenetration of bulk elements.

(d) Implementation of thermal interface elements. Those elements were absent from the code. They now account for the thermal resistance at the grain boundary as well as the flux decrease due to crack nucleation and propagation.

(e) Implementation of new temporal frameworks: static, quasi-static and dynamic. Those new frameworks account for the concurrent evolution of simulations at different scales.

Last but not least, the code has been parallelized on distributed memory. This time-consuming and cumbersome task allows for the speed-up of large simulations with great scalability performances.

5.3 Future Work

In the current work, complex microstructural features are considered. However, the macroscopic geometries studied are more simple. Future investigations of more complicated models can be of prime interest. For instance, the study of metamaterials such as presented in Figure 84 offers exciting possibilities. The deformation of the geometry is expected to

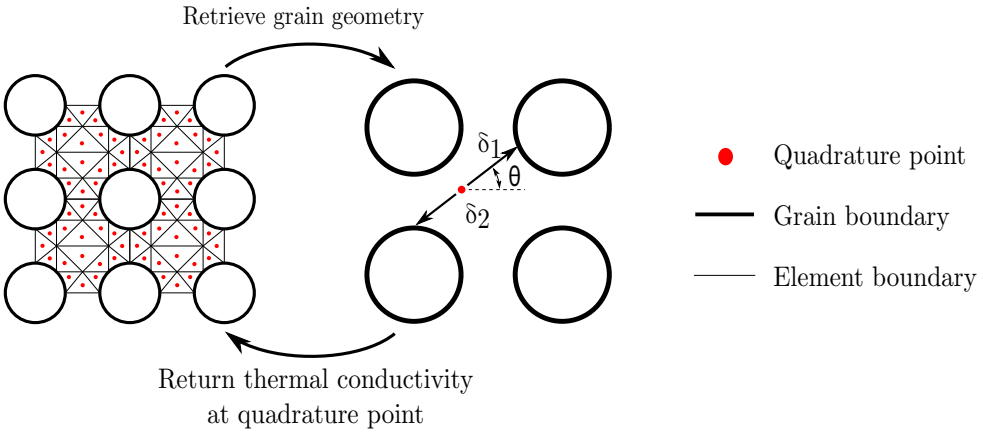

Figure 84: Framework applied to matematerial

have a significant impact on the phonon mean free path, offering the opportunity to obtain mechanical load-dependent thermal conductivity. The current work also focuses on relatively simple constitutive laws, but even more interesting problems could arise by considering complex constitutive laws with dissipation mechanisms that generate heat. The implemented FEM framework makes this kind of coupling straightforward to execute. As a final thought, composite material could be of interest.

Another direction should focus on the three-dimensional problems and the difference resulting from this more complete modeling. While all examples considered in Chapter 4 are bi-dimensional, the governing equations of the proposed model are three-dimensional in nature. In addition, most of the implementation has been developed in 3D, including among others: (a) the ray-casting technique, (b) the calculation of the size-dependent thermal conductivity, or (c) the thermal and mechanical interface element. Thus, the model can be directly applied to study fully three-dimensional problems. Nevertheless, solving such problems would require significantly higher computational power.

Finally, this research could extend more deeply in the study of thermomechanical cracks. For instance, the effect of the grain size and the grain distribution on the nucleation of thermal cracks for both steady-state and dynamic thermomechanical problems is a challenging task. While the framework allows for the insertion of any interface traction-separation law, the main task associated with that study is to ensure that the overall compliance of the model is size-independent, that is the spurious numerical artifact is independent of the grain size distribution. However, no such work has been reported in the literature and pursuing such a goal is highly attractive. Some possible methodologies to consider could involve discontinuous Galerkin methods [132] or extrinsic cohesive laws [133].

APPENDIX A

GENERATED CODE

A tremendous effort has been placed in the implementation of the developed methodology. In this Annex, the C++ classes added or significantly modified are reported by describing the key modifications. The added classes needed for the inheritance are not reported.

A.1 Added classes

A.1.1 Namespace: Element

Those classes mostly define the element geometries and kinetics parameters. For every object, the following components are present: LocalState, Energy<0>, Energy<1>, and Energy<2>.

Cohesive::Kapitza

Thermal interface element.

A.1.2 Namespace: Geometry

Those classes mostly define the geometries. The Solid::Mesh classes provide the mesh structure and the Solid::BRep classes provide the boundary representations. Those latter classes define the limit of the geometry. They are used to apply the boundary conditions as well as correctly define the grain on the limit of the model domain.

Algebraic::MatryoshkaComplex

Subdivide the initial mesh using the '8 subd.' technique.

Solid::Mesh::Hexagon

Mesh for a random hexagon. Typically represent a single grain.

Solid::Mesh::Meshfromfile

Generate mesh from data such as: vtu files or text files. Also read saved fields. More than a dozen of different constructors are presents accounting for various methodologies.

Solid::Mesh::UnitRectangle

Mesh for a rectangle whose dimensions are provided.

Solid::Brep:CircularSection

Provide the boundary representation of a circular section defined by a inner radius, an outter radius and an angle.

Solid::Brep::Hexagon

Provide the boundary representation of the class Solid::Mesh::Hexagon.

Solid::Brep::UnitRectangle

Provide the boundary representation of the class Solid::Mesh::UnitRectangle.

A.1.3 Namespace: Material

Those classes mostly define the material constitutive equations. For every material the following components are present: Data, LocalState, Energy<0>, Energy<1>, and Energy<2>.

Hookean::Anisotropic

Anisotropic hookean material with a 6×6 stiffness matrix.

Hookean::Orthotropic

Orthotropic hookean material with 9 elastic constants.

Transport::Anisotropic

Anisotropic thermal material.

Cohesive::Mixed

Cohesive element separately accounting for traction and shear components.

Cohesive::Mixed::Binding::PPR

Cohesive element with the PPR traction-separation law.

Kapitza::Plane

Transformation rules for Kapitza material from 3D to 2D.

Kapitza::Effective::Binding::UBER

Kapitza material - constitutive equations.

A.1.4 Namespace: Metis

This namespace is comprised of several classes. It is the entire Metis library. No code has been added to the original implementation.

A.1.5 Namespace: Solver

Solver::MPISolver

Provide the functions and tools to parallelize the solvers. Among others, it reduces the forces of the duplicated nodes across partitions to a single value. It also allows to perform dot and cross products over the whole models, without accounting several times for the duplicated nodes.

A.1.6 Namespace: FunctionJB

The classes and methods in FunctionJB are specific features of this thesis that did not fit in any other classes.

FunctionJB::Fracture

Provide all the tools necessary to handle the fracture across different partitions. Among other functionality, this class: (a) generates a specific numbering for the fracture complex, (b) creates a ghost layer for interface elements between several partitions, (c) updates the communication maps to account for the duplicated nodes, or (d) maps the class Fracture-Complex to the class MatryoshkaComplex.

FunctionJB::Mesh

Provide functions to modify some geometric features, such as the reduction or the translation of the entire geometry.

FunctionJB::ModelMPI

Provide critical features needed for the MPI process. Among other, this class: (a) provides different methodologies to partition the model, (b) defines the communication maps between the different partitions, (c) allows to subdivide the mesh after partitioning it, or (d) declares several mathematical operators to obtain quantities such as average or extremum, over several partitions.

FunctionJB::NumberMesh

Provide different rules for numbering cells and elements in the mesh. This is necessary to identify duplicated nodes and establish communication maps.

FunctionJB::Solver

Provide analysis capacities to the different solvers. For instance, it allows overwriting the residual forces to apply thermal flux boundary conditions.

FunctionJB::Thermal

Provide all the required functions for the calculation of the reduced thermal conductivity. Among others, this class: (a) calculates the distance from the quadrature point to the grain boundary, (b) derives the relationship for the group and phase velocities, or (c) performs the integration of the reduced thermal conductivity over the first Brillouin Zone.

A.2 Modified classes

Some exciting classes have been highly impacted by the parallel implementation of the code.

A.2.1 Namespace: Geometry

Solid::Mesh::Polycrystal

This class has been modified to account for the new type of subdivision within the polycrystal. As such, the polycrystal is a MatryoshkaComplex object.

Viz::Eureka2vtk

The class has been modified to display vector of size: 2,4 and 9.

A.2.2 Namespace: Solver

On top of adding the new class 'MPISolver' within this namespace, all the solver classes such as 'ExplicitDynamics', 'ForwardEuler' and 'PolakRibiere' have been highly modified to account for the needed communications across the different partitions. Those modifications are validated through partition-independent results.

A.3 Added libraries

The code has been linked to new dynamic libraries.

Triangle Library

This library is a a 'Two-Dimensional Quality Mesh Generator and Delaunay Triangulator.' It is used for the generation and subdivision of the Matryoshka complex in 2D.

Tetgen Library

This library is a a 'A Quality Tetrahedral Mesh Generator and a 3D Delaunay Triangulator.' It is used for the generation and subdivision of the Matryoshka complex in 3D.

REFERENCES

[1] D. Clarke, M. Oechsner, and N. Padture. Thermal-barrier coatings for more efficient gas-turbine engines. *MRS bulletin*, 37(10):891–898, 2012.

[2] S. Schmidt, S. Beyer, H. Knabe, H. Immich, R. Meistring, and A. Gessler. Advanced ceramic matrix composite materials for current and future propulsion technology applications. *Acta Astronautica*, 55(3):409–420, 2004.

[3] Z. Yufeng, T. Xiaoyun, C. Weiping, Z. Guowei, and L. Xiaowei. Study of mems packaging technology. In *2005 6th International Conference on Electronic Packaging Technology*, pages 1–4. IEEE, 2005.

[4] X. Cao, R. Vassen, and D. Stoever. Ceramic materials for thermal barrier coatings. *Journal of the European Ceramic Society*, 24(1):1–10, 2004.

[5] Z. Razavi Hesabi, M. Haghighatzadeh, M. Mazaheri, D. Galusek, and S. Sadrnezhaad. Suppression of grain growth in sub-micrometer alumina via two-step sintering method. *Journal of the European Ceramic Society*, 29(8):1371–1377, 2009.

[6] I.-W. Chen and X.-H. Wang. Sintering dense nanocrystalline ceramics without final-stage grain growth. *Nature*, 404(6774):168–171, 2000.

[7] J. Obare, W. Griffin, and H. Conrad. Effects of heating rate and dc electric field during sintering on the grain size distribution in fully sintered tetragonal zirconia polycrystals stabilized with 3% molar yttria (3y-tzp). *Journal of Materials Science*, 47(13):5141–5147, 2012.

[8] Y. Watanabe, A. Kawamoto, and K. Matsuda. Particle size distributions in functionally graded materials fabricated by the centrifugal solid-particle method. *Composites Science and Technology*, 62(6):881–888, 2002.

[9] M. Ortiz and A. Molinari. Microstructural thermal stresses in ceramic materials. *Journal of the Mechanics and Physics of Solids*, 36(4):385–400, 1988.

[10] V. Tvergaard and J. Hutchinson. Microcracking in ceramics induced by thermal expansion or elastic anisotropy. *Journal of the American Ceramic Society*, 71(3):157–166, 1988.

[11] J. Fish. *Multiscale methods: bridging the scales in science and engineering*. Oxford University Press on Demand, 2010.

[12] W. Sharpe, K. Jackson, K. Hemker, and Z. Xie. Effect of specimen size on young's modulus and fracture strength of polysilicon. *Journal of Microelectromechanical systems*, 10(3):317–326, 2001.

[13] E. Arzt. Size effects in materials due to microstructural and dimensional constraints: a comparative review. *Acta materialia*, 46(16):5611–5626, 1998.

[14] A. Eichler, J. Moser, J. Chaste, M. Zdrojek, I. Wilson-Rae, and A. Bachtold. Nonlinear damping in mechanical resonators made from carbon nanotubes and graphene. *Nature nanotechnology*, 6(6):339–342, 2011.

[15] S. Nemat-Nasser and M. Hori. *Micromechanics: overall properties of heterogeneous materials*, volume 37. Elsevier, 2013.

[16] Y. Zhou, L. Yang, and Y. Huang. *Micro-and Macromechanical Properties of Materials*. CRC Press, 2013.

[17] P. Raghavan and S. Ghosh. Concurrent multi-scale analysis of elastic composites by a multi-level computational model. *Computer methods in applied mechanics and engineering*, 193(6):497–538, 2004.

[18] D McDowell, M. Zhou, and Y. Li. A multiscale framework for predicting fracture toughness of polycrystalline metals. *Materials Performance and Characterization*, 3(3):157–172, 2014.

[19] M. Hautefeuille, J.-B. Colliat, A. Ibrahimbegovic, H. Matthies, and P. Villon. A multi-scale approach to model localized failure with softening. *Computers & Structures*, 94:83–95, 2012.

[20] J. Elliott. Novel approaches to multiscale modelling in materials science. *International Materials Reviews*, 56(4):207–225, 2011.

[21] Y. Asakuma, S. Miyauchi, T. Yamamoto, H. Aoki, and T. Miura. Homogenization method for effective thermal conductivity of metal hydride bed. *International Journal of Hydrogen Energy*, 29(2):209–216, 2004.

[22] K. Goodson and M. Flik. Electron and phonon thermal conduction in epitaxial high-tc superconducting films. *ASME Journal of Heat Transfer*, 115:17–25., 1993.

[23] Z. Wang, J. Alaniz, W. Jang, J. Garay, and C. Dames. Thermal conductivity of nanocrystalline silicon: importance of grain size and frequency-dependent mean free paths. *Nano letters*, 11(6):2206–2213, 2011.

[24] J. Ziman. *Electrons and phonons: the theory of transport phenomena in solids*. Clarendon Press Oxford, UK, 2001.

[25] D. Cahill, W. Ford, K. Goodson, G. Mahan, A. Majumdar, H. Maris, R. Merlin, and S. Phillpot. Nanoscale thermal transport. *Journal of Applied Physics*, 93(2):793–818, 2003.

[26] A. McConnell and K. Goodson. Thermal conduction in silicon micro-and nanostructures. *Annual review of heat transfer*, 14(14), 2005.

[27] M. Maldovan. Micro to nano scale thermal energy conduction in semiconductor thin films. *Journal of Applied Physics*, 110(3):034308, 2011.

[28] Q.-Y. Ye, R. Tsu, and E. Nicollian. Resonant tunneling via microcrystalline-silicon quantum confinement. *Physical Review B*, 44(4):1806, 1991.

[29] M. Maldovan. Phonon wave interference and thermal bandgap materials. *Nature materials*, 14(7):667–674, 2015.

[30] A. Minnich, J. Johnson, A. Schmidt, K. Esfarjani, M. Dresselhaus, K. Nelson, and G. Chen. Thermal conductivity spectroscopy technique to measure phonon mean free paths. *Physical review letters*, 107(9):095901, 2011.

[31] A. McGaughey and M. Kaviany. Observation and description of phonon interactions in molecular dynamics simulations. *Physical Review B*, 71(18):184305, 2005.

[32] J. Turney, E. Landry, A. McGaughey, and C. Amon. Predicting phonon properties and thermal conductivity from anharmonic lattice dynamics calculations and molecular dynamics simulations. *Physical Review B*, 79(6):064301, 2009.

[33] S. Ju and X. Liang. Thermal conductivity of nanocrystalline silicon by direct molecular dynamics simulation. *Journal of Applied Physics*, 112(6):064305, 2012.

[34] S. Sinha and K. Goodson. Review: Multiscale thermal modeling in nanoelectronics. *International Journal for Multiscale Computational Engineering*, 3(1), 2005.

[35] C. Jeong, S. Datta, and M. Lundstrom. Thermal conductivity of bulk and thin-film silicon: A landauer approach. *Journal of Applied Physics*, 111(9):093708, 2012.

[36] M. Maldovan. Thermal conductivity of semiconductor nanowires from micro to nano length scales. *Journal of Applied Physics*, 111(2):024311, 2012.

[37] Y. He and G. Galli. Microscopic origin of the reduced thermal conductivity of silicon nanowires. *Physical review letters*, 108(21):215901, 2012.

[38] M. Maldovan. Thermal energy transport model for macro-to-nanograin polycrystalline semiconductors. *Journal of Applied Physics*, 110(11):114310, 2011.

[39] Z. Zhang. *Nano/Microscale Heat Transfer*. McGraw-Hill Prof Med/Tech, 2007.

[40] M. Horstemeyer. Multiscale modeling: a review. In *Practical aspects of computational chemistry*, pages 87–135. Springer, 2009.

[41] Y.-J. Lee, Y.-H. Park, and T. Hinoki. Influence of grain size on thermal conductivity of sic ceramics. In *IOP Conference Series: Materials Science and Engineering*, volume 18, page 162014. IOP Publishing, 2011.

[42] P. Becher, E. Sun, K. Plucknett, K. Alexander, C.-H. Hsueh, H.-T. Lin, S. Waters, C. Westmoreland, E. Kang, and K. Hirao. Microstructural design of silicon nitride with improved fracture toughness: I, effects of grain shape and size. *Journal of the American Ceramic Society*, 81(11):2821–2830, 1998.

[43] R. Armstrong. The influence of polycrystal grain size on several mechanical properties of materials. *Metallurgical and Materials Transactions*, 1(5):1169–1176, 1970.

[44] M. Trunec. Effect of grain size on mechanical properties of 3y-tzp ceramics. *Ceram. Silik*, 52(3):165–171, 2008.

[45] S. Harris. *An introduction to the theory of the Boltzmann equation*. Courier Corporation, 2004.

[46] J.-B. Bouquet and J. Rimoli. A length-dependent model for the thermomechanical response of ceramics. *Journal of the Mechanics and Physics of Solids*, 2015.

[47] J.-B. Bouquet, F. Burgaud, and J. Rimoli. Exploiting length-dependent effects for the design of single-material systems with enhanced thermal transport properties. *International Journal of Heat and Mass Transfer*, 101:12271236, 2016.

[48] J.-B. Bouquet, C. Di Leo, and J. Rimoli. Modeling size effect in thermal conductivity through a quasi-kapitza model. *Submitted*, 2017.

[49] C. Kittel and P. McEuen. *Introduction to solid state physics*, volume 8. Wiley New York, 1976.

[50] R. Leighton. The vibrational spectrum and specific heat of a face-centered cubic crystal. *Reviews of Modern Physics*, 20(1):165, 1948.

[51] D. Griffiths. *Introduction to quantum mechanics*. Pearson Education India, 2005.

[52] M. Holland. Analysis of lattice thermal conductivity. *Physical Review*, 132(6):2461, 1963.

[53] E. Burkel. Phonon spectroscopy by inelastic x-ray scattering. *Reports on Progress in Physics*, 63(2):171, 2000.

[54] L. Kong. Phonon dispersion measured directly from molecular dynamics simulations. *Computer Physics Communications*, 182(10):2201–2207, 2011.

[55] D. Terris, K. Joulain, D. Lemonnier, D. Lacroix, and P. Chantrenne. Prediction of the thermal conductivity anisotropy of si nanofilms. results of several numerical methods. *International Journal of Thermal Sciences*, 48(8):1467–1476, 2009.

[56] G. Chen. Thermal conductivity and ballistic-phonon transport in the cross-plane direction of superlattices. *Physical Review B*, 57(23):14958, 1998.

[57] M. Parker. *Solid State And Quantum Theory for Optoelectronics*. Taylor & Francis Group, 2009.

[58] P. Klemens. Solid state physics. *Academic, New York*, page 7, 1958.

[59] L. Lindsay, D. Broido, and T. Reinecke. Phonon-isotope scattering and thermal conductivity in materials with a large isotope effect: A first-principles study. *Physical Review B*, 88(14):144306, 2013.

[60] H. Casimir. Note on the conduction of heat in crystals. *Physica*, 5(6):495, 1938.

[61] G. Chen. *Nanoscale Energy Transport and Conversion: A Parallel Treatment of Electrons, Molecules, Phonons, and Photons*. Oxford University Press, New York, 2005.

[62] A. Marconnet, T. Kodama, M. Asheghi, and K. Goodson. Phonon conduction in periodically porous silicon nanobridges.

[63] R. Hamilton and J. Parrott. Variational calculation of the thermal conductivity of germanium. *Phys. Rev.*, 178:1284–1292, Feb 1969.

[64] G. Srivastava. *The Physics of Phonons*. Taylor & Francis, New York, 1990.

[65] D. Ferry. *Semiconductor transport*. CRC Press, 2000.

[66] Y. Takeda and T. Pearsall. Failure of matthiessen's rule in the calculation of carrier mobility and alloy scattering effects in ga0. 47in0. 53as. *Electronics Letters*, 17(16):573–574, 1981.

[67] S. Chapman and T. Cowling. *The mathematical theory of non-uniform gases: an account of the kinetic theory of viscosity, thermal conduction and diffusion in gases*. Cambridge university press, 1970.

[68] C. Tien and J. Lienhard. Statistical thermodynamics/revised printing. *Washington, DC, Hemisphere Publishing Corp., 1979. 413 p.*, 1, 1979.

[69] C. Cercignani. *The Boltzmann equation*. Springer, 1988.

[70] Harald Ibach and Hans Lüth. Solid-state physics: an introduction to principles of material science. *Advanced Texts in Physics, Springer-Verlag berlin Heidelberg New York*, 2003.

[71] S. Dhillon. Boltzmann solver for phonon transport. 2009.

[72] K. Fuchs. The conductivity of thin metallic films according to the electron theory of metals. *Mathematical Proceedings of the Cambridge Philosophical Society*, 34(1936):100–108, 1938.

[73] E. Sondheimer. The mean free path of electrons in metals. *Advances in Physics*, 50(6):499–537, 1952.

[74] H. Bennett and J. Porteus. Relation between surface roughness and specular reflectance at normal incidence. *JOSA*, 51(2):123–129, 1961.

[75] A. Ekimov, A. Efros, and A. Onushchenko. Quantum size effect in semiconductor microcrystals. *Solid State Communications*, 56(11):921–924, 1985.

[76] M. Gurtin. An introduction to continuum mechanics academic. *New York*, 1981.

[77] Q. Yang, L. Stainier, and M. Ortiz. A variational formulation of the coupled thermo-mechanical boundary-value problem for general dissipative solids. *Journal of the Mechanics and Physics of Solids*, 54(2):401–424, 2006.

[78] L. Stainier and M. Ortiz. Study and validation of a variational theory of thermo-mechanical coupling in finite visco-plasticity. *International Journal of Solids and Structures*, 47(5):705–715, 2010.

[79] S. Brenner and R. Scott. *The mathematical theory of finite element methods*, volume 15. Springer Science & Business Media, 2007.

[80] P. Kotiuga. Data structures for geometric and topological aspects of finite element algorithms. *Progress in Electromagnetics Research*, 32:151–169, 2001.

[81] M. Desbrun, E. Kanso, and Y. Tong. Discrete differential forms for computational modeling. In *Discrete differential geometry*, pages 287–324. Springer, 2008.

[82] R. Quey, P. Dawson, and F. Barbe. Large-scale 3d random polycrystals for the finite element method: Generation, meshing and remeshing. *Computer Methods in Applied Mechanics and Engineering*, 200(17):1729–1745, 2011.

[83] M. Ebeida and S. Mitchell. Uniform random voronoi meshes. In *Proceedings of the 20th International Meshing Roundtable*, pages 273–290. Springer, 2011.

[84] P. Mullen, P. Memari, F. de Goes, and M. Desbrun. Hot: Hodge-optimized triangulations. In *ACM Transactions on Graphics (TOG)*, volume 30, page 103. ACM, 2011.

[85] J. Rimoli and M. Ortiz. A duality-based method for generating geometric representations of polycrystals. *International Journal for Numerical Methods in Engineering*, 86(9):1069–1081, 2011.

[86] J. Munkres. *Elements of algebraic topology*, volume 2. Addison-Wesley Menlo Park, 1984.

[87] A. Liu and B. Joe. Quality local refinement of tetrahedral meshes based on 8-subtetrahedron subdivision. *Mathematics of Computation of the American Mathematical Society*, 65(215):1183–1200, 1996.

[88] J. Stoer and R. Bulirsch. *Introduction to numerical analysis*, volume 12. Springer Science & Business Media, 2013.

[89] R. Courant, K. Friedrichs, and H. Lewy. On the partial difference equations of mathematical physics. *IBM journal*, 11(2):215–234, 1967.

[90] R. Cook. *Concepts and applications of finite element analysis*. John Wiley & Sons, 2007.

[91] K. Park, G. Paulino, and J. Roesler. A unified potential-based cohesive model of mixed-mode fracture. *Journal of the Mechanics and Physics of Solids*, 57(6):891–908, 2009.

[92] X.-P. Xu and A. Needleman. Void nucleation by inclusion debonding in a crystal matrix. *Modelling and Simulation in Materials Science and Engineering*, 1(2):111, 1993.

[93] E. Smith. A generalization of elliott's model of a crack tip. *International Journal of Fracture*, 11(2):295–299, 1975.

[94] K. Park and G. Paulino. Cohesive zone models: a critical review of traction-separation relationships across fracture surfaces. *Applied Mechanics Reviews*, 64(6):060802, 2011.

[95] P. Persson and G. Strang. A simple mesh generator in matlab. *SIAM review*, 46(2):329–345, 2004.

[96] R. Hiptmair. Discrete hodge operators: An algebraic perspective. *Progress In Electromagnetics Research*, 32:247–269, 2001.

[97] G. Karniadakis and R. Kirby II. *Parallel scientific computing in C++ and MPI: a seamless approach to parallel algorithms and their implementation*. Cambridge University Press, 2003.

[98] D. Sellan, J. Turney, A. McGaughey, and C. Amon. Cross-plane phonon transport in thin films. *J. Appl. Phys.*, 108:113524, 2010.

[99] J. Turney, J. McGaughey, and C. Amon. In-plane phonon transport in thin films. *Journal of Applied Physics*, 107:024317, January 2010.

[100] A. McGaughey, E. Landry, D. Sellan, and C. Amon. Size-dependent model for thin film and nanowire thermal conductivity. *Appl. Phys. Lett.*, 99:131904, 2011.

[101] D. Baillis and J. Randrianalisoa. Prediction of thermal conductivity of nanostructures: Influence of phonon dispersion approximation. *International Journal of Heat and Mass Transfer*, 52(11-12):2516 – 2527, 2009.

[102] S. Adachi. *Handbook on physical properties of semiconductors*, volume 2. Springer Science & Business Media, 2004.

[103] R. Tubino, L. Piseri, and G. Zerbi. Lattice dynamics and spectroscopic properties by a valence force potential of diamondlike crystals: C, si, ge, and sn. *The Journal of Chemical Physics*, 56(3):1022–1039, 1972.

[104] D. Sellan, J. Turney, A. McGaughey, and C. Amon. Cross-plane phonon transport in thin films. *Journal of Applied Physics*, 108(11):113524, 2010.

[105] W. Liu and M. Asheghi. Thermal conductivity measurements of ultra-thin single crystal silicon layers. *Journal of heat transfer*, 128(1):75–83, 2006.

[106] Y. Ju and K. Goodson. Phonon scattering in silicon films with thickness of order 100 nm. *Applied Physics Letters*, 74(20):3005–3007, 1999.

[107] W. Liu and M. Asheghi. Thermal conductivity measurements of ultra-thin single crystal silicon layers. *J. Heat Transfer*, 128:75, 2006.

[108] D. Li, Y. Wu, P. Kim, L. Shi, P. Yang, and A. Majumdar. Thermal conductivity of individual silicon nanowires. *Applied Physics Letters*, 83(14):2934–2936, 2003.

[109] W. Liu and M. Asheghi. Phonon–boundary scattering in ultrathin single-crystal silicon layers. *Applied Physics Letters*, 84(19):3819–3821, 2004.

[110] J.-P. Crocombette and L. Gelebart. Multiscale modeling of the thermal conductivity of polycrystalline silicon carbide. *Journal of Applied Physics*, 106(8):083520, 2009.

[111] T. Feng and X. Ruan. Prediction of spectral phonon mean free path and thermal conductivity with applications to thermoelectrics and thermal management: a review. *Journal of Nanomaterials*, 2014, 2014.

[112] B. Qiu, Z. Tian, A. Vallabhaneni, B. Liao, J. Mendoza, O. Restrepo, X. Ruan, and G. Chen. First-principles simulation of electron mean-free-path spectra and thermoelectric properties in silicon. *EPL (Europhysics Letters)*, 109(5):57006, 2015.

[113] K. Esfarjani, G. Chen, and H. Stokes. Heat transport in silicon from first-principles calculations. *Physical Review B*, 84(8):085204, 2011.

[114] M. Bendsøe and N. Kikuchi. Generating optimal topologies in structural design using a homogenization method. *Computer methods in applied mechanics and engineering*, 71(2):197–224, 1988.

[115] Qing Li, Grant P Steven, Osvaldo M Querin, and YM Xie. Shape and topology design for heat conduction by evolutionary structural optimization. *International Journal of Heat and Mass Transfer*, 42(17):3361–3371, 1999.

[116] Q. Li, G. Steven, Y. Xie, and O. Querin. Evolutionary topology optimization for temperature reduction of heat conducting fields. *International Journal of Heat and Mass Transfer*, 47(23):5071–5083, 2004.

[117] T. Yamada, K. Izui, and Shinji Nishiwaki. A level set-based topology optimization method for maximizing thermal diffusivity in problems including design-dependent effects. *Journal of Mechanical Design*, 133(3):031011, 2011.

[118] K. Suzuki and N. Kikuchi. A homogenization method for shape and topology optimization. *Computer methods in applied mechanics and engineering*, 93(3):291–318, 1991.

[119] G. Rozvany, M. Zhou, and T. Birker. Generalized shape optimization without homogenization. *Structural optimization*, 4(3-4):250–252, 1992.

[120] M. Bendsøe and O. Sigmund. Material interpolation schemes in topology optimization. *Archive of applied mechanics*, 69(9-10):635–654, 1999.

[121] Y. Xie and G. Steven. A simple evolutionary procedure for structural optimization. *Computers & structures*, 49(5):885–896, 1993.

[122] M. Yu Wang, X. Wang, and D. Guo. A level set method for structural topology optimization. *Computer methods in applied mechanics and engineering*, 192(1):227–246, 2003.

[123] J. Stegmann and E. Lund. Discrete material optimization of general composite shell structures. *International Journal for Numerical Methods in Engineering*, 62(14):2009–2027, 2005.

[124] G. Vanderplaats. *Multidiscipline design optimization*. Vanderplaats Research & Development, Incorporated, 2007.

[125] W. Hare, J. Nutini, and S. Tesfamariam. A survey of non-gradient optimization methods in structural engineering. *Advances in Engineering Software*, 59:19–28, 2013.

[126] L. Gosselin, M. Tye-Gingras, and F. Mathieu-Potvin. Review of utilization of genetic algorithms in heat transfer problems. *International Journal of Heat and Mass Transfer*, 52(9):2169–2188, 2009.

[127] E. Dede. Simulation and optimization of heat flow via anisotropic material thermal conductivity. *Computational Materials Science*, 50(2):510–515, 2010.

[128] P. Thoutireddy and M. Ortiz. A variational r-adaption and shape-optimization method for finite-deformation elasticity. *International Journal for Numerical Methods in Engineering*, 61(1):1–21, 2004.

[129] H. Dong, B. Wen, and R. Melnik. Relative importance of grain boundaries and size effects in thermal conductivity of nanocrystalline materials. *Scientific reports*, 4:7037, 2014.

[130] H.-S. Yang, G.-R. Bai, L. Thompson, and J. Eastman. Interfacial thermal resistance in nanocrystalline yttria-stabilized zirconia. *Acta Materialia*, 50(9):2309–2317, 2002.

[131] C.-W. Nan and R. Birringer. Determining the kapitza resistance and the thermal conductivity of polycrystals: A simple model. *Physical Review B*, 57(14):8264, 1998.

[132] R. Radovitzky, A. Seagraves, M. Tupek, and L. Noels. A scalable 3d fracture and fragmentation algorithm based on a hybrid, discontinuous galerkin, cohesive element method. *Computer Methods in Applied Mechanics and Engineering*, 200(1):326–344, 2011.

[133] I. Dooley, S. Mangala, L. Kale, and P. Geubelle. Parallel simulations of dynamic fracture using extrinsic cohesive elements. *Journal of Scientific Computing*, 39(1):144–165, 2009.